January 2011

# Structural And Thermophysical Property Studies Of Metallic Liquids And Glasses Using The Beamline Electrostatic Levitation Technique

Nicholas Mauro
*Washington University in St. Louis*

WASHINGTON UNIVERSITY IN ST. LOUIS

Department of Physics

Dissertation Examination Committee:
Kenneth F. Kelton, Chair
William E. Buhro
Patrick C. Gibbons
Kenneth Jerina
Zohar Nussinov
Li Yang

# STRUCTURAL AND THERMOPHYSICAL PROPERTY STUDIES OF METALLIC LIQUIDS AND GLASSES USING THE BEAMLINE ELECTROSTATIC LEVITATION TECHNIQUE

by

Nicholas Anthony Mauro

A dissertation presented to the
Graduate School of Arts and Sciences
of Washington University in
partial fulfillment of the
requirements of the degree
of Doctor of Philosophy

May 2011

St. Louis, Missouri

**ABSTRACT FOR THE DISSERTATION**

Structural and Thermophysical Property Studies of Metallic Liquids and Glasses Using the Beamline Electrostatic Levitation Technique

by

Nicholas Anthony Mauro

Doctor of Philosophy in Physics

Washington University in St. Louis, 2011

Professor Kenneth F. Kelton, Chairperson

An accurate description of atomic structures is at the heart of an improved understanding of the properties of condensed solids. By correlating structural information from high energy synchrotron X-ray diffraction with thermophysical properties important insights have been gained into the role of local structural evolution in undercooling and glass formation. Here, the results of a number of investigations into the structures and properties of some amorphous phases will be presented and analyzed. Phase separation in $Al_{88}Y_7Fe_5$ is identified prior to devitrification and is proposed as an explanation for extremely high observed nucleation rates. The development and construction of the Beamline Electrostatic Levitation Technique (BESL), which has shown increased utility over the past several years as an important probe of metallic systems, will be presented. Using BESL, atomic structures in equilibrium and supercooled liquids of $Zr_{80}Pt_{20}$ are explored using Reverse Monte Carlo methods, which indicate the presence of medium range atomic order that is dominated by Pt-Pt correlations. The thermophysical properties and atomic structures in the bulk metallic glass forming Ni-Nb and Ni-Nb-Ta liquids are examined. The high glass formability and low glass formability compositions

are compared and important differences are discussed. Finally, the X-ray structure factors and densities for liquid aluminum from 1123K to 1273K are presented and atomic structures as a function of temperature have been constructed from the diffraction data with Reverse Monte Carlo fits.

**Acknowledgements**

First and foremost, I would like to thank my advisor, Prof. Ken Kelton, for his guidance, support, endless patience and great faith in our scientific endeavors. His dedication to his students and enthusiasm for this work in the midst of the cacophony of voices screaming for attention has inspired many to strive for great works: I count myself among them. I thank him for this.

I would also like to thank Prof. Pat Gibbons, Prof. Zohar Nussinov and Dr. Anup Gangopadhyay for their guidance on a number of topics. Their expertise and advice made much of this work possible. Prof. Pat Gibbons was helpful in proof reading portions of this dissertation and I thank him this. I would also like to specifically thank Alan Goldman, Doug Robinson and Andreas Kreyssig for their incredibly valuable discussions on the topics of scattering and the development of the BESL—in every conversation I learned something new and valuable. I am also grateful for the collaboration developed with D. Holland-Moritz and D. Herlach of the DLR that made the BESL possible. Specifically, I wish to acknowledge Stefan Klein for sharing his experiences and providing key insights into the development of the instrument, hosting my first visit to Cologne, and joining the first BESL campaign. *Ich bin sehr dankbar*. Much of the BESL construction was possible because of the guidance of the shop guys: Todd Hardt, Denny Huelsman, and Tony Biondo.

Victor Wessels, James Bendert and Kisor Sahu all have expertise above and beyond my own and who taught and continue to teach me a tremendous amount: They are indispensible colleagues. My fellow BESL compatriots and graduate students, Adam Vogt, Matt Blodgett, Jen Gewin and Gus Rustan (of Iowa State University) I thank for useful discussions and dedication to the cause.

I would like to acknowledge the agencies that funded this work: NSF under grants DMR-06-06065, DMR-08-56199, DMR- 0815715; NASA under grants NNX07AK27G and NNX09AJ19H. The synchrotron measurements were made on the MUCAT beam-line at the Advanced Photon Source. Work in the MUCAT Sector at the APS, and the Ames Laboratory was supported by the Department of Energy, Basic Energy Sciences, under Contract No. DS-AC02-07CH11358. Use of the Advanced

Photon Source was supported by the U. S. Department of Energy, Office of Science, Office of Basic Energy Sciences, under Contract No. DE-AC02-06CH11357.

None of this work would have been possible without my family. For my parents, Tony and Jodie, my sister Bri, my Aunt Mo, Anne and Mike, Kate and Mark, and Molly: There are no words.

Above all, I am thankful to my wife, Emily, who knew what she was getting into and, for reasons that I will never fully understand, supported me each and every day. You are everything. Finally, I dedicate this work to Lima, who is approximately |----------| (this big) at the time of the writing of this dissertation.

## Table of Contents

## List of Figures

## Abbreviations and Common Terms

| | |
|---|---|
| 3DAP | Three-Dimensional Atom Probe Tomography |
| ADC | Analog to Digital Convertor |
| ANL | Argonne National Laboratory |
| APS | Advanced Photon Source |
| APT | Atom Probe Tomography |
| BCC | Body-Centered Cubic |
| BESL | Beamline Electrostatic Levitator |
| BESL2009 Campaign | Series of BESL experiments conducted in August, 2009, at the APS. |
| BESL2010 Campaign | Series of BESL experiments conducted in August, 2010, at the APS. |
| BMG | Bulk Metallic Glass |
| BOO | Bond Orientation Order |
| CRMC | Constrained Reverse Monte Carlo |
| DAC | Digital to Analog Convertor |
| DFT | Density Functional Theory |
| DLR | Deutsche Zentrum für Luft- und Raumfahrt (German Aerospace Center) |
| DRPHS | Dense Random Packing of Hard Spheres |
| DRPSS | Dense Random Packing of Soft Spheres |
| DSC | Differential Scanning Calorimetry |
| DTA | Differential Thermal Analysis |
| EAM | Embedded Atom Method |
| EDS | Energy Dispersive X-ray Spectroscopy |
| EML | Electromagnetic Levitator |
| ESL | Electrostatic Levitator |
| ETM-LTM | Early Transition Metal-Late Transition Metal |
| EXAFS | Extended X-ray Absorption Fine Structure |
| FCC | Face-Centered Cubic |
| GFA | Glass Forming Ability |
| GUI | Graphical User Interface |
| HA | Honeycutt Anderson |
| HC | Hypernetted-Chain |
| H.V. | High Voltage |
| HCP | Hexagonal Closed-Packed |
| HRTEM | High Resolution Transmission Electron Microscopy |
| ISRO | Icosahedral Short Range Order |
| LINAC | Linear Accelerator |
| LJ | Lennard-Joens |
| LMI | Linear Matrix Inequality |
| LRO | Long Range Order |

| | |
|---|---|
| LSW | Lifshitz ,Slyozov, and Wagner |
| LTM-TM | Late Transition Metal-Transition Metal |
| MCT | Mode Coupling Theory |
| MD | Molecular Dynamics |
| MIMO | Multiple Input-Multiple Output |
| M-MLD | Metal-Metalloid |
| MRO | Medium Range Order |
| MS | Melt Spinning |
| MSDS | Materials Safety Data Sheets |
| M-TM | Metal-Transition Metal |
| MUCAT | Midwestern Universities Collaborative Access Team |
| NESL | Neutron Electrostatic Levitator |
| NIST | National Institute of Standards and Technology |
| PPCF | Partial Pair Correlation Function |
| PSD | Position Sensitive Detector |
| PSF | Partial Structure Factor |
| PY | Percus-Yevick |
| RDF | Radial Distribution Function |
| RF | Radio Frequency |
| RMC | Reverse Monte Carlo |
| SRO | Short Range Order |
| $T_0$ | Ideal Glass Transition Temperature; Room Temperature |
| TE | Thermionic Emission |
| TEC | Thermoelectric Cooling |
| TEM | Transmission Electron Microscopy |
| $T_g$ | Glass Transition Temperature |
| $T_L$ | Liquidus Temperature |
| VI | Voronoi Polytetrahedral |
| VUV | Vacuum Ultra Violet |
| WU-BESL | Washington University Beamline Electrostatic Levitator |
| XRD | Low Energy X-ray Diffraction |

# Chapter 1

## Introduction

Liquids comprise one of the three states of matter and from a structural perspective, one of the most diverse and interesting. Knowledge of the structural and chemical properties of a liquid and an understanding the evolution of atomic order across multiple length scales as a liquid approaches and passes through a phase transformation is crucial for the development of materials for any application. Liquids, by definition, do not possess crystalline long range order (LRO), but that is not to say they are not ordered. It is now widely understood that liquids have a high degree of atomic short range order (SRO), and some liquids are also known to have a high degree of medium range order (MRO), extending on to nanometer length scales. Crystallization of a liquid is a highly complicated process; a competition between thermodynamic driving forces to phases that are accessible and the kinetic rearrangement of atoms into those phases. By rapidly cooling a liquid, the equilibrium phases can be bypassed. Nucleation, the first step in crystallization, can be avoided and the liquid can be solidified into an amorphous state, called a glass.

The glassy state is actually quite ubiquitous, although it usually isn't a focus in a standard condensed matter course. Amorphous silicates are common in window glass. They occur naturally as in obsidian, for example, the high-silicon solidification product of rhyolithic lava flows. The most likely appearance of amorphous materials in a standard solid state physics course would be in the context of photovoltaics where amorphous silicon has been utilized as a cheap [1], but low efficiency, material for solar cells. Most systems can be formed in the glassy state if the cooling rate is sufficiently

high. An example is amorphous metals, or metallic glasses, discovered almost 50 years ago. The first metallic glasses required extremely high cooling rates for their formation (of order a million degrees per second), limiting their usefulness. Recently alloys have been discovered that form glasses at cooling rates similar to those used for common silicate glasses. These glasses have unique structural properties such as high strength to weight ratio, high hardness and corrosion resistance [2, 3] that that make them technologically useful. The study of these new metallic glasses is an active area of research.

Fundamental to the formation of metallic glasses is the phenomenon of undercooling, also known as supercooling, where a liquid can be cooled below its equilibrium liquidus temperature without crystallizing. The liquidus is the temperature, at a specific composition, above which the system is completely liquid and below which an equilibrium mixture of liquid and crystallites can coexist. At a sufficiently low temperature, the undercooled liquid can transform into a solid amorphous phase, a process that is still not well understood. A metallic glass is characterized by a critical casting thickness (the maximum thickness that can be cast into glass) and a related critical cooling rate (how quickly the system must be cooled to form this phase). The cooling rate varies by some 11 orders of magnitude, from $10^{10}$ K/sec for pure Ni [4] to $10^{-1}$ K/sec for some Pd-based alloys. The reason why some alloys can be readily cooled into a glass and others cannot is one of the fundamental questions that the studies described in this thesis attempt to address. While some links between local atomic structure and glass formability (GFA) have been established [5] there have been other experimental and theoretical studies that have demonstrated the importance of atomic

dynamics and kinetics [6-9] in understanding GFA. In this thesis, the relationship between local topological and chemical order in the liquid and the phenomena of undercooling, the nucleation barrier, and glass formation is examined in some select systems. A variety of advanced techniques are discussed including the Beamline Electrostatic Levitator (BESL) and Reverse Monte Carlo (RMC) simulation techniques used in these studies. This introductory chapter will provide an overview of the basic concepts of non-crystalline order, glass formability, and the importance of studying "Bulk Metallic Glasses" (BMG's). It also contains a discussion of simulation and scattering techniques used to measure and quantify local atomic order and an overview of the thesis.

### 1.1. Non-Crystalline Order

The concept of non-crystalline order underlies much of the work discussed in this thesis. Normal liquids lack long-range order; the same is true of two-dimensional liquids or partially ordered liquid crystals. The smallest sub units of these structures—atoms, molecules or larger macromolecules—have translational, vibrational and rotational degrees of freedom. However, even with the high degree of translational freedom, liquids have a high degree of SRO [10-13]. When the liquid forms a glass, it loses the translational degrees of freedom while the SRO is retained. In some cases, the SRO in the glass is similar to that in the corresponding equilibrium crystal phase. To illustrate this point, consider the structural difference between crystalline quartz and amorphous silica as projected in two dimensions in Figure 1.1. The quartz structure (this particular form is called "critobalite") has periodic LRO, but also exhibits very similar SRO as the amorphous silica. The bond angle distribution varies between the two, but the nearest-

neighbor distances are nearly identical[1]. This is clearly shown in X-ray diffraction patterns from the two materials [14].

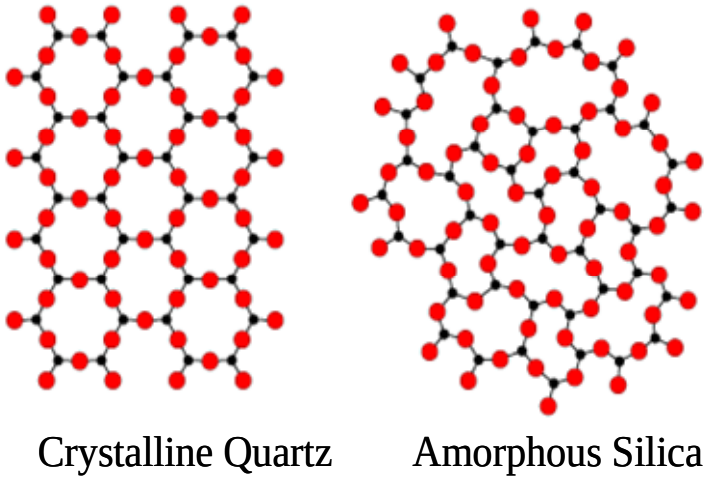


**Figure 1.1**- Schematic of the atomic structures of crystalline quartz and amorphous silica. The actual structures are three dimensional. The silicon atoms are shown as black and the oxygen atoms as red.

Amorphous structures can be grouped into two categories: tetrahedrally coordinated networks, common in semiconductors, (silicate glasses and chalcogenide glasses, i.e. those based on S, Se and Te) and metallic glasses, generally found in multi-component alloys [15]. The local structures of glasses and liquids are very similar, as many diffraction and simulation studies have shown, and we tend to think of the glass structure as a "frozen" liquid. The changes that occur during this glass formation motivate this work.

[1] The actual three-dimensional structure is most readily described as a network of interconnected $SiO_4$ tetrahedra, called a "tectosilicate." In Figure 1.1, the Si-O-Si bond links two tetrahedra and is not straight (180°) as shown, but forms an angle of 144°, or 36° out of the page.

## 1.2. Properties of Glasses and the Glass Transition

The most direct definition of a glass is "an amorphous solid that exhibits a glass transition." Network and metallic glasses are incredibly varied in their structure [16], and liquids have structures that are very similar to glasses in many cases [10, 11, 13]. When most liquids are cooled very slowly, thermodynamics dictates that a first order phase transition to a crystal or phase mixture of crystals occurs [17]. However, as the cooling rate increases, the formation of this equilibrium crystal phase mixture can be bypassed and the liquid freezes into an amorphous state. The temperature at which this happens, $T_g$, is called the glass transition temperature. Certain extensive thermodynamic variables (volume, entropy, enthalpy) are continuous through the glass transition however, quantities based on their derivatives (i.e. the specific heat, $C_p$, thermal expansion, $\alpha_T$, and isothermal compressibility, $\kappa_T$,) change abruptly from liquid-like to crystal-like values. The specific heat is almost identical in the crystal and amorphous phases because it is dominated by vibrational degrees of freedom [17]. The excess $C_p$ above $T_g$ is due to configurational degrees of freedom. This is illustrated in Figure 1.2, showing the classic result from Chen and Turnbull that gave the first thermodynamic evidence for a glass transition in a metallic glass [11, 18]. Striking is the similarity between the specific heat of the amorphous solid and crystalline solid below $T_g$. The behavior of the thermal expansion with temperature is similar to that of the specific heat, increasing over a very narrow temperature range near $T_g$.

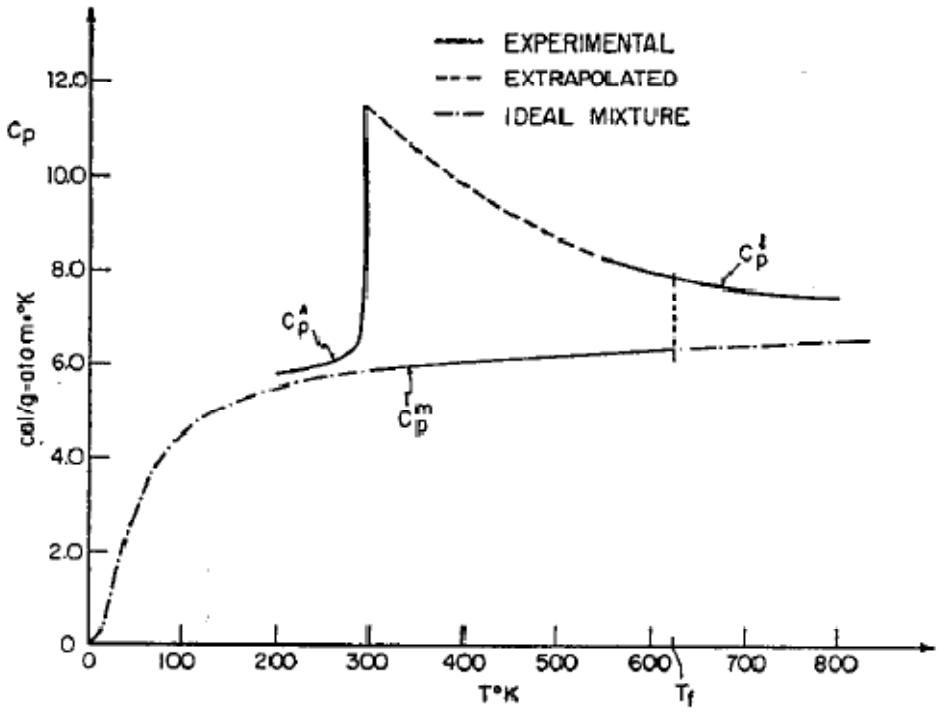


**Figure 1.2-** The specific heat signature of the glass transition in the metallic glass $Au_{77}Si_{9.4}Ge_{13.6}$. From [18].

When the liquid is cooled below the equilibrium liquidus temperature, it either crystallizes, which is an exothermic event, or continues to cool in the liquid phase. As it does, the viscosity increases, reflecting a decrease in atomic diffusion as described by the Einstein-Stokes relation [19]. Eventually, the viscosity becomes so high ($10^{12}$ or $10^{13}$ Poise) that the liquid "freezes" into a glass. The temperature of this transition, $T_g$, is not thermodynamically well defined, but depends on the cooling rate and varying quite a bit (20% for silicates, less for metals) with that rate. The free volume theory put forth by Turnbull and Cohen [20, 21] relates the cooling rate and $T_g$ implying that the kinetic aspects of the transition cannot be ignored.

The existence of a transition from a supercooled liquid to a glass was argued thermodynamically by Kauzmann in 1948 [11]. The excess specific heat above the crystalline value, measured for a supercooled liquid above $T_g$, is due to configurational degrees of freedom. As already noted, the cooling rate has a strong influence on $T_g$: The lower the cooling rate the lower $T_g$ is. Kauzmann argues that there is a thermodynamic lower limit on the glass transition. The lowest temperature at which the supercooled liquid can exist before freezing is governed by the requirement that the area under the $C_p$ vs. ln($T$) curve, the entropy, must be greater than or equal to the change in entropy upon crystallization of the liquid. Schematically, this is shown in Figure 1.3. In Figure 1.3b., the entropy difference between the glassy, liquid and crystalline phases are schematically shown. The rapid decrease in the difference in entropy near the glass transition is extrapolated (dashed line) to the "ideal glass transition temperature," $T_0$, where the difference goes to zero.

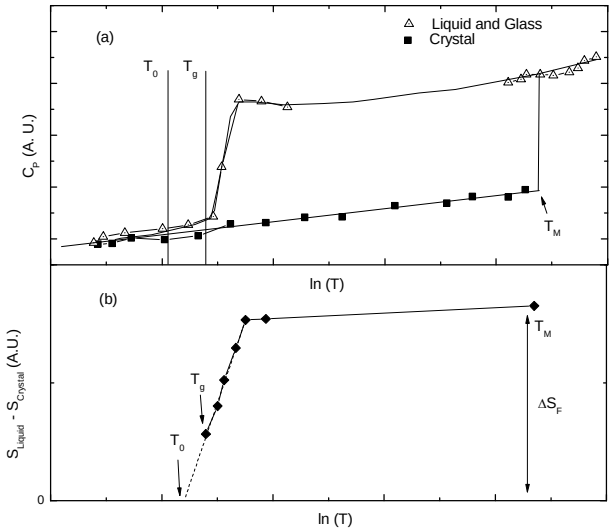


**Figure 1.3-** (a) Schematic diagram of specific heats of glassy, liquid, and crystalline phases in a glass forming compound, The data are plotted so that the integrated area under the curves gives the entropy. (b) The difference in entropy between the glassy, liquid, and crystalline phases. The entropy of fusion, $\Delta S_F$, is shown at the melting temperature, $T_m$. The rapid decrease in the difference in entropy near the glass transition is extrapolated (dashed line) to the "ideal glass transition temperature," $T_0$, where the difference goes to zero.

Experimentally, $T_g$ cannot be lower than $T_0$ or the entropy would be smaller than that of the crystal, violating the Third Law of Thermodynamics. This is often referred to as the "entropy crisis." In reality, the existence of glassy state with zero excess entropy, with $T_g$ near $T_0$, is not realistic given the infinitely small nucleation barrier near this temperature [11]. All experiments to date have shown that the entropy crisis is avoided and solidification intercedes at $T_g$ thereby vitrifying the sample before the ideal glass transition temperature. This has been interpreted by Gibbs and DiMarzo [22] to show that there are thermodynamic constraints on the kinetic influence on $T_g$.

While the glass transition has some properties of a second-order transition in the Ehrenfest scheme, this simple classification proves to be insufficient when considering all the experimental data. That the glass transition temperature is a strong function of cooling rate and thermal history indicates that the kinetic factors play in important role, more than would be expected if it were a pure thermodynamic transition [17]. A second order phase transition is distinguished from a first-order in that thermodynamic parameters such as the enthalpy and entropy change continuously. Considering the liquid as state 1 and the glass as state 2, at $T_g$, for example, the changes in the temperature and pressure must be such that $dS_1 = dS_2$, or

$$\left(\frac{\partial S_1}{\partial T}\right)_p dT + \left(\frac{\partial S_1}{\partial P}\right)_T dP = \left(\frac{\partial S_2}{\partial T}\right)_P dT + \left(\frac{\partial S_2}{\partial P}\right)_T dP \,. \tag{1}$$

By manipulating this equation, and using the definition of the specific heat, $C_{p,}$ as well as the Maxwell relation,

$$\left(\frac{\partial S}{\partial P}\right)_T = -\left(\frac{\partial V}{\partial T}\right)_P \tag{2}$$

the change in the glass transition temperature and the change in pressure can be related:

$$\frac{dT_g}{dp} = \frac{\Delta\kappa_T}{\Delta\alpha_T} \tag{3}$$

where $\Delta\kappa_T$ is the change in isothermal compressibility between the liquid and glassy states and $\Delta\alpha_T$ is the change in thermal expansion between the liquid and glassy states. This expression is almost never obeyed [17], indicating that the glass transition is likely not a pure second order phase transition. It also seems likely that other one parameter models can only partially explain the types of behavior seen [23]. In the Free Volume

Model referenced earlier [20, 21], the liquid is considered a collection as atomic hard spheres. The volume in the structure not occupied by the spheres is called the "free volume." In most cases these spheres are contained in a cage of surrounding atoms and cannot move; they simply oscillate thermally in the cage. These can be viewed as solid-like regions. In other parts of the liquid, however, the local free volume is larger and it is possible for the vibrations to cause a translation' these regions can be viewed as liquid-like. The free volume is shared communally and no change in internal energy is required to redistribute it. As the temperature is lowered the free volume contracts, giving rise to more solid-like regions, causing the atomic mobility to sharply decrease and eventually leading to glass formation. Cohen and Grest [24] developed these ideas further, arguing that the glass transition is a percolation transition of the solid-like regions. They conclude that the glass transition in their model is likely first order, which does not fit the experimental evidence. There are other problems with this approach. First, it is assumed that thermal expansion is linear which is generally not the case and that non-directional bonding is dominant. This last assumption makes the model better suited for metallic liquids, but the utility of the model for understanding the glass transition is likely qualitative.

Glasses have been characterized according to how the viscosity varies as a function of temperature. The logarithm of the viscosity is shown as a function of $T_g/T$, for a range of different glasses in Figure 1.4. Angell first noted the distinction between strong and fragile glasses [25]. For strong glasses, such as vitreous $SiO_2$, the viscosity increases exponentially as the temperature is lowered,

$$\eta = \eta_o e^{W/k_B T} . \tag{4}$$

The activation barrier, *W*, is a constant, giving a straight line, as shown in Figure 1.4. Non-Arrhenius behavior is observed in fragile glasses [26], corresponding to an activation barrier that increases with supercooling. The free volume model and the Adam-Gibbs entropy model [27] both predict non-Arrhenius viscosity. The entropy model dictates that the activation energy is inversely proportional to the configurational entropy, relying on the assumption that the *size* of a cooperatively rearranging region depends on the configurational entropy. This implies an increase in cooperativity upon cooling which is difficult to imagine given the decrease in thermal energy. However, the observation that different quenching conditions can subtly change the viscosity behavior suggests that the glassy atomic structure, which changes with cooling rate, is linked to fragility and supercooling.

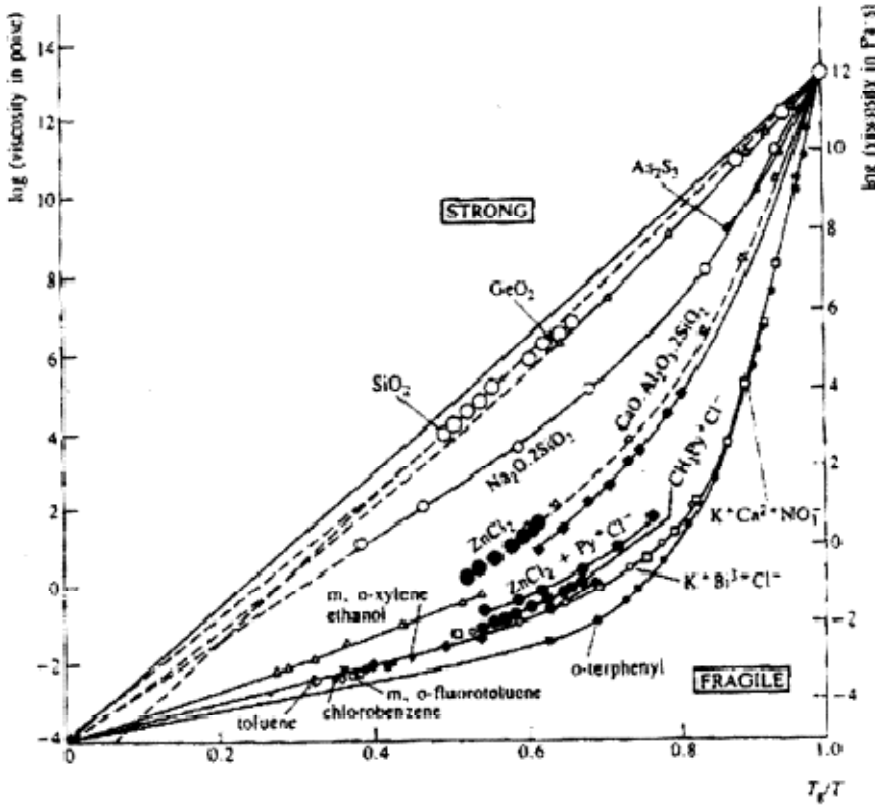


**Figure 1.4-** Viscosities of various materials scaled to the observed $T_g$. Strong glasses display Arrhenius behavior (straight line) and fragile ones deviate from a simple activated process. Plot reproduced from [28].

Models of the glass transition have been focused on explain this behavior and the evidence for strong to fragile transitions [29] are emerging. Mode Coupling Theory (MCT) [30] has emerged as a candidate that presents a dynamical picture of the freezing of atoms into amorphous structures. In this view, an energy landscape exists (of dimension 3N +1 for a system of N particles), which maps to the accessible atomic configurations.

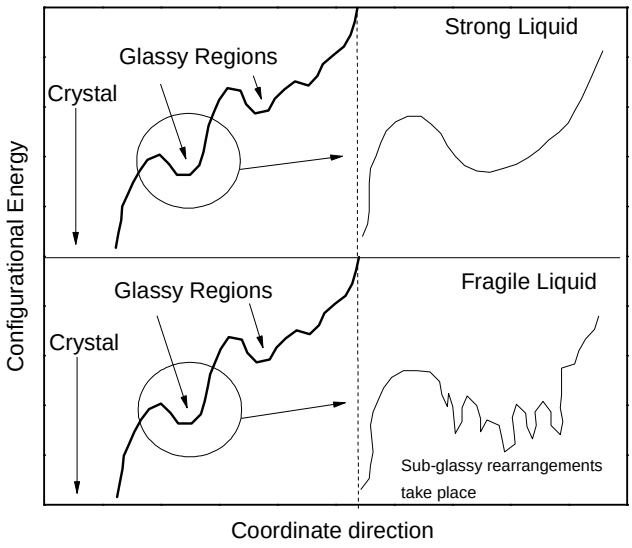


**Figure 1.5-** Energy landscape for liquid along one of the 3N +1 coordinate directions. An ergodic liquid has a large energy compared to the glassy regions. Strong liquids (top panel) have smooth glassy regions while fragile liquids (bottom panel) have local energy peaks and valleys within glassy rearrangements leading to sub-glassy or β-relaxations.

At high temperatures, the kinetic energy of the particles is large and the liquid is ergodic. As the temperature is lowered, the glass transition occurs when the liquid becomes trapped in a metastable state. Two categories of freezing occur: α-relaxation corresponds to primary freezing into local minima. Inside of these minima, β-relaxation occurs, in which "sub-glassy" rearrangements take place where local rearrangements are accessible or long range motion is not energetically favorable. Fragile glasses have many sub-glassy regions, while strong glasses do not. The entire dynamical freezing process is then a competition between the liquid exploring the crystal global minimum and the local glassy minima. β-relaxation has been observed readily in polymer glasses [11, 31, 32], where this relaxation corresponds to rotational or vibrational rearrangement

of small side-groups in polymers. The structural origin of β-relaxation in glasses is an area of open debate [33-35]. β-relaxation has been observed in fragile metallic glasses using dynamical mechanical properties measurements [36-40] In metallic glasses, the difficulty in observing β-relaxation directly in strong glasses [41] occurs because the relaxations are not well separated and the slow dynamics of β-relaxation are often obscured. Recently, evidence for a mode-coupling transition has been presented in ESL studies of Zr-based Vitreloy alloys [42], which may suggest systems in which structural aspects of the glass transition can be probed using the Beamline Electrostatic Levitation (BESL) technique, discussed in Chapter 4.

Energetic and steric aspects of amorphization and the glass transition have been considered since the work of Bernal and Finney, who constructed the first models of structurally frustrated systems. Bernal suggested that the important structural features of an amorphous liquid could be captured by randomly close packed ball bearings [43]. If the atoms in metals are approximated as hard spheres without long range interatomic potentials, structures without extended LRO exhibited the most efficient packing when they were composed primarily of randomly oriented tetrahedra. Three-dimensional space cannot be filled with the equilateral tetrahedra and the structures produced had “holes” or distortions in the structure. Finney further extended this approach [44] for larger systems calculating the coordination number, radial distribution function and used the voronoi polytetrahedral approach [44, 45] to identify local topology around atoms. Structural models based on the dense random packing of hard spheres (DRPHS) [44] generally show excellent agreement with the first peak in the static structure factor of metallic liquids [11]. Additionally, Bernal and Finney observed voronoi tessellation of the

DRPHS many five-edged faces, suggesting icosahedral-like structures. These approaches don't propose fundamental links between observed structural features and the interactions that underlie those features. We now consider models that propose links between interatomic potentials and structure.

Perhaps the first attempt to determine the pair correlation function, $g(r)$, was Kirkwood in the 1930s [46]. In this approach, integral equations are obtained for the pair correlation function by considering the higher-order correlation functions, empirical coupling parameters describe the magnitude of pair-wise nearest neighbor interactions, and they utilize a mean field approach for higher order interactions. These equations are difficult to solve and numerical solutions tend to reproduce basic features of experimentally determined pair correlation functions. Similar approaches differ in details (i.e. Born-Green-Yvon approach [10]), producing similar qualitative behavior in $g(r)$ while relying on the superposition approximation, which states that the energy of a local collection of atoms is the superposition of pair-wise potential energies.

The Percus-Yevick (PY) [10, 19, 47] and Hypernetted-Chain (HC) [10] equations consider contributions to the total correlation function from direct pair interaction and a small contribution from a third particle. The difference between the two manifest in the assumed relationship between the pair interaction, $\phi(r)$, and the pair correlation function, $g(r)$. The Ornstein-Zernike relation [10, 19, 48] (Equation 1) describes how the total correlation function, $h(r)$, relates to the direct pair correlation function, $f(r)$,

$$h(r) = f(r) + \rho_0 \int f(|\mathbf{r} - \mathbf{r}'|) h(\mathbf{r}') d\mathbf{r}' \quad (1)$$

where

$$f(r) \equiv \frac{1}{8\pi^3 \rho_0} \int \left[ \frac{S(q)-1}{S(q)} \right] \exp(-i\mathbf{q} \cdot \mathbf{r}) dq \,. \tag{2}$$

The PY model assumes a very strong dependence of *f(r)* on the pair interaction,

$$f_{PY}(r) = g(r)(1 - \exp(\phi(r))/T) \tag{3}$$

while the HC model only assumes a logarithmic relationship.

$$f_{HC}(r) = g(r) - 1 - \ln(g(r)) - \phi(r)/k_B T \,. \tag{4}$$

The PY equation, when applied to hard sphere models [49, 50], reproduces the basic features of liquid metals, however the deviations from experimental values at high momentum transfer is severe. The solution of the PY equation for hard spheres depends only on the packing fraction [50] which must be varied greatly between simple metallic systems, questioning the physicality of the model. An extension of the hard sphere PY approach for binaries was developed by Ashcroft and Langreth [51] with similar results. The dense random packing of soft sphere (DRPSS) has also been modeled using the PY equation [10, 47], which attempt to reproduce effective ion-ion and electron interactions and replaces the hard sphere $\phi(r)$ with various analytical forms including the Lennard-Jones potential [52]. In this work, Weeks, Chandler and Andersen found much better agreement between the calculated and experimental structure factors at high momentum transfer, but also found artifacts at low momentum transfer not observed in the DRPHS.

### 1.3. Bulk Metallic Glasses (BMGs)

As mentioned, although the first metallic glass was discovered in 1960 by Klement, Willens, and Duwez in $Au_{75}Si_{25}$ [53] the liquid had to be cooled at an extremely rapid rate ($10^5$ to $10^6$ K/s) limiting its technological usefulness. The key to glass formation is to

delay crystallization to the accessible intermetallic phases that are in competition with the glassy phases. If the stability of the liquid between the liquidus temperature, $T_L$, and $T_g$ were increased, this would lead to lower critical cooling rates. Following these ideas, and eliminating heterogeneous nucleation, the first bulk metallic glasses (BMGs), formed at more moderate cooling rates, were discovered in the 1980's and 1990's by Turnbull, Inoue, and others [54-56]. These had critical casting thicknesses of approximately 1 cm and cooling rates on the order of $10^1$ K/s. The first commercially viable BMG was discovered in 1992 by Peker and Johnson in $Zr_{41.2}Ti_{13.8}Cu_{12.5}Ni_{10.0}Be_{22.5}$ (Vitreloy1) [56].

The structures of metallic glasses are very sensitive to the conditions of the preceding quench and thermal processing of the glass. Annealing below $T_g$ and even room temperature aging can produce structural relaxation, which can be measured with scattering experiments [57] and by thermal analysis [58, 59]. When the temperature is reduced below the $T_L$, the free energy of the supercooled liquid is higher than that of the competing crystal phase mixture. The difference between these two free energies drives crystallization. The driving force increases with supercooling [60] as the liquid deviates further from thermodynamic equilibrium. Understanding the competition between thermodynamics, kinetics and structure is key to understanding glass formation.

Many pure elements have hexagonal-close packed (HCP) or face-centered cubic (FCC) structures at room temperature. However, pure metallic liquids have shown little close packed structures in their equilibrium and supercooled states [61]. Further, from a bonding enthalpy perspective, compared to FCC and HCP clusters, the icosahedron has a higher rotational symmetry, establishes more bonds [16], and is a more energetically stable structure. Experimental evidence supports the prevalence of icosahedral and

distorted icosahedral short range order in a wide range of metallic liquids [5, 61-63], as was originally postulated by Frank [64] in 1952. However, if one tries to pack a three dimensional space with icosahedra, frustration arises because of the well-known inability to reconcile 5 fold rotational symmetry and long range periodicity. Structural models of metallic glasses have focused on this frustration and some successes have been achieved by correlating glass formation with the correct elements and concentrations to form local clusters that fill space efficiently. For instance, D. Miracle describes a structural model for metallic glasses where solute centered clusters are used to decorate closed-packed structures to form a model for the glass. Good agreement was found for certain classes of alloys between predicted and experimentally observed optimum glass forming composition.

While the DRPHS and DRPSS models provide some structural information for real liquids and glasses, they do not emphasize the chemical order that thermodynamic models [65] and measurements [66-68] suggest exists. Even in the DRPHS some systems show solute-solute avoidance, but these trends don't extend intuitively into multi-component systems. The strong chemical order observed in the Metal-Transition Metal (M-TM) and Late Transition Metal-Transition Metal (LTM-TM) glasses cannot be explained by the DRPHS and appears to support a stereochemical approach [69, 70]. In this model short range order is well defined; clusters containing 10-14 atoms in the amorphous phase are very similar in average structure to ones in the equilibrium crystal phases. The difference between the crystal and the glass is then a difference in MRO arising from the ways in which the clusters are packed. Again, a length scale dichotomy is used where the local order is distinguished, fundamentally, from cluster packing [11].

Using this approach, Gaskell [69, 70] has reproduced the structures of some Metal-Metalloid (M-MLD) and LTM-NM glasses. The strength of the stereochemical approach is in providing a distinction between local clustering and the linking of those clusters through chains and other networks [71], although the model details vary greatly [72-76].

The fundamental assumption in the stereochemical approach that local ordering is crystal-like is challenged by recent experimental studies. Shen *et al.* [5], for example, have shown that the local order is closer to that of metastable icosahedral phases than the equilibrium crystal phases[2]. Recently, Sheng *et al.* [77] combined experimental and simulation studies of M-MLD, Early Transition Metal-Late Transition Metal (ETM-LTM) and Late Transition Metal-Transition Metal (LTM-TM) glass forming liquids to confirm that clustering and MRO exist across families of glass formers, but that the SRO is not necessarily crystal-like. Although these studies validate the clustering approach, the alloys could readily be deconstructed into solute and solvent. Many systems of interest, however, don't fall into this category, such as certain binary BMGs, discussed below.

Details of the chemistry and topology of local atomic structures are important for determining the properties of good and poor glass formers, and for tailoring these materials for applications. The fitting techniques used to construct structural models from experimental data will be discussed in detail in Chapter 2. For multi-component BMGs, experimental data from multiple sources, such as X-ray and Neutron diffraction data, EXAFS measurements and results from Molecular Dynamics (MD) simulations, are required to obtain realistic structures. While the best BMGs are found in multi-component alloys, often containing five or more elements, the simpler binary BMGs are

[2] This topic will be explored in the Zr-Pt system, where the *i*-phase also forms.

better suited for fundamental studies. Reverse Monte Carlo (RMC) and MD simulations become increasingly more difficult as the number of elements increases. At least three systems have been found that form 2 mm thick binary BMGs: Cu-Zr [63, 78-82], Cu-Hf [83, 84], and Ni-Nb [85]. Pd-Si [86] also forms a BMG, but requires fluxing. The binary BMGs are popular because they are often the base compositions for more complicated and better glass formers. These systems also form glasses over a wide composition range, making studies of structural changes as a function of GFA accessible. This isn't always the case for multi-component BMGs.

### 1.4. Methods to Achieve Supercooling

The theoretical approaches discussed previously in this chapter are tested using experimental and computer modeling approaches. The challenge is to achieve significant supercooling for a wide range of systems, ranging from pure metallic to multi-component liquids. Supercooling is typically limited by heterogeneous nucleation. Common examples of heterogeneous nucleation are high altitude jet engine exhaust trails and carbon dioxide bubble streams in carbonated beverages. In the former case soot particulates from the combustion of the fuel act as nucleation sites for super saturated water vapor; in the latter case imperfections in the glass or lint from a drying cloth are nucleation sites for dissolved carbon dioxide in the liquid. The key to achieving such a deep supercooling was the elimination of sites for heterogeneous nucleation. By minimizing the effect of heterogeneous nucleation, Turnbull [87] obtained the first significant supercooling of a metallic liquid, showing that liquid mercury could be cooled to 2/3 of the melting temperature before crystallization, as measured with a dilametric

technique. In many cases, heterogeneous nucleation is induced at the liquid/container boundary due to imperfections on the container surface, like the ones mentioned in the example of beer. However surface imperfections are not always the cause: For liquids in contact with solids, crystalline surfaces induce layering of the adjacent atoms [88, 89], which can lead directly to nucleation if the ordering is consistent with that of an accessible crystal phase.

Supercooling can be achieved in a number of ways. The original experiments by Turnbull were conducted with Hg droplets in a dispersion medium [87]. Other types of emulsion suspensions can be used to isolate the liquid from a nucleating surface, however, these techniques are inappropriate for high temperature or reactive metallic systems. In some cases, having a proper container helps to achieve supercooling. For instance, supercooling was achieved in the Au-Si eutectic liquid [90] by specifically engineering the substrate of the container. The technique evaporates Au particles onto a Si (111) substrate to induce a non-periodic pentagonal tiling, which is incompatible with the cubic structure of crystal Au-Si. This approach works for Au-Si, which has a very low melting temperature (650K = 377°C); it cannot be used for most of other metallic glass forming alloys. Further, the use of a container places limitations on the types of experiments that can be conducted on the liquid. As will be discussed in Chapter 4, non-contact precision measurements of density on levitated samples with no container are feasible as long as the entire sample is in view.

The development of containerless techniques using aerodynamic [91], acoustic [92], electromagnetic (EML) [93], and electrostatic (ESL) [94] levitation have provided a collection of experimental environments that have differing utility, depending on the

material of interest. EML and ESL provide the best sample environments for the study of metallic liquids. In EML, a sample is levitated in a coil that is excited by a RF current with a typical frequency that ranges from ten to several hundred kHz. The changing magnetic flux from the coil induces eddy currents in metallic samples, which produce a counter magnetic field, resulting in sample levitation. This technique has many applications, particularly for thermophysical property measurements [95], however it also has several disadvantages. Only samples that can efficiently couple to the RF field can be levitated. The coupled levitation and heating make it impossible to significantly supercool low-melting-temperature, high-density, samples, precluding, for example, radiative free cooling studies, which are useful for determining the specific heat of a liquid as a function of temperature. Further, the levitation coils can limit the view of the sample, thus limiting the *q*-range in X-ray and neutron diffraction measurements, and the number of coordinated thermophysical property measurements that are possible. In ESL the levitation and displacement forces arise from electrodes located above and below a sample that contains a surface charge. Since ESL does not rely on induced eddy currents for heating and levitation, metallic alloys, semiconductors, silicate glasses and ceramics can be processed. Samples can be heated using high power lasers, decoupling levitation and heating and allowing a maximum undercooling to be realized. Using these techniques Kelton, Johnson, Holland-Moritz, Paradis and others have achieved supercooling in a wide range of pure metals including Zr, Ti, Co, Al, Cu, Nb, and Ni, and related alloy systems [62, 96-99].

As a complement to the experimental studies, growing computing capabilities make possible increasingly realistic studies of liquid structures and crystal nucleation and

growth with molecular dynamics (MD) simulations. MD simulations are categorized as either classical or *ab initio* in nature. Classical MD simulations aim to predict the trajectories of atoms following Newton's equations of motion. By assuming different expressions for the potential energy term, different types of systems can be studied. For example, the most commonly used Lennard-Jones (LJ) potential [100] is limited to isotropic pair interactions. Improvements are made with *embedded atom methods* (EAM) [101], which are many-body approaches. An effective charge density is used to include the many-body effect, but most of the interactions are still spherically symmetric [101-107] making the approach appropriate for many metallic systems, which lack significant covalent or directional bonding.

First principles or *ab initio* simulations solve the electronic structures and atomic interactions using density functional theory (DFT) [108-116]. The technique is considered very accurate under certain circumstances [16]. However, since *ab initio* simulation results will be used in this work, a discussion of the limitations of the technique is important. Not all materials can be modeled using contemporary first principles MD [16]. Utilizing the exchange-correlation term to turn the many body problem into a problem of independent particles makes electronic structure calculations possible. However, the local density approximations commonly used are unphysical in certain systems [16], particularly for high-*Z* Rare Earth elements or other elements with highly localized bonding orbitals. The calculation is only expected to be accurate for the ground state energy and electron density so properties where excitations play a dominant role (i.e. superconductivity and ferromagnetism) may be inappropriate for study with this technique.

A central criticism of the use of MD for modeling structural changes in supercooled liquids and glasses is the extremely short simulation time, even when the simulation is limited to ~ 100 atoms. On picosecond time scales, those commonly achieved between configurations, atomic displacements are limited to a few atomic distances. Structures achieved in a quench, therefore, contain a high degree of history when the simulation is given insufficient time to relax. The reliability of first principles simulations of multi component glasses is particularly suspect, since frustration likely plays an important role in the glass transition. Large differences are observed between simulation and laboratory results for many systems [16]. The simulations become particularly untrustworthy when there are only a few atoms of a constituent present. Large statistical fluctuations are expected from simulation to simulation, so that the thermodynamic limit is not achieved.

Particularly relevant to studies discussed in this thesis is the uncertainty in the structures obtained from small models of a few hundred atoms. For typical number densities (0.04 to 0.07 atoms/$Å^3$), when the simulation is limited to 100 atoms the box is of order 1nm on a side. The periodic boundary conditions in such cases make third neighbor correlations unreliable. However, the nearest-neighbor SRO and even MRO are with experimental results in many cases. This will be shown in particular for the ETM-LTM metallic liquids, a focus in this thesis.

## 1.5. Summary

The topics discussed in this chapter lay the background for the work that will be discussed in following chapters. Three key topics will be examined in this thesis:

### 1.) Development of the Beamline Electrostatic Levitator (BESL)

High-energy X-ray diffraction studies of metallic liquids provide valuable information about structural evolution on the atomic length scale, leading to insights into the origin of the nucleation barrier and the processes of supercooling and glass formation. The containerless processing in BESL allows coordinated thermophysical and structural studies of equilibrium and supercooled liquids in a contamination-free, high-vacuum ($\sim 10^{-8}$ Torr) environment. In chapter 4, the development of a modular levitation facility that is optimized for diffraction studies of high-temperature liquids at high-energy synchrotron beamlines will be discussed. Unlike most previous electrostatic levitation facilities, BESL can be operated by a single user instead of a user team.

### 2.) Quantifying Local Structures in Metallic Glass Forming Liquids

Experiments and simulations have demonstrated that equilibrium metallic liquids often contain significant amounts of short-range and even medium-range order. In transition metal liquids, this is frequently dominated by icosahedral and icosahedral-like order. In most cases, the order becomes more extensive and better defined in the supercooled liquid. This order can have a significant impact on phase transitions in the liquid, including crystal nucleation, chemical ordering and glass formation. To date, Reverse Monte Carlo (RMC) simulations of atomic structures have relied on a single structural measurement for input. In chapters 5 and 6 of this work, we explore the atomic structures obtained by constraining the simulations with MD simulations of SRO.

### 3.) Exploring the Link Between Local Structure and Glass Formability

Binary bulk metallic glasses provide ideal systems to explore the links between structure and glass formability. The Ni-Nb glass forming system allows reliable interpretation of scattering data and first principles molecular dynamics simulations of local structure. This system is reported to display a strong compositional dependence on glass formability. In chapter 6 we will consider the structural differences that emerge between bulk forming and non-bulk forming compositions in this system and the implications for understanding glass formability and the glass transition.

## 1.6. References


[1] C. Kittel, Introduction to Solid State Physics, John Wiley & Sons, Hoboken (2005).
[2] A. L. Greer, *Science* **267,** 1947, (1995).
[3] S. Schneider, *Journal of Physics: Condensed Matter* **13,** 7723, (2001).
[4] J. J. Hauser, *Physical Review B* **17,** 1908, (1978).
[5] Y. T. Shen, T. H. Kim, A. K. Gangopadhyay and K. F. Kelton, *Physical Review Letters* **102,** 057801, (2009).
[6] S. Y. Wang, C. Z. Wang, M. Z. Li, L. Huang, R. T. Ott, M. J. Kramer, D. J. Sordelet and K. M. Ho, *Physical Review B* **78,** 184204, (2008).
[7] G. F. Syrykh, M. G. Zemlyanov, A. S. Ivanov, J. A. Stride, Y. V. Lisichkin and N. A. Klimenko, *Journal of Non-Crystalline Solids* **353,** 3188, (2007).
[8] S. M. Chathoth, B. Damaschke, J. P. Embs and K. Samwer, *Applied Physics Letters* **94,** 201906(2009).
[9] S. M. Chathoth, B. Damaschke, J. P. Embs and K. Samwer, *Applied Physics Letters* **95,** 191907(2009).
[10] Y. Waseda, The structure of non-crystalline materials, McGraw-Hill, New-York (1980).
[11] R. Zallen, The Physics of Amorphous Solids, John Wiley & Sons, New York (1983).
[12] T. Egami and S. J. L. Billinge, Underneath the Bragg Peaks, Pergamon, Oxford (2003).
[13] M. T. Dove, Structure and dynamics: an atomic view of materials, Oxford University Press, New York (2003).
[14] C. Suryanarayana and M. G. Norton, Plenum Press, New York (1998).
[15] N. P. Kovalenko, Y. P. Krasny and U. Krey, Physics of amorphous metals, Wiley-VHC, New York (2001).
[16] Y. Q. Sheng and E. Ma, *Progress in Materials Science* **56,** 379, (2011).

[17] S. R. Elliot, Physics of amorphous metals, Longman, New York (1983).
[18] H. S. Chen and D. Turnbull, *The Journal of Chemical Physics* **48,** 2560, (1968).
[19] D. A. McQuarrie, Statistical Mechanics, University Science Books, Sausalito (2000).
[20] D. Turnbull and M. H. Cohen, *Journal of Chemical Physics* **52,** 3038, (1970).
[21] D. Turnbull and M. H. Cohen, *Journal of Chemical Physics* **34,** 120, (1961).
[22] J. H. Gibbs and E. A. Dimarzo, *Journal of Chemical Physics* **28,** 373, (1958).
[23] I. Proggine and R. Defay, Chemical Thermodynamics, Longmans, London (1954).
[24] M. H. Cohen and G. S. Grest, *Physical Review B* **20,** 1077, (1979).
[25] C. A. Angell, *Science* **267,** 1924, (1995).
[26] J. C. Dyre, T. Christensen and N. B. Olsen, *Journal of Non-Crystalline Solids* **352,** 4635, ( 2006 ).
[27] G. Adam and J. H. Gibbs, *Journal of Chemical Physics* **43,** 139, (1965).
[28] S. R. Elliot, Physics of Amorphous Materials, Longman, New York (1990).
[29] C. Way, P. Wadhwa and R. Busch, *Acta Materialia* **55,** 2977, (2007).
[30] S. P. Das, *Reviews of Modern Physics* **76,** 785, (2004).
[31] B. Frick and D. Richter, *Science* **267,** 1939, (1995).
[32] P. Lunkenheimer, A. Pimenov, M. Dressel, Y. G. Goncharov, R. B. R and A. Loidl, *Physical Review Letters* **77,** 318, (1996).
[33] Z. Wang, H. B. Yu, H. Y. Bai and W. H. Wang, *Journal of Physics: Condensed Matter* **23,** 142202, (2011).
[34] H. Tanaka, *Physical Review E* **69,** 021502, (2004).
[35] K. L. Ngai, *Physical Review E* **70,** 063501, (2004).
[36] Z. F. Zhao, P. Wen, C. H. Shek and W. H. Wang, *Journal of Non-Crystalline Solids* **356,** 1198.
[37] H. Okumura, H. S. Chen, A. Inoue and T. Masumoto, *Journal of Non-Crystalline Solids* **130,** 304, (1991).
[38] P. Wen, D. Q. Zhao, M. X. Pan, W. H. Wang, Y. P. Huang and M. L. Guo, *Applied Physics Letters* **84,** 2790, (2004).
[39] Z. F. Zhao, P. Wen, W. H. Wang and C. H. Shek, *Applied Physics Letters* **89,** 071920, (2006).
[40] Z. F. Zhao, P. Wen, C. H. Shek and W. H. Wang, *Physical Review B* **75,** 174201, (2007).
[41] L. Hu and Y. Yue, *The Journal of Physical Chemistry B* **112,** 9053, (2008).
[42] J. J. Z. Li, W. K. Rhim, C. P. Kim, K. Samwer and W. L. Johnson, *Acta Materialia* **59,** 2166, (2011).
[43] J. D. Bernal, *Nature* **185,** 68, (1960).
[44] J. L. Finney, *Proceedings of the Royal Society Ser A - Math Physics Science* **319,** 479, (1970).
[45] J. L. Finney, *Nature (London)* **266,** 309, (1977).
[46] J. G. Kirkwood, *Zeitschrift für Physik* **33,** 57, (1932).
[47] J. K. Percus and G. J. Yevick, *Physical Review* **110,** 1, (1958).
[48] S. A. Rice and P. Gray, The Statistical Mechanics of Simple Liquids, Interscience, New York (1965).
[49] D. Henderson, *Condensed Matter Physics* **12,** 127, (2009).

[50] N. W. Ashcroft and J. Lekner, *Physical Review* **145,** 83, (1966).
[51] N. W. Ashcroft and D. C. Langreth, *Physical Review* **159,** 500, (1967).
[52] H. C. Andersen, J. D. Weeks and D. Chandler, *Physical Review A* **4,** 1597, (1971).
[53] W. Klement, R. H. Willens and P. O. L. Duwez, *Nature* **187,** 869, (1960).
[54] H. W. Kui, A. L. Greer and D. Turnbull, *Applied Physics Letters* **45,** 615, (1984).
[55] A. Inoue, T. Zhang and T. Masumoto, *Material Transactions JIM* **31,** 177.
[56] A. Peker and W. L. Johnson, *Applied Physics Letters* **63,** 2342, (1993).
[57] Q. Luo, B. Zhang, D. Q. Zhao, R. J. Wang, M. X. Pan and W. H. Wang, *Applied Physics Letters* **88,** 151915, (2006).
[58] T. Wang, Y. Q. Yang, J. B. Li and G. H. Rao, *Journal of Alloys and Compounds* **509,** 4569.
[59] J. N. Mei, J. L. Soubeyroux, J. J. Blandin, J. S. Li, H. C. Kou, H. Z. Fu and L. Zhou, *Journal of Non-Crystalline Solids* **357,** 110.
[60] R. Busch, J. Schroers and W. H. Wang, *MRS Bulletin* **32,** 620, (2007).
[61] K. F. Kelton, A. K. Gangopadhyay, T. H. Kim and G. W. Lee, *Journal of Non-Crystalline Solids* **352,** 5318, (2006).
[62] T. H. Kim and K. F. Kelton, *The Journal of Chemical Physics* **126,** 054513, (2007).
[63] V. M. Wessels, PHASE FORMATION, LIQUID STRUCTURE, AND PHYSICAL PROPERTIES OF AMORPHOUS AND QUASICRYSTAL-FORMING ALLOYS, *Physics*, Washington University, St. Louis (2009).
[64] F. C. Frank, *Proceedings of the Royal Society Ser A - Math Physics Science* **215,** 43, (1952).
[65] J. W. Allen, A. C. Wright and G. A. N. Connell, *Journal of Non-Crystalline Solids* **42,** 509, (1980).
[66] P. Panissod, D. A. Guerra, A. Amamou, J. Durand, W. L. Johnson, W. L. Carter and S. J. Poon, *Physical Review Letters* **44,** 1465, (1980).
[67] I. Vincze, D. S. Boudreaux and M. Tegze, *Physical Review B* **19,** 4896, (1979).
[68] T. M. Hayes, J. W. Allen, J. Tauc, B. C. Giessen and J. J. Hauser, *Physical Review Letters* **40,** 1282, (1978).
[69] P. H. Gaskell, *Nature* **276,** 484(1978).
[70] P. H. Gaskell, *Journal of Non-Crystalline Solids* **32,** 207, (1979).
[71] J. M. Dubois, P. H. Gaskell and G. Lecaer, *Proceedings of the Royal Society Ser A - Math Physics Science* **402,** 323, (1985).
[72] Y. Waseda and H. S. Chen, *physica status solidi (a)* **49,** 387, (1978).
[73] D. S. Boudreaux and H. J. Frost, *Physical Review B* **23,** 1506, (1981).
[74] P. Lamparter, *Physica Scripta* **57,** 72, (1995).
[75] A. V. Evteev, A. T. Kosilov and E. V. Levtchenko, *Acta Materialia* **51,** 2665(2003).
[76] W. K. Luo, H. W. Sheng and E. Ma, *Applied Physics Letters* **89,** 131927, (2006).
[77] H. W. Sheng, W. K. Luo, F. M. Alamgir, J. M. Bai and E. Ma, *Nature* **439,** 419(2006).
[78] D. Wang, Y. Li, B. B. Sun, M. L. Sui, K. Lu and E. Ma, *Applied Physics Letters* **84,** 4029(2004).
[79] D. Xu, B. Lohwongwatana, G. Duan, W. L. Johnson and C. Garland, *Acta Materialia* **52,** 2621(2004).

[80] V. Wessels, A. K. Gangopadhyay, K. K. Sahu, R. W. Hyers, S. M. Canepari, J. R. Rogers, M. J. Kramer, A. I. Goldman, D. Robinson, J. W. Lee, J. R. Morris and K. F. Kelton, *Physical Review B* **83,** 094116.
[81] G. Duan, D. Xu, Q. Zhang, G. Zhang, T. Cagin, W. L. Johnson and W. A. Goddard, *Physical Review B* **71,** 224208(2005).
[82] P. Yu, H. Y. Bai, M. B. Tang and W. L. Wang, *Journal of Non-Crystalline Solids* **351,** 1328(2005).
[83] A. Inoue and W. Zhang, *Material Transactions* **45,** 584, (2004).
[84] G. Duan, D. Xu and W. Johnson, *Metallurgical and Materials Transactions A* **36,** 455(2005).
[85] L. Xia, W. H. Li, S. S. Fang, B. C. Wei and Y. D. Dong, *Journal of Applied Physics* **99,** 026103(2006).
[86] K. Yao and N. Chen, *Science in China Series G: Physics Mechanics and Astronomy* **51,** 414(2008).
[87] D. Turnbull, *The Journal of Chemical Physics* **20,** 411(1952).
[88] S. H. Oh, Y. Kauffmann, C. Scheu, W. D. Kaplan and M. RÃ¼hle, *Science* **310,** 661(2005).
[89] H. Reichert, O. Klein, H. Dosch, M. Denk, V. Honkimaki, T. Lippmann and G. Reiter, *Nature* **408,** 839(2000).
[90] T. U. Schulli, R. Daudin, G. Renaud, A. Vaysset, O. Geaymond and A. Pasturel, *Nature* **464,** 1174(2010).
[91] L. Hennet, S. Krishnan, I. Pozdnyakova, V. Cristiglio, G. J. Cuello, H. E. Fischer, A. Bytchkov, F. Albergamo, D. Zanghi, J.-F. Brun, S. Brassamin, M.-L. Saboungi and D. L. Price, *Pure Appl. Chem.* **79,** 1643, (2007).
[92] E. H. Trinh, *Rev. Sci. Instrum.* **56,** 2059, 2059(1985).
[93] D. Holland-Moritz, T. Schenk, P. Convert, T. Hansen and D. H. Herlach, *Meas. Sci. Tech.* **16,** 372, (2005).
[94] W.-K. Rhim, M. Collender, M. T. Hyson, W. T. Simms and D. D. Elleman, *Rev. Sci. Instrum.* **56,** 307, (1985).
[95] K. F. Kelton and A. L. Greer, Nucleation in Condensed Matter-Applications in Materials and Biology, Elsevier, Amsterdam (2010).
[96] T. Schenk, D. Holland-Moritz, V. Simonet, R. Bellissent and D. M. Herlach, *Physical Review Letters* **89,** 075507(2002).
[97] D. Holland-Moritz, T. Schenk, R. Bellissent, V. Simonet, K. Funakoshi, J. M. Merino, T. Buslaps and S. Reutzel, *Journal of Non-Crystalline Solids* **312-314,** 47(2002).
[98] G. W. Lee, A. K. Gangopadhyay, K. F. Kelton, R. W. Hyers, T. J. Rathz, J. R. Rogers and D. S. Robinson, *Physical Review Letters* **93,** 037802(2004).
[99] D. Holland-Moritz, O. Heinen, R. Bellissent and T. Schenk, *Materials Science and Engineering: A* **449-451,** 42(2007).
[100] M. P. Allen and D. J. Tildesley, Computer simulation of liquids, Oxford University Press, Oxford (1989).
[101] M. S. Daw, S. M. Foiles and M. I. Baskes, *Materials Science Reports* **9,** 251(1993).
[102] S. M. Foiles, M. I. Baskes and M. S. Daw, *Physical Review B* **33,** 7983(1986).
[103] S. M. Foiles, *Physical Review B* **32,** 3409(1985).

[104] Y. Mishin, D. Farkas, M. J. Mehl and D. A. Papaconstantopoulos, *Physical Review B* **59,** 3393(1999).
[105] Y. Mishin, M. J. Mehl, D. A. Papaconstantopoulos, A. F. Voter and J. D. Kress, *Physical Review B* **63,** 224106(2001).
[106] M. I. Baskes, *Physical Review B* **46,** 2727(1992).
[107] Y. Mishin and A. Y. Lozovoi, *Acta Materialia* **54,** 5013(2006).
[108] P. Hohenberg and W. Kohn, *Physical Review* **136,** B864(1964).
[109] M. C. Payne, M. P. Teter, D. C. Allan, T. A. Arias and J. D. Joannopoulos, *Reviews of Modern Physics* **64,** 1045(1992).
[110] G. Kresse, Furthm, uuml and J. ller, *Physical Review B* **54,** 11169(1996).
[111] G. Kresse and D. Joubert, *Physical Review B* **59,** 1758(1999).
[112] R. Car and M. Parrinello, *Physical Review Letters* **55,** 2471(1985).
[113] G. Kresse and D. Joubert, *Phys. Rev. B* **59,** 1758, (1999).
[114] G. Kresse and J. Furthmüller, *Phys. Rev. B* **54,** 11169, (1996).
[115] G. Kresse and J. Furthmüller, *Computational Material Science* **6,** 15, (1996).
[116] G. Kresse, Technische Universität Wien (1993).

# Chapter 2

# Experimental Methods: Thermophysical, Structural characterization and Simulation Techniques

## 2.1. Introduction

The work presented in this thesis begins with master alloy preparation from which samples for multiple experiments are extracted. Basic thermophysical and structural characterization of the alloys, preparation of glassy ribbon or cast specimens, and processing in the Beamline Electrostatic Levitator (BESL) all rely on reproducible and impurity free compositions. In order to guarantee that features observed during experimentation are inherent to the *system* and not because of *impurities*, careful alloy preparation must be emphasized. In this section, the details of master alloy preparation are discussed followed by sample preparation methods that are specific for all the experiments discussed in this work. Techniques for rudimentary thermophysical and structural characterization are presented as well as a detailed discussion of high-energy synchrotron X-ray radiation and its application in structural studies of liquids and glasses. Finally, Reverse Monte Carlo (RMC) simulations of liquid structures and subsequent atomic structural quantization using Honeycutt and Anderson (HA) indices, Bond Orientational Order (BOO) parameters and Voronoi Polytetrahedral (VI) indices are discussed. Although the use of the BESL is an integral part of this work, discussion of this technique is reserved for a later section, which includes a comprehensive discussion of the experimental apparatus and measurement techniques.

## 2.2. Sample Preparation

### *2.2.1. Master Ingot Production*

Source materials of varying purity were purchased almost exclusively from Alfa Aesar [1]; they are summarized in Table 2.1. The materials were stored in a vacuum chamber (~30 mTorr) when not being processed to minimize contamination and oxidation. The vast majority of the elements are highly non-reactive and no preprocessing, cleaning, or etching was done on the materials before use. The detailed distributions of impurities in all the raw materials are available from the manufacturers [1] and for some the Materials Safety Data Sheet (MSDS) is located in Compton 050 at the writing of this document.

**Table 2.1-** Raw materials used for the studies presented in this thesis.

| Element | Company | Stock/Lot | Purity (%) | Used in System |
|---|---|---|---|---|
| Al | AA/Pura | 10573/F01R022 | 99.999 | Al, $Al_{88}Y_7Fe_5$ |
| Au | AA | 13394/H15H20 | 99.99 | $Zr_xAu_{100-x}$ |
| Fe | AA | 42384/A22S019 | 99.95 | $Al_{88}Y_7Fe_5$ |
| Hf | AA | 39711/A19K06 | 99.5 (excluding 3% Zr) | $Ni_{60}Nb_{35}Hf_5$ $Hf_xPt_{100-x}$ |
| Ir | AA | 44714/unknown | 99.9 | $Zr_xIr_{100-x}$ |
| Ni | AA/Pura | 42333/D18M33 42333/J12R002 | 99.995 | Ni, $Ni_xNb_{100-x}$, $Ni_{60}Nb_{30}Ta_{10}$, $Ni_{60}Nb_{35}(Ti,Zr,Hf)_5$, $Zr_xNi_{100-x}$ |
| Nb | AA | 42846/I28N13 | 99.95 (excluding Ta) | Ni, $Ni_xNb_{100-x}$, $Ni_{60}Nb_{30}Ta_{10}$, $Ni_{60}Nb_{35}(Ti,Zr,Hf)_5$ |

| | | | | |
|---|---|---|---|---|
| Pd | AA | 10961/I22N15 | 99.99 | $Zr_xPd_{100-x}$ |
| Pt | AA | 43288/J02U012 | 99.95 | $Zr_xPt_{100-x}$<br>$Hf_xPt_{100-x}$ |
| Rh | AA | 11575/K15R14 | 99.8 | $Zr_xRh_{100-x}$ |
| Ta | AA | 42826/E08L09 | 99.95 | $Ni_{60}Nb_{30}Ta_{10}$ |
| Ti | AA/Pura | 42394/C18Q29 | 99.995 | $Ni_{60}Nb_{35}Ti_5$ |
| Y | AA | 00615/D03R011 | 99.9 | $Al_{88}Y_7Fe_5$ |
| Zr | AA | 42556/A03S011<br>42556/D21K11<br>42558/F29U045 | 99.95 (excluding 3% Hf) | Zr-(Ni, Pd, Pt, Au, Ir, Rh)<br>$Ni_{60}Nb_{35}Zr_5$ |

The masses of the elements used to prepare the master ingots were determined using a Mettler Toledo AB54/FACT mass to an accuracy of $\pm$ 0.1mg. The total target mass of the master ingots was typically ~1g. A Mettler Toledo AT261 mass balance with an accuracy of $\pm$ 0.02mg was used for the density measurements of the $Ni_xNb_{100-x}$ ($55.0 \leq x \leq 65.0$) liquids, discussed in Chapter 6. Typically, the elemental component of the alloy that is the most difficult to work with is held fixed at a convenient mass (usually a quantum of the packaging unit) and the masses of the other constituent elements are determined according to Equation 1,

$$m_i = MF_i * \frac{m_f}{MF_f} \quad (1)$$

where $m_i$ is the mass of the constituent of interest, $MF_i$ is the mass fraction of the constituent of interest, $m_f$ is the mass of the constituent initially held fixed, and $MF_f$ is the mass fraction of the constituent held fixed. Any given mass fraction can be

determined by considering the atomic concentration of each element in the alloy, $c_i$, and the atomic weight of each element, $MA_i$ according to

$$MF_i = \frac{c_i * MA_i}{\sum_j c_j * MA_j} \quad (2)$$

where the sum ranges over all constituents. Unless otherwise indicated, all alloy compositions will be reported in atomic percent as opposed to weight or mass percent.

The source materials are alloyed using an in-house "arc-melter," which uses a Miller Syncrowave 250 constant current AC/DC arc welding power source connected to a tungsten tip through a vacuum feed-through to resistively heat the constituents to their melting points. A schematic description of the arc-melter is shown in Figure 2.1. The source material is arranged on the water-cooled copper hearth and then the chamber is evacuated with a forepump to a pressure of ~10 mTorr. It is then backfilled with 99.98% (grade 4.8) Ar gas to nearly one atmosphere of pressure. This pumping/backfilling sequence is repeated 4-5 times to effectively remove oxygen and other gases and the chamber is backfilled with Ar a final time. Before the source material is placed on the hearth, the surface is cleaned by sanding, followed by acetone and methanol or ethanol scrubbing with Kimwipes™. Unwanted alloying of the source materials with the copper hearth is minimized because copper readily develops an oxide coating[3], the hearth has a large thermal mass, and it is water-cooled

[3] Oxygen has almost no solubility in Cu; both CuO and $Cu_2O$ readily form and both have melting temperatures around 1230°C (1503K).

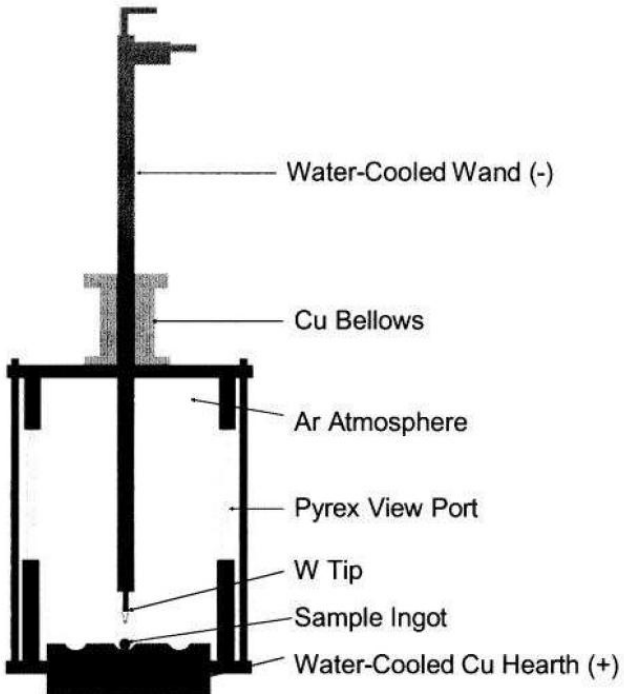


**Figure 2.1-** Arc-melter apparatus used for producing master ingots and ESL samples. Image taken from [2].

Once the chamber is backfilled with Ar for the last time, a foot pedal is used to strike an arc from the replaceable Tungsten tip, ionizing the Ar, and passing current though the sample to the hearth. Shape irregularities in the tungsten tip create a diffuse arc or cause arcing from multiple points on the tip. As a rule of thumb, when grinding a tip the taper should begin roughly 2/3 of the way down the tungsten and the tip itself should be very slightly flattened at the end. The tightest arc is achieved when the tip is ground axially and not radially, creating striations along the long axis of the tip.

The process of ingot melting begins first by melting a Ti/Zr "getter": A Ti/Zr getter of mass approximately 1g with approximately equal mixture of Ti and Zr has a melting temperature near 1540°C [3] and a large oxygen solubility. Melting the getter before each sample melt purifies the chamber atmosphere further and should be done

each time that the arc is formed. If the tip is touching the hearth surface when first forming the arc the surface can become pitted, creating sites for contamination, so it is best to form the arc on the Ti/Zr getter. Once the getter is melted, moving the tip around the periphery of the sample enhances mixing.

Observations of the getter as it is melted allow an additional indication of the vacuum quality in the chamber. If a vacuum leak is present, the increase in oxygen concentration causes a discoloration of the gas around the getter or a "blackening" of the getter surface. When this happens, processing should be stopped until the source of the contamination is determined. The arc-melter used in this work has an isolation valve for the roughing forepump. When this valve is closed after evacuation of the air in the chamber, the pressure rise should be no more than 5-10mTorr within a minute; otherwise there is a vacuum leak.

In most cases, when a small amount of a second element (solute) is added to the solvent (majority elements) the melting temperature decreases, although there are some exceptions to this rule (Ag-Al, Au-Pb, and Al-Mn for instance). This means that the melting order of the elements is crucial. If there is a large disparity between the melting temperatures of the constituents, if the lower melting temperature element is melted first, the higher melting temperature element may never melt and mix. Often this is a subtle effect. The masses of ingots are always measured after melting to check for mass loss or gain upon melting, but this failure to mix properly would not be detected. Ingots are manually broken after melting, and an inspection of the microstructure can sometimes show this "mis-alloying." Several batches of an alloy should be made and checked for consistency to guarantee proper alloying. Often (although not in this work) multi-

component alloys are prepared in steps to maximize mixing and minimize selective evaporation of the elements, which would shift the alloy composition.

For this work, ingots were typically melted for 30 to 45 seconds and then flipped over (to help insure mixing); this was repeated for a total of 3 melt cycles. The mass of the ingot was determined and it was inspected for obvious signs of surface contamination and discarded if this was found to be the case of if the mass loss or gain was greater than 0.25%; a mass loss of 0.1% was easily attained for the alloys reported here.

### *2.2.2. Melt Spun Ribbon Preparation*

Glass formability is highly variable amongst the alloys studied and for some of these the metastable amorphous state is only accessible at cooling rates of ~$10^6$ K/sec. The critical cooling rate of $Al_{88}Y_7Fe_5$ is of this order [4] and for the nucleation studies in this alloy glassy samples were obtained by rapidly cooling or "quenching" ribbons by utilizing the "Melt Spinning" (MS) technique. In this technique, source ingots (previously prepared using the arc-melter) are melted in a quartz tube, or suitable container in the tube, and ejected from a small hole in the bottom of the tube onto a large spinning copper wheel. This rapidly cools the sample and continuously removes the quenched material off the wheel surface into a storage area, presenting a clean surface to new liquid. A schematic of the MS apparatus, or "quench-box," is shown in Figure 2.2.

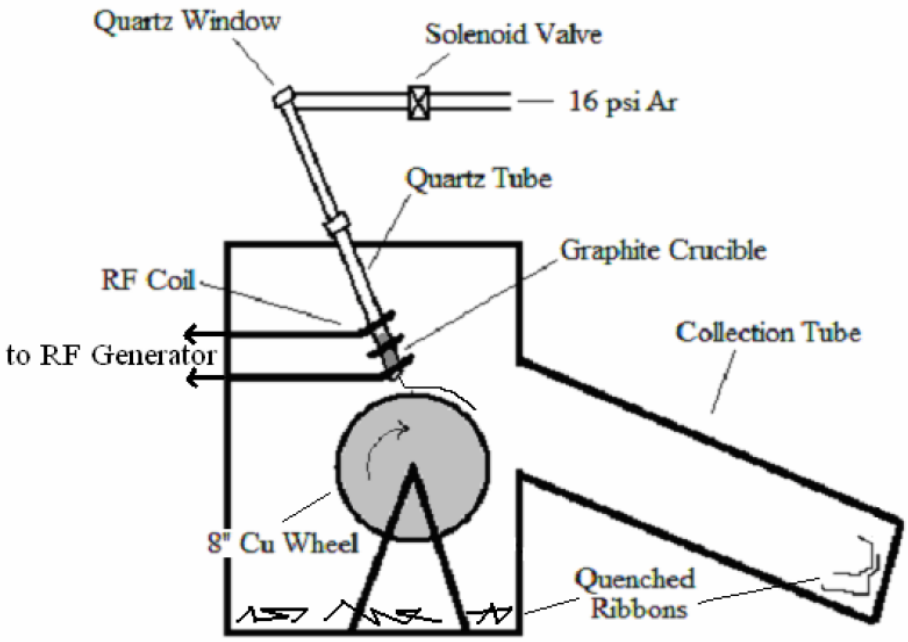


**Figure 2.2-** Schematic of the melt-spinning (MS) apparatus. Image taken from [5].

In melt spinning, the sample is heated inductively with a radio frequency (RF) generator (Lepel T-10-3-KC-HW) by creating a current in a coil of water-cooled copper tubing placed around the sample. Not all materials couple efficiently to the RF field and so samples are often placed inside a graphite crucible (melting temperature 3527°C), which does couple well to the field. The crucible is prepared from a graphite rod into which a hole is drilled leaving the wall of the crucible approximately 1mm thick and the length approximately 25mm. One end of the crucible is open while the other end is closed except for a small (~1mm diameter) hole through which the liquid is ejected onto the wheel. Before the sample is loaded, the crucibles were cleaned by sonication in

acetone and ethanol and heated for 5 minutes in a quartz tube with an oxygen and acetylene torch while under vacuum (~ 50mm Torr). The crucible is then placed in the bottom of the quartz tube (which also has a small hole at the end next to the wheel). The quartz and crucible are then inserted into the quench box through a quick-disconnect vacuum seal. During processing, the carbon crucible is heated until the sample is completely melted, which is confirmed from an optical pyrometer (IRCON UX-10) placed above a quartz window that is located at the top of the quartz tube and providing a direct line-of-sight onto the sample (Figure 2.2). The top end of the tube is connected to a solenoid value that is opened to allow Ar gas (grade 5.0) at 16 PSI to eject the liquid sample onto the wheel.

The copper wheel used is approximately 200mm in diameter and is driven by an AC motor, located in the chamber, and powered by a Variac variable transformer; electrical connections are made *via* a vacuum feed-through. A maximum tangential speed of 100 m/s for the wheel is possible, measured with a homemade circuit that is calibrated using a flashing strobe. Like arc-melting, melt-spinning takes place in an argon atmosphere at slightly below atmospheric pressure. Unlike arc-melting, the Ar isn't necessary for the melting of the sample in the quench box, but is used for cooling the motor. The atmosphere of the quench box is purified in the same fractional distillation process as the arc-melter, cycling 4-6 times.

Melt spun ribbons tend to have variable thickness, nominally between 30μm and 100μm, and widths that depend on the crucible geometry. They can be continuous for lengths of several centimeters and even up to meters in some cases. The widths of the $Al_{88}Y_7Fe_5$ samples discussed in this thesis were 2-3mm. Samples used for

thermophysical, TEM and structural study were taken from the center of continuous lengths of 5cm or longer.

### *2.2.3. Samples for Electrostatic Levitator*

ESL samples are prepared using the arc-melter following the procedure outlined in Section 2.2.1, but with samples 1.5mm – 4.0mm in diameter. The current in the arc-melter is reduced when melting the samples to minimize selective evaporation. Additionally, since mixing isn't the primary goal, once the sample is melted, the arc is moved off the sphere. Prepared master ingots are broken into smaller pieces and weighted to allow the preparation of samples of desired sizes. Since the density of the alloy at room temperature is generally unknown until processed in ESL, it is estimated from the room temperature densities of the elemental constituents, assuming the rules of mixtures (ideal solution). This approximation doesn't adversely affect sample levitation. From volume conservation,

$$\rho_{approx} = \left( \sum_i \frac{MF_i}{\rho_i} \right)^{-1} \quad , \tag{3}$$

where $\rho_{approx}$ is the density used for the ESL sample mass calculation, $MF_i$ is the elemental mass fraction in the alloy composition, $\rho_i$ is the room temperature density of the elements used. The sum ranges over all of the elemental constituents in the alloy.

## 2.3. Thermophysical/Structural Characterization

### *2.3.1. Low Energy X-ray Diffraction*

Routine structural characterization using low energy X-ray diffraction (XRD) was carried out using a Rigaku Geigerflex diffractometer with a stationary Cu $K_\alpha$ X-ray source ($\lambda$ = 1.5418 Å). How the scattering data was analyzed and used will be discussed in a later section, but for the $Al_{88}Y_7Fe_5$ ribbons it was used to determine whether the quenched sample was amorphous and to identify the primary devitrification products. In most cases, samples were either powdered or cut into ~1cm strips and attached with petroleum jelly to a glass slide for the XRD studies, made in a reflection geometry. In other studies, strips were attached to an open aluminum slide using double sided tape to minimize background scattering from the slide; a reflection geometry was still used. Care must be taken when using XRD to test amorphousness. The diffraction pattern from amorphous materials contains a series of broad peaks. Therefore, because crystallite size is manifest inversely with the diffraction peak width, crystallites smaller than a size threshold cannot be distinguished from an amorphous phase. The Scherrer Formula [6] is often used to calculate the coherence length or crystallite size, *L*,

$$L = \frac{.94\lambda}{B\cos(2\theta/2)} \quad , \tag{4}$$

where $\lambda$ is the X-ray wavelength, and *B* is the full-width at half-maximum of the crystal peak of interest. If we assume that the first broad peak in a rapidly quenched $Al_{88}Y_7Fe_5$ ribbon is due to small crystallites then, Equation 4 indicates that they must be smaller than 2nm. In fact, certain Mg-based "glasses" [7], thought to be amorphous from XRD measurements actually contain micron sized crystallites embedded in an amorphous

matrix, based on SEM and TEM studies. Additional studies in this and other groups [8] have shown that the formation of nanocrystals during a quench or in the first stages of devitrification can sharpen the first amorphous peak very slightly. These findings raise skepticism concerning claims of amorphousness based solely on XRD studies.

### *2.3.2. Differential Scanning Calorimetry (DSC)/Differential Thermal Analysis (DTA)*

Differential Scanning Calorimetry (DSC) is a thermal characterization technique that directly measures the time derivative of the energy (power) transferred between a sample and a reference when they are simultaneously subjected to a controlled temperature or temperature program. A typical experimental setup places a sample in a container, or "pan", on one heater and a reference pan on another heater. The DSC compares the power that is required to keep the two pans at the same temperature. Since power is a measure of instantaneous energy transfer, these measurements can be used to determine the specific heat and enthalpies of transition of the samples.

The DSC measurements in this work were made using a Perkin Elmer DSC 7, which is a power compensation DSC. A comprehensive overview of this type of instrument is available from Perkin Elmer as well as in an excellent review by G. Höhne *et al.* [9, 10]. In this apparatus, the differential power between the sample and reference pans is measured while a computer-controlled furnace maintains a set heating rate (for a scanning, or non-isothermal, measurement) or temperature (for an isothermal measurement). Importantly, the sample and reference pan are maintained under a constant pressure throughout the experiment, typically by slowly flowing inert Ar gas through the "head", containing the pans and heaters.

The enthalpy, *H*, is naturally expressed as a function of the entropy, *S*, and the pressure, *P*:

$$\begin{aligned} H &= H(S,P) \\ dH &= \left(\frac{\partial H}{\partial S}\right)_P dS + \left(\frac{\partial H}{\partial P}\right)_S dP\,. \\ dH &= TdS + VdP \end{aligned} \tag{5}$$

If the pressure is held fixed, and remembering that

$$dq = Tds \tag{6}$$

for reversible processes, then

$$dH = dq. \tag{7}$$

Since, in DSC power is measured,

$$\frac{dH}{dt} = \frac{dq}{dt}. \tag{8}$$

Thus, for a controlled atmosphere, the power is equal to the time rate of change of the enthalpy. Unlike other calorimeters, the DSC measures the energy flow rate and not the energy, making it sensitive to subtle phase transformations, which have small heat signatures but may have rapid onsets. The enthalpy of transformation can be estimated by integrating the differential power (once properly normalized).

In this work, the DSC was used for devitrification studies of $Al_{88}Y_7Fe_5$. Regardless of the mode of operation (*i.e.* isothermal or non-isothermal), ribbon samples were first prepared using the quench-box, and DSC samples were prepared by cutting the ribbons into ~.5cm long ribbons to produce 4-6 mg of ribbon, which was then placed in Perkin-Elmer series 0219 aluminum sample pans. Lids were placed onto the pans and tweezers were used to crimp the sides of the pans over the lid. Care was taken to make

sure that no sample material was crimped outside of the pan and that the bottom of the pan remained flat without indentations.

An example of several non-isothermal scans is shown in Figure 2.3 for as-quenched $Al_{88}Y_7Fe_5$. The baseline has been subtracted in these measurements. The baseline is constructed by running the same program twice. The second run will not show the same transformation character, but rather will show a monotonically increasing signal (more endothermic in character) with temperature. A pre-baseline subtraction non-isothermal scan of $Al_{88}Y_7Fe_5$ is shown in Figure 2.4 for reference.

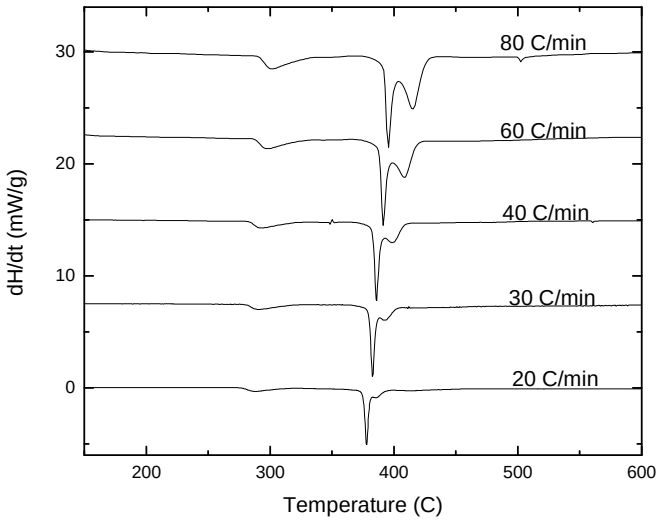


**Figure 2.3-** DSC non-isothermal scans at varying heating rates for $Al_{88}Y_7Fe_5$ as-quenched ribbons. The scans are offset in power, and the baseline is subtracted. Exothermic is down.

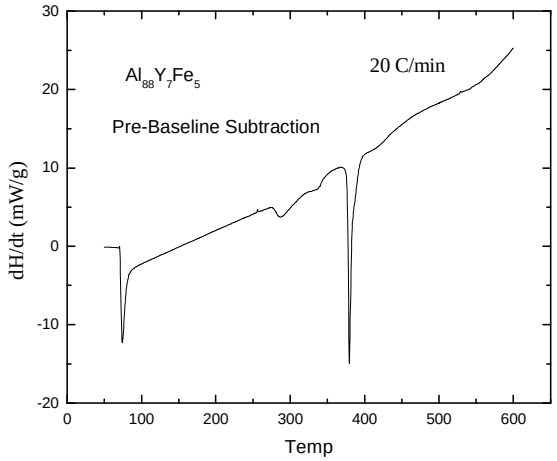


**Figure 2.4-** DSC non-isothermal at 20 C/min for an $Al_{88}Y_7Fe_5$ as-quenched ribbon. The scan is shown without baseline subtraction. Exothermic is down.

As can be seen in Figure 2.3, there is a systematic shift in the peak positions as a function of scan rate. Each one of the peaks corresponds to a crystallization event, a first-order phase transformation. The location of the peak in first-order phase transformations shifts in temperature with varying scan rate. When multiple scan rates are required (for example in a Kissinger analysis [11], as discussed in Chapter 3), the instrumental shift must be calibrated as a function of scan rate. This is typically done by running a sample with a known second order phase transition, since the temperatures of second order phase transitions, such as the Curie transition in Ni, don't shift as a function of scan rate. Any shifts observed then are due to instrumental shift. By measuring the shift as a function of scan rate, the instrumental shift can be determined and subtracted from shifts in the first order phase transitions to produce shifts that are only representative of the nucleation and growth kinetics.

DSC non-isothermals can also provide information about the endothermic glass transition, $T_g$, which manifests as a DSC endothermic signal prior to exothermic devitrification. This transition can often be observed and is an indication of the amorphous character of a sample, but it is also useful as a measure of the supercooled region, i.e. the temperature range between the glass transition and the onset of primary crystallization. The width of the supercooled region is commonly used to characterize good and poor glass formers, although its validity in that has been questioned.

Differential Thermal Analysis (DTA) is another thermal characterization technique. It is similar to DSC in some respects, but for DTA the difference in temperature, not the power, between a sample and reference is measured. The sample and reference pan are heated or cooled using a common furnace and the temperature difference between the two is measured. In this work a Setaram Labsys DTA/DSC was used to measure the solidus temperature for certain ESL samples. This data was primarily used to calibrate the absolute temperature scales of the pyrometers used in WU-BESL. For the DTA measurements, approximately 30mg samples were taken from ESL samples and placed in $Al_2O_3$ crucibles that had been filled to approximately one-third full of $Al_2O_3$ powder. The sample was placed in this powder without touching the sides of the crucible, and then completely covered with more $Al_2O_3$ powder. A reference crucible that was chosen to be as identical to the sample crucible as possible was prepared in the same fashion, except without a sample. During operation, grade 5.0 Ar gas at 36PSI flowed over the crucibles to maintain a constant pressure environment.

DTA suffers from a variable temperature offset, so several standards were used for calibration. In the study of $Ni_{60}Nb_{30}Ta_{10}$, Ni, Ag, Cu and Mn were used for

calibration, since their known melting temperatures are near the expected solidus temperature of the alloys of interest. When the alloy temperature is raised to the solidus temperature a heat of transformation is evolved, creating a temperature plateau at the same temperature as is observed in the ESL. This is the only use for the DTA in this work.

### *2.3.3. Resistivity*

Measurements of the change in electrical resistivity using a four-probe technique allow quantitative studies of the phase transformation kinetics over a wider temperature range than is possible with DSC and other calorimetric techniques [12]. Resistivity is a function of crystal morphology and volume fraction in an amorphous sample. The details of a quantitative analysis will be presented in Section 3. For these studies, ribbons of ~ 3cm length (~ 40mg) were placed in an insulating MACOR® holder that was inserted into a furnace constructed from a large copper cylinder (~1 kg). The samples were initially held in a water-cooled copper block; they were inserted into the furnace after it had stabilized at the desired temperature. All measurements were made in Ti-gettered high-purity (99.995%) argon atmosphere after the chamber was pumped and backfilled several times. A thermocouple was used to monitor sample temperature; the thermal stability was typically ±0.1% over 80 hours.

The measurement circuit is designed to overcome common problems associated with resistance measurements at elevated temperatures over long time scales. The physical contact to the ribbon was made with either tungsten or tantalum pins, both highly non-reactive elements (good corrosion resistance) with extremely high melting

points to resist alloying and self-diffusion. Annealed spring steel is used to press the pins to the sample. A detailed discussion of the apparatus and measurement circuit is provided elsewhere [13]. Briefly, in the four-point probe, the four pins are placed in a row. Current is passed through the sample with the two outer pins and the voltage difference is measured between the two inner pins using a Fluke digital volt meter. A computer controlled switching circuit is used to alternate the current direction to avoid thermocouple effects; 1024 – 4096 measurements are averaged to produce a single data point. Isothermal and Non-isothermal measurements provide information about the kinetics of a particular transformation when combined with information about the transformation microstructure, as will be discussed in later sections.

### 2.4. Scattering Formalism for Studies of Amorphous States

Disordered amorphous alloys contain order on varying length scales, not the long range periodicity (LRO) associated with crystalline alloys, but rather short range (SRO) and medium range (MRO) order extending out to several coordination shells. The dominant length scales will scatter preferentially incoming probes that have a wave nature. This approach requires the experimenter to understand the interaction mechanisms between the probes (commonly electrons, X-rays, or neutrons) and the alloy. X-ray and neutron diffraction are the two common techniques for studying liquids. It is possible to generate each probe in the wavelength range that is necessary to explore Angstrom and nanometer length scales. Each probe also allows an extremely diverse set of experiments with complicated and subtle intricacies that must be understood for accurate interpretation. Neutron and X-ray diffraction experiments have several important differences. (1)

Neutrons interact with atomic nuclei via the strong interaction and with the atomic electrons via spin interactions, allowing both atomic structure and magnetic properties to be probed. (2) The dispersion relation is different for neutrons and X-rays. Neutron energies associated with Angstrom scale wavelengths are much smaller than X-rays; these energies correspond to fundamental excitations in the material, such as self-diffusion and phonons, allowing dynamical information to be obtained. (3) With isotopic substitution, the differences in scattering factors for neutrons and X-rays make it possible to directly explore chemically specific length scales and decoration. For systems where multiple isotopes are available, elemental substitution with atoms containing different numbers of neutrons than the naturally occurring and readily available isotopes provide a different scattering factor while retaining the same chemistry.

However, neutron studies suffer from some extreme technical and financial challenges. High flux neutron sources are extremely over-subscribed [14]. This and the time involved in incorporating the ancillary equipment typically required for liquid studies into a neutron beamline make X-ray studies generally more practical and certainly more common. Detailed descriptions of X-ray generation techniques are presented in Appendix II.1. followed by a discussion in Appendix II.2. pertaining to the characteristics of X-ray probes used in BESL studies. The goal of this section is to develop a formalism for extracting meaningful information about the dominant structural elements in real liquids and glasses (multi-component alloys) from the Beamline Electrostatic Levitation Technique (described in Chapter 4) with an aim towards using this information to test structural models produced by inverse fitting methods (such as Reverse Monte Carlo (RMC)) and Molecular Dynamics (MD) simulations.

In the classical description of the scattering of an electromagnetic field (such as X-rays), a charged particle, typically an electron, is accelerated by the oscillating electric field. To a good approximation, in WU-BESL, the incoming beam is highly planer and is nearly 100% polarized [15, 16] in the horizontal plane. Because the mass of an electron is over a thousand times lighter than that of a nucleon, the acceleration of the charged particles in the nucleus by the X-ray is much less than that in the electron. Thus, X-ray interactions provide information about correlations with the electrons in the atoms comprising the alloy of interest, having a spatial density $\rho(\mathbf{r})$, NOT the atomic centers. We seek to solve the quantum mechanical scattering problem, finding a spatial and temporal solution to the Schrödinger Equation. However, when atomic motions are slow compared to the transit time of the photons (which is well justified), steady state solutions, $\Psi(\mathbf{r})$, to Equation 9 are sought, which generally includes the superposition of the incident wave and all the scattered waves.

$$\left(\nabla^2 + k^2\right)\psi(\mathbf{r}) = U(\mathbf{r})\psi(\mathbf{r}) \tag{9}$$

This quantum mechanical formalism is one approach to understanding the interactions of X-rays with liquids and glasses. However, since the formalism used in subsequent chapters is more classical in nature, the derivation of the solution to the quantum mechanical scattering problem is discussed in Appendix II.3.

The scattering from an atom with *Z* electrons is to be described. The resulting radiation field is the superposition of all of the contributions from all different volume elements of the charge distribution on the scattering process. Let ***k'*** and ***k*** be the wave vectors of the incident and the scattered wave, respectively. Then the phase difference

between a wave that is scattered by a volume element at the origin and one scattered at a point **r** is:

$$\Delta\phi = (\mathbf{k} - \mathbf{k}') \cdot \mathbf{r} = \mathbf{q} \cdot \mathbf{r} \quad , \tag{10}$$

where ***q*** is the momentum transfer vector. The scattering length, or atomic form factor, is the Fourier transform of the electron charge density, $\rho(\mathbf{r})$

$$f(\mathbf{q}) = \int e^{-i\mathbf{q}\cdot\mathbf{r}} \rho(\mathbf{r}) d\mathbf{r} \, . \tag{11}$$

In the limit of small *q*, all elements within the localized charge density scatter in phase, so that as $q \to 0$ the form factor is simply the integral of the charge density, giving the number of electrons (for X-rays) in the scattering element. In the other limit, as $q \to \infty$, we expect all of the phases to cancel, and the scattering length, or often called the atomic form factor, should go to zero. The semi-analytical forms for the form factors for most elements have been tabulated [17]; the form factors for Zr and Pt are plotted in Figure 2.5. An isotropic distribution of charge is assumed, so $f(\mathbf{q}) \to f(q)$. This is the typical form for $f(q)$ when the X-ray energy is far away from any atomic resonances.

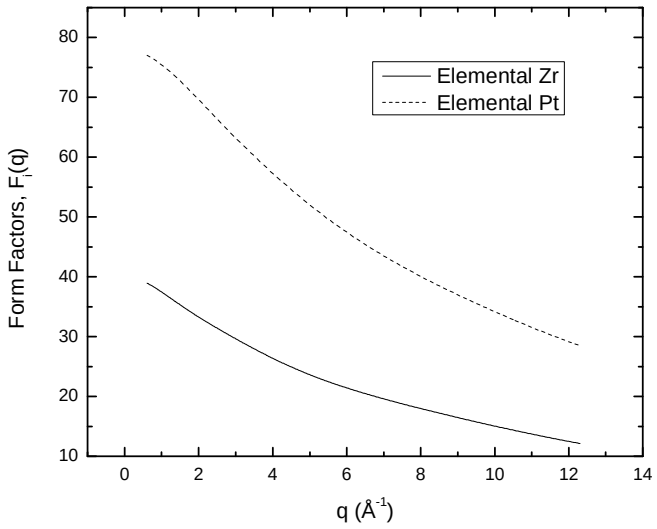


**Figure 2.5-** Form factors from a semi-empirical model (from [3]).

It is instructive to explore the behavior of two or more electrons in various distributions to develop a physical intuition about the scattering from multiple or extended potentials. The simplest case, then, is the scattering of an incident plane wave (or wave packet) from two point sources with potentially different scattering factors, $f_1$ and $f_2$. The scattering amplitude is

$$A(\mathbf{q}) = f_1 + f_2 e^{-i\mathbf{q}\cdot\mathbf{r}} \tag{12}$$

where we place one scattering center at the origin and another at a distance **r** away. After an orientational average, the intensity is then,

$$\langle I(\mathbf{q})\rangle = I(q) = \langle A^*(\mathbf{q})A(\mathbf{q})\rangle = f_1^2 + f_2^2 + 2 f_1 f_2 \langle e^{-i\mathbf{q}\cdot\mathbf{r}}\rangle . \tag{13}$$

The result depends on the details of the configuration of the scattering centers. Figure 2.6 shows the simulated scattering intensity, $I(q)$, (a) for two stationary electrons, (b) one fixed electron and one allowed to orbit at a fixed distance, ***r***, but with random

orientations, and (c) two scattering centers with a localized (but uniform) electron density at a fixed orientation. The distribution of electron density has a non-trivial impact on the scattering intensity, and our primary concern will eventually be to use simulated scattering experiments of atomic models to reconstruct experimentally observed intensities. This concept can be extended analytically to a limited number of alloys, but numerical techniques provide powerful tools for validating structural models of liquids and glasses. We desire a complete description of atomic arrangement from experiment, but evidence from diffraction experiment is limited to two-body correlations. Higher order correlations cannot be measured by traditional techniques.

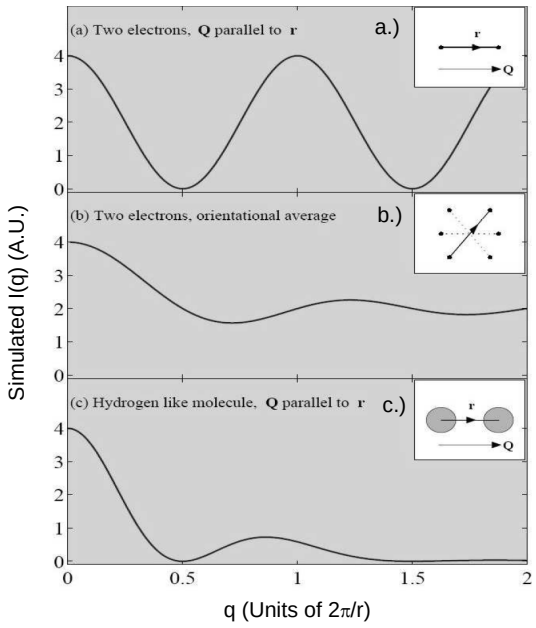


**Figure 2.6-** Simulated $I(q)$ (a) for two stationary electrons, (b) one fixed electron and one allowed to orbit at a fixed distance, $r$, but with random orientation, and (c) two scattering centers with localized (but uniform) electron density at a fixed orientation. (Picture from [18].)

The goal now is to develop the formalism further to deal with real liquid alloys. For multiple atomic scattering sites, the potential is written as a superposition of local potentials centered on points, $\boldsymbol{R}_i$:

$$U(\mathbf{R}) = \sum_i u(\mathbf{R} - \mathbf{R}_i). \tag{14}$$

This form doesn't preclude extended charge distributions; the amplitude of a scattered X-ray from a single atom can be computed using Equation 15:

$$A(\mathbf{q}) = f(\mathbf{q}) \exp(-i\mathbf{q} \cdot \mathbf{R}). \tag{15}$$

Remembering that we measure the intensity and not the amplitude in a scattering experiment,

$$I(\mathbf{q}) = A^*(\mathbf{q})A(\mathbf{q}) = |A(\mathbf{q})|^2, \tag{16}$$

the measured intensity for multiple scattering sites is

$$I(\mathbf{q}) = \left| \frac{1}{V} \int \sum_i u(\mathbf{R} - \mathbf{R}_i) e^{-i\mathbf{q}\bullet\mathbf{R}} d\mathbf{V} \right|^2. \tag{17}$$

By a transformation of variables

$$I(\mathbf{q}) = \frac{1}{N^2} \sum_i e^{-i\mathbf{q}\bullet(\mathbf{R}_i - \mathbf{R}_j)} \left| \frac{N}{V} \int u(\mathbf{R}') e^{-i\mathbf{q}\bullet\mathbf{R}'} d\mathbf{V}' \right|^2, \tag{18}$$

where we have written the intensity for a single element, with the same scattering $u(\boldsymbol{R'})$. The formalism generalizes for multi component alloys, which will be discussed in later sections. For now, we will limit ourselves to single elemental systems. The intensity is

$$I(\mathbf{q}) = \frac{1}{N} S'(\mathbf{q}) |u(\mathbf{q})|^2 \tag{19}$$

and $S'(\mathbf{q})$ is an atomic center static structure factor. $S'(\boldsymbol{q})$ represents the atom center correlations, not the electron correlations; Real scattering experiment which include contributions from electron correlations within atoms. $S'(\mathbf{q})$ can be written as

$$S'(\mathbf{q}) = \frac{1}{N}\rho_{\mathbf{q}}\rho_{-\mathbf{q}} \tag{20}$$

where $\rho_{\mathbf{q}}$ is the Fourier component of the microscopic density,

$$\rho(\mathbf{r}) = \sum_i \delta(\mathbf{r} - \mathbf{r}_i). \tag{21}$$

When the density is only considered in terms of the atom centers, we can substitute the delta function form of the density (Equation 21) into the Fourier transform of the electron charge density (Equation 11) giving:

$$\rho_{\mathbf{q}} = \int \rho(\mathbf{r})\exp(-i\mathbf{q}\cdot\mathbf{r})d\mathbf{r} = \sum_i \exp(-i\mathbf{q}\cdot\mathbf{r}_i) \tag{22}$$

and the structure factor, Equation 20, becomes:

$$\begin{aligned} S'(\mathbf{q}) &= \left\langle \frac{1}{N}\sum_i \sum_j \exp(-i\mathbf{q}\cdot\mathbf{r}_i)\exp(i\mathbf{q}\cdot\mathbf{r}_j) \right\rangle \\ &= \left\langle \frac{1}{N}\sum_i \sum_j \exp(-i\mathbf{q}\cdot(\mathbf{r}_i - \mathbf{r}_j)) \right\rangle \end{aligned} \tag{23}$$

and

$$S'(\mathbf{q}) = \left\langle \frac{1}{N}\iint \sum_i \sum_j \exp(-i\mathbf{q}\cdot(\mathbf{r}-\mathbf{r}'))\delta(\mathbf{r}-\mathbf{r}_i)\delta(\mathbf{r}'-\mathbf{r}_j)d\mathbf{r}d\mathbf{r}' \right\rangle. \tag{24}$$

Utilizing a common definition for the two body correlation function [19],

$$\begin{aligned} S'(\mathbf{q}) &= \left\langle 1 + \frac{1}{N}\iint \sum_{i\neq j} \exp(-i\mathbf{q}\cdot(\mathbf{r}-\mathbf{r}'))\{\delta(\mathbf{r}-\mathbf{r}_i)\delta(\mathbf{r}-\mathbf{r}_j)\}d\mathbf{r}d\mathbf{r}' \right\rangle \\ &= 1 + \frac{1}{N}\iint \exp(-i\mathbf{q}\cdot(\mathbf{r}-\mathbf{r}'))\{\rho_N^{(2)}(\mathbf{r}-\mathbf{r}')\}d\mathbf{r}d\mathbf{r}' \end{aligned} \quad . \tag{25}$$

In this description it becomes clear that, for atomic centers, the Fourier transform of the density is manifest as the static structure factor.

$$S'(\mathbf{q}) = 1 + \frac{1}{N}\iint \exp(-i\mathbf{q}\cdot\mathbf{r})g(r)d\mathbf{r} \tag{26}$$

In this step, the relationship between the two-body correlation function and the pair distribution function was used. This relationship between the static structure factor and the pair correlation function is slightly different from what is generally presented [20]. The extended nature of the electron distribution is not the concern - rather that the Fourier transform is generally written as

$$S'(\mathbf{q}) = 1 + \frac{1}{N}\iint \exp(-i\mathbf{q}\cdot\mathbf{r})(g(r)-1)d\mathbf{r}\,. \tag{27}$$

(The difference is that in Equation 26 g(r) is Fourier transformed while in Equation 27 $g(r)$ - 1 is Fourier transformed.) To explain this difference, we go back to measured scattered intensity. For X-rays, with actual q-dependence in the form-factors, orientational averaging over a single atom gives:

$$I(q)=\left\langle A(\mathbf{q})^* A(\mathbf{q})\right\rangle=\left\langle f(\mathbf{q})^* \exp(i\mathbf{q}\cdot\mathbf{r}) f(\mathbf{q})\exp(-i\mathbf{q}\cdot\mathbf{r})\right\rangle \tag{28}$$

or

$$I(q)=\left\langle A(\mathbf{q})^* A(\mathbf{q})\right\rangle=\left\langle f(\mathbf{q})^* f(\mathbf{q})\right\rangle \tag{29}$$

and generalizing to multiple scatters:

$$I(q)=\left\langle \sum_i\sum_j f_i(\mathbf{q})^* \exp(i\mathbf{q}\cdot\mathbf{r}_i) f_j(\mathbf{q})\exp\left(-i\mathbf{q}\cdot\mathbf{r}_j\right)\right\rangle. \tag{30}$$

For single component systems, with a uniform distribution of electrons in each atom, the intensity is given by

$$I(q)=Nf(q)^2+\left\langle \sum_i \sum_{j\neq i} f_i(\mathbf{q})^* f_j(\mathbf{q})\exp\left(-i\mathbf{q}\cdot\left(\mathbf{r}_j-\mathbf{r}_i\right)\right)\right\rangle. \tag{31}$$

The mathematics of the orientational average is straightforward and is presented in Appendix II.4. For isotropic form factors, orientational averaging gives the predicted

intensity for an isotropic and homogeneous material. Let the difference in atomic positions between the $i^{th}$ and $j^{th}$ atoms be $\mathbf{r}_i - \mathbf{r}_j = \mathbf{r}_{ij}$. Then

$$I(q) = Nf^2(q) + \sum_i \sum_{j \neq i} f^2(q) \frac{\sin(qr_{ij})}{qr_{ij}}. \tag{32}$$

Considering the cross terms, since the microscopic density can be expressed as a sum of delta functions (Equation 21), contributions to the sum when the atomic density is non-zero can be replaced with the atomic density, integrated over the volume

$$I(q) = Nf^2(q) + f^2(q) \sum_i \int \rho(r_{ij}) \frac{\sin(qr_{ij})}{qr_{ij}} dV \quad . \tag{33}$$

Adding and subtracting the term

$$f^2(q) \sum_i \int 4\pi r^2_{ij} \rho_0 \frac{\sin(qr_{ij})}{qr_{ij}} dr_{ij}$$

the total intensity is then expressed as

$$\begin{aligned} I(q) = Nf^2(q) + f^2(q) \sum_i 4\pi r^2_{ij} \int (\rho(r_{ij}) - \rho_0) \frac{\sin(qr_{ij})}{qr_{ij}} dr_{ij} \\ + f^2(q) \sum_i \int 4\pi r^2_{ij} \rho_0 \frac{\sin(qr_{ij})}{qr_{ij}} dr_{ij} \end{aligned} \quad . \tag{34}$$

The third term in Equation 34 contributes only at small scattering angles, which is why it does not appear in most derivations. Strictly speaking, it should be included. Changing the variable $r_{ij} = r$, which is a more conventional notation, and summing over all of the atoms gives.

$$I(q) = Nf^2(q) + Nf^2(q) 4\pi\rho_0 \int r^2 (g(r) - 1) \frac{\sin(qr)}{qr} dr \quad . \tag{35}$$

Usually, the static structure factor is defined as

$$S(q) = 1 + \frac{I(q) - Nf^2(q)}{Nf^2(q)} = 1 + 4\pi\rho_0 \int r^2 \left(g(r) - 1\right) \frac{\sin(qr)}{qr} dr \tag{36}$$

Here, $g(r) = \frac{\rho(r)}{\rho_0}$ and is often the quantity of interest. This, the pair-distribution function, represents the average probability that, given an atom at the origin, another atom is located in a shell of thickness *dr* at a distance *r* away. Different materials have characteristic *g*(*r*) and *S*(*q*) behavior, shown schematically in Figure 2.7.

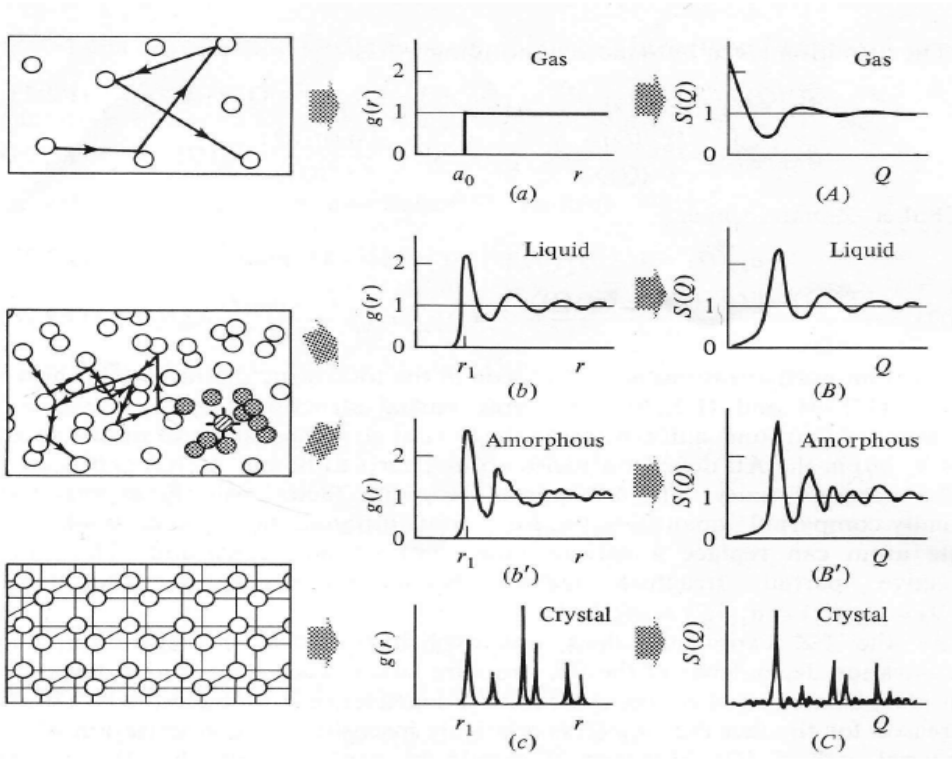


**Figure 2.7**-Characteristic *g*(*r*) and *S*(*q*) for a gas, liquid, amorphous solid and crystal. Figure from [21].

The relationship between *S*(*q*) and *g*(*r*) provides the basis for the structural analysis in amorphous phases.

## 2.5. Data Collection

### *2.5.1. Obtaining I(q)*

The intensity versus momentum transfer, $q$, is measured during a typical BESL experiment. Since liquid scattering data from metals is of principle interest, the isotropic assumptions are well justified. The details of the measurement of $I(q)$ are now presented for the case where the atomic form factors are well approximated by the form shown in Figure 2.5, or when the X-ray energy is high enough and sufficiently far from any atomic absorption edges that the scattering is primarily elastic.

The diffraction experiments presented in this work were made at the Advanced Photon Source (APS) at Argonne National Lab in beamline Sector 6 ID-D, a high energy beamline station. In the past this group has routinely worked with stationary samples, such as as-cast rods and as-quenched amorphous ribbons; the details of those studies are not a focus of this work and are presented elsewhere [5]. Many of the data reduction techniques used, however, are the same for liquids and glasses since both are isotropic materials.

The basic geometry for a diffraction experiment is shown below in Figure 2.8, with an example diffraction pattern also shown. An isotropic liquid produces broad diffraction rings, with no statistically significant differences in the intensity at any two values of $\phi$. Unless otherwise noted, all the scattering data in this work were taken with a GE Revolution 41-RT amorphous Si flat panel detector. The detector has an active area of 41×41 $cm^2$ with a 200×200 $\mu m^2$ pixel size. It has a maximum capturing rate of 8 frames per second (fps) when operating in an un-binned mode and 30 fps in a binned or region of interest (ROI) mode [22], which is the mode used in this work. The effective

bin size for the detector in this case is 400x400 $\mu m^2$. There are three contributions to the measured intensity. (1) Real contributions to counts that come from liquid diffraction data as well as from any background scatter from the Be windows, secondary scattering from the chamber and other spurious sources. (2) When the X-ray shutter is closed and there are no X-rays incident on the sample or chamber a large number of counts are still detected. This *dark current* is relatively constant with time, but has some temperature dependence. It has a distribution that, once azimuthally averaged over the detector face, is a nearly monotonically decreasing function of *q*. (3) Finally, there is a *detector burn-in* remnant from previous acquisitions when the shutter was open. It is reported in a characterization of the GE detector for synchrotron use by J. H. Lee *et al*. [22] that this burn-in has a very rapid time decay called the "lagging" residual signal. Since the finite decay constant of the phosphor is measured as 1 μsec, this makes an insignificant contribution to the observed burn-in. The burn-in from crystal patterns can persist for tens to hundreds of seconds, depending on the length of the previous exposure.

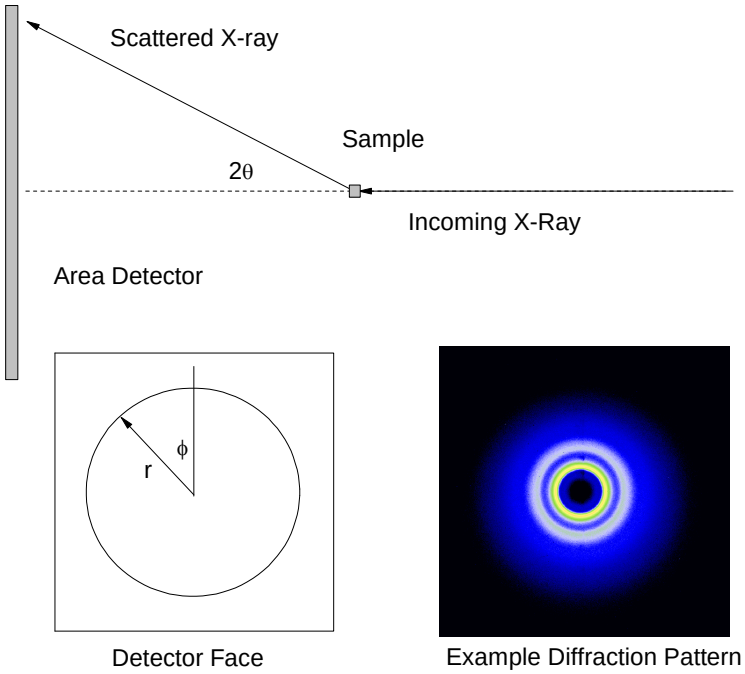


**Figure 2.8-** Schematic diagram of the diffraction geometry for a BESL experiment with an example diffraction pattern.

The different contributions to the intensity can be approximately removed to leave only the liquid intensity as a function of *q* by limiting the exposure time for the crystal patterns obtained during the crystallization of the liquid. If the exposure time is less than 10 sec, the burn-in is minimal and generally undetectable in subsequent liquid structures, when the time between liquid exposures is also approximately 10 sec. However, when the exposure time to crystal diffraction is substantial, a dark exposure taken prior to liquid exposure, with the subtraction of a previous dark (with the shutter closed and no burn-in remnant) exposure can sometimes be useful in removing spurious burn-in peaks. When data is obtained in Step Hold mode, a dark exposure, taken directly after the liquid diffraction pattern, is usually subtracted from liquid data. For data acquisition, the burn-in from the liquid diffraction peaks persists frame to frame, causing the intensity of the

liquid diffraction peaks to be artificially high in subsequent diffraction frames. However, since it is difficult to estimate the amount of burn-in decay that occurs while acquiring liquid data with the shutter open, it is difficult determine to what extent the correction from the dark exposure subtraction is correct. The decay of the burn-in remnant of the liquid diffraction peaks has been measured, but only after the shutter is closed. The detector burn-in remnant from exposure to the liquid diffraction is small, from as little as 0.1% for a 1 sec exposure to nearly 3% for a 20 sec exposure. This is fortunate, since it is not possible to perform a dark exposure subtraction in the Free Cool mode, for which the exposure is limited to a few seconds.

In the standard data acquisition procedure, an exposure is first taken of an "empty chamber" with the x-ray shutter open at the sampling rate for which experimental data are taken. The empty chamber exposure contains contributions to the scattered signal arising from scattering of the direct beam off the exit and entrance windows, background scattering from the vacuum path leading to the detector, scattering from the beamstop and secondary scatter from within the chamber. Empirically, aside from unusual circumstances, there is no difference in the empty chambers exposures taken before or after an experiment, and with or without a sample sitting on the bottom of the electrode assembly. This empty chamber exposure, once properly scaled for the number of frames, is subtracted from the liquid exposure and burn-in dark exposure frames before the construction of $S(q)$ and $g(r)$.

### *2.5.2. Labview™ Detector Synchronization*

The detector was operated using a graphical interface program provided by the APS. It has the option of switching a TTL signal to the "high" state when the detector is

acquiring frames. By using an USB Analog-to-Digital converter with TTL input the Labview™ acquisition program can then record when the detector is recording frames. With a knowledge of the frame rate, the frames of interest can be identified.

### *2.5.3. Batch Processing*

Raw image files were collected in single composite image files of image type 16-bit unsigned, width 1024 pixel, height 1024 pixel in little-endian byte order with an 8192 byte header. The raw image files were divided into relevant image, dark and background image files using in-house batch-processing software [23] in a script written in Perl. An example of the script is provided in Appendix II.5. The script isolates the frames of interest (which can be identified in the Labview™ acquisition program or Image J), conducts a pixel by pixel background subtraction (frame normalized), multiplies each pixel by the gain map (normalizing for underperforming or over performing regions of the detector face) and outputs the frames of interest by summing them together or outputting individual files. These 16-bit unsigned, 1024 pixel by 1024 pixel frames can then be processed to obtain $I(q)$.

### *2.5.4. Fit2D*

Fit2D [24] is an image processing program that takes the raw image files and converts then into $I(q)$. First, the diffraction pattern from polycrystalline Si is used to calibrate the detector distance to the sample and the detector orientation relative to the input scattering axis. Because the diffraction pattern is well known in Si (diamond, lattice parameter

5.431 Å [25]) the distance and deviation from circular diffraction pattern can be used for calibration. ESL Si samples were prepared by arc-melting raw materials into tear drop shapes and mechanically grinding the samples into spherical samples. The ESL samples were then levitated and *in-situ* diffraction data were used for calibration for each new carousel of samples. A fit was typically made to the inner diffraction ring. As a second calibration standard, NIST SRM 640C powdered Si was placed in a capillary, which was aligned with the electrode assembly to check for errors in the distance calibration due to lattice distortions. The error between an ESL sample and a NIST standard was within the error of multiple calibrations.

A "mask" was constructed to remove any bad pixels before processing the image files. This particular mask, show in Figure 2.9, was created by manually locating pixels that which read zero intensity. Additionally, a threshold mask could be used which removes any pixels that read less than or greater than a certain individual pixel value.

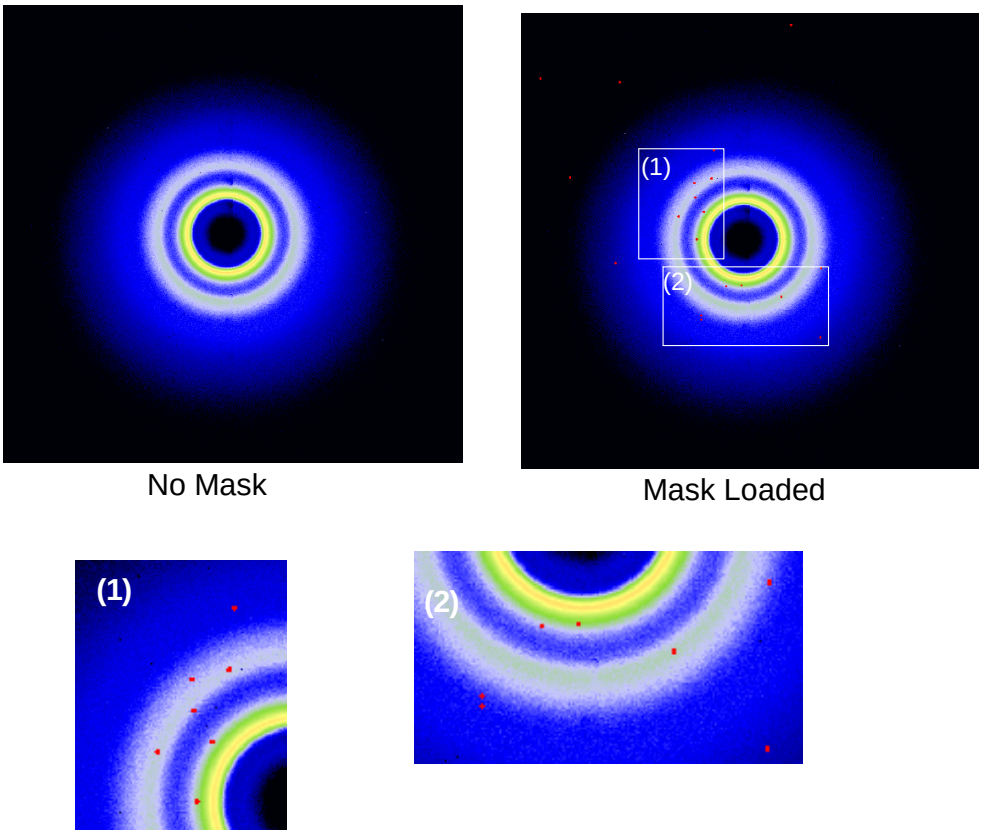


**Figure 2.9-** Mask employed (red pixels) in Fit2D to remove bad pixels before azimuthal averaging. Regions (1) and (2) are shown larger.

After the calibration and mask steps, the image is azimuthally averaged and the detector distance used to convert the radial distance on the detector face into *q*-space (momentum transfer). The "geometry" correction is used to correct for changes in distance and obliqueness at higher angles due to the flat face of the image plate, as compared with a small detector that can be scanned in *q*-space to always keep the face of the detector perpendicular to the sample. The correction maps detector area increment, *da*, to scattering solid angle, $d\Omega$, both quantities are defined in Figure 2.10. First, the solid angle is converted into area, *dA*, on the sphere of radius *r*:

$$\frac{dI}{d\Omega} = r^2 \frac{dI}{dA} = \frac{d^2}{\cos(2\theta)^2} \frac{dI}{dA}. \tag{37}$$

On the surface of the sphere, a general area element is

$$\begin{aligned} dA &= r^2 \sin(2\theta) d(2\theta) d\phi \\ dA &= \frac{d^2}{\cos(2\theta)^2} \sin(2\theta) d(2\theta) d\phi \end{aligned} \tag{38}$$

while, on the detector face, a general surface area element is

$$da = y dy d\phi. \tag{39}$$

Since

$$y = D \tan(2\theta), \tag{40}$$

and

$$dy = D \sec(2\theta)^2 d(2\theta), \tag{41}$$

the detector surface area element becomes

$$da = D^2 \frac{\sin(2\theta)}{\cos(2\theta)^3} d(2\theta) d\phi. \tag{42}$$

By inspection, we can then relate *da* and *dA*:

$$\frac{dA}{\cos(2\theta)} = da \tag{43}$$

so

$$\frac{dI}{d\Omega} = \frac{d^2}{\cos(2\theta)^3} \frac{dI}{da}. \tag{44}$$

Thus, the geometry correction acts to increase the intensity with increasing *q*, with the correction being almost 7% at 18 $Å^{-1}$, but only about 0.2% around the first peak in *S(q)*.

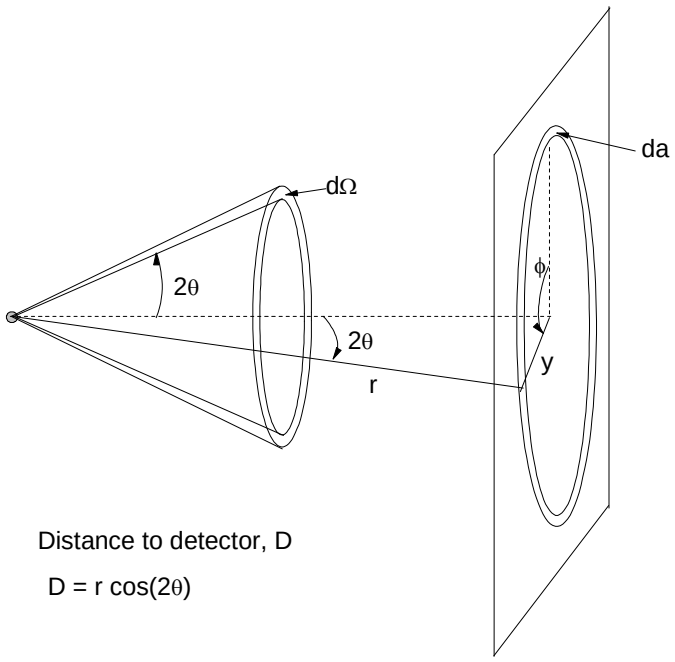


**Figure 2.10-** Coordinate system and references for the geometry correction in Fit2D®.

The synchrotron radiation is highly polarized in the plane of the ring, which is also perpendicular to the dipole direction in the undulator. The undulator and other aspects of synchrotron X-ray generation are presented in Appendix II.1. and Appendix II.2. Estimates place the polarization from 98% to 99.99% [15]. When polarized radiation is incident on a scattering center, that center will be accelerated, emitting radiation in response. Because the radiation will be emitted in directions other than the incident radiation the effect of scattering into other polarization states must be considered. A short derivation is informative. We begin with the instantaneous power radiated into the complex polarization state **p**, by a particle with charge *e* in the non-relativistic limit [26]

$$\frac{dP}{d\Omega} = \frac{e^2}{4\pi c^3}\left|\mathbf{p}^* \bullet \mathbf{a}\right|^2 \quad , \tag{45}$$

where **a** is the acceleration of the particle, provided by the plane wave. The electric field of the incident plane wave is written as

$$\mathbf{E}(\mathbf{x},t) = \mathbf{p}_0 E_0 e^{i(\mathbf{k}_0 \bullet \mathbf{x} - \omega t)} \tag{46}$$

where $\mathbf{p_0}$ is the incident polarization state. The acceleration of the charged particle is also along the polarization direction

$$\mathbf{a}(t) = \mathbf{p}_0 \frac{e}{m} E_0 e^{i(\mathbf{k}_0 \bullet \mathbf{x} - \omega t)}. \tag{47}$$

If we assume that the particle moves negligibly in one photon cycle of oscillation, i.e. the mass of the particle is large such that the acceleration is small, the time average power radiated per unit solid angle is

$$\left\langle \frac{dP}{d\Omega} \right\rangle = \frac{c}{8\pi} |E_0|^2 \left( \frac{e^2}{mc^2} \right)^2 \left| \mathbf{p}^* \bullet \mathbf{p}_0 \right|^2. \tag{48}$$

Since the power radiated per solid angle is related to the differential scattering cross section [26], the dot product in the above expression is of interest. If we introduce the coordinate system in Figure 2.11, where $\mathbf{K_0}$ is the incident X-ray momentum, **n** is the direction of the scattered X-ray, and the scattered polarization state is represented as $\mathbf{p} = \vec{\varepsilon}_1 + \vec{\varepsilon}_2$. The polarization vector $\boldsymbol{\varepsilon}_1$ is in the plane defined by $\mathbf{K_0}$ and **n**; $\boldsymbol{\varepsilon}_2$ is perpendicular. In this coordinate system, the detector face is the plane *x*-*y* and the azimuthal angle is $\phi$.

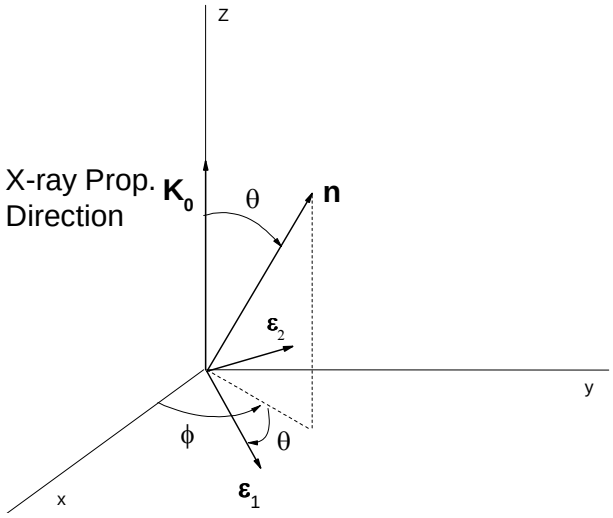


**Figure 2.11-** Coordinate system for polarization in scattering process. (The geometry is consistent with Jackson [26]; see that for a more comprehensive discussion.)

The polarization vectors written in terms of the coordinate axes are

$$\begin{aligned} \vec{\varepsilon}_1 &= \cos\theta\left(\hat{x}\cos\phi + \hat{y}\sin\phi\right) - \hat{z}\sin\theta \\ \vec{\varepsilon}_2 &= -\hat{x}\sin\phi + \hat{y}\cos\phi \end{aligned} \quad . \tag{49}$$

The incoming beam from the undulator is polarized. This modifies the image plate intensity distribution because scattering into different polarization states includes an angular, $2\theta$, dependence. If the incident radiation is a linear combination of polarization states, then the true intensity, $I(2\theta,\phi,)$, is multiplied by a factor

$$\left(f_h\left(\cos^2\theta\cos^2\phi + \sin^2\phi\right) + f_v\left(\cos^2\theta\sin^2\phi + \cos^2\phi\right)\right) \tag{50}$$

where $f_h$ and $f_v$ are the fractions of polarization of the incident beam in the horizontal ($x$) and vertical ($y$) directions, respectively. The angular and azimuthal dependence is found by summing over the final polarization states. However, we can see that because the intensity measured on the image plate, $I$, does not have an azimuthal dependence for liquid diffraction data, an average over $\phi$ gives

$$\begin{aligned}\langle I\rangle_{\phi} &= \langle I(2\theta,\phi)*\left(f_h\left(\cos^2\theta\cos^2\phi+\sin^2\phi\right)+f_v\left(\cos^2\theta\sin^2\phi+\cos^2\phi\right)\right)\rangle \\ &= I(2\theta)\left\{\cos^2\theta\left(f_h\langle\cos^2\phi\rangle+f_v\langle\sin^2\phi\rangle\right)+\left(f_h\langle\sin^2\phi\rangle+f_v\langle\cos^2\phi\rangle\right)\right\} \\ &= I(2\theta)\left\{\cos^2\theta\left(f_h\frac{1}{2}+f_v\frac{1}{2}\right)+\left(f_h\frac{1}{2}+f_v\frac{1}{2}\right)\right\}\end{aligned} \quad . \tag{51}$$

Since $f_h + f_v = 1$,

$$\langle I(2\theta)\rangle_{\phi} = I(2\theta)\frac{1}{2}\left(1+\cos^2(2\theta/2)\right). \tag{52}$$

This expression shows that the measured intensity, once azimuthally averaged, will be artificially reduced due to the polarization of the incident beam. A polarization correction is used to correct this. A few notes follow. (1) For liquid samples, as long as the diffraction pattern is truly isotropic, the actual values of the polarization fractions are irrelevant; the correction in Fit2D just needs to be turned "on." (2) If diffraction patterns from anisotropic materials are analyzed, then the orientation of the detector and the details of the polarization of the incident beam may be important and should be considered. For example, in BESL2010, the detector was placed on its side so that the ring plane was vertical, *not* horizontal. For a perfectly polarized beam in this orientation, the polarization factor should be -1.00. All of the corrections discussed are implemented in a macro, an example of which is given in Appendix II.6.[4] The result of using this will be to produce a ".chi" file, which refers to an $I(q)$ file.

[4] Note that the mask must be loaded manually before the macro is executed. This is done by opening an image file and then loading the mask of interest. Once the mask is loaded, as long as the program remains open and the mask isn't cleared, it will be placed on all images loaded.

### *2.5.5. PDFGetX2*

#### *2.5.5.1.* General Considerations

PDFGetX2 is a program with a graphical interface designed to generate $S(q)$ and $G(r)$ from experimental scattering data. The previously discussed liquid, dark, and background subtraction are first individually scaled and then combined to give the $I(q)$ data used as input for PDFGETX2. The construction of $S(q)$ is deceptively simple using this program, and can lead to mistakes. It is critical that the various corrections be understood before being used. Although laborious, we now explore the most important corrections. Many of the corrections are also discussed comprehensively in the PDFGetX and PDFGetX2 manuals [27][28][29], which are not always entirely transparent.

#### *2.5.5.2. File Input*

Files (in *.chi* format) are used as input to PDFGetX2 using the graphical user interface (GUI) shown in Figure 2.12. Liquid data are input using the *Sample* tab, the Empty Chamber file using the *Sam. Bkg*. tab and the Dark Current (when appropriate) using the *Container* tab. Each file input has a different multiplicative constant that is applied before subtraction from the liquid file. The constants can be negative and the Xmin and Xmax specify the range of data (in $nm^{-1}$). (Note that the X Column is labeled as 2Theta but will take input in either 2Theta or *q* format, which is specified in the I(q) Setup/Calibration tab).

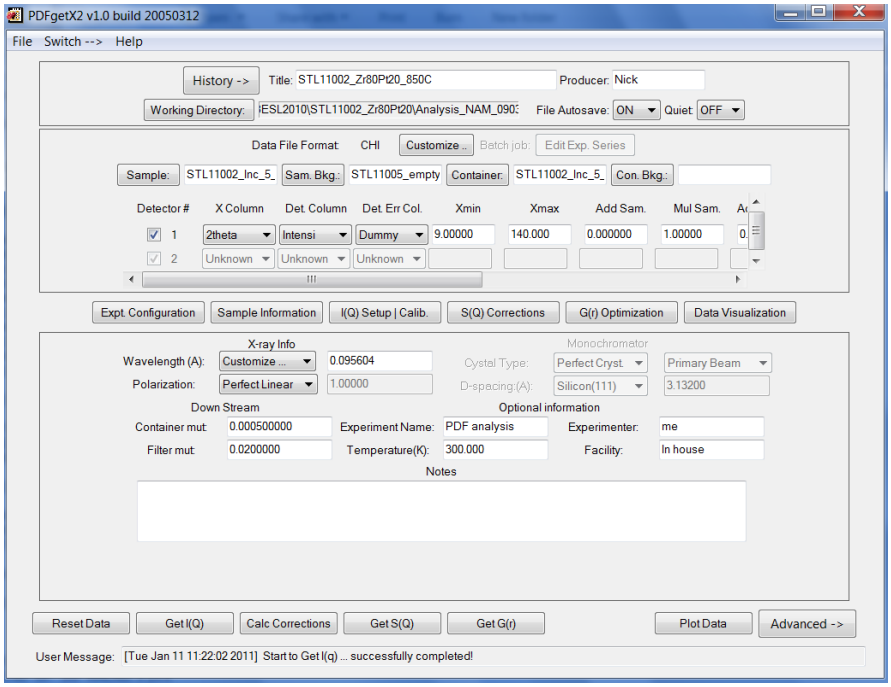


**Figure 2.12-** PDFGetX2 GUI showing the file input and Experimental Configuration and other tabs.

### *2.5.5.3. Experimental Configuration*

The X-ray wavelength is the only parameter entered here**,** as shown in Figure 2.12. The polarization correction is applied in Fit2D, and the entry for Down Stream mut ($\mu$*t) is small since we don't have any experimental data concerning the absorption of the detector.

### *2.5.5.4. Sample Information*

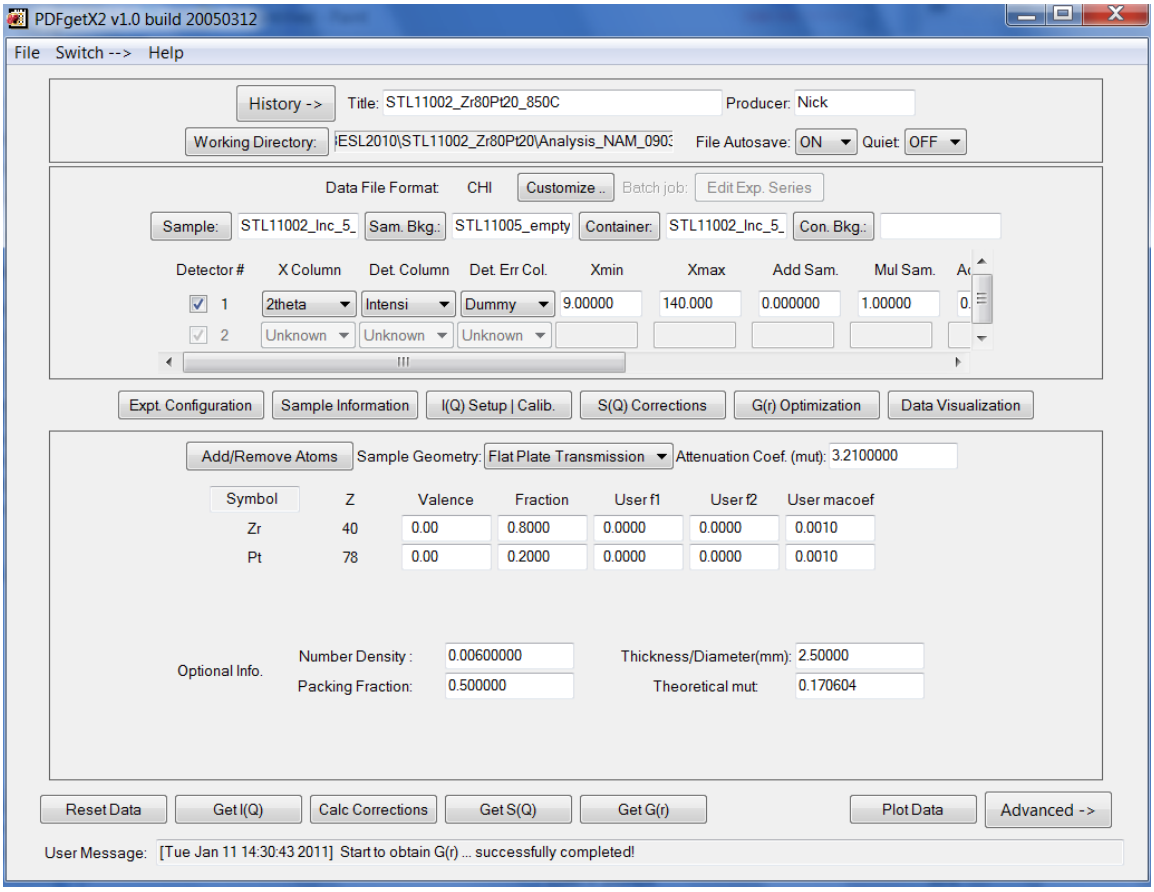


**Figure 2.13-** PDFGetX2 sample information tab.

In the Sample Information tab, Figure 2.13, the chemical composition of the alloy is first entered, ignoring the possibility of valence and ignoring the optional information since they don't influence corrections. The attenuation coefficient is a density, composition, and X-ray energy dependent term that attempts to correct for attenuation of the X-ray beam as it enters the sample and the scattered beam as it propagates through the sample. There are 4 options for the sample geometry: Flat Plate Reflection, Flat Plate Transmission, Flat Plate Stationary (IP) and Cylindrical Capillary. In the various geometries, the attenuation enters in a different functional form. Historically this group

has used Flat Plate Transmission geometry, however this has recently been debated. The geometry of the sample has an important influence on the attenuation correction *q*-dependence. This correction is not trivial, and a great deal of literature exists for very specific geometries (for example see W. Pitschke *et* al. [30]). For two of the geometries in PDFGetX, we can see that the attenuation enters differently in the two expressions for the multiplicative absorption factor:

1.) Flat Plate Reflection

$$A = \left(1 - e^{-2\mu t / \sin(2\theta/2)}\right) / 2\mu t \tag{53}$$

2.) Flat Plate Transmission

$$A = \mu t \cdot e^{\left(-\mu t / \cos(2\theta/s)\right)} / \cos(2\theta/2) \tag{54}$$

The attenuation coefficient is calculated using the NIST X-ray attenuation coefficients [31], which give the attenuation coefficients (per unit mass density) for each element as a function of incident energy. Thus, to calculate the attenuation coefficient, $\mu$, for an alloy:

$$\mu = \rho_{ave} \sum_i \left(\mu / \rho\right)_i MF_i \tag{55}$$

where $\left(\mu / \rho\right)_i$ are the tabulated attenuation coefficients, $MF_i$ are the mass fractions of each constituent, *i*, and $\rho_{ave}$ is the experimental mass density.

### *2.5.5.5. I(q) Setup/Calibration*

This tab (Figure 2.14) is used only to specify the format of the independent variable for the input data. We can could chose to input 2Theta or *q* data. Since we don't have any information about effective absorption, nor is a filter applied to the data, these tabs are

not used. Additionally, the literature is particularly sparse on the nature of these corrections, so it isn't clear how they would even operate. The "Reset Negative Value" input is -1.00000 by default, but it isn't clear what this option does and the value itself seems to have no impact on *S(q)* generation.

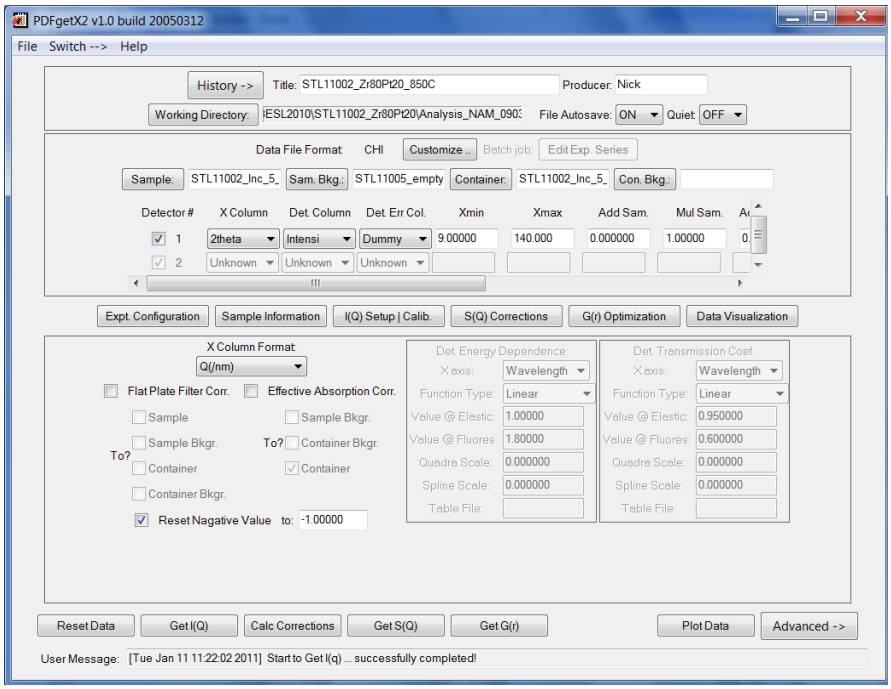


**Figure 2.14-** PDFGetX I(q) setup and Calibration tab.

### *2.5.5.6. S(Q) Corrections*

There are several major corrections that be made in the S(Q) Corrections tab, shown in Figure 2.15. It should be noted that our understanding of this program and the accuracy of the corrections continues to evolve. We begin with the assumption that the measured X-ray intensity can be expressed [21]:

$$I_{meas} = PAN\left( I^{coh} + I^{incoh} + I^{multiple} + \frac{I^{Fluor}}{P} \right) \tag{56}$$

where $I_{meas}$ is the measured intensity, $P$ is the polarization factor (which is corrected for in Fit2D), $A$ is the absorption (whose form and attenuation coefficient is defined in the Sample Information tab), $N$ is a normalization factor, $I^{coh}$ is the coherent, elastic scattering contribution, $I^{incoh}$ is the incoherent or Compton scattering contribution, $I^{multiple}$ is the multiple scattering contribution and $I^{Fluor}$ is the isotropic fluorescence correction.

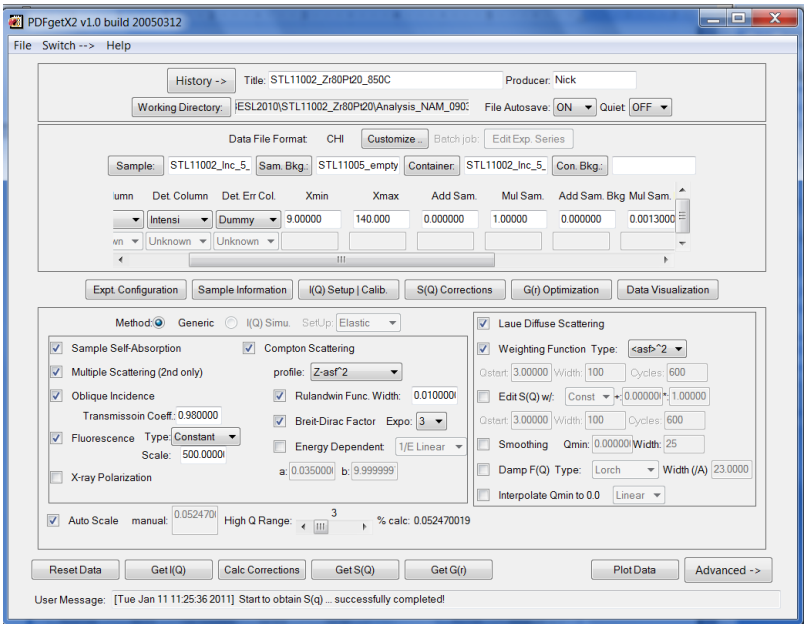


**Figure 2.15-** PDFGetX S(q) Corrections tab.

a.) *Multiple Scattering Correction*

The Multiple Scattering correction is complicated, but PDFGetX follows the treatment by Warren [6]. Contributions to the total scattering signal from multiple scattering become increasingly less important with each scattering event. (A comprehensive treatment of the multiple scattering correction is provided elsewhere [32-34].) Warren only considers second-order corrections; PDFGetX follows suit.

The multiple scattering correction tab should be turned on; the amount of the correction depends on the absorption coefficient and thus the particular geometry. Since each term in the multiple scattering correction depends, to some extent, on the scattering cross-sections of the constituents, the larger the absorption coefficient the larger will be the correction. In all transmission geometries, the correction is *q*-dependent, increasing with increasing *q* [27].

b.) *Polarization*

The polarization should be turned off in PDFGetX to avoid double correction.

c.) *Self Absorption*

The Self Absorption (or just "Absorption") is discussed above in the Sample Information tab and should be turned on.

d.) *Oblique Incidence*

The oblique incidence is a different correction than the geometry correction applied in Fit2D. Historically, it was believed that these two corrections were redundant [5], however, careful analysis found that the two corrections have a different functional form. It is now understood that this correction is used to account for the fact that the detector plate is flat, with near uniform thickness pixels, and as the incidence angle to the detector increases, a given photon sees a greater pixel thickness. Since the active element in the detector is amorphous Si, each pixel is highly X-ray transparent. X-ray detection is statistical in nature, and depends on the

amount of material the X-ray travels through. As 2θ increases, any given part of the X-ray beam sees more material. Simple geometric arguments suggest that the correction should be proportional to $\cos(2\theta)$, and thus is in opposite direction to the geometry correction made in Fit2D. This correction should be turned on.

e.) *Fluorescence*

The fluorescence correction is necessary because elements have energy resonances that can be activated by high-energy X-rays. In fluorescence, if the energy of the X-ray is sufficiently high, it causes the ejection of an electron from its orbital from atoms in the sample, creating a lower energy vacancy that is subsequently filled by an electron in a higher energy orbital. The difference in the two energy levels is the energy of the photon emitted. The energy of this fluorescence photon is always less than or equal to that of the incident photon. The emission is highly isotropic and to a good approximation *q*-independent, however, the detection of the fluorescence depends on the details of the detector. If the detector is sensitive to a wide energy range, then fluorescence may be an important correction. On the other hand, since fluorescence is related to the attenuation coefficient, it seems likely that only elements or alloys with a large attenuation coefficient need a fluorescence correction. At this point, little is known about the appropriate size of the correction and it has been used as an adjustable parameter. Fluorescence should play a more prominent role in future BESL experiments on high-z elements, since it has been shown that in some alloys (Zr-Ir, Zr-Pt, Zr-Au, Hf-Pt, Cu-Hf, Au-Si, etc.) with

large attenuation coefficients, fluorescence can affect the heights of the first and second peaks in $S(q)$ in a non-trivial way.

f.) *Compton Scattering*

Compton, or incoherent, scattering is due to momentum transfer from the X-ray photon to the electrons of the scattering atom, and the subsequent wavelength shift in the scattered X-ray as a function of scattering angle. In high-energy X-ray diffraction experiments, Compton scattering is an important effect, particularly at high $q$ where it dominates. The PDFGetX manual [27] presents the coherent and incoherent contributions to a diffraction experiment and shows that even as high as 10 $Å^{-1}$ the Compton contribution is substantial. The manual also notes that due to the difficulty in analysis, whenever possible a discriminating analyzer crystal should be placed in the diffracted beam or a solid state detector with a very narrow energy range should be used.

PDFGetX allows three Compton scattering profiles to be used: Empirical Form, Tabulated, and $Z$-asf$^2$. The details of the Z-asf$^2$ profile are still unclear, but the first two profiles use a semi-empirical Compton scattering formula [35] based on experimental data obtained by Cromer and Mann [36]. In the tabulated profile, experimentally tabulated data are used to determine the atomic form factors, while in the empirical form, multiple term Gaussian fits are made to the tabulated data and that empirical form is used to generate the atomic form factors.

$$I^{incoh}(q) = R^3 \sum_{i=1}^{n} c_i Z_i \frac{(b_i q)^{a_i}}{1+(b_i q)^{a_i}} \tag{57}$$

$$a_i = 2.6917\frac{1}{Z_i} + 1.2450$$
$$b_i = 1.1870\frac{1}{Z_i} + 1.075\cdot 10^{-1} + 4.36\cdot 10^{-3} Z_i - 2.381\cdot 10^{-4} Z_i^2 + 2.875\cdot 10^{-6} Z_i^3 \quad (58)$$

$$R = \left(\frac{\lambda}{\lambda'}\right) = \frac{1}{1 + \frac{2h}{mc}\frac{\sin^2(2\theta/2)}{\lambda}} \quad , \quad (59)$$

Where R is the *Breit-Dirac* recoil factor [37]. In order to remove the Compton scattering in the mid *q* region, PDFGetX uses the method suggested by Ruland [38] in which Compton profile can be approximated by a Cauchy distribution convoluted with a band-pass function (the width of which is the "Rulandwin Func. Width" in the S(q) corrections tab). The width is presumably the wavelength band around the incident X-ray wavelength. Empirically, we find that values of the width larger than .006 don't seem to affect the calculation of $S(q)$, but narrowing the window causes the Ruland Window Function (visualizable in the program) to fall off more drastically with increasing *q*. It isn't clear what the correct value is.

The Breit-Dirac recoil factor should be exponentiated by 2 for detectors that measure *photon counts* [37], while exponentiated by 3 when the detector measures intensity, as is the case with the Ge detector.

g.) *Normalization*

The diffracted intensities in the liquid file are in arbitrary units and must be normalized by the average atomic scattering power. The general form for the measured intensity, $I_{meas}$, including the polarization, $P$, attenuation coefficient, $A$, multiple scattering, $I^{multiple}$, and fluorescence, $I^{Fluor}$, is

$$I_{meas} = PAN\left( I^{coh} + I^{incoh} + I^{multiple} + \frac{I^{Fluor}}{P} \right). \quad (60)$$

We now consider the normalization. After applying the corrections discussed, the measured *corrected* intensity is of the form

$$I_{cor} = N\left(I^{coh} + I^{incoh}\right). \quad (61)$$

The incoherent scattering is of the form described previously at all $q$, but at high $q$ the coherent scattering is dominated by the atomic form factors of the elements. More specifically, at high $q$ the atomic structural contribution is small compared with the average atomic form factor (squared). Thus, for sufficiently high $q$, the coherent scattering in Equation 61 is replaced with $\left\langle f^2 \right\rangle$. By integrating over some range of the high-$q$ data, we can calculate N:

$$\int_{q\max(1-a/100)}^{q\max} I^{cor}\, dq = N \int_{q\max(1-a/100)}^{q\max} \left( \left\langle f^2 \right\rangle + I^{incoh} \right) dq\,. \quad (62)$$

The odd notation on the bottom limit was used to emphasize how the program calculates the lower limit in the integral. The value $a$ is the number on the slider bar shown in Figure 2.15. The lower the number, the larger the $q$-value is for the lower limit. The decimal on the right side of the slider indicates the scaling factor, $N$. Auto scaling should be turned on. In the program, the atomic scattering factors are calculated using an analytical form from D. Waasmaier and A. Kirfel [39].

h.) *Laue Diffuse Scattering and Weighting Factor*

The Laue Diffuse Scattering correction should always be turned on. It accounts for scattering when there is no short range order and the atoms are distributed

randomly; it decreases monotonically with increasing scattering angle [6]. For random binary alloys the contribution is $c_a c_b (f_a(q) - f_b(q))^2$ but is generally $\langle f^2 \rangle - \langle f \rangle^2$. The weighting factor should be turned on and set to $\langle f \rangle^2$ which specifies the denominator in the conversion to *S(q)*:

$$S(q) = \frac{I_{eu}^{coh} - \left( \langle f^2 \rangle - \langle f \rangle^2 \right)}{\langle f \rangle^2}. \tag{63}$$

Other normalization are sometimes used, but for this work, we restrict ourselves to the Faber-Ziman [40] formalism.

i.) *Smoothing*

Smoothing should not be used, since it can have a dramatic effect on the height of the first peak.

### *2.5.5.7. G(r) Optimization*

The *G*(*r*) optimization tab, shown in Figure 2.16, allows the Fourier transformation (FT) to be adjusted. Generally speaking, the most influential parameter is the Qmin and Qmax for *S*(*q*), which allows the termination of *S*(*q*) at a crossing point between the peaks at unity, reducing truncation ripples. However, the values of the various parameters available are very poorly explained in the manual; the author therefore prefers to use a program written in Fortran and given in Appendix II.7 to make the FT. In this program, a decaying exponential is used to damp the very high-*q* data to zero, reducing the

truncation error. However, if it is desired to use PDFGetX for this process, the default values for the parameters used are shown in Figure 2.16.

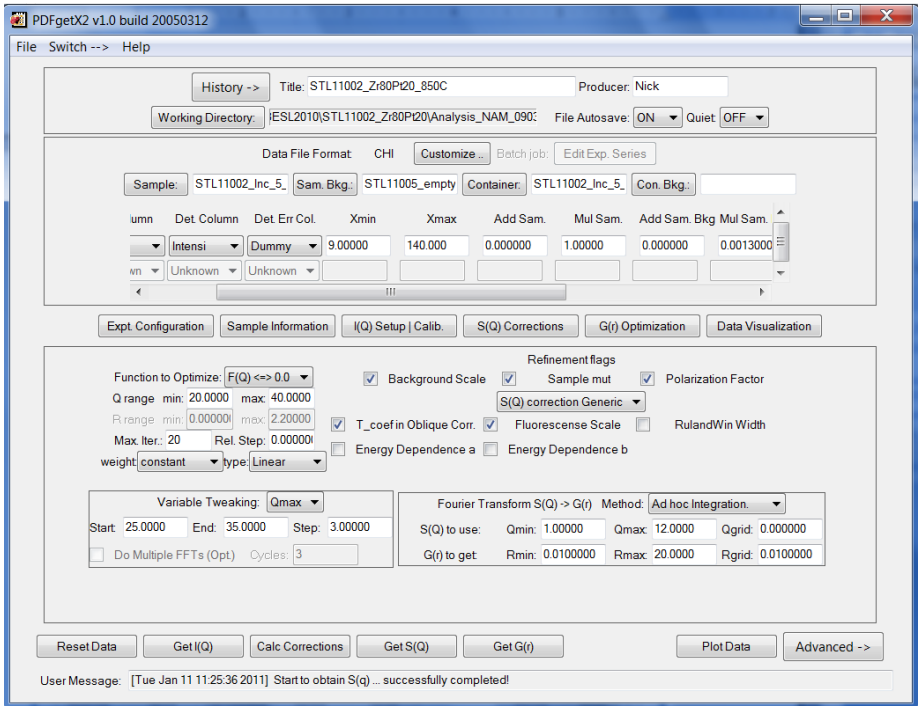


**Figure 2.16-** PDFGetX G(r) Optimization Tab.

### *2.5.5.8. Data Visualization*

The data visualization tab, shown in Figure 2.17, allows the user to view nearly all of the input data, the corrections applied, and the output *S(q)* and *G(r)*. Typically, the background is multiplied by a constant that can differ slightly from unity before it is subtracted from the data. When deciding on the correct constant it is useful to visualize *F(q)* since it is more sensitive to deviation from zero at high *q*.

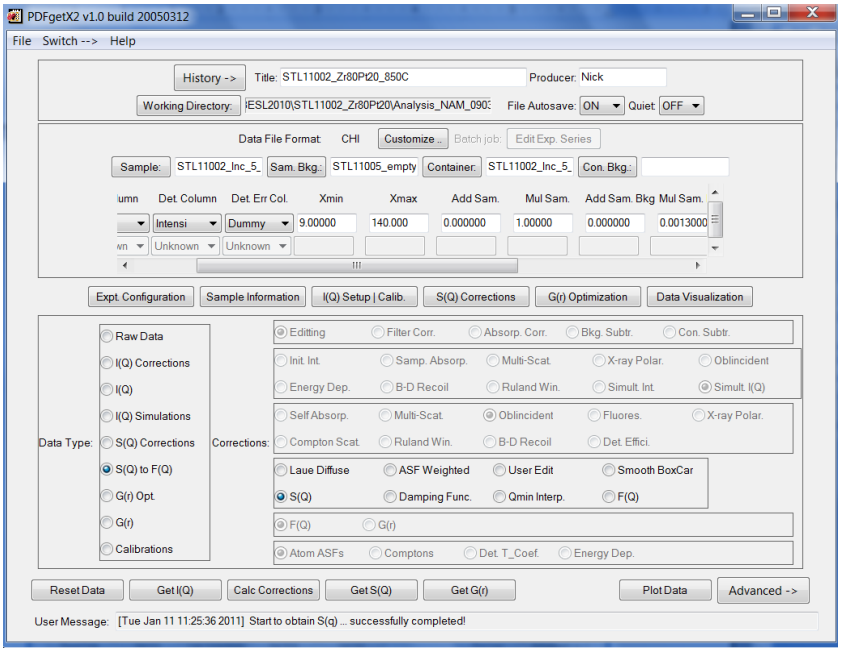


**Figure 2.17-** PDFGetX Data Visualization Tab.

## 2.6. Reverse Monte Carlo (RMC)

### *2.6.1. Introduction*

After analysis, the BESL scattering data is represented as one-dimensional *S(q)* and *g(r)* functions, which contain information about the distribution of short range order (SRO) and medium range order (MRO) in the liquid. However, since all phase information is lost in a diffraction experiment, this data cannot be used to directly reconstruct the atomic positions. Further, a time-averaged structure is obtained. Even the fastest Ge detector frame rates available (~30 fps) are many orders of magnitude slower than the atomic motion time scales [41]. Aside from molecular dynamics simulations, which will be discussed in some detail later, the only other technique that can be used to construct a

large ensemble of atoms and simulate the diffraction experiment is Reverse Monte Carlo (RMC).

RMC is a technique used to obtain structural information by fitting experimental data [42]. It was originally developed for analysis of liquid and amorphous data so it is well suited to these experiments. RMC can fit to multiple data sets allowing the inclusion of neutron diffraction data, other simulation data, and also Extended X-ray Absorption Fine-Structure (EXAFS) data. The details of the technique are discussed in this section.

The RMC technique uses a variation of the Metropolis Monte Carlo Method [43]. An initial configuration of $N$ atoms of a particular average stoichiometry is generated in a box of size consistent with the experimental density. The total structure factor, partial structure factors (PSFs) and partial pair-correlation functions (PPCFs) are calculated and compared with experimental data. Atoms in the configuration are then randomly moved to make the simulation more consistent with the experimental data. Certain constraints are employed, discussed below, to attempt to keep the simulation and any moves physically realistic. Once the configuration converges, the atomic structures can be decomposed and quantitatively analyzed.

We first discuss the procedure for obtaining the output from PDFGetX2 and using this to conduct RMC fits. A more comprehensive discussion will follow focusing on the benefits and limitations of the technique. Next, incorporation of multiple data sets will be discussed in Constrained RMC (CRMC), as will be employed in the study of local structures in Zr-Pt (Chapter 5) and Ni-Nb (Chapter 6). Finally, the techniques for quantitatively analyzing the local structures obtained are presented and discussed.

### *2.6.2. Reverse Monte Carlo Fits-RMCA v3.14*

Most fits were conducted using an executable program that is consistent with RMCA version 3.14. This is compatible with windows XP, Vista and 7, and can be run in Linux using the Wine Windows environment. The following files must be created:

1.) *S(q) input file*

The PDFGetX2 output file must be slightly modified to use it as input for RMC. First, the PDFGetX2 *S(q)* file contains a 136 line header that must be removed. The 3rd and 4th columns, *dQ* and *dS(Q)*, respectively, also need to be removed. In the RMC output files, the columns in order are:

$$q\ (\text{Å}^{-1})\ S(q)\ \gamma_{1\text{-}1}\ \gamma_{1\text{-}2}\ \gamma_{1\text{-}3}\ldots\gamma_{2\text{-}2}\ \gamma_{2\text{-}3}\ldots\gamma_{N\text{-}N}.$$

The Faber-Ziman Gamma functions, $\gamma$, are arranged in the order of the composition, so, for instance, the columns in $Ni_{60}Nb_{30}Ta_{10}$ are:

$$q\ (\text{Å}^{-1})\ S(q)\ \gamma_{Ni\text{-}Ni}\ \ \gamma_{Ni\text{-}Nb}\ \ \gamma_{Ni\text{-}Ta}\ \ \gamma_{Nb\text{-}Nb}\ \ \gamma_{Nb\text{-}Ta}\ \ \gamma_{Ta\text{-}Ta}.$$

This ordering is maintained throughout the program. The RMC *S(q)* file has a two line header. The first line is the number of data points; the second is not read by the program but allows the user to keep track of the columns. The data follows from line three until the end of the file. An example file is shown on the next page. The columns are tab delimited and the fragment if from *STL11039_53_12172010_fq_RMC.dat*:

424

| Q(/A) | S(Q) | Ni-Ni | Ni-Nb | Ni-Ta | Nb-Nb | Nb-Ta | Ta-Ta |
|---|---|---|---|---|---|---|---|
| 0.9127 | -0.0196 | 0.2128 | 0.3105 | 0.1864 | 0.1133 | 0.1361 | 0.0409 |
| 0.936 | -0.0172 | 0.2127 | 0.3104 | 0.1866 | 0.1133 | 0.1361 | 0.0409 |
| . | . | . | | | | | |
| . | . | . | | | | | |
| . | . | . | | | | | |
| 13.9999 | 1.0001 | 0.1707 | 0.2886 | 0.1962 | 0.1220 | 0.1659 | 0.0565 |

The Faber-Ziman functions are the PSF weighting factors used to reconstruct the total *S(q)*. They are defined [40] as

$$\gamma_{i-j} = \frac{c_i c_j f_i(q) f_j(q)}{\left(\sum_i c_i f_i(q)\right)^2} \tag{64}$$

where the $c_i$ are the atomic concentrations in the alloy and the $f_i(q)$ are the q dependent atomic form factors.

The RMCA manual is somewhat ambiguous about the details of the calculation of the weighting factors. While there are only 6 independent partials for a 3 component alloy, there are actually 9 partials:

Ni-Ni Ni-Nb Ni-Ta <u>Nb-Ni</u> Nb-Nb Nb-Ta <u>Ta-Ni</u> <u>Ta-Nb</u> Ta-Ta

The redundant partials are underlined. When RMC specified a weighting function input for one of the redundant partials, $\gamma_{i-j}$, it actually requires $\gamma_{i-j} + \gamma_{j-i} = 2 \cdot \gamma_{i-j}$. Thus, a close inspection of the example file shown above will reveal this factor of 2 is used in the Ni-Nb, Ni-Ta, and Nb-Ta weighting factors.

2.) *g(r) input file*

The program can also use the total pair-correlation function as input. In this case, no weighting factors are included in the file. Also, note that the PDFGetX output is not *g(r)* but is rather *G(r)*, usually, but not always, called the Radial Distribution Function (RDF),

$$g(r) = 1 + \frac{G(r)}{4\pi\rho_0 r} \quad , \tag{65}$$

where $\rho_0$ is the average density, determined experimentally. As previously mentioned we usually generates *g(r)* manually rather than using the PDFGetX output. The format is two column, two line header, tab delimited, as shown below:

1000

r g(r)

0.00 0.2741

0.1 0.2741

0.2 0.2741

. .

. .

. .

19.8 0.99898

19.9 0.99896

3.) *Initialization file*

The initialization file has the following information (for more detailed information about the parameters, refer to the RMCA 3.14 manual):

Line 1: Header, with information for the user only, and not read by RMC

Line 2: Number density in $Å^{-3}$

Line 3: The nearest approaches for each pair of atoms. This is a constraint to ensure that the fit is physical. Ideally, another experiment or fit will provide information about the cutoff distance. Otherwise, calculating it from the atomic radii is often a good first step. Generally, the fit improves as the cutoff distances become unreasonably small. However, this is one of the adjustable parameters for which we often don't have sufficient information to specify. Atomic size is not the only thing that contributes to the cutoff distance, as we will see in the study of Zr-Pt. In this alloy, the large negative heat of mixing alters the Zr-Pt partial. V. Wessels [5] and T. H. Kim [44] describe a cutoff distance refining technique that is used to "optimize" the distances. The author is skeptical of this procedure, and prefers independent data for the cutoff distances. Note, the order of the cutoff distances follows the naming convention described (Ni-Ni, Ni-Nb, Ni-Ta, Nb-Nb. . . ).

Line 4: Maximum jumps in atomic distance for each species in the metropolis algorithm.

Line 5: The *r* spacing. Choosing a spacing that is too small can overload the active memory, which will trigger an error. Optimally, the spacing should be $\frac{2\pi}{q_{\max}}$, the maximum resolution.

Line 6: Move-out option. The move-out option is an option that should be set to .true. only if there are some particles that don't satisfy the cut-off restrictions. This option is somewhat ambiguous. The manual indicates that turning this option on (.true.) will preferentially choose these species that don't satisfy the cutoff distance to be moved. It isn't clear if this is done at each iteration or it is only done at the beginning of the calculation. Empirically, the final PPCFs obtained with the option on or off show no significant differences. Finally, there are frequently spurious spikes in the PPCFs at lower *r* than the cutoff distances should allow, even with the move-out option turned on.

Line 7: Number of configurations to collect after convergence is reached. Setting this to zero is the default, causing configurations to be collected at each printing.

Line 8: How often, in accepted moves, the output is written.

Line 9: The total time of the calculation and the time when configurations should be saved (both expressed in minutes). The configurations are saved at the conclusion of the time limit.

Line 10: The number and type of experimental data entered. 0 0 1 0 refers to an X-ray *S(q)* file assuming that the weighting factors are in the file. See V. Wessel's Thesis for an example of an initialization file with constant weighting factors.

Line 11: File containing the experimental data.

Line 12: Line numbers that contain the experimental data.

Line 13: Constant to subtract, set to 1.0 if the experimental data oscillates around 1, which is the case for the *S(q)* output from PDFGetX.

Line 14: Standard deviation for the data, which is determined by the user, and defined in Equation 66.

Line 15: The renormalization option is used when there are multiple data sets to account for small errors that appear during the FFT, but is set to .false. for a single data set.

Line 16: The offset is used if refining the polynomial background. It isn't clear from the manual what this actually means. Historically, this is set to true, but, empirically, this option doesn't have much effect.

Line 17: Coordinate Constraints.

Line 18: Average Coordinate Constraints.

Line 19: External potential, if one exists. This is typically left .false.

An example initialization file is shown below, with the "default" settings described previously. (STL11039 is $Ni_{60}Nb_{30}Ta_{10}$).

```
STL11039_1350_09132010
0.0696                              ! number density
1.750 1.908 1.908 2.050 2.050 2.050 ! cut offs
0.3 0.3 0.3                         ! maximum moves
0.1                                 ! r spacing
.true.                              ! moveout option
0                                   ! number of configurations to collect
1000                                ! step for printing
600 20                              ! time limit (total time), time for saving
0 0 1 0                             ! sets of experiments, 0 1 0 0 for s(q), 1 0 0 0 for g(r)
STL11039_53_12172010_fq_RMC.dat
3 426                               ! points to use, start and end lines in the input file
1.0                                 ! const. to subtract
0.005                               ! sigma
```

| | |
|---|---|
| .false. | ! renormalize |
| .true. | ! offset |
| 0 | ! no of coord. constr. |
| 0 | ! no of av. coord. contsr. |
| .false. | ! potential |

4.) *Initial Atomic Configuration file*

The initial atomic configuration file contains the (*x, y, z*) coordinates of all of the atoms, with the atoms listed according to the naming scheme outlined. For instance, in $Ni_{60}Nb_{30}Ta_{10}$, if there are 10,000 atoms in the fit, the first 6000 are Ni, the next 3000 are Nb and the final 1000 are Ta. The program *Random*, written by T. H. Kim, constructs a file of the correct format, with atoms randomly distributed in a box with dimensions consistent with the experimental density. All of the parameters are shown in Figure 2.18 and the header is given in Appendix II.8. For several of the studies presented in this work, non-random initial configurations were generated to check convergence in configuration space. Additionally, the configuration file must have the extension *.cfg* and must have the same name as the initialization file.

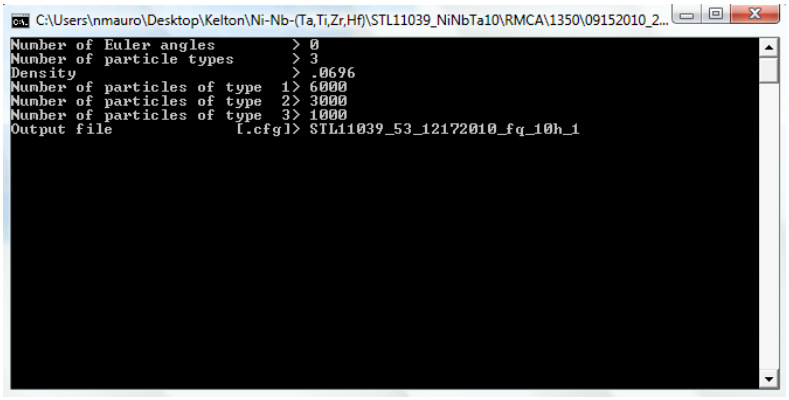


**Figure 2.18-** Input for the program *Random.exe* for $Ni_{60}Nb_{30}Ta_{10}$.

5.) *Output Files*

Depending on the input data the output file contains a combination of PPCFs, PSFs, total *g(r)*s and total *S(q)*s in a *.out* file with the same prefix as the initialization file. For X-ray experiments where *S(q)* and the weighting factors are entered, the PPCFs, PSFs, and total *S(q)* are output. To reconstruct the total *S(q)* sum all the PSFs appropriately weighted with the γ factors.

### *2.6.3. Reverse Monte Carlo Fits-RMC++*

In the course of this work, the author began exploring another implementation of the RMC program: RMC++ [45]; collaborators at Iowa State University have been transitioning to this program. Constrained RMC (CRMC) fits of Zr-Pt and Ni-Nb with MD PPCFs were made using this program; the results are discussed in Chapter 5 and

Chapter 6. Since the procedure of implementation is a little different than RMCA some of the relevant features are described here. The program can be used for unconstrained RMC as well, but for clarity we'll describe the use of RMC++ for a constrained RMC.

1.) *Input Files*

The *S(q)* input files are exactly the same as RMCA. However, note that when specifying the lines of data in the initialization file the program assumes a 2 line header. Therefore, although the data starts on line 3 in the actual file, we specify that it begins at line 1 in the initialization file. The PPCFs are of the same format, but the r spacing in the files has to match that indicated in the Initialization File.

2.) *Initialization File*

The Initialization File is reproduced below. A few things should be noted. For each PPCF included, the Faber-Ziman coefficients are specified for the partial in the file and 0.0000 for the others. The order of the coefficients follows the ordering convention laid out earlier. Also note that there the types of experiments are indicated (3 0 1 0), the data must be entered in this order-the first three partials first, followed by the experimental data. Also note, for the *S(q)* input data, the constant to subtract is set to 0.0000, although the input data oscillates around 1. The constant can be set to 1.000 or 0.000 and the program seems to subtract the correct constant.

```
BESL 2009 STL1015 Pt20Zr80 1588 K
0.0445                          ! number density
2.0 2.0 2.0                     ! cut offs
```

0.3 0.3 ! max moves

0.06 ! r spacing

.true. ! whether to use moveout option

0 ! no of configurations to collect, frequency for collecting

4000 ! step for printing

600 5 ! time limit, step for saving

3 0 1 0 ! no. of g(r), neutron, xray and exafs expts

ab_initio_1600K_Zr-Zr.gr

1 150 ! range of points

0.000 ! constant to subtract

0.4519 0.0000 0.00000 ! partial coefs

0.005 ! standard deviation

.true. ! whether to vary amplitudes

ab_initio_1600K_Zr-Pt.gr

1 150 ! range of points

0.000 ! constant to subtract

0.00000 0.44067 0.00000 ! partial coefs

0.005 ! standard deviation

.true. ! whether to vary amplitudes

ab_initio_1600K_Pt-Pt.gr

1 150 ! range of points

0.000 ! constant to subtract

0.00000 0.0000 0.10743 ! partial coefs

0.005 ! standard deviation

.true. ! whether to vary amplitudes

STL11002_Inc_5_33_49_1345C.sq

1 424 ! range of points

0.000 ! constant to subtract

| | |
|---|---|
| 0.002 | ! standard deviation |
| .true. | !multiplicative renorm switch |
| .true. | !additive renorm switch |
| 0 | ! no of coordination constraints |
| 0 | ! no of average coordination constraints |
| .false. | ! whether to use a potential |

3.) *Initial Atomic Configuration File*

The details of the initial configuration file are the same as for RMCA *except* there is an additional line in the header. As with RMCA, the initialization file and configuration file must have the same name.

### *2.6.4. Discussion of RMC Technique*

RMC fits shouldn't be conducted without an understanding of the details and limitations of the procedure. While it is relatively easy to setup the fits, it is also easy to conclude more than is justified by the technique. A tremendous amount of literature exists critical of the technique, in part, because it is misused. Nearly as much literature exists in which claims of "uniqueness" or "correctness" of configurations, which isn't a feature of this technique, leading to understandable criticism and skepticism about RMC. A discussion of the technique and lessons learned is useful at this point.

The basic procedure is a variation on the Monte Carlo [43] method in which the metropolis algorithm dictates the migration from one configuration to another based on the statistical fit to experimental data. The process begins by placing *N* atoms in a volume with periodic boundary conditions. The volume is dictated by experimentally

determined density and the configuration can be random or ordered or can be the result from a previous fit. The PPCFs are calculated, Fourier Transformed to PSFs, summed together weighted appropriately to produce *S(q)*, and then compared to the experimental *S(q)* according to

$$\chi_O^2 = \sum_i \frac{(S_O(q_i) - S_E(q_i))^2}{\sigma^2(q_i)} \tag{66}$$

where $\chi_O^2$ is the statistical measure of goodness of fit between the "old" static structure factor, $S_O(q)$, from the configuration and the experimental static structure factor, $S_E(q)$. Sigma, $\sigma$, appearing in the denominator, is the statistical uncertainty specified in the RMC initialization file.

Atoms, chosen at random, are moved randomly in space, up to the maximum move specified. If the atoms moves too close to another atom, specified by the maximum approaches, the move is rejected and another atom is randomly selected and moved. A new statistical fit is calculated:

$$\chi_N^2 = \sum_i \frac{(S_N(q_i) - S_E(q_i))^2}{\sigma^2(q_i)}. \tag{67}$$

If $\chi_N^2 < \chi_O^2$, the move is accepted and the new configuration becomes the old, and the process is repeated. If $\chi_N^2 > \chi_O^2$ then the move is accepted only with a Boltzmann weighted probability. This tends to keep the configuration from getting locked into a local energy minimum, and explores the entire configurational landscape for the global minimum.

This process produces a Markov chain of configurations where the structure factor plays the role of the energy, driving the model. The result is a converged

configuration that is consistent with experimental data. For X-ray data, in particular, it is desirable to fit the structure factor itself, rather than the pair distribution function which can hide systematic errors in the data. For instance, poorly background corrected $S(q)$ generally show a tail at high-$q$. This often manifests as rippling on top of the $g(r)$ but may not. McGreevy [42] agrees with this perspective. Additionally, the $q$-dependent weighting factors can only be input with $S(q)$ not $g(r)$.

In this work, no interaction potential is used. This has many advantages: MD fits, which do employ an interaction potential, are notoriously computation intensive and only allow hundreds or a few thousand atoms. Even the embedded atom method which allows more atoms in a fit, rely on assumptions about the interactions which themselves raise questions about the structure of the result and how that structure is affected by those assumptions in the interaction. RMC allows a much larger sampling size and uses constraints, particularly the closest-approach distance and density, as the "interaction potential." Information about the cutoff distances can be taken from the experimental $g(r)$, but care must be taken: the Fourier Transform of the X-ray structure factor often doesn't fall to zero at the low-r side of the $g(r)$ main peak, as it theoretically should indicating a hard-sphere-like cutoff distance, because of the finite experimental data range and other significant systematic errors. The effects of other constraints, such as coordination number constraints have not been explored in metallic liquids in this group.

One of the main misconceptions about RMC modeling is that the configurations produced are not unique and therefore not "correct." Firstly, the configurations are, of course, not unique. Many configurations produce indistinguishable structure factors. However, we would never know whether or not a structure is "true" or "correct;" that is

we would never be able to determine if one configuration produced atomic positions that were the same as the experimentally sampled volume.

Liquid samples are not static on the time scales sampled, and even static alloys have thermal vibrations and diffusion. Ignoring this point about thermal motions, diffraction information is never completely error free. McGreevy also points out that RMC models are never unique and there are an infinite number of configurations that are consistent with each and the experimental data [42, 46]. Additionally, if a method can only produce one configuration, then the configuration is, indeed, unique to that method. But that still doesn't guarantee correctness or that no other configuration is consistent with the experimental data. For a critic, it is nice to think that a unique structure exists, and that a method of modeling is only valid if it produces that unique structure, and thus RMC is invalid. This is simply not realistic.

RMC is a way of exploring configurations that are consistent with experimental data. We know that experimental data always have errors, and these errors are difficult to quantify and even to recognize. One of the very interesting aspects of RMC modeling is the appearance of certain features in *S(q)*. Take, for instance, a feature that doesn't appear in the configuration which is known to manifest in other experiments. There are two reasons why the feature doesn't exist-McGreevy says there is only one. The first (also pointed out by McGreevy) is that RMC models are based on the data and the constraints. If the missing features don't follow from the input information this tells us something about the nature of the feature itself. The other reason involves exploration of configuration space by the Markov process. If the energy landscape contains deep local minima, the algorithm can be locked into a particular configuration or set of consistent

configurations themselves *inconsistent* with other configurations of lower energy. There is evidence that certain initial configurations in the relatively simple Al liquid (Chapter 7) don't converge to the same area of phase space; thus multiple paths in phase space should be explored.

## 2.7. Quantization of local structures

Atomic structural models produced using the RMC method must be quantitatively analyzed. In this section, we present four methods that are used for that analysis.

### *2.7.1. Honeycutt and Andersen (HA) Indices*

In the HA analysis [47], the local atomic configurations are deconstructed into root pairs and local atoms. The order is categorized in a 4-digit indexing scheme. The first digit indicates the order of nearest neighbor, i.e. nearest, next-nearest, etc. Nearest neighbors appear in the first coordination shell, next-nearest neighbors in the second, and so on. The second index counts the number of atoms close enough to the root pair to be considered nearest neighbors. The third index counts the number of those neighbors close enough to be nearest neighbors to each other. The fourth index distinguishes structural tropes with the same first three indices. This technique doesn't give complete topological information about the neighborhood around any one atom, but certain indices are present in common clusters. Measuring the occurrence of various indices can determine what kind of order is common and the trends with temperature and

composition. By deconstructing icosahedral, rhombohedral, FCC, HCP, and BCC order, the following indices appear:

1551: Perfect Icosahedral

1541, 1431, 1311, 1321: Distorted Icosahedral

1441, 1661: BCC

1421, 1422: FCC, HCP

1331, 1321, 1311: Rhomohedral

(See the theses of V. Wessels [5] and T. H. Kim [44] for graphical representations of some of these structures). The cutoff distance for the nearest neighbor distance is taken from the experimental $g(r)$.

### *2.7.2. Bond Orientational Order (BOO)*

In the Bond Orientational Order (BOO) parameter analysis [48], the complete topological order around a central atom is analyzed in terms of rotational invariants. For each atom in the configuration, the nearest neighbor bond distribution is expressed in terms of spherical harmonics, $Y_{lm}(\theta,\phi)$, and the rotational invariant (following the common convention [5, 44, 48]), is defined as:

$$Q_l = \left[ \frac{4\pi}{2l+1} \sum_{m=-l}^{l} \left| \langle Q_{lm} \rangle \right|^2 \right]^{1/2} \tag{68}$$

where

$$Q_{lm} = Y_{lm}\left(\theta(\mathbf{r}), \phi(\mathbf{r})\right) \tag{69}$$

and

$$\langle Q_{lm} \rangle = \frac{1}{N_{Bonds}} \sum_{Bonds} Q_{lm} \ . \tag{70}$$

The information about the local topology is then compressed into distribution of scalar $Q_l$. If we begin with a series of common topological basis units, (FCC, HCP, BCC and Icosahedron), we see that (Figure 2.19) the bases have characteristic distributions of parameters. While this can be a useful tool in some cases, most simulations show a distribution of parameters that is different from any one basis. It should also be noted that the distributions in Figure 2.19 don't have any odd indices. This is due to the spatial symmetry of these clusters. The majority of the clusters observed in RMC fits show distortions that lead to odd indices, which can't be readily interpreted with these clusters. T. H. Kim [44] provides an excellent reference of related material as well as a discussion of third order invariants not used in this work.

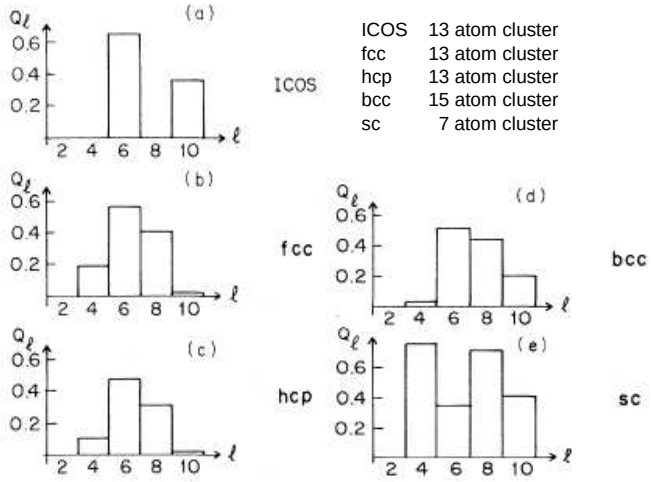


**Figure 2.19-** BOO parameter distributions for common single clusters. (reproduced from V. Wessels [5])

### *2.7.3. Voronoi Polytetrahedral (VI) Analysis*

The Voronoi Polytetrahedral (VI) analysis of local structures [49, 50] attempts to quantify the local topography around an atom in a more complete way than HA indices by using closed three-dimensional polyhedra. The polyhedra are constructed in the same manner as Brillion Zones [20] are constructed for crystalline structures. A central atom is identified and a line segment is extended to all atoms around it within a set bonding distance. The normal bisecting plane to each segment is created and extended in all space. The closed three-dimensional structure produced is the polyhedron that defines the topological environment around the atom. As an example of this procedure, consider the two-dimensional atom distribution shown in Figure 2.20 (left panel), which is easier to visualize than the three-dimensional case, and the Voronoi construction of the structure (right panel).

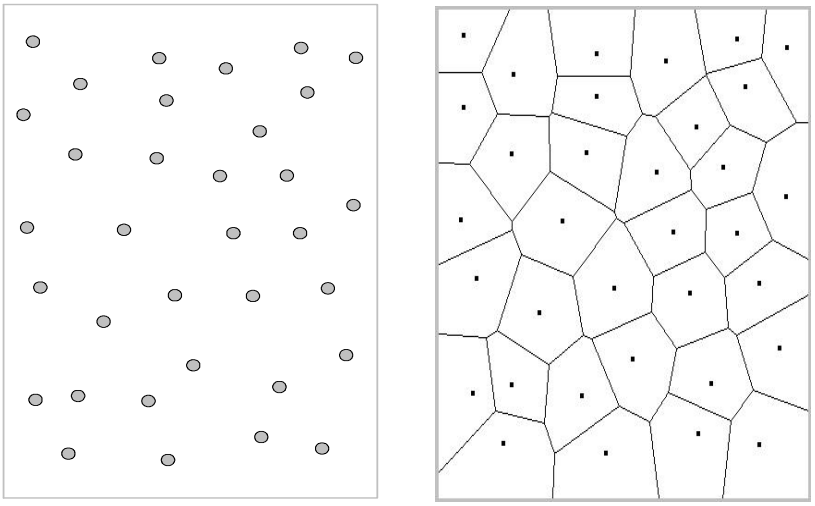

**Figure 2.20-** Voronoi Tessellation for two-dimensional atom distribution.

The Voronoi polyhedra are characterized by the number of faces of a type, $n_i$, where the subscript $i$ corresponds to the number of edges for that face. The number of

faces, then, corresponds to the number of nearest neighbors and the geometry of those faces provides information about the local symmetry around the central atom. Distinct polyhedra correspond to different sets of indices of the form $<n_3,n_4,n_5,n_6,n_7>$.

As with the HA and BOO analysis, intuition can be gained by considering single cluster Icosahedron, FCC (HCP), BCC and SC Voronoi tessellations. By considering the primitive unit cell for each of the bases above, we can see (Figure 2.21) that each has a defined three dimensional shape, but it also has an index that is characteristic of that order. However, as with BOO, there is overlap in the numbers in each index; a real liquid will be composed of distorted structures. For many of these structures, their relationship to the basis set isn't clear so caution must be used when describing any one Voronoi index as "BCC-" or "Icos-" like.

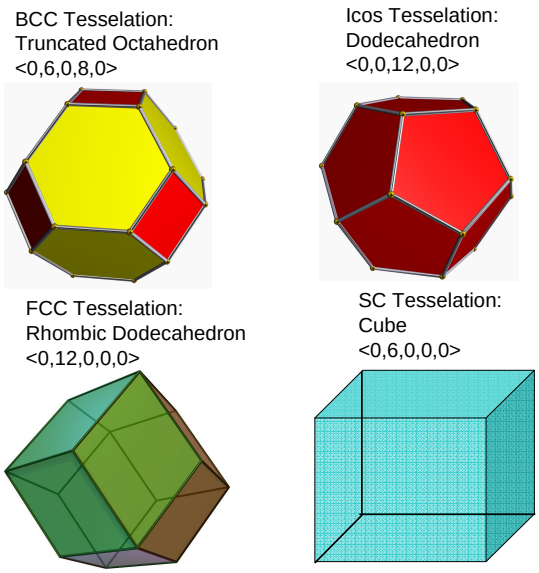


**Figure 2.21-** Voronoi Tessellation for BCC, Icosahedron, FCC and SC primitive cells.

That being said, there are some structures that are *closely* related to the basis set above. It was noted by Hao *et al.* [51] that by a simple distortion of the nearest neighbor structure, adding a neighbor, or subtracting a neighbor, certain indices could be related to each other. Several distortions were developed for the study of dominant atomic structures in Zr-Pt. Figure 2.22 shows the Voronoi construction for a perfect icosahedron. In Figure 2.22a, the Voronoi representation of the complete icosahedron is illustrated: it is a dodecahedron. A five atom sub-cluster is shown in Figure 2.22b to emphasize the procedure for plane construction of the Voronoi tessellation. Each colored plane corresponds to a different numbered atom in the sub-cluster.

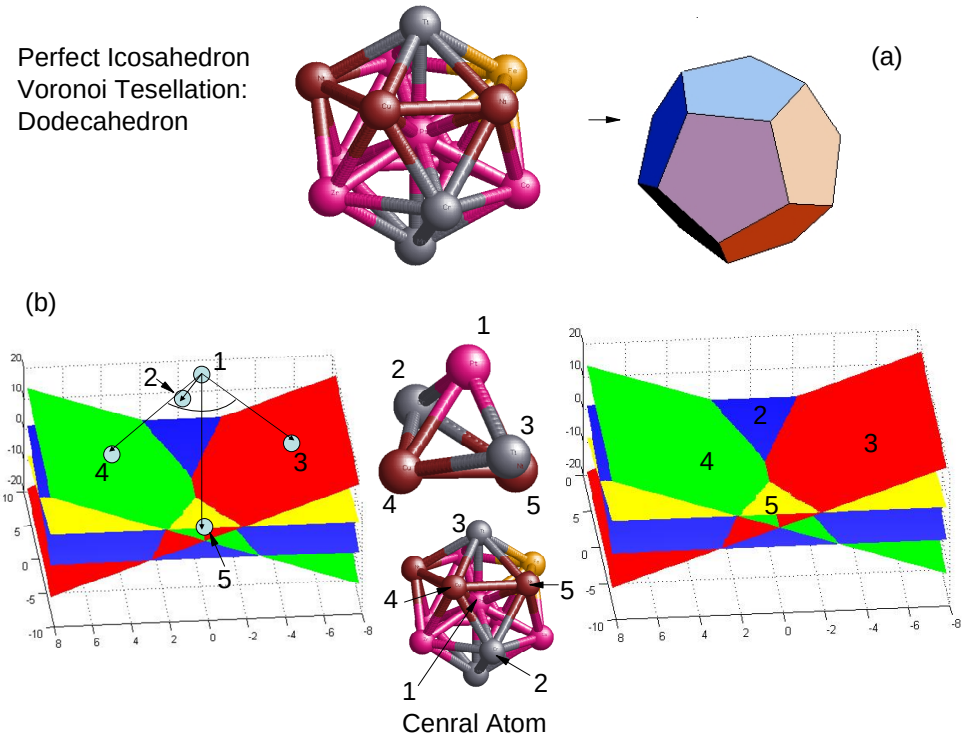


**Figure 2.22-** Voronoi plane construction for a perfect icosahedron. (a) The Voronoi representation of the complete icosahedron is a dodecahedron. (b) A five atom sub-cluster is shown to illustrate the procedure for plane construction of the Voronoi tessellation. Each colored plane corresponds to a different numbered atom in the sub-cluster.

This procedure helps to understand how distortions of three kinds can produce different Voronoi indices. A distortion of the first kind will refer to a changing bond angle, like the angle shown between atoms 3 and 4 in Figure 2.22b. As the angle increases, the edge between planes 2 and 5 becomes smaller. Figure 2.23 shows a schematic demonstration of a Voronoi distortion of the first kind, i.e. bond angle distortion. Figure 2.23a shows the undistorted sub-cluster reproduced from Figure 2.22a. Figure 2.23b shows the same sub-cluster (in a slightly different orientation; use the plane numbers as reference) but with a 35 degree bond distortion between atoms 4 and 3, referenced to the central atom[5]. In Figure 2.23c, the resultant cluster changes from a perfect icosahedron to a distorted icosahedron. In this example, the index changes from <0,0,12,0,0> to <0,2,8,2,0>: Planes 3 and 4 decrease their respective number of edges from 5 to 4, and planes 2 and 5 increase their number of edges from 5 to 6.

[5] Note, that a 35 degree bond distortion isn't necessary for a index shift from <0,0,12,0,0> to a distorted index: A 15 degree distortion will produce the same shift, but a large angle is shown for emphasis.

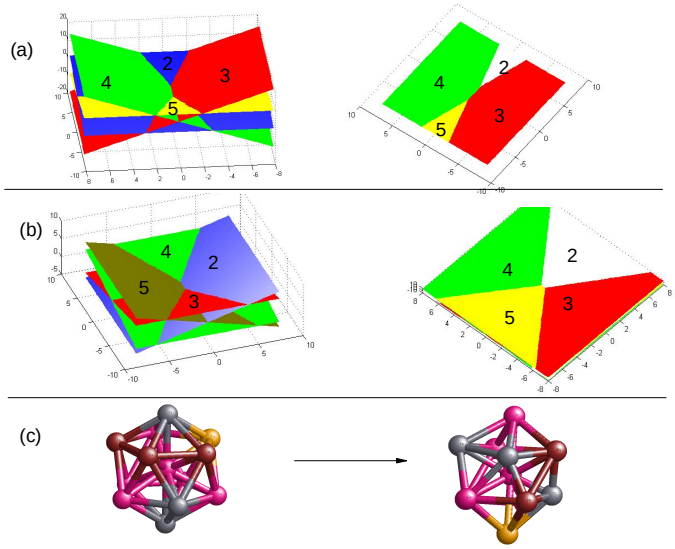


**Figure 2.23-** Demonstration of a Voronoi distortion of the first kind: bond angle distortion. (a) The undistorted sub-cluster from Figure 2.22. (b) The same sub-cluster (in a slightly different orientation (use the plane numbers as a reference) but with a 35 degree bond distortion between atoms 4 and 3, referenced to the central atom. (c) The resultant cluster change from a perfect icosahedron to a distorted icosahedron.

Voronoi distortions of the second and third kind, adding and removing a nearest neighbor, respectively, also change the Voronoi index. Increasing the number of nearest neighbors by one, at the site indicated in Figure 2.24, for example, changes the index from <0,2,8,2> to <0,1,10,2>. Several more distortions are shown in Appendix II.9., but a comprehensive list is difficult to compile, given the many permutations of the distortions and the sites at which they may act.

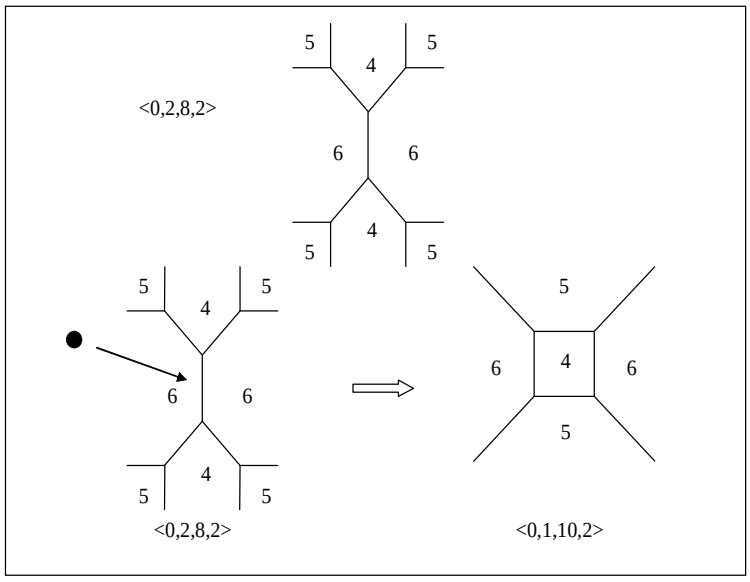


**Figure 2.24-** Voronoi distortion of the second kind. Increasing the number of nearest neighbors by one, at the site indicated, the index changes from <0,2,8,2> to <0,1,10,2>.

### *2.7.4. Mutual information*

All of the schemes presented for a quantitative analysis of atomic structures rely on the definition of a basis set of structures and the expression of the RMC configurations in terms of that set. It would be best if natural structural units could be identified rather than biasing the measured distribution by starting with a basis set. There is, thus, a need for tools that enable the detection of relevant structures on all spatial scales. Work by P. Ronhovde *et al.* [52] suggests a new method by invoking ideas from network analysis and information theory. This method is said to efficiently identify candidate natural structures in amorphous configurations, where a clear definition of order is lacking. The most important and relevant point is that the algorithm does not require a guess as to which of the system properties should be deemed as important. Initial work analyzing the RMC configurations of Liquid $Zr_{80}Pt_{20}$ from BESL2009 data identified large clusters,

which may be consistent with the MRO manifest in the prepeak. Those large clusters were not found using this analysis in amorphous phases that showed no prepeak. It is the author's opinion that this approach to structural analysis of constrained RMC fits is valuable and should play an important role in the research into amorphous structures.

## 2.8. References


[1] A. Aesar, Research Chemicals, Metals and Materials, (2011).

[2] D. B. Williams and C. B. Carter, Transmission electron microscopy: a textbook for materials science, Plenum Press, New York (1996).

[3] Smithells Metals Reference Book, Butterworth Heinemann, Boston (1992).

[4] J. C. Foley and J. H. Perepezko, *Journal of Non-Crystalline Solids* **205-207,** 559(1996).

[5] V. M. Wessels, PHASE FORMATION, LIQUID STRUCTURE, AND PHYSICAL PROPERTIES OF AMORPHOUS AND QUASICRYSTAL-FORMING ALLOYS, *Physics*, Washington University, St. Louis (2009).

[6] B. E. Warren, X-Ray Diffraction, Dover Publications, Inc., New York, NY (1990).

[7] V. Wessels, Discussion of Crystallites in Mg-Based Glasses, In: N. A. Mauro, Editor, St. Louis (2011).

[8] L. Xia, W. H. Li, S. S. Fang, B. C. Wei and Y. D. Dong, *Journal of Applied Physics* **99,** 026103(2006).

[9] Perkin-Elmer, Ther Perkin-Elmer 7 Series Thermal Analysis System. DSC 7 Differential Scanning Calorimetry, Perkin-Elmer (1986).

[10] G. Hohne, W. Hemminger and H.-J. Flammersheim, Differential scanning calorimetry, Springer, New York (2003).

[11] H. E. Kissinger, *Analytical Chemistry* **29,** 1702(1957).

[12] A. K. Gangopadhyay, T. K. Croat and K. F. Kelton, *Acta Materialia* **48,** 4035(2000).

[13] K. F. Kelton and J. C. Holzer, *Review of Scientific Instruments* **59,** 347(1988).

[14] K. F. Kelton, A. I. Goldman, T. Egami and X.-L. Wang, Subsription rates at neutron sources, (2010).

[15] D. Robinson, K. F. Kelton and A. I. Goldman, Discussions of polarization of X-ray beam in sector 6ID-D, In: N. A. Mauro, Editor (2009).

[16] D. M. Mills, Synchrotron Radiation: Properties and Production, *National School for Neutron and X-ray scattering*, Oakridge, TN (2010).

[17] I. Szaloki, *X-ray Spectrometry* **25,** 21, (1996).

[18] D. McMorrow and J. A.-Nielsen, Elements of Modern X-ray Physics, Wiley, London (2011).
[19] J. P. Hansen and I. R. McDonald, Theory of Simple Liquids, Elsevier Academic Press, Burlington (2006).
[20] N. W. Ashcroft and N. D. Mermin, Solid State Physics, Rinehard and Winston, New York (1976).
[21] Y. Waseda, The structure of non-crystalline materials, McGraw-Hill, New York (1980).
[22] J. H. Lee, J. Almer, C. Aydner, J. Bernier, K. Chapman, P. Chupas, D. Haeffner, K. Kump, P. L. Lee, U. Lienert, A. Miceli and G. Vera, *Nuclear Instruments and Methods in Physics Research Section A: Accelerators, Spectrometers, Detectors and Associated Equipment* **582,** 182(2007).
[23] M. Blodgett, Batch Processing Software, BESL2010, (2010).
[24] A. P. Hammersley, FIT2D: An Introduction and Overview, *ESRF Internal Report, ESRF97HA02T* (1997).
[25] N. I. o. S. a. Technology, **SRM 640b** - Silicon X-Ray Diffraction data (2008).
[26] J. D. Jackson, Classical Electrodynamics, John Wiley & Sons Inc., (1999).
[27] I. Jeong, J. Thompson, T. Proffen and S. Billinge, User's Manual PDFgetX, (2003).
[28] X. Qiu and S. Billinge, PDFGetX2 Manual, (2004).
[29] I. K. Jeong, J. Thompson, T. Proffen, A. M. P. Turner and S. J. Billinge, *Journal of Applied Crystallography* **34,** 536, (2001).
[30] W. Pitschke, J. A. Collazo, H. Hermann and V. D. Hildenbrand, *Journal of Applied Crystallography* **29,** 561, (1996).
[31] N. I. f. S. a. Technology, X-Ray Mass Attentuation Coefficients, (2010).
[32] C. W. Dwiggins and D. A. Park, *Acta Crystallography* **A27,** 264, (1971).
[33] C. W. Dwiggins, *Acta Crystallography* **A28,** 155, (1972).
[34] R. Serimaa, T. Pitkanen, S. Vahvaselka and T. Paakkari, *Journal of Applied Crystallography* **23,** 11, (1990).
[35] B. J. Thijse, *Journal of Applied Crystallography* **17,** 61, (1984).
[36] D. T. Cromer and J. B. Mann, *Journal of Chemical Physics* **47,** 1892, (1967).
[37] S. Ergun, Physics and Chemistry of Carbon, Marcel Dekker, New York (1968).
[38] W. Ruland, *Journal of Applied Physics* **15,** 1301, (1964).
[39] D. Waasmaier and A. Kirfel, *Acta Crystallography* **A51,** 413, (1995).
[40] T. E. Faber and J. M. Ziman, *Philosophical Magazine* **11,** 153, (1965).
[41] A. Meyer, R. Busch and H. Schober, *Physical Review Letters* **83,** 5027(1999).
[42] R. L. McGreevy, *Journal of Physics: Condensed Matter* **13,** R877, (2001).
[43] N. Metropolis, A. W. Rosenbluth, M. N. Rosenbluth, A. H. Teller and E. Teller, *Journal of Physical Chemistry* **21,** 1087, (1953).
[44] T. H. Kim, STRUCTURAL STUDY OF SUPERCOOLED LIQUIDS AND METALLIC GLASSES BY HIGHE ENERGY X-RAY DIFFRACTION AND REVERSE MONTE CARLO SIMULATION, *Physics*, Washington University, St. Louis (2007).
[45] G. Evrard and L. Pusztai, *Journal of Physics: Condensed Matter* **17,** S1, (2005).
[46] M. L. McGreevy, *Journal of Physics: Condensed Matter* **3,** F9, (1991).

[47] J. D. Honeycutt and H. C. Andersen, *Journal of Physical Chemistry* **91,** 4950, (1987).
[48] P. J. Steinhardt, D. R. Nelson and M. Ronchetti, *Physical Review B* **28,** 784, (1983).
[49] J. L. Finney, *Proceedings Royal Society London A* **319,** 479, (1970).
[50] J. L. Finney, *Nature (London)* **266,** 309, (1977).
[51] S. G. Hao, C. Z. Wang, M. J. Kramer and K. M. Ho, *Journal of Applied Physics* **107,** 053511(2010).
[52] P. Ronhovde, S. Chakrabarty, M. Sahu, K. F. Kelton, N. A. Mauro, K. K. Sahu and Z. Nussinov.

# Chapter 3

## Phase Separation Mediated Devitrification in $Al_{88}Y_7Fe_5$ Glasses[€, ¥]

[€]Much of this work appears in the manuscript *"Phase Separation Mediated Devitrification of $Al_{88}Y_7Fe_5$ Glasses."* K. K. Sahu, N. A. Mauro, L. Longstreth-Spoor, D. Saha, Z. Nussinov, M. K. Miller and K. F. Kelton. *Acta Materialia*. **58** (2010) 4199.
[¥]The 3-dimensional atom probe experiments were conducted and analyzed by L. Longstretch-Spoor and K. K. Sahu. The TEM images were taken by D. Saha.

## 3.1. Introduction

Light-weight Al-rare-earth-transition metal (Al-RE-TM) metallic glasses typically have good corrosion resistance, high yield strength and other key properties that make them interesting for potential structural applications. However, in contrast with the discovery of bulk metallic glasses in several alloy families [1-3], essentially all of the Al-RE-TM glasses require quenching rates of $10^5$-$10^6$ $^oC/s$ for their formation, limiting their technological usefulness. Further, while appearing to be amorphous from X-ray diffraction and transmission electron microscopy (TEM) studies, many of these glasses show no discernable glass transition. The devitrification pathway is highly varied and extremely sensitive to small changes in composition [4, 5]. Many of these glasses crystallize to nanocomposite materials with an extremely high grain density ($10^{21}$-$10^{23}$ $m^3$). The mechanisms for such a high nucleation rate, presumably the reason for poor bulk glass formability and the lack of a glass transition in the $Al_{88}Y_7Fe_5$ system, are not completely understood. The devitrification of Al-based glasses has been studied extensively [6-11] and several explanations for the high nucleation rates have been presented. The growth of quenched-in nuclei has frequently been proposed [12-16]. However, during a rapid quench, the decrease in kinetics governing the evolution of the cluster distribution with decreasing temperature will cause the cluster population to

deviate from that expected for steady state nucleation [17]. As a result, the nucleation rate during the quench can be orders of magnitude less than the steady state rate [18]. Were the crystal density observed after annealing (of order $10^{21} - 10^{23}/m^3$) to arise from nuclei produced during the quench, then, the steady-state nucleation rates would appear to be unreasonably high.

Recently, three-dimensional atom probe tomography (APT) studies of $Al_{89}Ni_6La_5$ glasses showed chemical phase separation into regions of approximately 95% Al concentration [19]. The similarity between the number density of these regions ($\sim 5x10^{23}$ $m^{-3}$) and the grain density of $\alpha$-Al in the devitrified glass suggests that these regions are favorable sites for nucleation. There have been earlier reports of phase separation in metallic glasses [20-23]. However, these have often been based on observations of contrast fluctuations in TEM which can be artifacts from the TEM specimen preparation [24, 25]. These artifacts are limited to sample surfaces [26] and no links have been established between these and chemical phase separation in interior of samples. While phase separation could explain the high nucleation rate in $Al_{88}Y_7Fe_5$, there have been no previous studies showing this.

Here, results from APT, differential scanning calorimetry (DSC), electrical resistivity, and TEM studies of the devitrification process in rapidly quenched $Al_{88}Y_7Fe_5$ alloys are presented. Previous studies by this group showed an isothermal DSC signature consistent with coarsening, suggesting that the rapidly quenched alloys were not glasses. However, the results presented here show that this is not the case. The anomalous DSC curves arise from an extremely high nucleation rate coupled with diffusion-limited growth. Further, our APT studies provide the first evidence for phase separation into

regions of high Al concentration (with a spatial separation of approximately 74-126 nm) prior to crystallization in the quenched $Al_{88}Y_7Fe_5$ alloys. As in the $Al_{87}Ni_6La_5$ glasses, these regions appear to act as preferential sites for the nucleation of α-Al.

### 3.2. Experimental

$Al_{88.5}Y_7Fe_5$ ingots were prepared by arc-melting mixtures of Al (99.99%, Alfa Aesar), Y (99.9%, Alfa Aesar), and Fe (99.98%, Alfa Aesar) on a water-cooled copper hearth in a chamber that had first been evacuated to ~4 Pa and backfilled with high-purity Ar gas (99.998%). A Ti/Zr getter located close to the sample was melted prior to arc-melting to further reduce the oxygen from the chamber. Each ingot was melted two to three times to ensure a homogeneous composition; the duration of each melt cycle was approximately one minute. The ingots were melted by RF-induction heating to 1100-1150 °C (above the liquidus temperature) in a graphite crucible under an Ar atmosphere and rapidly quenched onto a copper wheel rotating at ~70 m/s, producing ribbons that were continuous for 3-10 cm, with an average cross section of 1-2 mm by 20-30 μm.

The as-quenched ribbons were characterized by X-ray diffraction (Rigaku, Cu $K_\alpha$, $\lambda$ = 1.54Å radiation), DSC (Perkin-Elmer, model *DSC 7*), and electrical resistivity measurements. *In-situ* resistivity measurements were made using a four-probe technique, with a Fluke 8505A digital volt meter and a computer controlled switching circuit to reduce thermocouple effects [27]. For these studies, ribbons of ~ 3cm length (~ 40mg) were placed in an insulating MACOR® holder that was inserted into a furnace constructed from a large copper cylinder (~1 kg). The samples were initially held in a water-cooled copper block; they were inserted into the furnace after it had stabilized at

the desired temperature. All measurements were made in Ti-gettered high-purity (99.995%) argon atmosphere. A thermocouple was used to monitor sample temperature; the thermal stability was typically ±0.1% over 80 hours.

Additional scattering experiments were conducted on the as-quenched ribbons using High-Energy Synchrotron X-rays generated at the Advanced Photon Source (APS). A vacuum flight path was built to reduce the contribution to the background intensity due to x-ray scattering from air. The details of the apparatus including dimensions and material properties are available elsewhere [28]. The path consisted of a sample chamber, outfitted with a small goniometer for positioning of the sample, and a large cylindrical chamber to allow passage of the diffracted cone. The entire chamber was evacuated using a scroll pump to roughly 100 mTorr. Raw data collected from the MAR3450 detector were processed using the procedures outlined in chapter 2.

The sample microstructures of the as-quenched and annealed samples were examined using a JEOL 2000FX transmission electron microscope. TEM specimens were prepared by ion milling with liquid nitrogen cooling (GATAN, model 600). For the studies of annealed glasses, the ribbons were wrapped in aluminum foil and completely immersed in a lead-tin solder bath. The high thermal conductivity of the foil allowed the samples to reach the annealing temperature quickly; the large thermal mass of the bath enabled the temperature to remain stable over the duration of the anneal. High Resolution TEM (HRTEM) studies were made with a JEOL 2100F, using samples that were thinned by electropolishing in a mixture of nitric acid and methanol at 18V DC.

Atom Probe Tomography measurements were made on as-quenched ribbons using the Imago Scientific Instruments Local Electrode Atom Probe (LEAP). The LEAP

has a single atom crossed delay line detector and a 200 kHz voltage pulse generator. It has a maximum field of view of ~100 nm. Data sets of over $10^8$ atoms can be obtained routinely. Two methods were used to prepare the sample tips for the APT measurements. In one case, a focused ion beam-based annular milling technique [29] was used to fabricate samples with 75 – 150 nm tip diameters. These samples showed a high failure rate in the LEAP so most samples were prepared by electropolishing in a solution of nitric acid and methanol at 12V DC. The ribbons were first cut into 7- 10 mm long sections and ground to an approximately square cross-section with 1000 grit sandpaper. A loop-based pulse polishing technique was used to polish these blanks into atom probe specimens [30]. Once prepared, the samples were quickly loaded into the LEAP to minimize oxidation. The chemical distribution of collected atoms was analyzed and confirmed to only deviate from the nominal composition by .01% for each species.

## 3.3. Results

### *3.3.1. Structural Characterization*

X-ray diffraction (XRD) characterization studies of as-quenched $Al_{88}Y_7Fe_5$ have previously been reported [4, 8, 31]. The XRD patterns show the broad diffraction peaks characteristic of a glass, shown in Figure 3.1. While Cu $K_\alpha$ radiation can't definitely rule out the presence of nanocrystals, this circumstantial evidence is backed up by other characterization measurements. Additionally, not shown here, the as-quenched ribbons were powdered using a mortar and pestle, and subsequently characterized: No evidence for crystallization was seen.

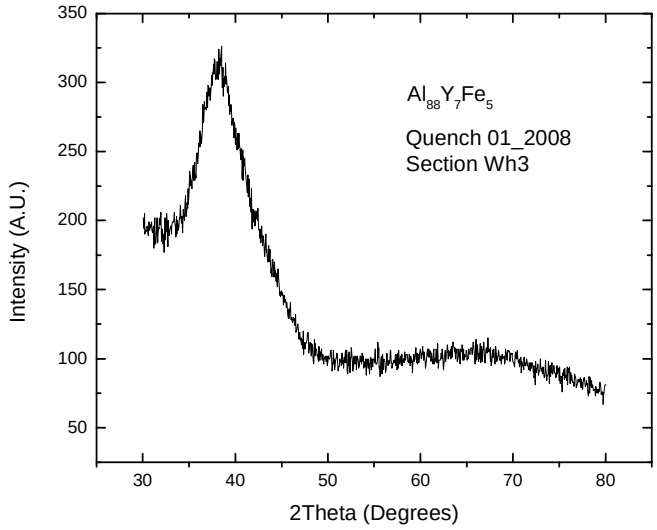


**Figure 3.1-** Low Energy X-ray diffraction scan for as-quenched $Al_{88}Y_7Fe_5$ ribbon, from quench 3, wheel side, used in Resistivity and DSC characterization.

Additional scattering experiments were conducted on the as-quenched ribbons using High-Energy Synchrotron X-rays generated at the Advanced Photon Source (APS). While intended for use with Reverse Monte Carlo simulations, the intensity profile for the as-quenched $Al_{88}Y_7Fe_5$ ribbons using 100keV photons ($\lambda \sim 0.99$ Å$^{-1}$) from the APS, shown in Figure 3.2 also shows an amorphous character. Assuming that crystallites were present in the main peak, the Scherer formula [32] was used to estimate the smallest crystallites that could pass detection (producing peak widths on the order of the main peak). Using this rough estimate, crystallites of size less than ~ 2 nm wouldn't be detected, which places an upper bound on the crystallite size. However, "crystals" of this size would raise the questions of whether ordered regions of this size can even have the coherence length to be considered crystals and not nanometer-sized ordered regions.

We'll discuss this in some detail in later sections, but to the resolving power of 100keV photons, the as-quenched ribbons appear amorphous.

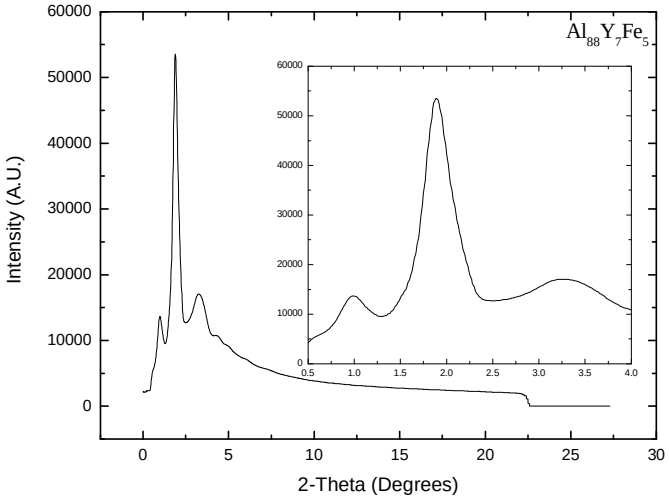


**Figure 3.2-** Intensity profile for as-quenched $Al_{88}Y_7Fe_5$ ribbons using 100keV photons ($\lambda \sim .99$ Å$^{-1}$) from the APS. X-ray images were collected on the MAR345 detector and corrected for polarization, detector tilt, and unwarped (to account for flat plate detector geometry).

### *3.3.2. DSC/Microstructural Analysis*

The sample microstructures of the as-quenched and annealed samples were examined using a JEOL 2000FX transmission electron microscope (TEM). Because the reports haven't been documented in others' theses, we'll discuss the details of the studies relevant to this experiment, though the microscopy was actually conducted by D. Saha and L.-L. Spoor. The preparation technique has been briefly summarized in the experimental section, although for a complete description, the reader is referred elsewhere [33, 34].

The primary crystallization mechanism is of interest, thus the annealing treatments were chosen to generate populations of the primary phase. Extensive DSC and X-ray diffraction (XRD) characterization studies of as-quenched $Al_{88}Y_7Fe_5$ have previously been reported [4, 8, 31]. The XRD patterns show the broad diffraction peaks characteristic of a glass, and non-isothermal DSC scans show a peak corresponding to crystallization. This has been confirmed in this study. Figure 3.3 shows the non-isothermal DSC scan (20 K/min) for as-quenched $Al_{88}Y_7Fe_5$ ribbons. The primary crystallizing phase was indexed to FCC-Al ($\alpha$-Al) using Cu $K_\alpha$ radiation after annealing into the first peak (onset ~270°), as shown in Figure 3.4. The onset is defined as the beginning of the exothermic heat signature indicating crystallization.

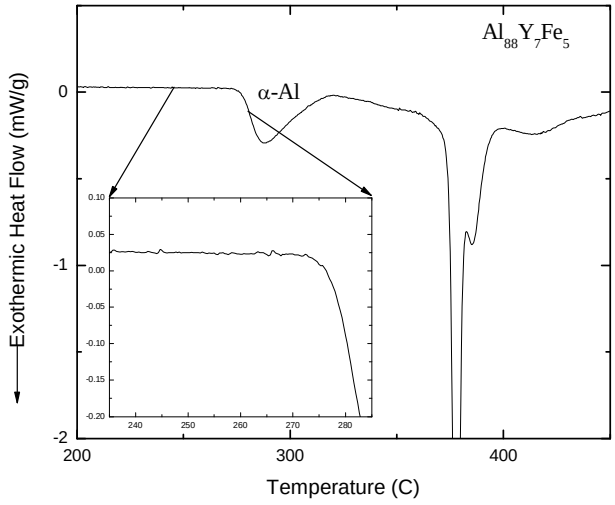


**Figure 3.3-** Non-isothermal DSC scan (20 K/min) for as-quenched $Al_{88}Y_7Fe_5$ ribbons. The primary crystallizing phase was indexed to FCC-Al ($\alpha$-Al)

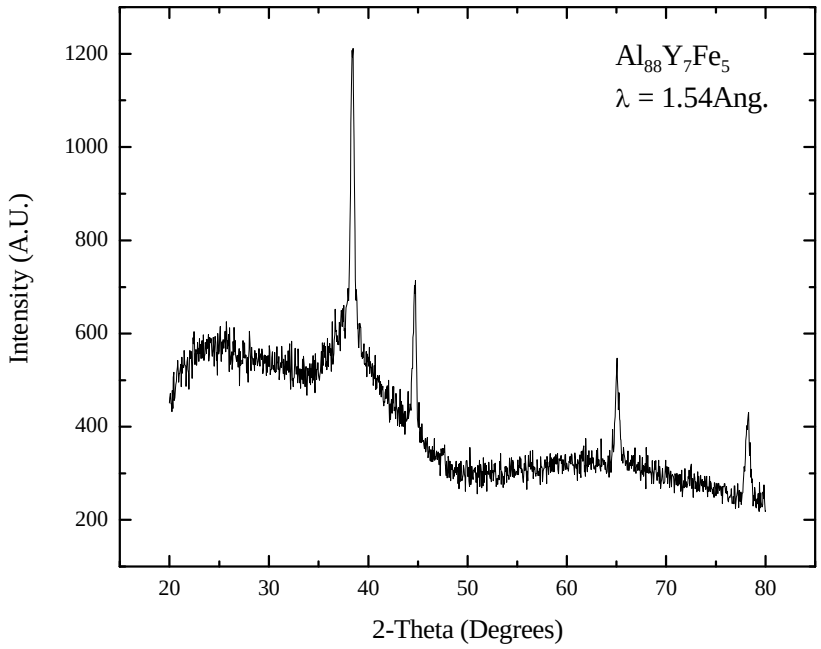


**Figure 3.4**- X-ray scan showing formation of FCC-Al as the primary crystallizing phase in DSC non-isothermal scans of $Al_{88}Y_7Fe_5$.

As can be seen in Figure 3.3, there is no evidence of a glass transition in the non-isothermal scan, shown in the inset. Many glasses don't show a strong glass transition endothermic feature in DSC non-isothermal. However, isothermal DSC data do not show the expected peak for a nucleation/growth-based transformation, but instead show an exothermic curve that decreases monotonically in magnitude with annealing time. The isothermal DSC data, for annealing at 250 is shown in Figure 3.5, shows no exothermic peak. Longer isothermals and isothermals at higher temperatures up to the onset temperature (270°) also show this behavior.

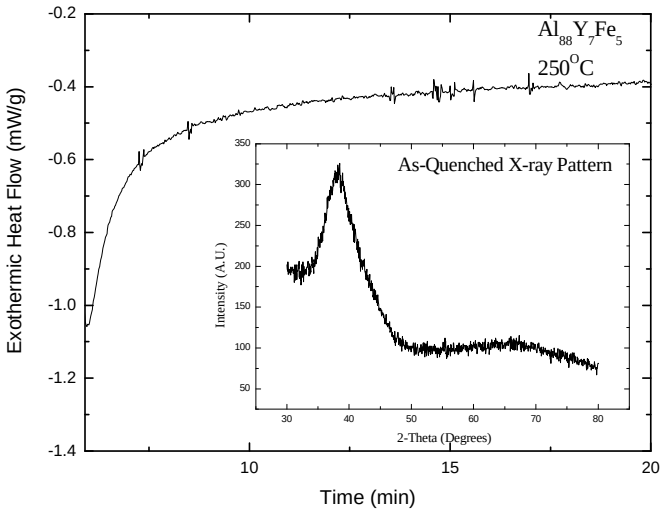


**Figure 3.5**- Isothermal DSC curve showing the lack of an exothermic peak characteristic of a nucleation on growth crystallization process.

This character of the isothermal DSC data has traditionally been associated with coarsening [35], but can also be explained by an extremely high nucleation rate with slow, diffusion-limited growth [36]. As was pointed out in an earlier publication [14], care must be taken when interpreting heating data for Al-based alloys since the crystal nucleation rates are so high that DSC studies of the transformation can be misleading.

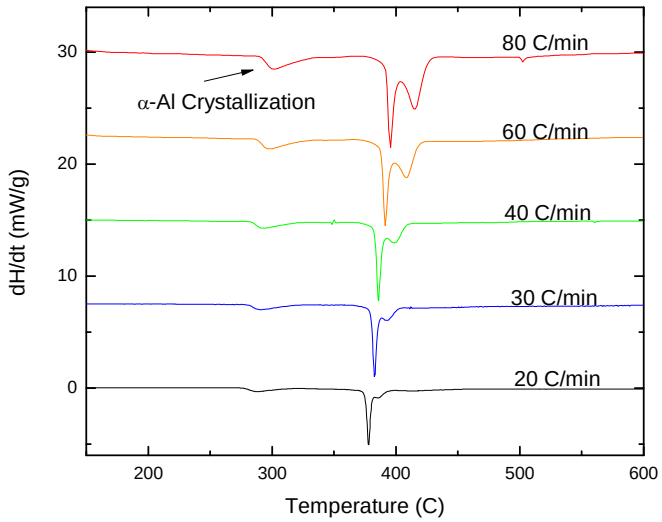


**Figure 3.6-** DSC non-isothermal scans at varying heating rates for $Al_{88}Y_7Fe_5$ as-quenched ribbons. The scans are offset in power, and the baseline is subtracted

As-quenched ribbons of $Al_{88}Y_7Fe_5$ were annealed at 250°C ($T_{ax}$ = 269°C) in a lead-tin bath to study microstructural development during crystallization. Non-isothermal DSC scans (as shown in Figure 3.6) were used to obtain a reasonable annealing temperature. TEM bright field images of the as-cast ribbons were featureless, and the corresponding diffraction patterns showed broad rings, both consistent with amorphous samples. Spheroidal crystals are observed in the annealed ribbons, particularly for short annealing times, in contrast with the strongly dendritic grains commonly observed for many related aluminum alloy glasses [4, 5, 37]. A sequence of TEM micrographs at various annealing times are shown in Figure 3.7.

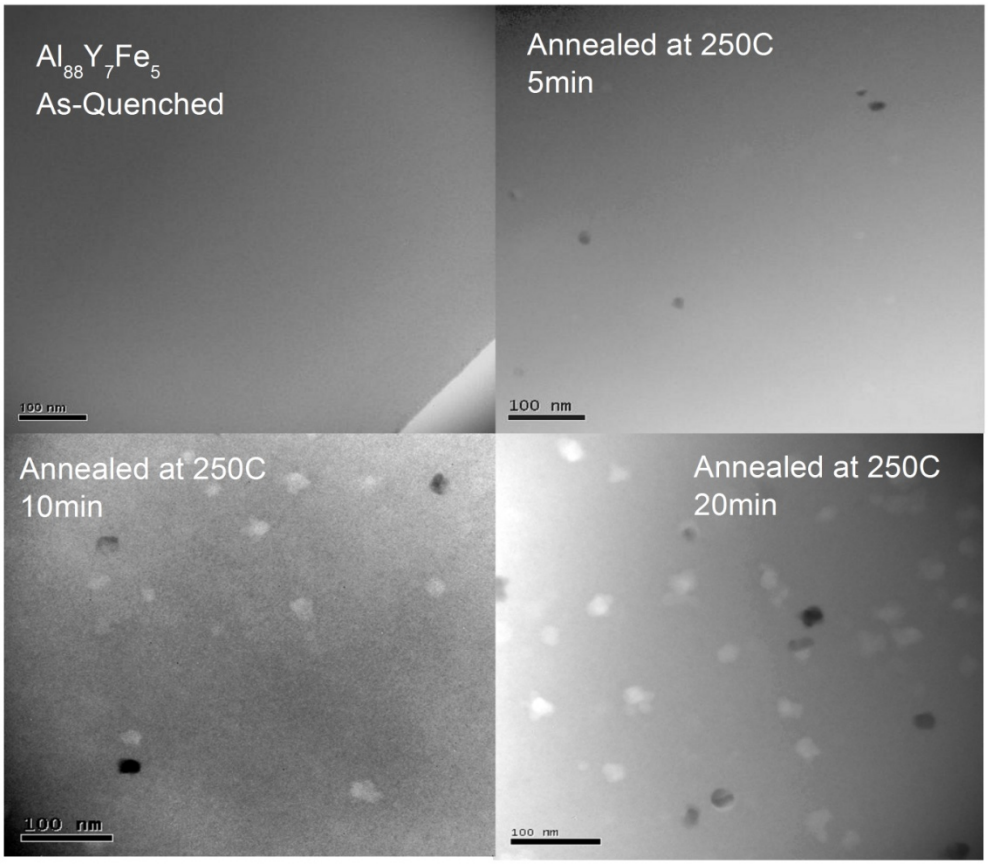


**Figure 3.7-** Select TEM micrographs showing α-Al crystals at different annealling times at 250°C.

Quantitative measurements of particle size distributions from TEM studies are problematic for a number of reasons. Firstly, because of the limited field of view, only very select portions of a ribbon can be observed. In fact, some regions may appear to be amorphous while others show crystallization. Secondly, the distribution of crystallite sizes likely varies from image to image, making the measurement of those distributions time consuming. Finally, because two-dimensional slices are examined, a statistical analysis has to be conducted to reconstruct the actual distribution (more below). The results are somewhat dependent on the model used to reconstruct that distribution from

measured data. These problems will be discussed, but it is important to point out that the number density is a robust quantity.

The particle number density was measured by examining TEM micrographs at various annealing times, assuming that the localized high contrast regions shown in Figure 3.7 were crystallites. The number of crystallites increases approximately linearly with annealing time at 250°C, with a rate of ~ $2x10^{20}$ $m^{-3}min^{-1}$ ($3x10^{18}$ $m^{-3}s^{-1}$), until saturation occurs at 20min (Figure 3.8). The particle number density of crystallites increasing with annealing times seems to be inconsistent with coarsening, where the number density would be expected to decrease with time [38, 39].

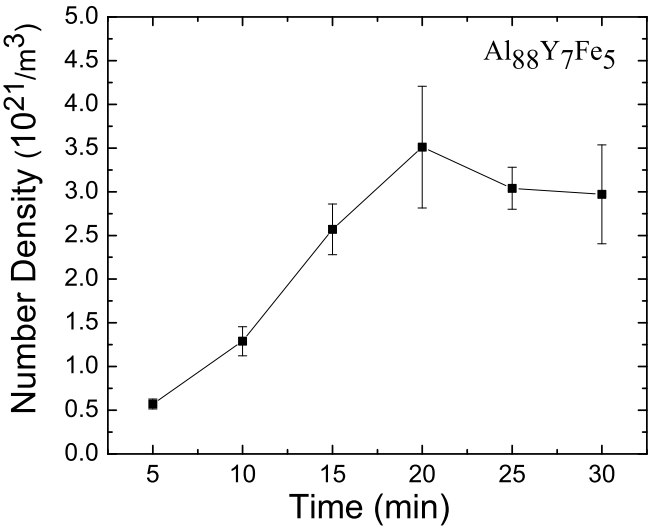


Figure 3.8- Number density of α-Al crystallites during annealing at 250°C determined from bright field TEM images. The increase in number density with increased annealing time is characteristic of a nucleation and growth dominated transformation.

Due to poor contrast, arising from the TEM specimen thickness (50 – 100 nm) and medium-range order in the glass, it is difficult to definitively observe crystallites that are

smaller than approximately 5 nm in diameter. It is possible, then, that such crystallites might be present in the as-cast samples. Additionally, if precipitation had gone to near completion, the size distribution of those precipitates would result in coarsening with annealing. Particles would grow to a visible size and thus appear to increase in number, mimicking nucleation. To examine this in more detail, the particle size distribution was determined from TEM images of the as-quenched ribbon and after annealing times of 5, 10, 15, 20, 25, and 30 min. To accumulate adequate statistics, many images from different parts of the samples were taken to give a total of several hundred particles for the short annealing times and more than a thousand particles for longer annealing times. A spherical growth morphology was assumed for the analysis. While the number of crystallites observed is readily measured, it was necessary to use a probabilistic approach to reconstruct the three dimensional particle-size distribution from the two dimensional projection measured by TEM. The commonly used approach of Saltykov was initially followed. In this technique, it is assumed that a 2-D image of particles is a mapping of a three dimensional distribution. This image will have a distribution of sizes, but because a slice is made through a 3-D region, the observed distribution will differ from the actual ones. The correction method first bins the observed particles into some number of size groupings. The number of bins is somewhat arbitrary; too few bins and the distribution lacks resolution but too many bins and Poisson statistics lead to large uncertainty. It isn't entirely clear which metric should be employed to determine the correct number of bins, however this group has traditionally used 15-25.

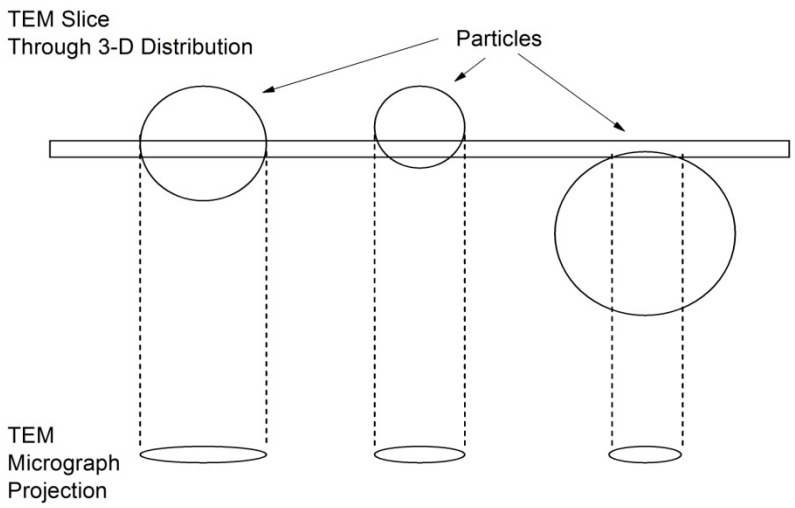


**Figure 3.9-** Schematic of 2-D TEM projection of 3-D particle distribution.

Observed particles in the largest size group are assumed to show their full diameters. However, it can be seen that these larger particles may also be sliced in a position such that their full diameter is not observed, shown schematically in Figure 3.9; therefore only a truncated diameter is observed. In principle, smaller size groups will contain contributions from larger groups, but no larger groups contain contributions from smaller particles. It is then a matter of correcting the smaller bins by redistributing their contributions back to larger bins. Several techniques exist for conducting this correction, and the differences between those techniques primarily lie in how the correction is made. Our chosen techniques attempt to limit error propagation by correcting each bin separately, rather than correcting all subsequent bins from one starting bin. A comprehensive overview, for interested readers, is provided by R. T. De Hoff [40]. When combined with a thickness correction (the Saltykov method assumes thin foils) a

corrected particle size distribution can be analyzed for average radius evolution as a function of annealing time.

The thickness correction, qualitatively, might seem to be unnecessary; particularly since the TEM slices are so thin. However, consider an infinitely thin slice; in this case, the true diameter would be projected only when the slice hit the diameter of the particle. TEM slices are roughly 50-100nm thick [41]. We found that for long times the largest bin must accommodate 100nm diameter spheres, with the most sampled bin being roughly 40-50nm in diameter. This means that if the thickness is 50nm, there is a wide range of slices, shown schematically in Figure 3.10, which will project the correct diameter. This implies, among other things, that the measured distribution is closer to the true distribution than the infinitely thin slice approximation would imply.

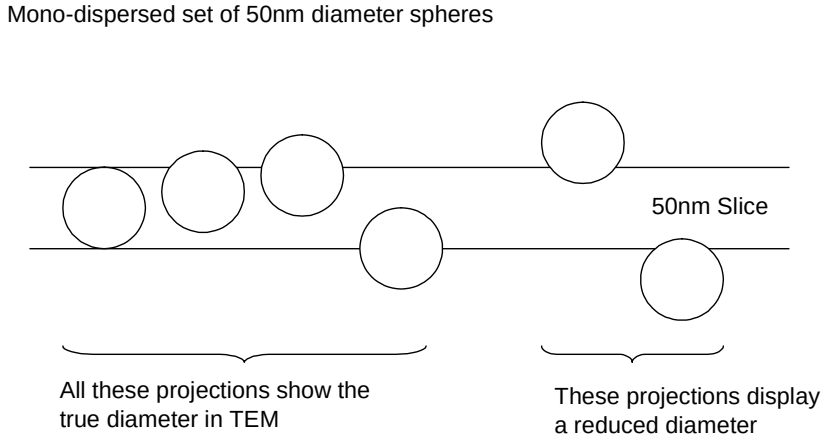


**Figure 3.10-** Schematic of projections of spherical crystallites in TEM.

To find the correct distribution of particles, we need to generate the transfer matrix $\alpha$, which calculates the contributions from larger bins to smaller ones. Let $NA_{(25)}$ be the number of measured particles in the largest class (say there are 25 classes), and $NA_{(i,j)}$ be the contribution from j$^{th}$ larger class to the i$^{th}$ smaller one. The actual number of particles in a given bin is then $NA_{(i,i)}$. Then, the measured number in each class has contributions

$$\begin{aligned} NA_{(25)} &= NA_{(25,25)} \\ NA_{(24)} &= NA_{(24,25)} + NA_{(24,24)} \\ NA_{(23)} &= NA_{(23,25)} + NA_{(23,24)} + NA_{(23,23)} \\ &\text{K} \\ NA_{(1)} &= NA_{(1,25)} + NA_{(1,24)} + NA_{(1,23)} + \text{K} + NA_{(1,1)} \end{aligned} \tag{1}$$

Solving this system of 25 linear equations, we find

$$\begin{aligned} NA_{(25,25)} &= NA_{(25)} \\ NA_{(24,24)} &= NA_{(24)} - NA_{(24,25)} \\ NA_{(23,23)} &= NA_{(23)} - NA_{(23,25)} - NA_{(23,24)} \\ &\text{K} \\ NA_{(1,1)} &= NA_{(1)} - NA_{(1,25)} - NA_{(1,24)} - \text{K} - NA_{(1,2)} \end{aligned} \tag{2}$$

Each $NA_{(i,j)}$ is determined by the transfer matrix and depends on the model used and whether a thickness correction is used. The coefficients in the transfer matrix are assumed to come from the intersection of the plane randomly of a sphere of the size class indicated. Thus, including the finite thickness correction, the coefficients are essentially proportional to the amount that the diameter can be intersected and project to a given class. The Saltykov method initially used 12 binning classes. However this method, which bins the observed particles into size classes, frequently generates negative values for smaller size classes. This is clearly not physical. In spite of this, a comparison with

the distribution computed from another commonly used approach, the 25F association method [42], showed that the average radius was robust, with the values obtained from the two approaches agreeing to within 1% for all annealing times.

### *3.3.3. Coarsening Model*

In coarsening, larger crystallites grow at the expense of smaller ones due to the size-dependent chemical potential, which shifts the equilibrium concentration of solute at the interface according to the Gibbs-Thompson equation [43]. The Lifshitz ,Slyozov, and Wagner (LSW) [38, 39] treatment was used to determine whether this could explain the TEM observations. The LSW model predicts the following size distribution for particles of radius *r*

$$g(r/\bar{r}) = g(z) = \begin{cases} \dfrac{3^4}{2^{5/3}} \dfrac{z^2 \exp\left(\dfrac{2/3\, z}{2/3\, z - 1}\right)}{(z+3)^{7/3}(3/2 - z)^{11/3}} & \text{if } 0 < z < 3/2 \\ \\ 0 & \text{else} \end{cases}, \qquad (3)$$

where $z = r/\bar{r}$ and $\bar{r}$ is the average radius. Average quantities, $\langle x \rangle$, are calculated from the distribution in the usual way

$$\langle x(t) \rangle = \frac{\int dr\ g(r,t)\, x(r,t)}{\int dr\ g(r,t)}. \qquad (4)$$

Because $\bar{r}$ increases with time, the singly-peaked distribution shifts and broadens with time, as is illustrated in Figure 3.11. Assuming a lower limit for crystal detection of 2.5

nm radius (following the earlier discussion), if the initial distribution lies completely below this size, no crystallites are observed. As the distribution evolves beyond the detection limit, new particles appear, mimicking nucleation and growth and hiding the actual coarsening character of the transformation.

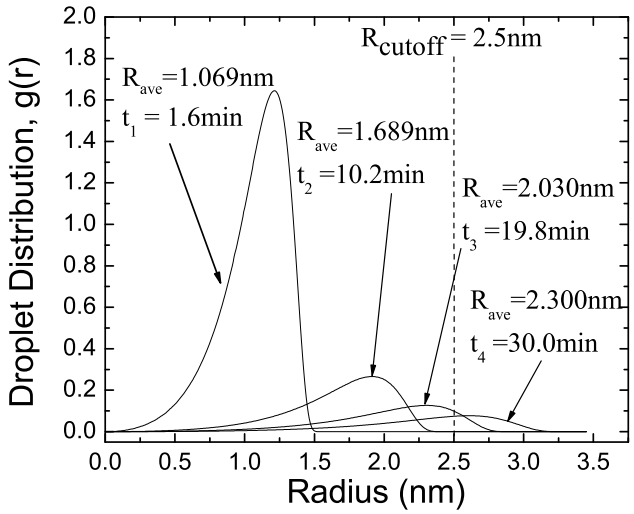


**Figure 3.11-** Evolution of a sample droplet distribution given by LSW coarsening theory. As the droplet distribution evolves in time, the average radius increases and the distribution spreads. For this example (TEM visualization cutoff of 2.5nm) the distribution initially lies completely below the cutoff and the true character of the transformation is hidden.

This was investigated further by calculating the average radius as a function of annealing time at 250°C for coarsening, and comparing it with the data obtained from the TEM investigations. The growth of the average radius was assumed to follow the result from LSW theory for diffusion-limited growth

$$\overline{r} = \left(r_o^{\,3} + k\left(T\right)t\right)^{1/3}, \tag{5}$$

where $r_o$ is the initial average radius and $k(T)$ is the isotropic volume growth rate per unit time. To determine reasonable values of the initial average radius, we note that a comparison between the experimentally determined values and the permissible values used in the coarsening simulation, shown in Figure 3.12, indicates that for certain starting values of $r_0$, the model predicts no visible particles at t = 5min, which isn't observed. This places a physical boundary, given the growth rate determined from DSC measurements at 250°C

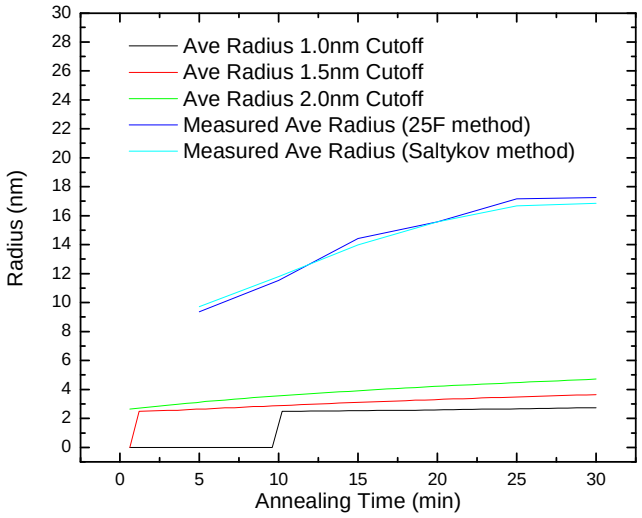


**Figure 3.12-** Average radius comparison between the experimentally determined values and the permissible values used in the coarsening simulation. For certain starting values of $r_0$, the model predicts no visible particles at t = 5min, which isn't observed.

To calculate the growth rate, we use the fact that, in DSC, we measure the heat evolved, $\dot{Q} = \frac{dQ}{dt}$. However, enthalpy is naturally a function of pressure and entropy,

$$H = H(S, P) \tag{6}$$

and

$$dh = \frac{\partial H}{\partial s} ds + \frac{\partial H}{\partial p} dp . \tag{7}$$

If the pressure is kept constant, as it is in DSC then, the heat release is equal to the enthalpy release (up to a factor of the temperature. Following Chen and Spaepen [35], the evolution of the interfacial enthalpy can be written as

$$-\dot{H} = \left( \frac{H_0 r_0}{3} \right) \frac{k(T)}{\left[ r_0^3 + \frac{k_B T^2 k(T)}{Qb} \right]^{4/3}} \tag{8}$$

where $\dot{H}$ is the time rate of enthalpy release (measured as a function of temperature in DSC non-isothermal scans), $H_o$ is the total enthalpy of transformation, $k_B$ is Boltzmann's constant, $Q$ is the apparent activation energy of the transformation, and $b$ is the scan rate. All quantities (except the initial radius) were extracted from nonisothermal DSC experiments at 5 scan rates: 10°C/min, 20°C/min, 40°C/min, 60°C/min, and 80°C/min. The Curie transition of Ni, which was not a function of scan rate, was measured simultaneously to correct for the contribution of instrumental transients to the shifts in the peak of the transition with scan rate. Based on a Kissinger analysis [44] of the corrected data, the effective activation energy for the transformation is 2.62±.03eV. By integrating the enthalpy released over time, $H_o$ = 19.07±0.43 J/g

Equation 8 was solved to obtain $k(T)$ for a range of initial radii, $r_o$, since it could not be determined from calorimetric data. The average radius, $\bar{r}$, was computed as a function of annealing time at 250°C using these values for $k(T)$ and the lower bound

stated earlier for the radius of crystal that could be observed (2.5nm). The error in the experimentally determined average radius was calculated from the standard deviation. The calculated and measured values of $\bar{r}$ are shown in Figure 3.13.

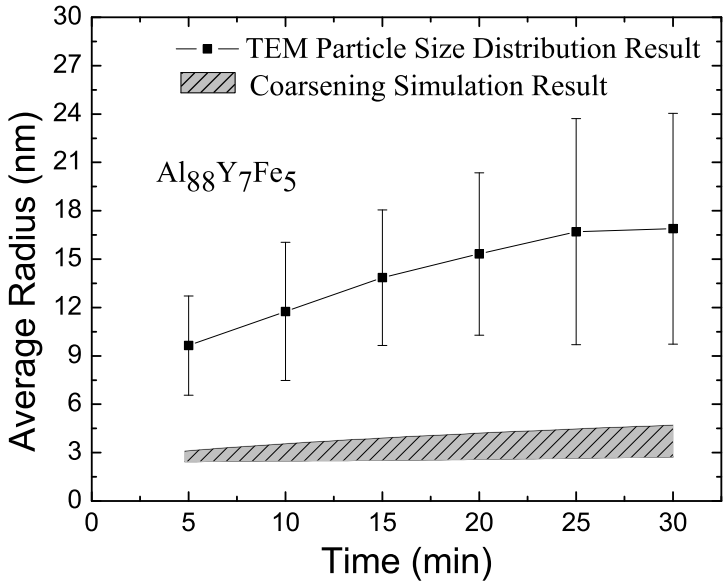


**Figure 3.13-** Comparison between the TEM particle size distribution result for average radius and the coarsening model when corrected for the TEM visualization cutoff. The coarsening model data are presented as the range of all possible values bounded on the low side by the value of the initial radius that gives observable crystallites at 5 minutes of annealing and the high side by the lack of observable crystallites in bright field TEM images of as-quenched samples.

Predictions from the coarsening model are in poor agreement with the experimental data. Taken in concert with electrical resistivity and APT results discussed later in this section, it is clear that the anomalous DSC isothermal data signal corresponds to a nucleation and growth process and not coarsening. From Figure 3.8, the nucleation rate is very high, approximately $3x10^{18}/m^3s$; growth is likely very slow, dominated by the diffusion rate of Y in the glass [14].

### *3.3.4. Electrical Resistivity Measurements*

The nucleation rates for α-Al in $Al_{88}Y_7Fe_5$ glasses are so high and the crystal growth rates are so slow that the earliest stages of the transformation are likely buried in the instrumental transients of DSC and later enthalpy releases are very small [32]. Taken with the coarsening studies just discussed, the featureless DSC isothermal curves, such as those obtained for the primary crystallization of $Al_{88}Y_7Fe_5$, do not reflect the true nature of the transformation.

The electrical resistance of the partially devitrified nano-composite, consisting of the α-Al phase (volume fraction $f_\alpha$ and resistivity $\rho_\alpha$) embedded in an amorphous phase (volume fraction $f_m$ and resistivity $\rho_m$) is [45],

$$\rho_{sample} = \frac{\rho_m}{2}\left(1 - {f_\alpha}/{x}\right) + \frac{\rho_\alpha}{2}\left(1 - {f_m}/{x}\right) + \left(\left[\frac{\rho_m}{2}\left(1 - {f_\alpha}/{x}\right) + \frac{\rho_\alpha}{2}\left(1 - {f_m}/{x}\right)\right]^2 - \rho_m\rho_\alpha\left(1 - {1}/{x}\right)\right)^{1/2} \quad . (9)$$

The crystal phase is modeled as an ellipsoid of revolution with eccentricity *x*. Because the resistivity of the $Al_{88}Y_7Fe_5$ is much greater than that of the α-Al (~$2\times10^{-3}$ Ω-m compared with $2.6\times10^{-5}$ Ω-m at room temperature), changes in the measured resistivity will be dominated by the growth of the α-Al phase. The measured resistivity of the sample ($\rho_{sample}$) is then approximately

$$\rho_{sample} \cong \frac{\rho_m}{2}\left(1 - {}^{f_\alpha}/_{x}\right). \quad (10)$$

This approximation has been experimentally validated. The rate of enthalpy released, d*H*/d*t* scales linearly with the rate of volume fraction transformed. From eq. (6), the magnitude of d$\rho_{sample}$ /dt should scale in the same way. Measured values for $\left|\mathrm{d}\rho_{sample} / dt\right|$ and $\left|\mathrm{d}H / \mathrm{d}t\right|$ for a non-isothermal scan (Figure 3.14) of the as-quenched samples at 2°C/min from room temperature to 400°C showed the same peak shape, with an onset at 255°C and a maximum at 265°C. The similarities of the two sets of data in Figure 4 confirm the approximations made in Equation 9 and Equation 10, allowing these equations to be used to quantitatively analyze the crystallization kinetics in isothermal studies.

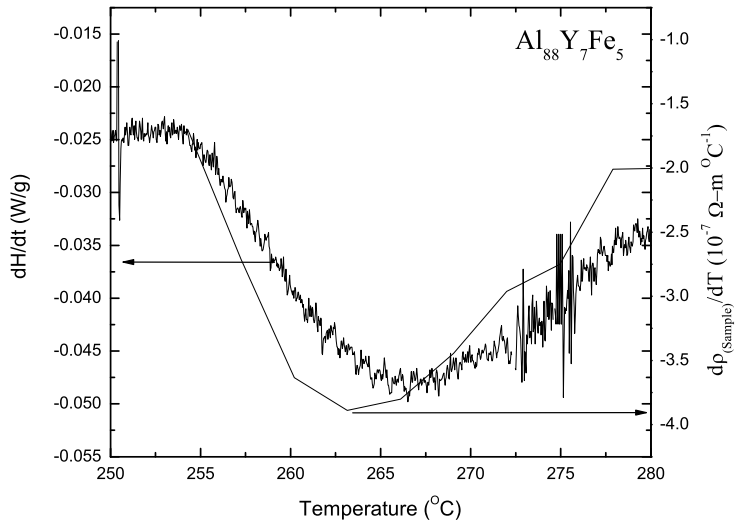


**Figure 3.14-** Comparison between measured values for $\left|\mathrm{d}\rho_{sample} / dt\right|$ and $\left|\mathrm{d}H / \mathrm{d}t\right|$ for a non-isothermal scan of the as-quenched samples at 2°C/min from room temperature to 400°C. The similarity of the peak shape and position validate the assumption made that the resistance is proportional to the volume fraction transformed of crystalline α-Al.

The changes in resistance of rapidly-quenched samples $Al_{88}Y_7Fe_5$ with isothermal annealing were measured as a function of time for several annealing temperatures below the onset of significant α-Al crystallization, as measured in a non-isothermal scan. The sample temperature measured during isothermal annealing was stable to ± 0.5°C over 80 hours. The data were generally collected until the resistance change appeared to be near saturation; within their limit of sensitivity, XRD measurements confirmed that the transformation product was only α-Al.

The measured normalized resistivity values (resistance normalized to the initial resistance, assuming no changes in sample volume) for isothermal anneals at 215°C, 235°C, 240°C, 245°C, and 250°C are shown in Figure 3.15. Although the data for the higher annealing temperatures show a monotonic decrease in resistivity, consistent with the DSC data and reminiscent of coarsening, the lower temperature data (215°C and 235°C) show the expected sigmoidal-type behavior (i.e., change from an initially negative to positive curvature in the plot of resistance as a function of time). This behavior is consistent with a nucleation and growth transformation. For clarity, the resistivity change with annealing at 215°C for short times is included to clearly show the plateau in the initial stage of the transformation (inset in Figure 3.15, from 35 min. < t < 200 min.). All resistance data show a small (~.25%) resistance decrease due to probe settling near the beginning of the run, accounting for the decrease in resistance observed near 35 min. for the 215°C isothermal anneal (inset). The 215°C data set was truncated to allow the initial plateau of the sigmoidal curve to be observed in contrast with the data from the higher temperature. The curvature inflection of the sigmoidal curve occurs near

an annealing time of 5000 min for that data. The rate of change of the electrical resistivity decreases for long annealing times in all data sets. This long-time behavior was fit well to an exponential function; all data converged to the same long-time asymptotic normalized resistance of 0.748±0.008. Like the isothermal DSC results, the lack of a sigmoidal character at high temperatures can be explained by a high nucleation rate, causing the rapid production of a high density of nanocrystals [32]. This rapid transformation occurs during the instrumental transient and is not observed. The observed change in resistance at those temperatures reflects further growth and coarsening of the nanocrystals.

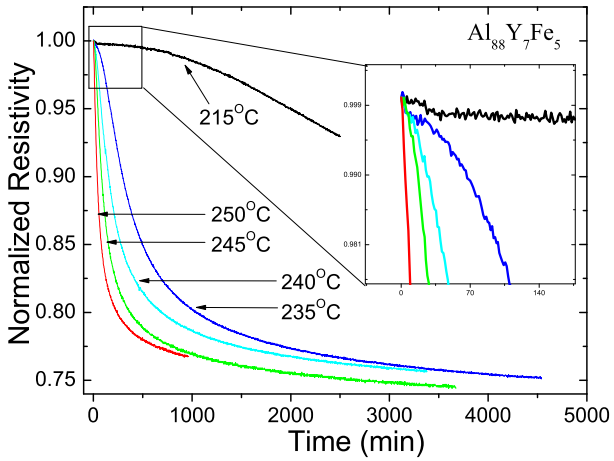


**Figure 3.15-** Normalized resistivity changes during isothermal annealing at various temperatures of as-quenched $Al_{88}Y_7Fe_5$.

### *3.3.5. Evidence for Phase Separation Prior to Crystallization*

From the APT studies, atom maps were constructed for the as-quenched $Al_{88}Y_7Fe_5$ alloy. A high density ($10^{24}$ - $10^{25}/m^3$) of pure Al zones (henceforth referred to as "pure Al

nanoregions") is observed (Figure 3.16) some containing up to 50 atoms, when corrected for the detection efficiency of the LEAP.

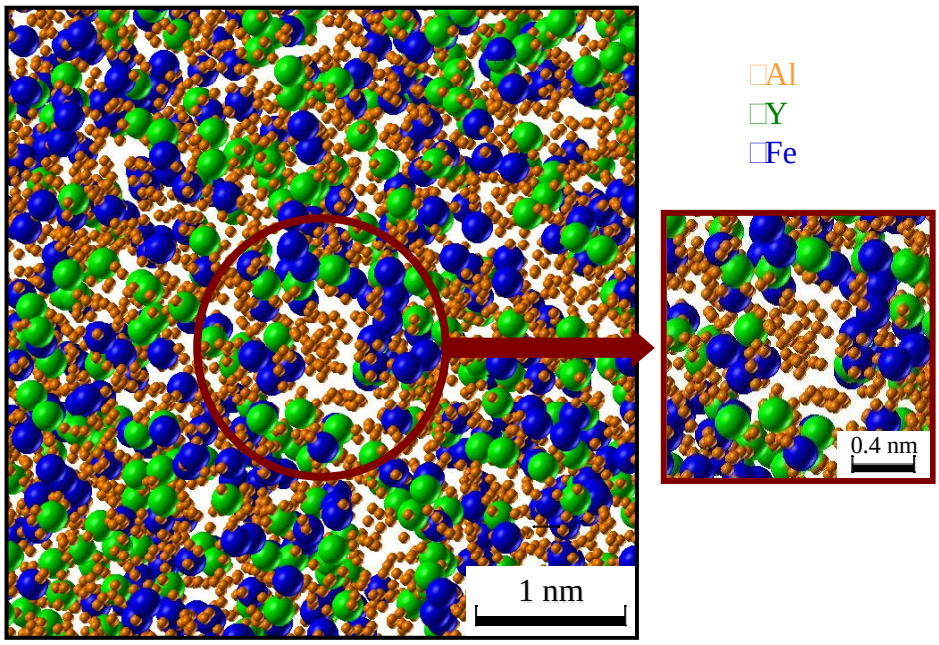


**Figure 3.16-** Example APT map of a selected region showing pure aluminum regions.

Confirming this quantitatively, Figure 3.17 shows the calculated probability of having no solute atoms in regions of different radius. The data set is discretized, and each curve in Figure 3.17 shows the probability distribution within each discrete region. The results fall into two different groups suggesting a fluctuation over a length scale that is larger than the region size. No evidence of crystallographic planes was observed in these pure Al zones. Such a high density of pure Al zones has not been experimentally observed previously, although it is consistent with a statistical random distribution of the solvent atoms [46]. We have demonstrated that a quantitative analysis of these data show that the distribution of pure Al zones is random spatially, in agreement with earlier predictions [45].

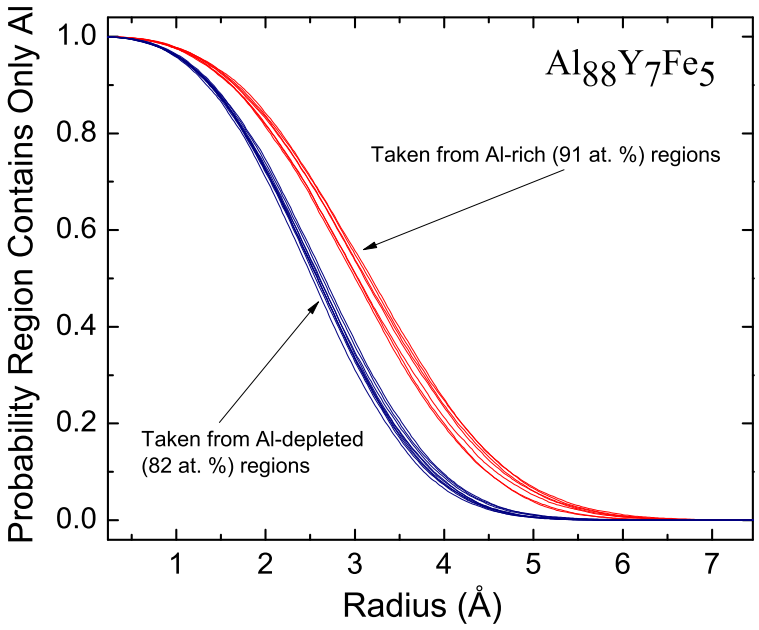


**Figure 3.17-** The probability, in percent, that a region of a given size will contain no solute atoms, computed from the APT data for Al88Y7Fe5. The different curves correspond to different cubes of data. The set of red curves correspond to cubes located in the Al-rich (91 at.%) regions of the sample, while the set of blue curves correspond to cubes located in Al-depleted regions (82 at.%).

To investigate possible chemical inhomogeneity on a length scale longer than the nanometer sized pure Al regions, the chemical composition is averaged over cubes of edge length 8.75nm. A longer-range chemical fluctuation is confirmed in Figure 3.18, showing a separation between Al-rich (91 at.%) and Al-depleted (82 at.%) along line *aa*. As expected, these are anti-correlated with the solute rich regions, (Figure 3.19 and Figure 3.20). An interpolating polynomial shading scheme was used to produce a continuous compositional map. We will show later in this section that this does not introduce artifacts into the results. By direct spatial comparison, the measured chemical fluctuations are found not to be correlated with the species-independent atom collection

density (Figure 3.21), indicating that they are real and not a function of the any biased counting efficiency.

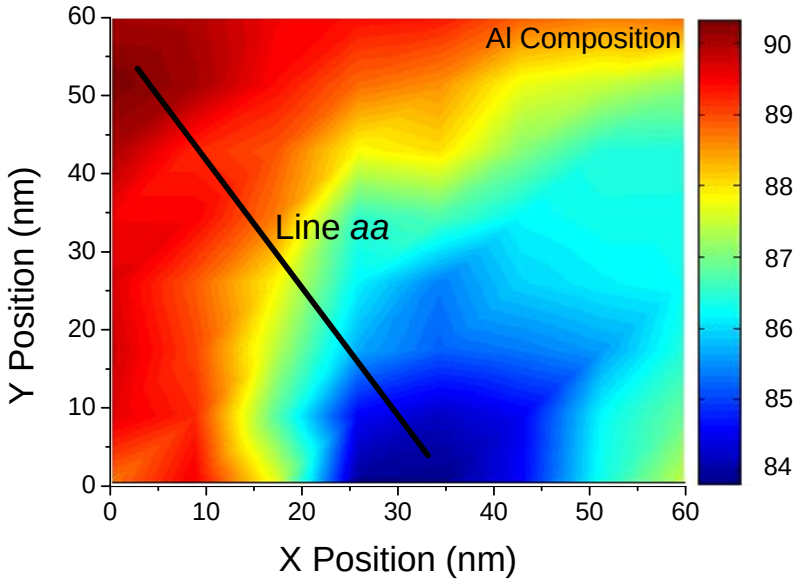


**Figure 3.18**- Al compositional profile in the $Al_{88}Y_7Fe_5$ glass. An interpolating polynomial has been used for shading the areas other than the cube centers, for which the data is available. The color bar on the side shows the color coding for the concentration (in at.%).

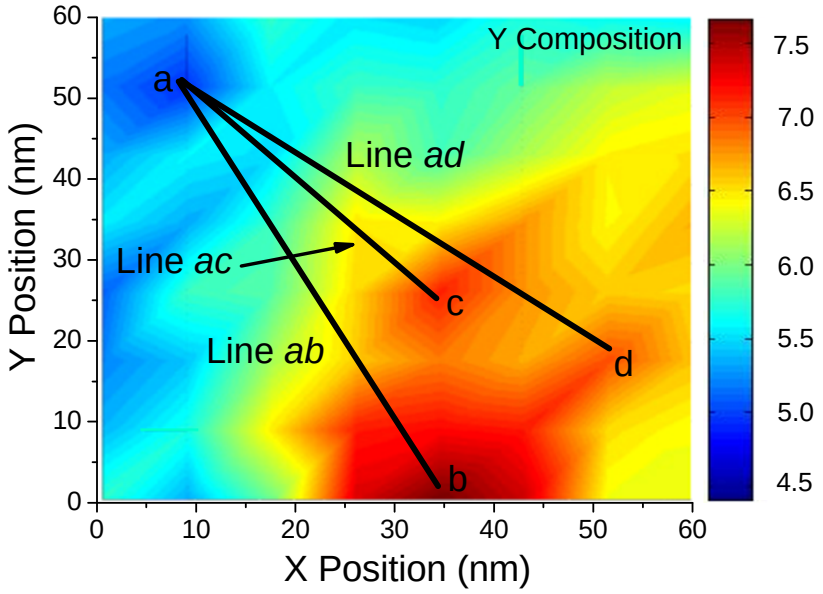


**Figure 3.19**- Y compositional profile in the $Al_{88}Y_7Fe_5$ glass. The lowest Y concentration is 5.0% while the highest is 7.9%. The cuts ab, ac and ad are approximately 59, 37 and 56 nm, respectively.

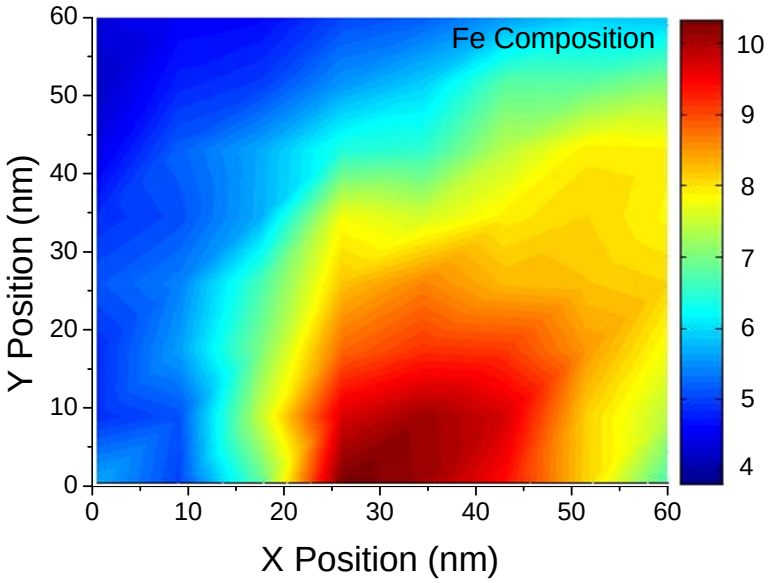


**Figure 3.20**- Fe compositional profile in the $Al_{88}Y_7Fe_5$ glass. The highest and lowest Fe concentrations are 10.3% and 4.2% respectively.

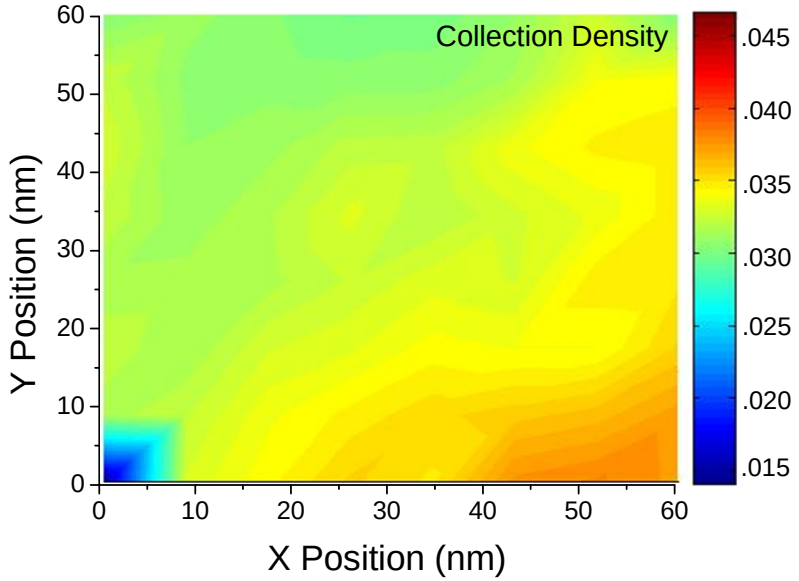


**Figure 3.21**- The collection density the $Al_{88}Y_7Fe_5$ glass. The lack of correlation of the fluctuations in this figure with those in Figure 3.18, Figure 3.19, and Figure 3.20 indicates the concentration fluctuations are not artifacts of preferential loss of particular atom species.

In APT, the atomic species is determined from time of flight mass spectrometry. Since there is a $Fe^{++}/Al^{+}$ overlap of the mass-to-charge state, Y data was used to determine the nature of the spatial fluctuation. The Y concentration along the line *ac* in Figure 3.19, is shown in Figure 3.22. As expected from Figure 3.17, the fluctuation is not random, but suggests chemical phase separation. No interpolation was used for these data. That they agree with the trends observed in Figure 3.19 indicates that the interpolation scheme used to produce the compositional maps introduces no measurable artifacts. Line *aa* in Figure 3.18 is approximately 63 nm in length; lines *ab*, *ac* and *ad* in Figure 3.19 are approximately 59, 37 (Figure 3.22) and 56 nm in length, respectively. Unfortunately, the volume of analysis was too small to obtain APT data over a sufficiently large region to observe a complete wavelength. Assuming, however, that the

fluctuations roughly follow a sinusoidal pattern, these distances correspond to a half wavelength (minimum to maximum), indicating a length scale for phase separation of 74 to 126 nm.

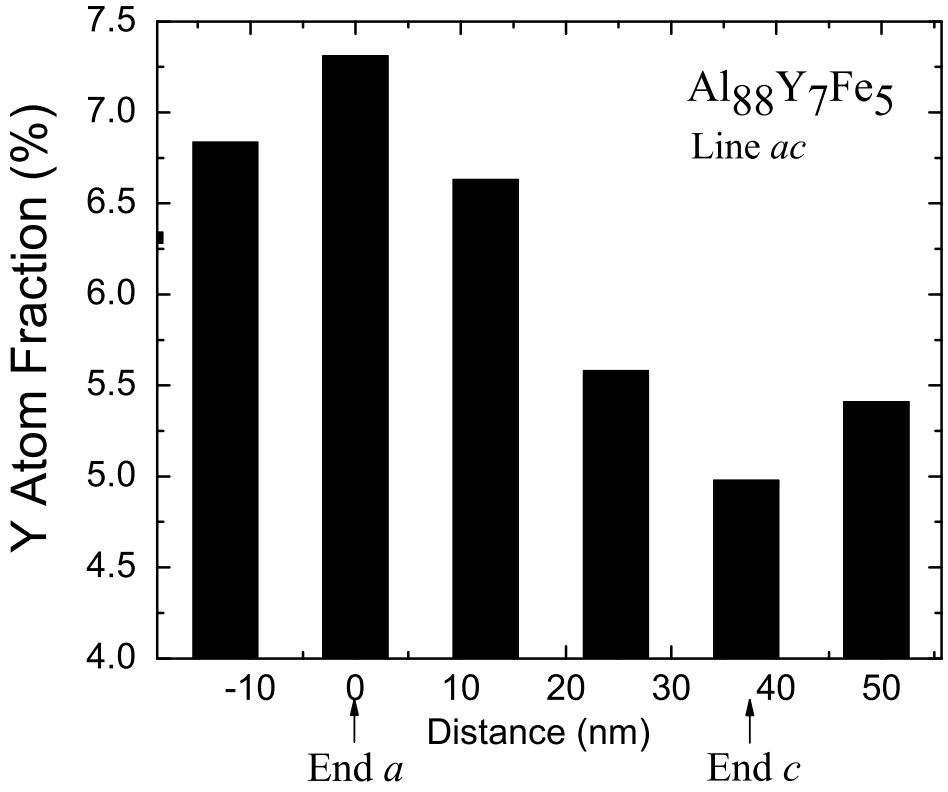


**Figure 3.22**- The Y composition profile along line ac of Figure 3.19 showing a smooth profile between a local minimum and a local maximum. Two extra cubes have been added to clarify the sinusoidal profile. This profile partly validates the interpolating polynomial shading scheme used in figure 6 and indicates that there is no sharp interface between the phase separated regions.

### 3.4. Discussion

Competition between diffusion and interfacial attachment can dramatically decrease the nucleation rate [47]. Therefore, the data suggest that the formation of α-Al during

annealing occurs in the pure Al nanoregions located in the high aluminum concentration regions of the sample. Guidance can be obtained by using the Classical Theory of Nucleation [17] to estimate the critical size and nucleation rate. Calculating the driving free energy from the measured enthalpy, assuming the measured interfacial free energy for α-Al and its melt [17], and using the measured crystal growth rate [14, 15] to estimate the interfacial mobility, the critical size for nucleation of α-Al from a pure Al liquid (or glass) at these temperatures is approximately 120 atoms and the nucleation rate is approximately $10^{21}/m^3s$. Note that this is an underestimate of the rate, since the measured growth rate used was likely dominated by Y diffusion [14, 15]. Most of the pure Al nanoregions are much smaller than the critical size (Figure 3.17), however, causing the actual nucleation rate to be less than would be expected. Assuming the estimated rate, only 1 in 1000 to 1 in 10,000 of the pure Al nanoregions (total number of order $10^{24}$-$10^{25}/m^3$) would need to nucleate α-Al to account for the crystallite number density observed (Figure 3.8). Based on the observed length scales of phase separation (74 to 126 nm) the density of Al-rich regions is between $5x10^{20}$ $m^{-3}$ and $3x10^{21}$ $m^{-3}$, the same order as the number of α-Al crystallites in the fully nucleated sample, suggesting that on average only one of the pure Al nanoregions in each Al-rich region forms an α-Al that grows. Once nucleated and grown to a size larger than the pure Al nanoregion, the α-Al grows by diffusion-limited rejection of Y [14, 15]. Soft impingement of the crystallites quickly shuts down further nucleation and growth, resulting in the amorphous/ nanostructured material observed. While the nucleation estimates are made by extrapolating the Classical Theory into a regime of metastability where it is likely not quantitatively valid, the predicted trends remain qualitatively correct.

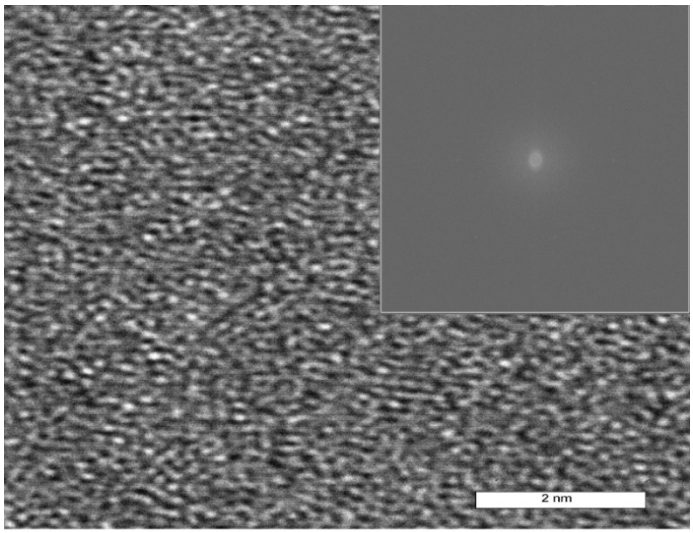


**Figure 3.23-** HRTEM image of as-quenched ribbon. Insert is the direct Fourier Transform, showing to evidence for crystal length scales.

Given the extremely high nucleation rate one might argue that the pure Al nanoregions would already be transformed in the as quenched sample. It might be possible to determine this from high-intensity x-ray diffraction and high resolution TEM (HRTEM) studies. As can be seen in Figure 3.23, HRTEM images show no evidence for crystallization. As mentioned earlier, while this isn't definitive proof that the sample is amorphous , a large survey of quenched ribbons produced no evidence for crystallites on any scale. Additionally, in a previous report [4] the as-quenched $Al_{88}Y_7Fe_5$ samples were examined using was probed using high-energy X-rays ($\lambda$ = .12488 Å). The scattering data are shown in Figure 3.2. Based on the peak widths (assuming that they correspond to crystal peaks and using the Scherrer formula [32] an upper bound on the sizes of $\alpha$-Al crystallites would be ~2 nm, smaller than the critical sizes calculated from the observed crystal density, suggesting that the regions of high Al concentration are amorphous.

Initial work on the glassy ribbons using Fluctuation Electron Microscopy [34] produced rastered nanoprobe diffraction studies (using a probe diameter of 1.2 nm) also

gave no evidence of for nanocrystallization [48]. However, they did reveal medium-range order in the glass, with a coherence length of 1.7 nm and a local order like that expected for crystal Al. Similar observations were reported earlier for Al-Sm [9]. These ordered regions are likely the pure Al nanoregions observed in the APT measurements. Even though they are not "crystals" in the conventional sense, the existing order would substantially lower the nucleation barrier for the α-Al, making them a type of "quenched-in nuclei" as has been suggested previously [8, 14].

### 3.5. Conclusions

In conclusion, quantitative studies of the crystallization of rapidly quenched $Al_{88}Y_7Fe_5$ alloys show that the transformation initially proceeds by rapid nucleation and not by coarsening as was proposed earlier [49]. Previous studies suggest [14] that given the composition difference between the crystallization product (FCC-Al) and the nominal composition of the matrix, the initial nucleation step is followed by slow diffusion-controlled growth. Based on APT measurements, we present the first evidence for nanoscale phase separation into Al-rich and Al-poor regions in these alloys. The pure Al zones in Al-rich regions likely are the sites for the rapid nucleation of α-Al, where the nucleation barrier is small. The tendency for many Al-based metallic glasses to crystallize to a amorphous/nanocrystal composite and the recently reported evidence for phase separation in a related glasses ($Al_{89}Ni_6La_5$) [19] raises the question of whether nanoscale phase separation is common in Al-based glasses.

## 3.6. References


[1] A. Peker and W. L. Johnson, *Applied Phyics Letters* **63** (1993), p. 2342.

[2] X. H. Lin and W. L. Johnson, *Journal of Applied Physics* **78** (1995), p. 6516.

[3] A. Inoue, T. Nakamura, N. Nishiyama and T. Masumoto, *Mater Trans JIM(Jpn Inst Met)* **33** (1992), p. 937.

[4] K. S. Bondi, A. K. Gangopadhyay, Z. Marine, T. H. Kim, A. Mukhopadhyay, A. I. Goldman, W. E. Buhro and K. F. Kelton, *Journal of Non-Crystalline Solids* **353** (2007), p. 4723.

[5] S. J. Hong, P. J. Warren and B. S. Chun, *materials science and engineering A* **31** (2001).

[6] J. H. Perepezko, J. Hamann, R. J. Hebert, H. Rosner and G. Wilde, *materials science and engineering A* **449-451** (2007).

[7] M. Calin and U. Koester, *Material Science Forum* **269** (1998), p. 749.

[8] J. H. Perepezko, R. J. Hebert, R. I. Wu and G. Wilde, *Journal of Non-Crystalline Solids* **317** (2003), p. 52.

[9] W. G. Stratton, J. Hamman, J. H. Perepezko, P. M. Voyles, X. Mao and S. V. Khare, *Applied Physics Letters* **86** (2005), p. 141910.

[10] A. Inoue, K. Othera, A.-P. Tsai and T. Masumoto, *Japanese Journal of Applied Physics* **27** (1988), p. L280.

[11] Y. Zhang, P. Warren and A. Cerezo, *Material Science and Engineering A* **327** (2002).

[12] S. Omata, Y. Tanaka, T. Ishida, A. Sato and A. Inoue, *Philosophical Magazine A* **76** (1997), p. 1477.

[13] A. P. Tsai, T. Kamiyama, Y. Kawamura, A. Inoue and T. Masumoto, *Acta Materialia* **45** (1997), p. 1477.

[14] J. C. Foley, D. R. Allen and J. H. Perepezko, *Scripta Materialia* **35** (1996), p. 655.

[15] D. R. Allen, J. C. Foley and J. H. Perepezko, *Acta Metallurgica* **46** (1997), p. 431.

[16] T. Gloriant, D. H. Ping, K. Hono, A. L. Gleer and M. D. Bario, *Material Science and Engineering A* **304-306** (2001), p. 315.

[17] K. F. Kelton In: H. E. a. D. Turnbull, Editor, *Solid State Physics*, Academic Pres, Boston (1991).

[18] K. F. Kelton and A. L. Greer, *Journal of Non-Crystalline Solids* **79** (1986), p. 295.

[19] B. Radiguet, D. Blavette, N. Wanderka, J. Banhart and K. L. Sahoo, *Applied Phyics Letters* **92** (2008), p. 103126.

[20] L. E. Tanner and R. Ray, *Scripta Metallurgica* **14** (1980).

[21] B. J. Park, H. J. Chang, D. H. Kim, W. T. Kim, K. Chattopadhyay, T. A. Abinandanan and S. Bhattacharyya, *Physical Review Letters* **96** (2006).

[22] W. C. Wang, J. H. Li, F. Zeng, Y. L. Gu and B. X. Liu, *Journal of Alloys and Compounds* **478** (2009).

[23] A. K. Gangopadhyay, T. K. Croat and K. F. Kelton, *Acta Materialia* **48** (2000), p. 4035.

[24] D. Nagahama, T. Ohkuba and K. Hono, *Scripta Materialia* **49** (2003).

[25] J. H. Na, Y. C. Kim, W. T. Kim and D. H. Kim, *Metals and Materials International* **14** (2008).

[26] N. Tian, M. Ohnuma, T. Ohkubo and K. Hono, *Materials Transactions* **46** (2005).

[27] K. F. Kelton and J. C. Holzer, *Review of Scientific Instruments* **59** (1988), p. 347.
[28] V. M. Wessels, PHASE FORMATION, LIQUID STRUCTURE, AND PHYSICAL PROPERTIES OF AMORPHOUS AND QUASICRYSTAL-FORMING ALLOYS, *Physics*, Washington University, St. Louis (2009).
[29] T. F. Kelly and M. K. Miller, *Review of Scientific Instruments* **78** (2007).
[30] M. K. Miller, Atom Probe Tomography, Springer, New York, NY (2000).
[31] R. J. Herbert, N. Boucharat, J. H. Perepezko, H. Rosner and G. Wilde, *Journal of Alloys and Compounds* **434** (2007).
[32] B. E. Warren, X-Ray Diffraction, Dover Publications, Inc., New York, NY (1990).
[33] Y. Shen, Transient nucleation and local structure in Zr-based metallic glasses, *Physics*, Washington University, St. Louis (2007).
[34] K. S. Bondi, Analysis of the effects of microalloying on glass formation in Al-Y-Fe alloys by fluctuation electron microscopy and other techniques *Physics*, Washington University, St. Louis (2009).
[35] L. C. Chen and F. Spaepen, *Journal of Applied Physics* **69** (1991), p. 679.
[36] K. F. Kelton, *Journal of Alloys and Compounds* **434-435** (2006).
[37] N. Bassim, C. S. Kiminami and M. J. Kaufman, *Journal of Non-Crystalline Solids* **273** (2000).
[38] I. M. Lifshitz and V. V. Slyozov, *Journal of Physical and Chemical Solids* **19** (1961), p. 35.
[39] K. C. Wagner, *Z. Electrochem* **65** (1961), p. 581.
[40] R. T. D. Hoff, Quantitative Microscopy, Mcgraw-Hill, New York (1968).
[41] Y. Shen and K. S. Bondi, Discussion of Ribbon Thickess in TEM, (2007).
[42] Y.-H. Xu and H. C. Pitot, *Computer Methods and Programs in Biomedicine* **72** (2003), p. 1.
[43] L. D. Landau and E. M. Lifshitz, Statistical Physics; 3rd Edition, Part 1, Elsevier, (1980).
[44] H. E. Kissinger, *Analytical Chemistry* **29** (1957), p. 1702.
[45] A. Davidson and M. Tinkham, *Physical Review B* **13** (1976), p. 3261.
[46] J. E. Spowart, D. B. Miracle and H. M. Mullens, *Journal of Non-Crystalline Solids* **336** (2004).
[47] K. F. Kelton, *Acta Materialia* **48** (2000), p. 1967.
[48] T. L. Daulton, K. S. Bondi and K. F. Kelton, *Private Communication*.
[49] L. Q. Xing, A. Mukhopadhyay, W. E. Buhro and K. F. Kelton, *Philosophical Magazine Letters* **84** (2004).

# Chapter 4

## Design and Construction of the Washington University Beamline Electrostatic Levitation (WU-BESL) Facility[€]

[€]Portions of this work appear in the manuscript *"A Highly-Modular Beamline Electrostatic Levitation Facility, Optimized for In-Situ High-Energy X-ray Scattering Studies of Equilibrium and Supercooled Liquids."* N. A. Mauro and K. F. Kelton. *Review of Scientific Instruments*. **82** (2011) 035114.

### 4.1. Introduction

Diffraction information from high energy X-ray and neutron diffraction studies of metallic alloys has been instrumental in understanding how local structural evolution relates to glass formation [1-3], the glass transition [4-6], and the nucleation barrier [7, 8]. Recently, the development of the Beamline Electrostatic Levitation Technique (BESL) [9] has allowed the extension of measurements of thermophysical properties of equilibrium and undercooled liquids to include high energy X-ray [8, 10-12] and neutron diffraction studies providing structural information in a containerless, high vacuum ($10^{-7}$ – $10^{-8}$ Torr) environment. Although high-energy synchrotron studies of levitated liquids are generally confined to the elastic regime, measurements of the static structure factor provide invaluable information about short and medium range atomic order. However, the increased use of this technique has highlighted unique problems associated with X-ray diffraction studies of weakly scattering liquids. Additionally, the increased use of structure factors derived from X-ray intensity profiles for quantitative measures of local atomic structures rely on fidelity of the signal between the sample and detector. Subtle features of the structure factor used for Reverse Monte Carlo (RMC) [13] simulation and *ab initio* molecular dynamics (MD) [3, 14, 15] potential refinement are susceptible to distortion due to the low signal to noise inherent in scattering from liquid samples.

The study of undercooled liquids presents significant challenges. The reactivity of many compounds with the ambient environment requires innovative approaches for sample isolation and non-contact measurements, particularly for the study of metastable, undercooled liquids. The development of containerless levitation techniques such as aerodynamic [16], acoustic [17], electromagnetic (EML) [18, 19] and electrostatic [20] has provided a suite of experimental environments that have differing utility depending on the material of study. EML and ESL provide the best sample environments for the study of metallic liquids, however, EML suffers from several drawbacks. In EML, a sample is levitated in a coil fed by an ac current with a typical frequency ranging from about ten kHz up to several hundreds of kilohertz. The eddy currents induced in the sample interact with those in the coil giving rise to a Lorentz force that repels the body from the coil, levitating the sample. Only materials that can efficiently couple to the rf field can be levitated Further, coupling produces heating of the sample, sometimes above the liquidus, either precluding free cooling studies, which are useful in determining the specific heat of a liquid as a function of temperature, or limiting the amount of supercooling accessible. Most importantly for coordinated structural and thermophysical property studies, the coils used to produce the levitation field limit the unobstructed view of the sample, thus limiting the range of the static structure factor, and generally limiting the number of coordinated measurements that can take place. In ESL, a surface charge is applied to the sample; electrodes located above and below the sample are used to create strong electric fields to levitate and maintain the sample position. This allows metals, semiconductors, glasses and ceramics to be processed. Heating lamps and more commonly heating lasers are then used to maintain sample temperature. Because the

positioning is completely decoupled from heating, maximum undercooling can be realized. Additionally, the electrode geometry (shown in Figure 4.3) allows a much larger field of view. For the BESL described in this report, an X-ray momentum transfer ($q = 4\pi \sin\theta / \lambda$) range of $.3\text{Å}^{-1} \leq q \leq 20\text{Å}^{-1}$ is achievable using high energy synchrotron radiation.

Here we describe the development of a low cost, highly autonomous and modular BESL (Washington University BESL, WU-BESL) optimized for *in-situ* studies of undercooled liquid phases and rapid phase diagram determination. This chapter is organized into two broad sections. First, the electrostatic levitator is described in extensive detail presenting the chamber design, electrode assembly, levitation implementation and stability trials, thermophysical property measurements and details of the heating and melting process. Second, we describe beamline integration, focusing on the challenges associated with weakly scattering liquids and the alignment stage necessary for use of the chamber in a high energy beamline.

## 4.2. Chamber Design

### *4.2.1. General Design Considerations*

The design for the electrostatic levitator chamber attempts to incorporate several and sometimes opposing design elements. First and foremost, the chamber is optimized for structural studies using high-energy synchrotron X-ray radiation in transmission geometry. As described earlier, the X-ray radiation is required to produce a probe on the order of atomic length scales. The high energy (~125keV) is required because the attenuation (absorption) associated with transmission experiments decreases

exponentially with increasing energy (aside from excitation edges). An example is shown in Figure 4.1.

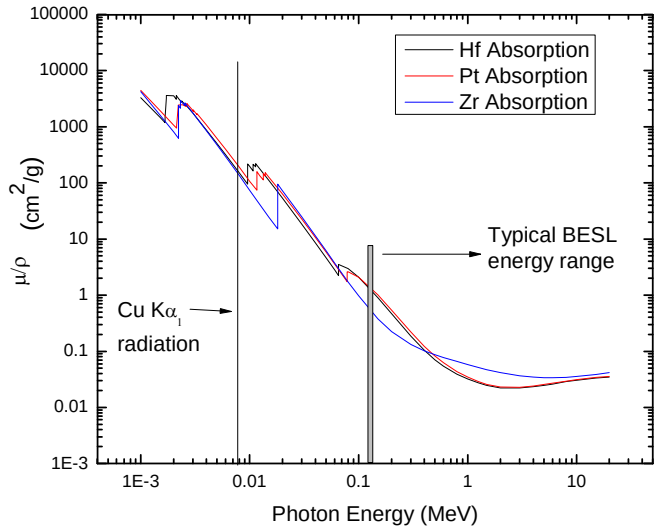


**Figure 4.1 -** Absorption coefficients for some materials relevant to BESL studies [21]**.**

A second reason that 125keV photons are used is that the momentum transfer $q$ is inversely proportional to the photon wavelength, $\lambda$; a larger energy allows the experiment to sample a larger $q$. This is important not just to attain information about correlations at higher $q$, but may in fact be most important because many of the corrections applied to the scattering data have asymptotic behaviors as $q \to \infty$. Finite $q$ leads to artifacts in the reduced data that are often difficult to correct for but are usually even more difficult to identify. The simplest transmission geometry requires a large exit window, which allows an unobstructed "scattering cone" to be detected directly downstream of the sample and axial with the incoming beam.

### *4.2.2. Vacuum Chamber*

Scattering data are most useful when correlated with thermophysical property data, particularly density (required for conversion between $G(r)$ and $g(r)$ and RMC experiments) and temperature. A minimum number of access ports are required for these measurements. As will be discussed in subsequent sections, the basic implementation of the ESL requires a minimum of 13 ports. The final chamber design is then a compromise between several competing requirements: A large scattering window (for high $q$); allowing many ports with line of sight on the sample; a portable chamber for integration in the beamline (as will be discussed in detail in later sections); and fast vacuum pump-down time, which argues for a minimum total volume for the chamber.

One of the ways to reduce the chamber volume while allowing port access is to begin with a basic full nipple vacuum chamber and then attach line of sight ports with smaller flange sizes, shown schematically below in Figure 4.2, also showing a possible instrument port assignment. Auxiliary ports can be added by including canted ports, consistent with the electrode geometry. However, in order to facilitate line of sight on the entire sample, the port canting angle must be small, fitting within that allowed by the geometry of the electrode assembly. Finite size effects (Figure 4.3) of the sample require that the allowed port canting angle follow

$$\theta_{allowed} = \tan^{-1}\left(\frac{\frac{d_z}{2} - \frac{d_{sample}}{2}}{\frac{d_{electrode\ assembly}}{2}}\right)$$

$$\theta_{\max} = \tan^{-1}\left(\frac{d_z}{d_{electrode\ assembly}}\right) \quad (1)$$

where $d_z$ is the vertical electrode spacing, $d_{sample}$ is the diameter of the sample, $d_{electrode\ assembly}$ is the diameter of the electrode assembly, and $\theta_{max}$ is the angle from the center of the sample to the edge of the electrode assembly. For the WU-BESL, $\theta_{allowed}$ is 7.59° and $\theta_{max}$ = 14.93°, based on the German Aerospace Agency (DLR) design [22].

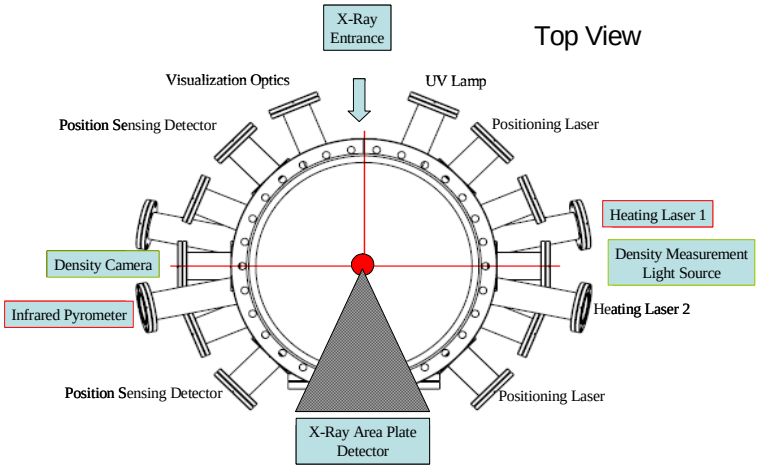


**Figure 4.2-** Schematic example port of the configuration in the ESL chamber. In this version, sight lines can also be increased by adding canted ports whose angles are consistent with the electrode assembly geometry.

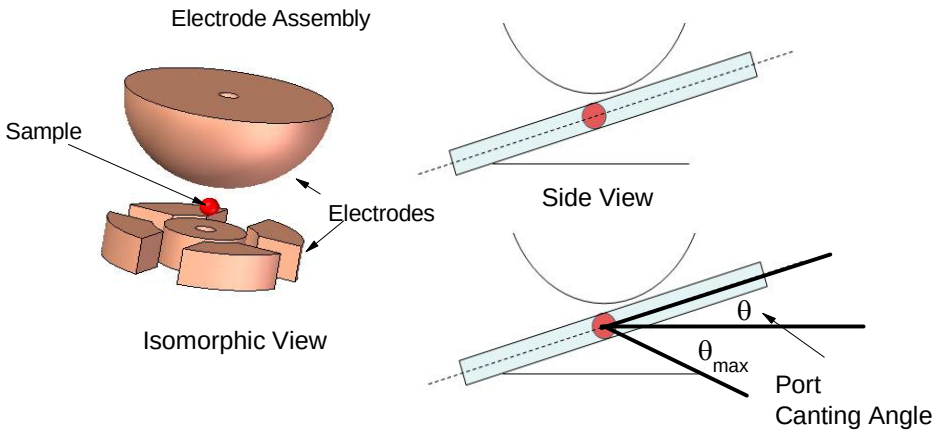


**Figure 4.3-** Electrode assembly with port canting angle. In order to have line of sight on the entire sample, any ports that are added are done so at the port canting angle. For the WU-BESL this angle is 7.59° to allow line of sight on a 4mm diameter sample.

The final chamber design is essentially a vertical stainless steel full nipple with 12" Conflat(CF)® flanges on either side. A large 8" CF flange is used for the exit window and all other instrument flanges are 2.75" CF flanges; four of these are canted at 7.59° to the horizontal and the rest are oriented in a horizontal plane at sample level. Ancillary ports are added above and below the sample level for additional instrumentation, feedthroughs, and chamber access. Detailed dimensions are presented in Appendix IV.1 while a series of isomorphic views are shown in Figure 4.4, Figure 4.5, and Figure 4.6, presenting the chamber, electrode assembly and optical table for instrument mounting.

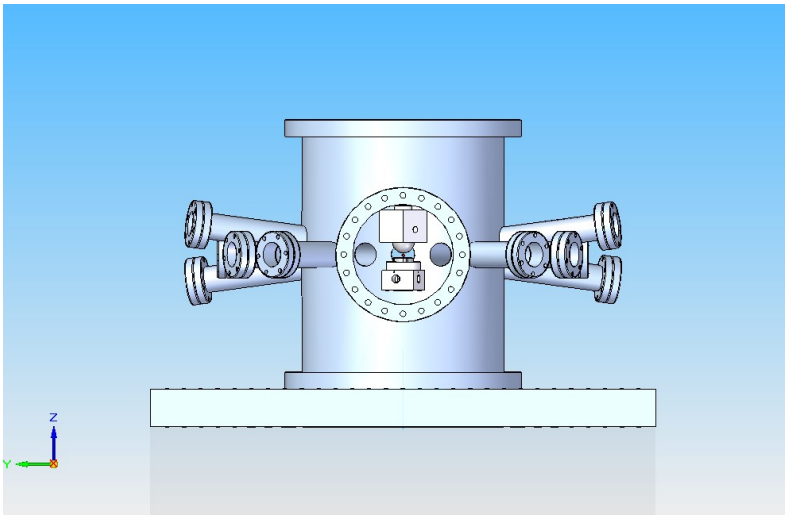

**Figure 4.4**- Front View of chamber with electrode assembly shown inside for context.

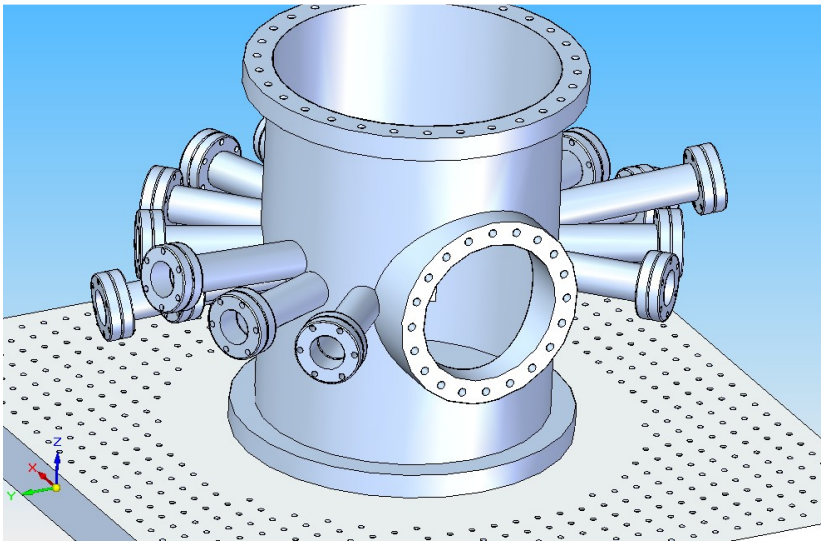

**Figure 4.5**- Isomorphic view of chamber. Note the canted ports entering above and below the sample plane.

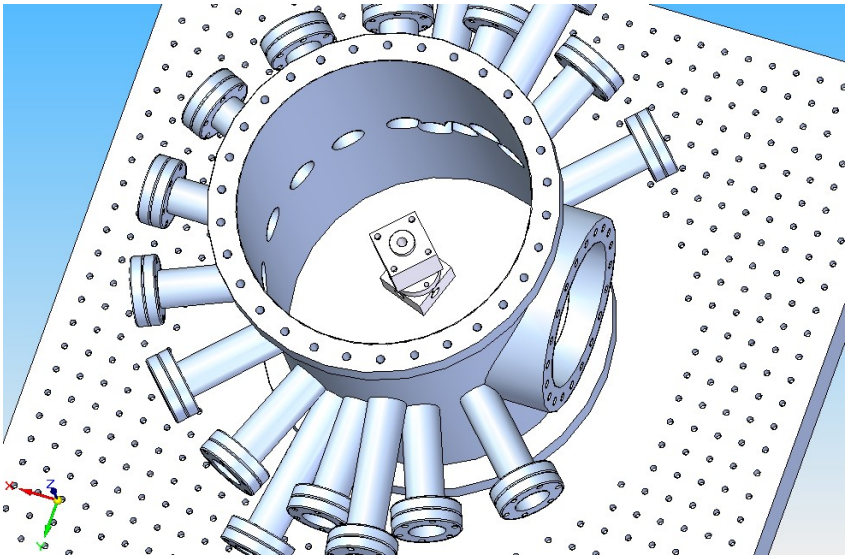

**Figure 4.6**-Top/isomorphic view of chamber with electrode assembly inside.

### *4.2.3. Window Protective Inserts*

One of the most pervasive problems associated with extended ESL operation is the evaporation of sample material onto chamber components. A closed system that is partially filled with liquid is in equilibrium with a certain amount of vapor that is dictated by the respective chemical potentials. For example an open container of water evaporates until the humidity in the air rises to the equilibrium partial pressure. The same basic principles drive liquid evaporation of an ESL sample. Chemical reactivity necessitates a high vacuum (~$10^{-7}$ Torr) environment for most metallic systems of interest. Empirical vapor pressure vs. temperature curves for several elements [23] are presented in Appendix IV.2. The higher the vapor pressure, the faster the element evaporates. Compounding the problem, and to be discussed in more depth in subsequent sections, evaporated material is charged and the strong electric fields around the sample tend to remove material from the sample/vacuum interface rapidly, driving the system away from

thermodynamic equilibrium. Ultimately, the sample continues to evaporate continuously in the liquid state, at a rate roughly proportionally to the vapor pressure. Since all ports with instrumentation require direct line of sight, deposition occurs on all viewports. This has adverse effects on nearly all thermophysical and scattering measurements (to be discussed in later sections) and deposited material bonds strongly to metals, UV transparent materials, and transparent silicates, common in viewport materials.

In order to circumvent the problem, aluminum inserts have been designed to hold standard 25mm x 75mm x 1mm microscope slides (Figure 4.7). Measurement problems associated with deposition are thus mitigated by periodically replacing the glass slides, which are considered consumables. Since these inserts are located nearer to the source, the rate of deposition on the glass slides is higher than on the optical components located farther away, making it necessary to frequently replace the slides. However, empirically, we have found that this is a manageable compromise for everything but the highest vapor pressure systems, i.e. Mn, Ag, and Co.

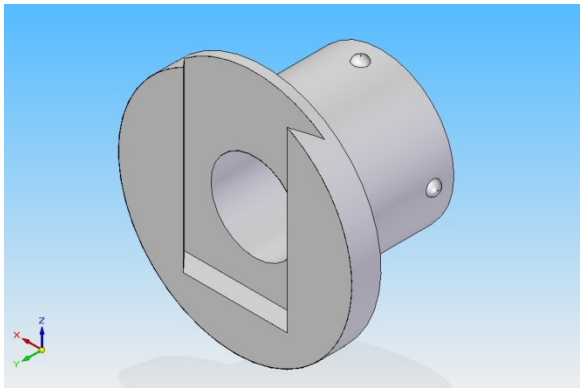

**Figure 4.7**- Protective insert for WU-BESL ports. The insert is placed in the port and a disposable glass slide placed in the socket. Evaporated sample is deposited on the slide which is periodically replaced.

### *4.2.4. Vacuum System*

The vacuum system was designed to be simple, clean (hydrocarbon-free), portable, vibration free, robust, and to be able to quickly achieve $10^{-7}$ Torr pressure. A high speed turbo-molecular pump is the natural choice for this application. A turbo-pump resembles a jet engine: it has several stages of rotors, each with multiple, angled blades that rotate at very high angular speeds. Since the pump is not influenced by gravity, it can be mounted in any orientation. When gas molecules strike the underside of the angled blades, momentum is transferred from the blade, and pushes the molecule to lower stages. Eventually, after several successive momentum transfers, the molecules are led to the exhaust port, usually a roughing pump or a smaller turbo. Because turbo-pumps must operate at very high speeds, thermal energy is generated due to friction, requiring active cooling. Magnetically levitated bearings have been used to reduce friction, maintenance requirements, and increase lifetime. A complete discussion of this and other vacuum systems can be found elsewhere [24].

For the WU-BESL an Osaka Vacuum USA, Inc. model TG420MCWB was chosen. The relevant properties for this pump are shown in Table 4.1. A standard scroll pump from Oerlikon Leybold Vacuum (Model SC15D) with a pumping speed recommended for this pump directly backs the turbo on the outlet side.

**Table 4.1-** Relevant specifications of the turbo-pump used in the WU-BESL design.

| **Model TG420MCWB** | |
|---|---|
| Inlet Flange | 8" CF |
| Outlet Flange | KF25 |
| Cooling System | Water (1.5 L/min, at 25C) |

| | | |
|---|---|---|
| Bearing System | | Active 5-axis control magnetic bearings |
| Volume Flow rate | N2 | 400L/s |
| | H2 | 300L/s |
| Maximum Compression Ratio | N2 | $10^8$ |
| | H2 | $5*10^3$ |
| Ultimate Pressure | | $8*10^{10}$ Torr |
| Maximum Backing Pressure | | 3 Torr |
| Recommended Backing Pump | | 160L/min |
| Permissible Bakeout Temperature at Inlet | | 120C |
| Vibration Peak | | .01 Micron |
| Permissible Ambient Temperature | | 10C-40C |
| Mass | | 17kg |

A pneumatically actuated gate valve (K.J. Lesker, model SG0600MVCF) is installed between the turbo-pump inlet and the chamber to allow fast isolation of the turbo-pump in the event of unintended vacuum breach. A simple pressure monitor is intended to trip the gate valve to quickly close (< 0.3 sec) protecting the vacuum system. At the time of the writing of this document, the gate valve is operated manually, without an automated isolation system.

### 4.3. Electrode Assembly

The electrode assembly contains the metal electrodes used to create the electric field for levitation and the insulating assembly used to house and align these electrodes. The basic premise is simple: three sets of orthogonal electrodes, one vertical set, and two lateral sets, have various potentials applied to them, creating an electrostatic field that is used to

levitate a charged sample. The field is modulated to keep the sample in a nominal position by adjusting the potentials according to a series of input signals, which will be discussed in detail in section 4.5. In order to keep line of sight on the sample, the lateral electrodes are placed below the sample level and the vertical control is then coupled to the lateral directions.

The WU-BESL electrode design was initially inspired by the DLR electrode design; it is shown in Figure 4.8.

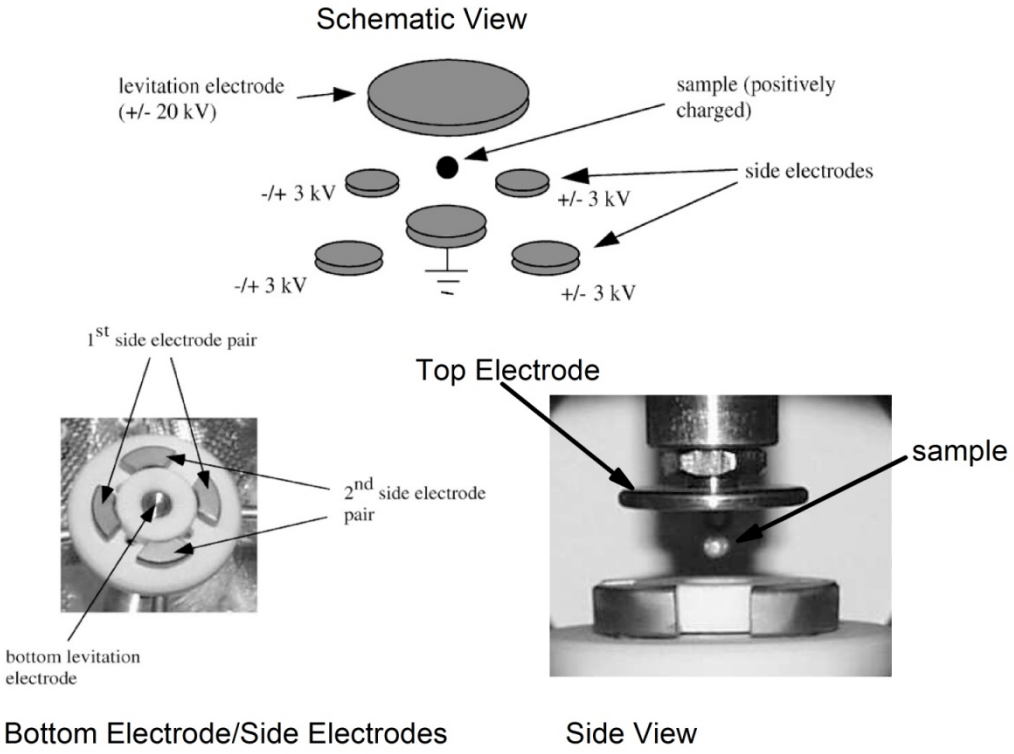


**Figure 4.8**- DLR electrode assembly, as of June 2008 taken from [22]. Note, in this incarnation, the top electrode and bottom electrode are flat, without holes.

Reproducing the DLR design facilitated an ease of implementation of the algorithm used to the control sample position. A few observations about the electrode assembly and the control algorithm are made below:

1. The algorithm updates at 500Hz and since most conventional machinable metals have conductivities between 0.1 and 0.6 $10^6$ Ohm/cm, the electrode material is not a critical factor in the design and should be tailored for the application in mind. Empirically, we find no difference in sample stability when using Cu, Al and Stainless Steel 304 or 316 as electrode materials. The WU-BESL is designed for 24 hour operation with sample processing at high temperature (~2500°C) for several hours continuously. The electrode material properties should be appropriate for this use.
2. In the course of an experiment, liquid samples are known to spontaneously destabilize and collide with the electrodes and thus these electrodes should be of sufficient mass, melting temperature, and thermal conductivity to survive these incidents.
3. Extended liquid processing produces deposition, as previously noted. This problem is compounded for the electrode assembly due to the close proximity to the sample. This has two main implications for the electrode assembly. First, the electrodes themselves are periodically sanded, and second, the assembly needs to resist the tendency to evaporate metallic connections between the electrodes. The high voltage (H.V.) amplifiers used to produce the strong electric fields have current trip points of a few micro Amperes and thus any short circuiting of the electrodes will cause the experiment to end prematurely.

4. Sample sizes usually range from 2 mm to 4 mm diameter, and the vertical electrode spacing is on the order of ~ 10 mm. In the region of the sample, the electrodes cannot create a 3-D electrostatic potential minimum (from Poisson's equation) and this places the sample in an unstable equilibrium during levitation. As such, any quickly varying fields with respect to position tend to increase instability. This means that all electrodes need to be devoid of sharp edges and corners where charge tends to accumulate and the field varies quickly.
5. The assembly should be made out of a machinable insulating material. MACOR (Morgan Advanced Ceramics) is a suitable source material. It is readily machinable, has a low residual out-gasing, is cheap, and withstands relatively high temperatures (~1000°C). It is, however, extremely brittle and easily abrades.

Over the course of the WU-BESL development, we have examined a variety of electrode configurations to aid levitation and implementation of a sample carousel and pre-processing post, not employed by the DLR. The initial design is shown in Figure 4.9.

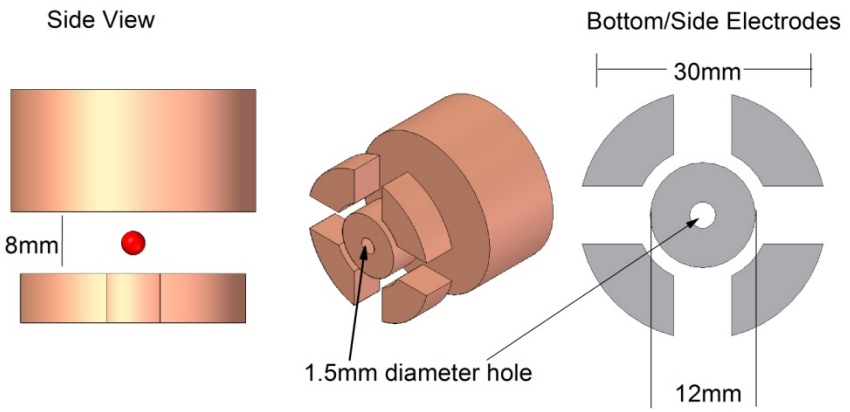


**Figure 4.9**- Initial electrode design for WU-BESL.

First, efficiently was greatly improved by including a sample carousel (discussed in section 4.4.) capable of holding up to 35 samples before breaking vacuum. This is a critical improvement in WU-BESL over the DLR design. The NASA ESL chamber used for previous BESL studies had a bottom loaded carousel. Space limitations didn't allow a bottom loaded carousel in WU-BESL and a gravity fed carousel was developed instead, which allowed sample changing through the top electrode. This requires that a 0.157" diameter hole (4mm) be bored through the top electrode, deviating from the DLR design (Figure 4.8). Initial trials showed that levitation with this electrode was extremely unstable. This was unexpected as a hole of similar size exists in the lower electrode. Simulations by J. C. Bendert [25] provided some insight into the nature of the instability and how to improve stability further. The details can be found elsewhere [26] but a Laplace solver was uses to simulate the electric field produced by various electrode

configurations without a sample present. A cylindrical symmetry was assumed for the simulation. The effect of the hole in the top and bottom electrodes on the radial profile of the potential is shown in Figure 4.10. The addition of a hole in the top makes the curvature of the potential more negative, thus causing the equilibrium to become even more unstable.

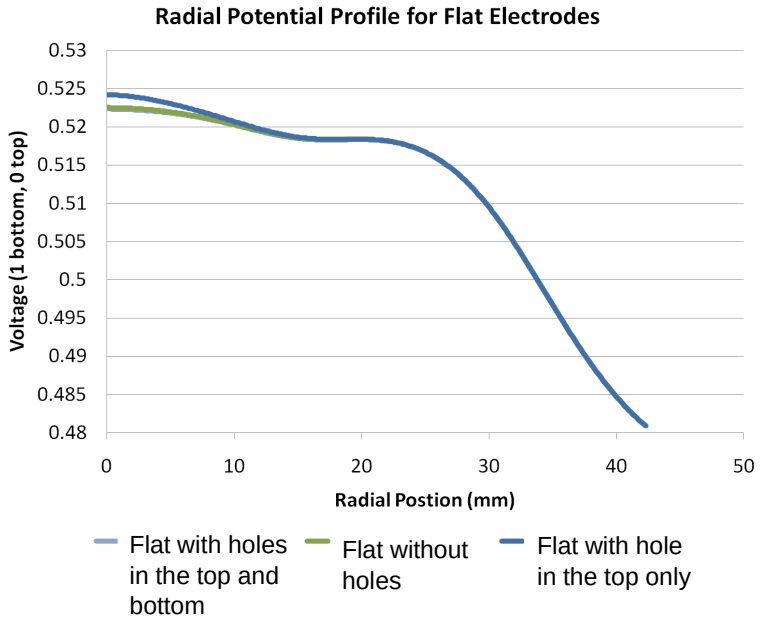


**Figure 4.10**- The radial profile of the potential for the electrode assembly having a flat top, exploring the effect of holes. As can be seen, the addition of a hole in the top increases the curvature of the potential, thus causing the equilibrium to become even more unstable. (Figure from [25].)

From simple physical arguments, one would expect that by curving the top and bottom electrodes, the curvature in the potential might be improved. Indeed, this is the case. By changing the top electrode as in Figure 4.11, where the curvature in the top

electrode is ~15mm, we can produce the calculated radial potential profile shown in Figure 4.12.

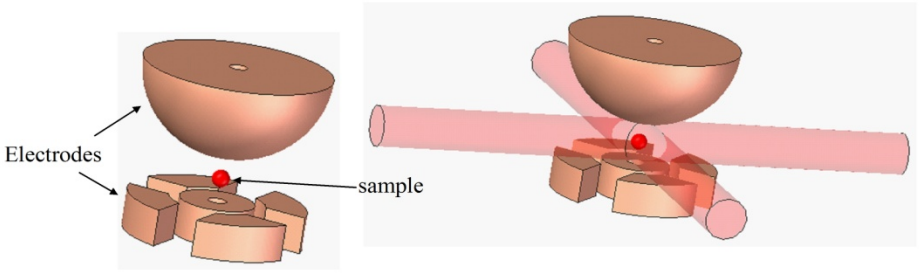


**Figure 4.11-** WU-BESL curved top electrode. The red cylinders represent the positioning lasers passing through the electrode assembly.

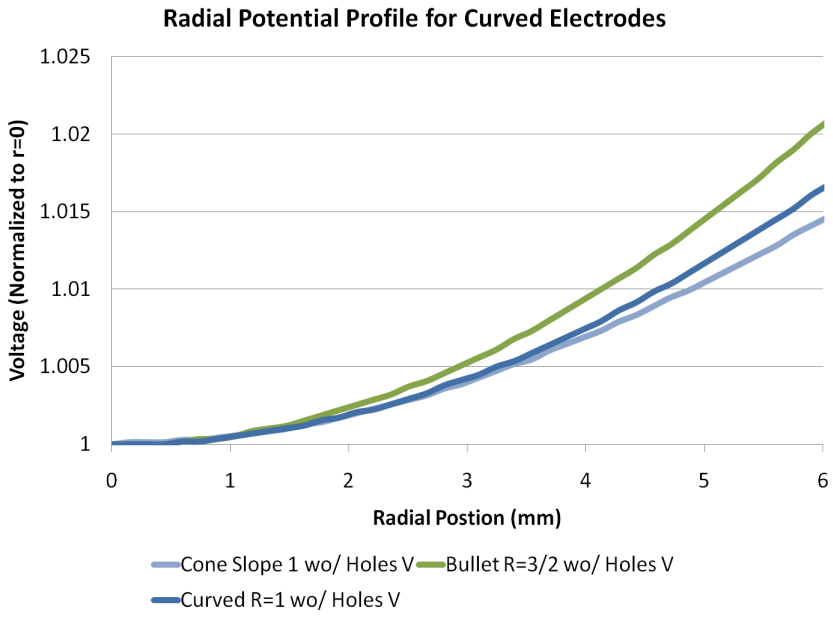


**Figure 4.12-** The radial profile of the potential for the electrode assembly having a curved top electrode. We can see that even with holes in the electrodes the curvature in the potential is still positive, thus we've created a stable equilibrium in the lateral directions. (Figure from [25].)

Even with holes in the electrodes the curvature in the potential remains positive, creating a stable equilibrium point in the lateral directions. Of course, this is only the potential due to the lateral fields. As shown in Figure 4.13, even with a flat electrode, the equilibrium is unstable in the vertical direction; curving the top electrode makes the potential more unstable. This has been shown to be an acceptable compromise, however, with stability in both directions around 50μm.

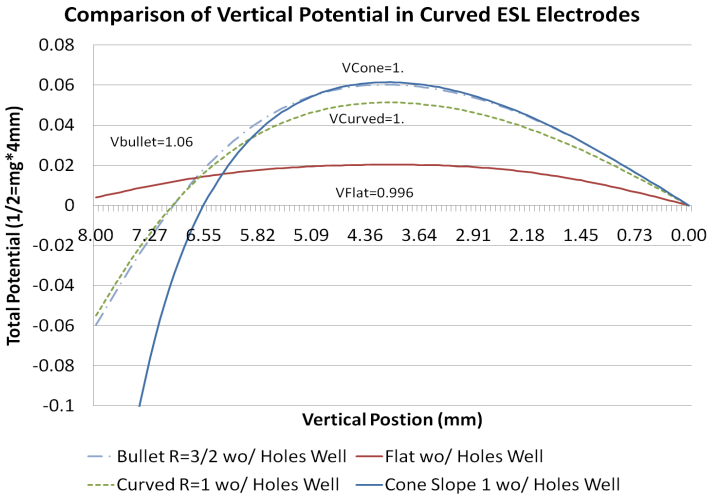


**Figure 4.13-** Potential profile along the vertical direction for flat and curved top electrodes. (Figure from [25].)

The electrodes are mounted in MACOR insulating mounting pieces (Figure 4.14). MACOR has a breakdown voltage that is greater than the required 5 kV/mm that is present in the assembly. The top electrode is mounted in an insulating block that is mounted to the top cover of the chamber (Figure 4.15) to allow ease of cleaning and electrode replacement in both assemblies. The bottom electrode assembly is mounted into a rotatable steel slab which is used to align the side electrodes with the chamber and positioning laser (more in section 4.5.4.). Detailed drawings including dimensions are presented in Appendix IV.3.

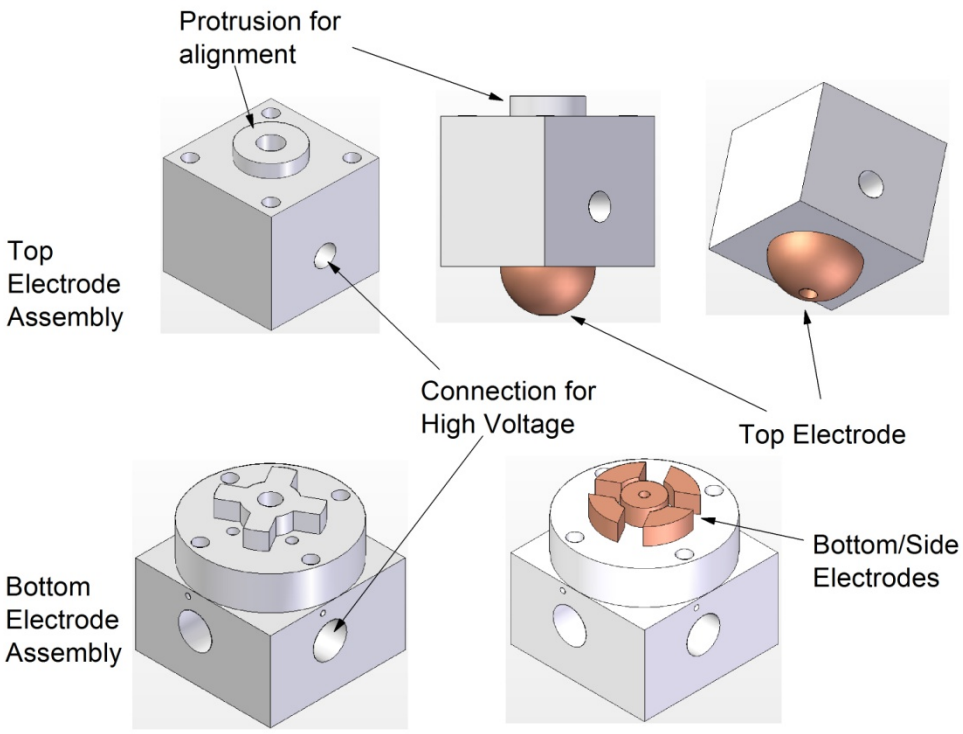


**Figure 4.14-** Electrode Assembly in WU-BESL.

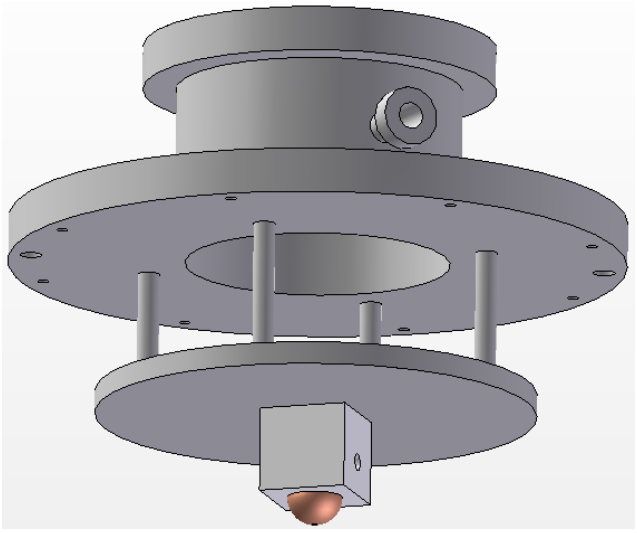

**Figure 4.15-** Top Electrode Assembly attached to the chamber lid. The Turbo Pump sits on the top of this flange.

Although the electrode assembly has worked adequately since installation, it is worth discussing a potential replacement for the bottom assembly that would circumvent a number of problems encountered. These are enumerated below:

1. Replacement of side electrodes is exceptionally difficult. They are secured from the bottom side of the assembly, and the bolts used to secure them can't be accessed without having to remove the entire assembly, thus eliminating the rotational alignment of the electrodes.
2. The current sample retrieval system is extremely flawed. A ramp is placed around the bottom electrode assembly, which funnels the samples into a container. However, the samples routinely get stuck in the ramp, aren't caught in the ramp at all, or find their way into the holes on the exterior of the assembly where the high voltages are connected.
3. The rotational alignment really isn't necessary. A fixed orientation in the chamber is preferred and will remove one degree of freedom.
4. The H.V. wiring in the chamber is disorganized and not rigid enough. The new design is simpler, easier to implement, and removes the problem entirely of samples finding their way into H.V. connections. (It should be noted that during the BESL2010 campaign, samples that found their way into the H.V. connection actually caused intermittent ground faults and probably cost eight hours of lost time and four sets of data.)

A proposed design is shown in Figure 4.16.

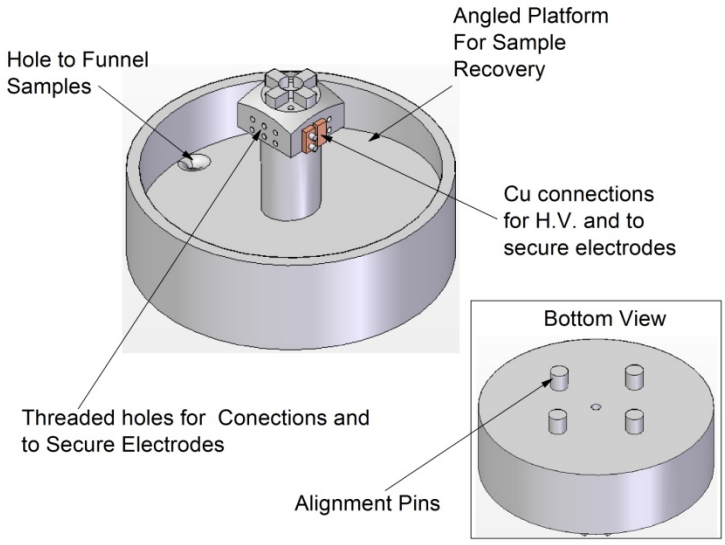


**Figure 4.16-** Proposed new bottom electrode assembly. The fixture has no rotational degrees of freedom, and samples are funneled on the angled ramp to a retrieval container.

## 4.4. Preprocessing Post/Sample Exchange

One of the most significant improvements of the WU-BESL over the DLR ESL is the incorporation of sample exchange and preprocessing mechanisms. WU-BESL is designed for fast installation into synchrotron X-ray beamline stations. Previously, one of the most time consuming aspects of the experiment has been sample exchange. The chamber design includes a large front port that, while convenient for sample access when not used for scattering studies, becomes inaccessible when the Beryllium (Be) scattering exit window is used. In this configuration, the loading of a sample requires bringing the chamber up to atmosphere, opening the top lid (or side port for vacuum tweezers insertion), loading the sample and pumping the chamber back down. This process can take up to 60 min when a $10^{-7}$ Torr vacuum is required. An *in-situ* sample changing mechanism is preferable.

When preparing samples for BESL study, typically a source ingot (~1g) is prepared and then smaller (~60mg) samples are produced by arc melting. Ideally, the sample would be put immediately into the ESL, minimizing contamination including rapid contamination like hydrocarbon and water vapor surface layers, longer term processes like oxidation, or contamination by repeated handling.. Surface contamination very likely leads to little contamination in the bulk, although there are limited reports of low level hydrocarbon contamination in processed ESL samples from previous experiments using energy dispersive X-ray spectroscopy (EDS) [27]. The more important difficulty associated with surface contamination occurs during the initial heat-up of the sample. Since the sample has an excess surface charge, any contamination that evaporates off the surface leads to a decrease in charge, resulting in a larger voltage necessary for levitation. More often, the sample becomes momentarily unstable during this process, which can lead to the loss of levitation.

The initial BESL experiments were conducted using the NASA ESL chamber [28, 29] which did have a preprocessing post. Annealing treatments were conducted prior to processing on a Zr post, at a range of temperatures, but always above 500°C and several hundred degrees below the melting point, to attempt to remove surface contamination. This approach was repeated in WU-BESL. When empirical studies were conducted on its effectiveness, very little difference in the behavior of any given sample upon heat-up was observed.

A series of experiments were conducted on 50mg ESL samples of pure (99.995%) nickel under different preprocessing conditions[6]: (1) no preprocessing, (2) annealing at

[6] This experiment was conducted in collaboration with A. K. Gangopadhyay.

2/3 $T_m$ (~900°C) for different periods of time, and (3) *in-situ* melting on the Mo preprocessing post. Pure nickel is a difficult system to work with; during the NASA studies, only a handful of successful processings occurred and these only after annealing treatments. The difficultly in these experiments occurred around 800°C when the charge of the sample decreases to a point where levitation isn't sustainable. Considering that the vaporization temperature of water and most common hydrocarbons [30] is well below 500°C (lowered further by the vacuum environment), the onset of stability is unlikely to be related to surface contaminants. It was thought that the instability might be due to the sudden release of gases (possibly oxygen free radicals) that are trapped in the grain boundaries of the sample. A pre-annealing of the samples at high temperature in vacuum prior to ESL processing could release these trapped gases due to a decreasing grain boundary area with grain coarsening. This idea was tested by annealing Ni samples in a sealed, evacuated, quartz tube in a furnace at 900°C for 24 hours. A comparison was made between the as arc melted samples and the annealed samples by powdering the samples and characterizing the crystalline structure using low energy, Cu $K_\alpha$ ($\lambda$ = 1.54Å), X-rays, as described in Chapter 2. The diffraction patterns are shown in Figure 4.17. The peaks have been indexed using Jade [31]. Differences in the two samples correspond to the coarsening of the FCC polycrystalline phase, although to within error, the Scherrer formula [32] gives the same coherence length, indicating minimum grain coarsening. The study was therefore inconclusive. The annealing treatments proved to be ineffective in aiding the initial heating, but little coarsening was observed, as determined by the X-ray studies.

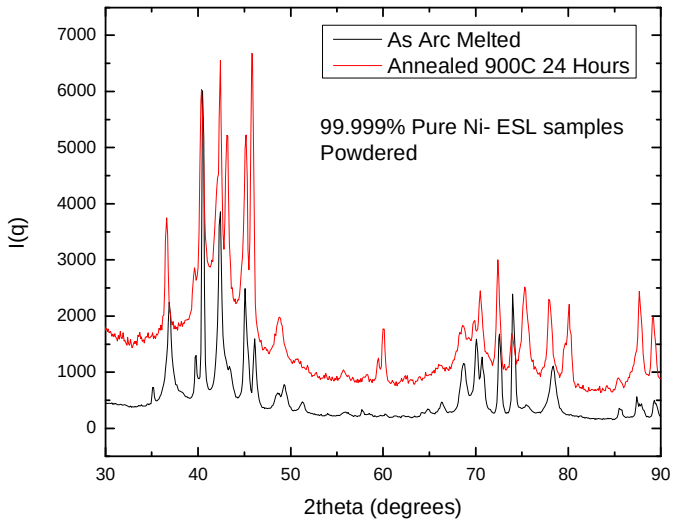


**Figure 4.17-** Diffraction patterns for as arc-melted (black) and annealed (red) pure Ni ESL samples. The differences in the two plots correspond to coarsening in the bulk.

Much better success was obtained when the sample was melted on a Mo preprocessing post, which cause significantly greater out-gasing. Pure Ni became consistently processible with a partial *in-situ* melting. In fact, most samples become easier to process once partially melted on this post. This technique, more than any other, seems to have improved the processability of many alloy families. The BESL2010 campaign included the processing of CoPd, $Si_{50}Ge_{50}$, Al, HfPt, and Fe-, Au-, La-, and Nd- based bulk formers for the first time.

The preprocessing post is presented schematically in Figure 4.18. The assembly is located below the electrode assembly with a stepper motor used to transmit rotational motion through a high vacuum feed-through to a high vacuum gearbox that lifts the post vertically. All components are greaseless, but since rotational speeds don't usually exceed 1 rev/sec, no lubrication is required.

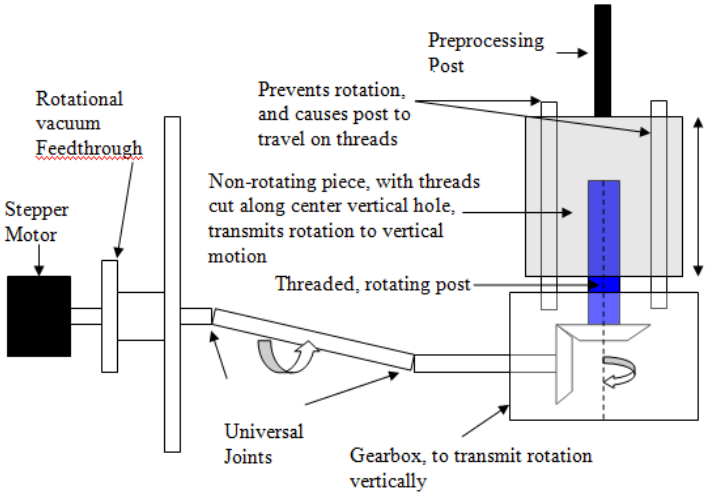


**Figure 4.18-** Schematic view of the preprocessing post. This assembly is located below the electrode assembly; a stepper motor used to transmit rotational motion through a high vacuum feed-through to a high vacuum gearbox that lifts the post vertically.

The post assembly mounted in the bottom of the chamber without any electrode assembly is shown in Appendix VI.4.

The carousel mechanism, like the preprocessing post, uses a rotational feed-through to transmit rotation from a stepper motor to index a 35 sample carousel. The carousel mechanism was machined without any oil to avoid contamination and the hole sizes were chosen to allow for up to 4mm spheres to pass through to the electrode assembly. The mechanism is shown in Figure 4.19. The brass disk, indexed with samples, rotates on top of a fixed plate containing a hole that funnels samples down to the electrode assembly. A worm gear mechanism transmits the rotational motion vertically to the brass holder. Again, no lubricants were used in any of the motion mechanisms.

The carousel is used in tandem with the preprocessing post to deliver samples to the electrode assembly. First the post is raised through the entire assembly until it is recessed up into the hole in the top electrode. The carousel is then rotated until a sample falls through the funnel onto the post, which is concave to hold the sample. The post and sample are then lowered to the processing position. The carousel assembly installed in the chamber is shown in Appendix IV.4, as are potential improvements to the assembly.

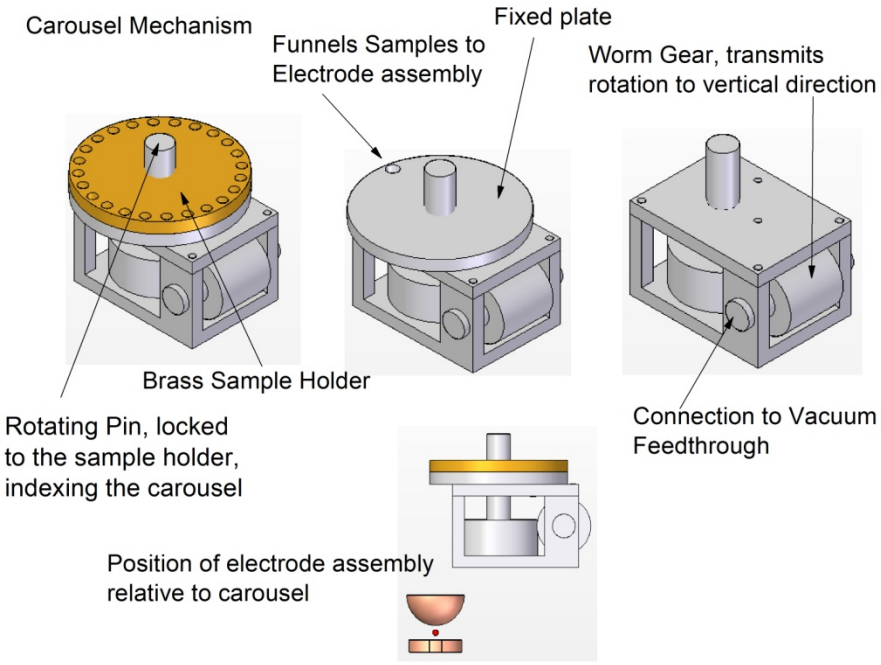


**Figure 4.19-** Carousel mechanism in multiple perspectives. The brass disk, indexed to the samples, rotates on top of a fixed plate with a hole that funnels samples down to the electrode assembly. A worm gear mechanism transmits the rotational motion vertically to the brass holder.

## 4.5. Sample Levitation

### *4.5.1. General Considerations*

Beamline experiments can be conducted by two people, and the entire process of beamline integration has been carried out by four people. This is due in large part to the development of the levitation algorithm by Meister *et al.* [22]. The ESL technique was pioneered by W. K. Rhim *et al*. [20]. The levitation technique uses light sources directed in the horizontal plane, orthogonal to one another, to project the shadow of a sample onto two (also orthogonal) detectors. A schematic of the projection of the sample is shown in Figure 4.20b. A computer algorithm takes as input a generalized error function, which is a measure of the deviation from some nominal sample position, and outputs signals to produce an electric field that returns the sample (with an applied net surface charge) to that position. Fundamental to the operation of the ESL are the following:

1. The electric field produced must have components in three directions. This (somewhat trivial) observation has important complications. Since the projection of the sample is used as the input, the lateral electrodes are generally placed below the plane of the sample (Figure 4.20a). This couples the lateral and vertical electric fields and complicates any control algorithm. A choice must be made here: the electrodes could, in fact be placed at the sample level, as shown in Figure 4.20c, but if the electrodes are too large, the entire sample is obscured and there is no error signal for the control algorithm. However, making the electrodes smaller tends to produce larger gradients in the field, leading to instability in the sample position. It tends to be simpler to adjust the algorithm to account for the coupling in the directions. This approach has the additional advantage of allowing complete line of sight on the sample.

2. In ESL, the electric fields used for levitation are DC, modulated at the systems sampling rate. To estimate the necessary algorithm sampling rate, assuming that the sample is in free fall from its equilibrium, and ignoring the effect of the stabilizing field, the sample falls a distance $\Delta x = \frac{g}{2}(\Delta t)^2$, where $\Delta t$ is the maximum necessary sampling time. A typical stability requirement is estimated as $\Delta x = 10\,\mu m$ for a 2 mm diameter sample, giving a $\Delta t$ of ~ 1 ms.
3. A surface charge is required for force balance. For ~ 50 mg samples, with typical densities of ~8 mg/mm$^3$, applying 10 kV fields using high slew rate high, voltage amplifiers, approximately 1 nC of net charge is required. This can be supplied in different ways, but two of the most common are photoelectric ionization from a UV source and capacitive charging on a pedestal.
4. Because the electric field satisfies Laplace's Equation in the region between the electrodes, a three dimensional potential minimum can't be established. However, by judicious use of electrode design, we can produce a potential minimum in the two lateral directions.

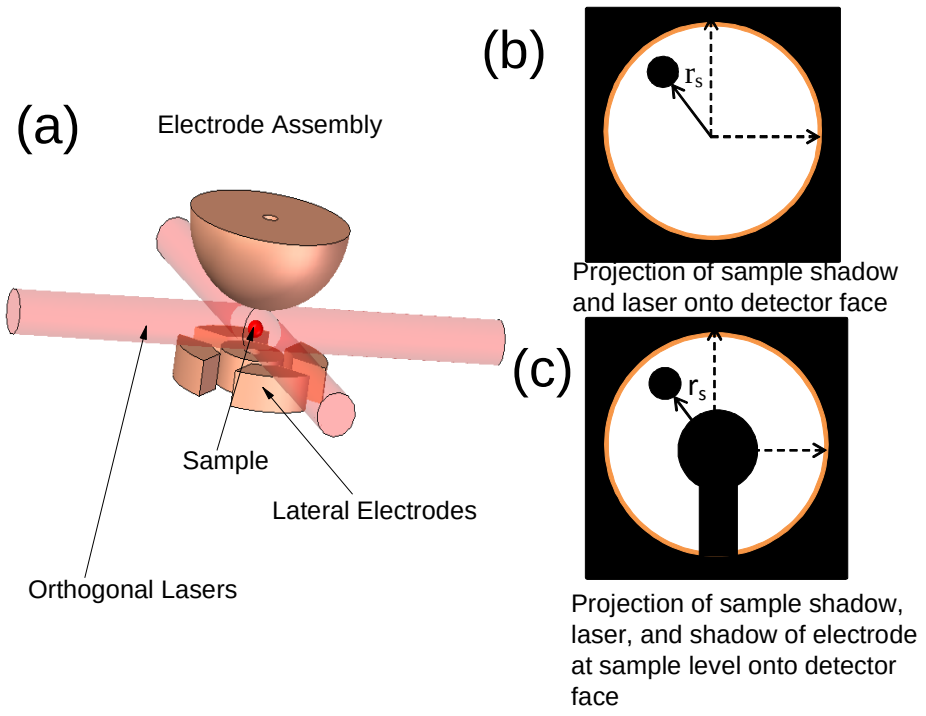


**Figure 4.20-** (a) Electrode assembly, with orthogonal lasers and projection of (b) sample and (c) possible sample level electrode.

### *4.5.2. Levitation Control Algorithm*

The WU-BESL requires extreme autonomy and ease of operation. Previous beamline experiments using the NASA ESL [28, 29] required three people just for the operation of the instrument, and another for the structural studies. In collaboration with the German Aerospace Institute (DLR), we modified a previously developed algorithm designed by T. Meister [22] for use with Microsoft® Windows XP, and implemented using Matlab® *Simulink* and xPC *Target Explorer*. The details of the algorithm can be found elsewhere but a basic understanding of the control algorithm is necessary, and presented in this section.

Positioning of the sample is a force balance problem. Taking the vertical direction as the prototypical problem to be solved, the unstable equilibrium must be maintained by varying the potential on the electrode. This is made difficult because the sample charge is time varying. In this model, a non-linear Kalman filter is used to estimate the sample charge. This type of a filter essentially uses the positional measurement and a physical model to predict sample charge. In practice, the filter is only applied in the *z*-direction, where fluctuations tend to be the greatest. This estimation is passed as the variable in the "gain-scheduling" in the non-linear gain-scheduling control algorithm.

The non-linear control is based on a force balance equation, extended beyond a point charge approximation to first order using the method of images. Given this, the force required for a sample of mass *m*, charge $q_s$, voltage $U_z$, and electrode spacing *d*, positioned at $0 \le z \le d$ is

$$F = -q_s \frac{U_z}{d} + \frac{q_s^2}{16\pi\varepsilon_0}\left(\frac{1}{(d-z)^2} - \frac{1}{z^2}\right). \qquad (2)$$

This approximation assumes flat electrode spacing and a gap spacing much smaller than the size of the electrodes. This isn't strictly speaking justified since the top electrode is only ~10 times larger than the sample diameter. However, empirical studies have shown that stable levitation is still achieved under this assumption. The coupling between the lateral and vertical fields is also ignored.

The lateral fields are not easy to determine: They are not homogeneous in this system as the parallel plate capacitor approximation is not relevant. However, assuming point side electrodes, positioned in the centroid of a given electrode, the force due to one of those electrodes is

$$F = \cos\left(\arctan\left(\frac{z}{x_d/2}\right)\right)\frac{q_s 2U_x}{x_d}\ , \tag{3}$$

where $U_x$ is the voltage and $x_d$ is the lateral distance from the center of the sample. This approximation is made more relevant by designing the electrodes to remove large gradients in the lateral field. The electrodes are not point sources, but instead wrap around approximately $\pi/4$ radians, and have chamfered surfaces, as shown in Figure 4.14.

The algorithm uses multiple inputs, the *x*, *y*, and *z* positions, the applied voltages ($u_x$, $u_y$, $u_z$), and generates multiple outputs (the multiple input/multiple output (MIMO) model) at the discretized sampling time intervals to model the levitation process. The algorithm then generates a parameter that is directly proportional to the estimated charge to interpolate the local linear control parameters in the model. The Linear Matrix Inequality (LMI) toolbox in Matlab is used to design both state feedback gains and integrator gains. The integrator gains are steady state constraints on the position. They act as long time integrators to control absolute drift. In the discrete time approach, the eigensolutions to the LMI problem lie inside an ellipsoid in parameter space characterized by three coordinates, *q*, $r_1$, and *r*2. These are essentially heuristic tuning parameters; as the abscissa, *q*, is moved closer to the origin, the correction of the sample tends to be too great, and overshoot of the sample nominal position is observed. For a value of *q* that is too large the setting time is too long. A similar behavior is observed for $r_1$. The value of $r_2$ is directly related to the overshot, and the inverse of this parameter is essentially a damping term [22]. The LMI parameters are different for the two directions related to the steepness of the potential maximum. For most systems, experience has

shown that values ($q$, $r_1$, $r_2$) of (.67, .30, .10) and (.67, .30, .01) are appropriate in the horizontal and vertical directions, respectively.

Meister *et al.* [22] compares this algorithm to a fixed gain approach and finds that it achieves significantly faster charge-variable induced instability reduction than traditional counterparts. However, even if this isn't the case, the ease of implementation and use is of extreme benefit for this application. One drawback is that control parameters can't be changed mid-experiment. The user can adjust the sample position, but this is the practical limit of user control. This is not detrimental to the experiment, since ~90% of all samples are well controlled with the parameters just described for (*q, r1, r2).*

### *4.5.3. Positioning Optics and Signal Conversion into Position*

In this version of ESL, the position of the sample is determined by using a set of orthogonal lasers, with the beams expanded to fill the space between the electrodes, casting the shadow of the sample on two Position Sensitive Detectors (PSDs). A PSD consists of an n-type silicon substrate with two resistive layers (top and bottom) separated by a p-n junction. The front side has an ion implanted p-type resistive layer with two contacts at opposite ends. The back side has an ion implanted n-type resistive layer with two contacts at opposite ends placed orthogonally to the contacts on the front side. A point of light of the appropriate frequency will generate a photocurrent that flows from the incident point through the resistive layers to the electrodes. The resistivity of the ion implanted layer is extremely uniform so the photo-generated current at each electrode is inversely proportional to the distance between the incident spot of light and electrodes. This linearity extends to 80% of the detector face. So for the 10mm by 10mm model

(PSM 2-10) used in WU-BESL, the PSD is linear for 8mm by 8mm. The typical resolution for standard laser wavelengths is 500nm on the face. Empirical response curves for some typical materials are shown in Figure 4.21.

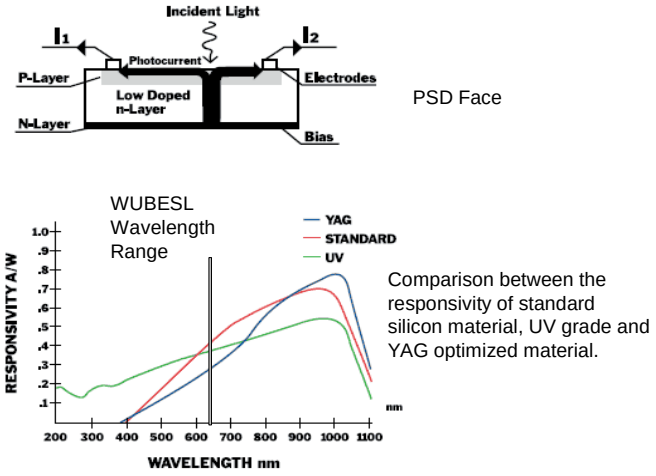


**Figure 4.21-** The response distribution for typical PSD materials. The wavelength of the WU-BESL positioning lasers is in the range 623nm- 660nm. (Figure reproduced from [33].)

For light from a point source that is incident on the PSD face (consider a face with a horizontal axis, *x*, and a vertical axis, *y*) the position is determined from Equation 4:

$$x_{pos} = \frac{x_1 - x_2}{x_1 + x_2}\left(\frac{L}{2}\right) \qquad y_{pos} = \frac{y_1 - y_2}{y_1 + y_2}\left(\frac{L}{2}\right) \tag{4}$$

where $x_1$ and $x_2$ are the photocurrents in the negative and positive *x* directions, respectively, and $y_1$ and $y_2$ are the photocurrents in the negative and positive *y* directions, respectively. For an extended light source, the centroid position is mapped to the output.

The PSD output is interpreted by the levitation algorithm described in the previous sections.

If $S(x,y)$ is the photon intensity distribution at any time, the total intensity is given by

$$I_{Tot} = \int_{-L/2}^{L/2}\int_{-L/2}^{L/2} S(x,y)dxdy\,. \tag{5}$$

Generally speaking, $S(x,y)$ need not be constant and uniform, and most lasers have an approximately Gaussian profile for the 00 harmonic. For an ESL experiment, the intensity distribution, $S(x,y)$, is far from uniform; this deviation from uniformity is how the sample position is determined.

The current vector, **I**, defined as

$$\mathbf{I} \equiv I_x\hat{x} + I_y\hat{y}\,, \tag{6}$$

provides the information about the sample position. It is related to the intensity distribution on the PSD face by Equation 7.

$$\mathbf{I} = \frac{2}{L}\int_{-L/2}^{L/2}\int_{-L/2}^{L/2} S(x,y)\mathbf{r}dxdy\,. \tag{7}$$

As shown schematically in Figure 20, the intensity distribution is a superposition of the expanded laser profile centered at the origin and having radius $r_l$, and the shadow of the sample with radius $r_s$, located at a position ***r***. The laser is expanded to smooth out the distribution and make $S(x,y)$ more uniform. The laser has a Gaussian intensity distribution

$$I(r)/I_0 = e^{\frac{-2r^2}{\sigma^2}}\,, \tag{8}$$

where $I_0$ is the intensity of the peak, $r$ is a radial distance and $\sigma$ is the distance at which the intensity drops to $1/e^2 * I_0$, or $1 / (2.72)^2 I_0 = .135 I_0$. For the Newport Model R-30995 17.0 red HeNe lasers used in the WU-BESL, $\sigma = 0.49$ mm.

The Gaussian-distributed laser intensity falls off at large $r$, causing a decreasing contrast between that intensity and the sample shadow on the PSD as the sample moves from the center of the beam. The algorithm interprets this as indicating that the sample is closer to the center than it actually is, causing stability to suffer. Expanding the laser creates a more uniform intensity distribution, counteracting this problem. At 16 times expansion, the ratio of $I(r)/I_0$ is 0.95, 0.93, 0.88, and 0.60 at $r$ = 1.25mm (outer edge of most samples), 1.50mm, 2.0mm, and 4mm (outer edge of beam), respectively. At 20 times expansion, the ratio of $I(r)/I_0$ is 0.97, 0.95, 0.92, and 0.72 at $r$ = 1.25mm, 1.50mm, 2.0mm, and 4mm. Both of these expansions produce stable levitation and 20 times beam expanders were chosen because they were readily available (Melles Griot, Model 09 LBX 005).

With an approximately uniform distribution of laser intensity, $S(x, y) = S_0$, an analytical form for the output voltage can be derived and implemented in the control program. Since the shadow of the sample corresponds to zero intensity on the PSD, the distribution of light is the sum of the uniform beam plus a negative contribution from the sample. A series of amplifiers converts the current signal into a voltage that varies from 0V to ±10V; $\kappa$ is the proportionality constant that relates the two. The vector voltage, (referring to a two dimensional array containing PSD voltage outputs in the $x$ and $y$ directions) is the signal input into the control program, **v',** and is then,

$$\mathbf{v}' = \frac{2\kappa}{L}\int_{y=y_l-r_l}^{y=y_l+r_l}\int_{x=x_l-r_l}^{x=x_l+r_l} S_o \mathbf{r}_l \, dxdy - \frac{2\kappa}{L}\int_{y=y_s-r_s}^{y=y_s+r_s}\int_{x=x_s-r_s}^{x=x_s+r_s} S_o \mathbf{r}_s \, dxdy \ , \tag{9}$$

where the subscript *l* refers to the laser and the subscript *s* refers to the sample. The limits on the integrals are the Cartesian coordinates for the circular intensity distributions. Equation 9 accounts for the possibility of a laser located away from the origin and the sample (radius *l*) located anywhere within the laser beam. For either integral in the expression of the form

$$\mathbf{v}' = \frac{2\kappa}{L}\int_{y=y_l-r_l}^{y=y_l+r_l}\int_{x=x_l-r_l}^{x=x_l+r_l} S_o \mathbf{r}_l \, dxdy \, , \tag{10}$$

the position of the center spot, $\mathbf{r_l}$, can be expanded in Cartesian coordinates to give

$$\begin{aligned} \mathbf{v}' &= \frac{2\kappa}{L}\int_{y=y_l-r_l}^{y=y_l+r_l}\int_{x=x_l-r_l}^{x=x_l+r_l} S_o (x\mathbf{x} + y\mathbf{y}) dxdy \\ &= \frac{2\kappa}{L}\int_{y=y_l-r_l}^{y=y_l+r_l}\int_{x=x_l-r_l}^{x=x_l+r_l} S_o x\mathbf{x} dxdy + \frac{2\kappa}{L}\int_{y=y_l-r_l}^{y=y_l+r_l}\int_{x=x_l-r_l}^{x=x_l+r_l} S_o y\mathbf{y} dxdy \\ &= S_o \frac{2\kappa}{L}\int_{y=y_l-r_l}^{y=y_l+r_l} dy \int_{x=x_l-r_l}^{x=x_l+r_l} x\mathbf{x} dx + S_o \frac{2\kappa}{L}\int_{x=x_l-r_l}^{x=x_l+r_l} dx \int_{y=y_l-r_l}^{y=y_l+r_l} y\mathbf{y} dy \end{aligned} \ . \tag{11}$$

Equation 11 simplifies easily to

$$\begin{aligned} \mathbf{v}' &= S_o \frac{2\kappa}{L}\left(4r_l^2 (x_l\mathbf{x} + y_l\mathbf{y})\right) \\ &= S_o \frac{2\kappa}{L}\left(4r_l^2 (\mathbf{r}_l)\right) \end{aligned} \ . \tag{12}$$

Evaluating the original integral in Equation 9, including the sample term, and normalizing for the total intensity,

$$S = \int S(x,y) dA = \pi S_0 \left(r_l^2 - r_s^2\right) \tag{13}$$

the vector current signal is given by

$$\mathbf{v}' = \frac{8\kappa}{\pi L}\frac{r_l^2\mathbf{r}_l - r_s^2\mathbf{r}_s}{r_l^2 - r_s^2}. \tag{14}$$

For a laser centered at the origin,

$$\mathbf{v}' = \frac{8\kappa}{\pi L}\frac{-r_s^2\mathbf{r}_s}{r_l^2 - r_s^2} = \frac{8\kappa}{\pi L}\frac{-\frac{r_s^2}{r_l^2}\mathbf{r}_s}{1-\frac{r_s^2}{r_l^2}}. \tag{15}$$

Despite the loss of the 2-D information, we see that for a judicious choice of laser profile, the sample position can be extracted. The photocurrent is converted to a voltage signal by the post-processing boards (On-Trak Photonics Model OT-301DL - Position Sensing Amplifier For Duolateral PSDs). Combing the constants in Equation 15 into one empirically determined constant, $1/\kappa_c$, the vector voltage, $\boldsymbol{v}'$, can be written

$$\mathbf{v}' = \frac{1}{\kappa_c}\frac{-\frac{r_s^2}{r_l^2}\mathbf{r}_s}{1-\frac{r_s^2}{r_l^2}}, \tag{16}$$

or

$$\mathbf{r}_s = \kappa_c\left(\frac{r_l^2}{r_s^2} - 1\right)\mathbf{v}'. \tag{17}$$

The proportionality constant, was empirically determined for the WU-BESL as 4.467e-4 mm/V for each face direction on the PSD.

A schematic illustration of the optics and optomechanics needed to implement the levitation algorithm discussed is shown in Figure 4.22. A more detailed description is presented in Appendix IV.5, where part numbers for a possible positioning optics system

are listed.[7] He/Ne (17mW) lasers are chosen for their output stability (<.3% fluctuation over 8 hours after a 30min heat up), however they must be mounted vertically in order to fit easily into the Sector 6-ID-D beamline station. The beam is expanded and then masked to have an 8 mm diameter before entering the chamber. In order to prevent interference with other light sources inside the chamber, a polarizer is placed in front of the PSD, oriented to coincide with the polarization orientation of the laser. A narrow band pass filter is used for the laser wavelength.

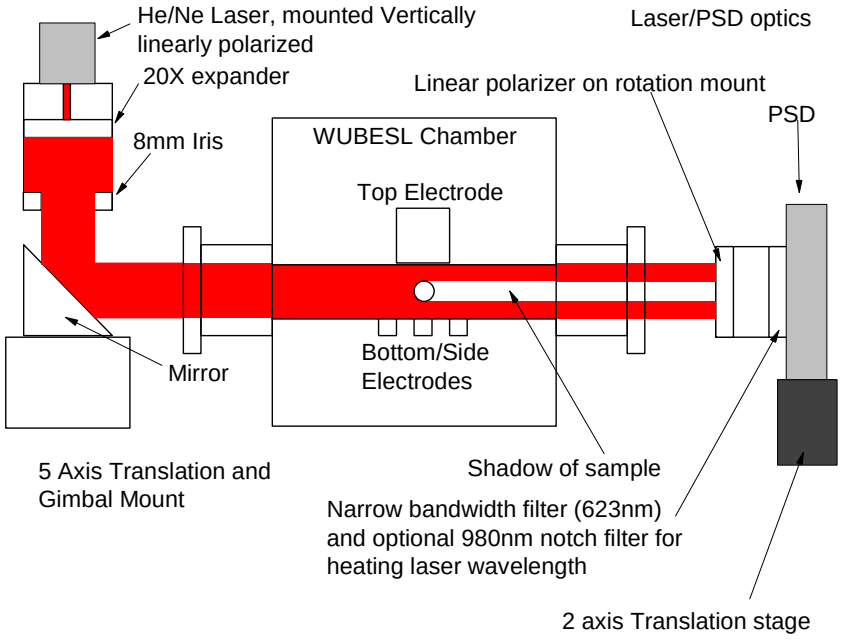


**Figure 4.22-** Schematic diagram showing the positioning optics and optomechanics.

[7] These optics are for an alternative version of the ESL which uses fiber-coupled diode lasers with wavelength 640nm, which are not mounted vertically.

### *4.5.4. Implementation of Algorithm for Sample Positioning*

As described, the control algorithm adjusts the voltages of the high-voltage amplifiers (Vertical-Trek, model 20/20C, Lateral-Matsusada Precision Inc., model AMS-31310) based on the signals from the PSDs. The schematic block diagram for signal routing is shown in Figure 4.23. After amplification, the PSD signals are routed through unity gain Op-Amp buffers and isolation circuits, after which they are split to digital displays on a rack mounted unit and to 12-bit analog to digital (ADC) channels of a PCI card (Measurement Computing Corporation, model PCI-DAS1200/JR) located in the Target PC computer[8] (see Figure 24). A differential mode is used in which the PSD amplifier signal is measured relative to local PSD ground. The digital output is used by an executable program prepared by *Simulink* and *Xpc Targe*t, running on the Target PC to generate a signal, output by a 12-bit digital to analog converter (DAC) PCI card (Measurement Computing Corporation, model PCI-DDA08/12) that is also located in the Target computer, to control the high-voltage amplifiers. The details of the signal routing are described in more detail in Appendix IV.5.

[8] The "Target" PC refers to a dedicated PC that houses the PCI DAC and ADC cards and runs the executable files created by *Simulink* and *Xpc Target*. The Target PC is booted with a floppy disk and the entire memory is dedicated to the task of running the control program.

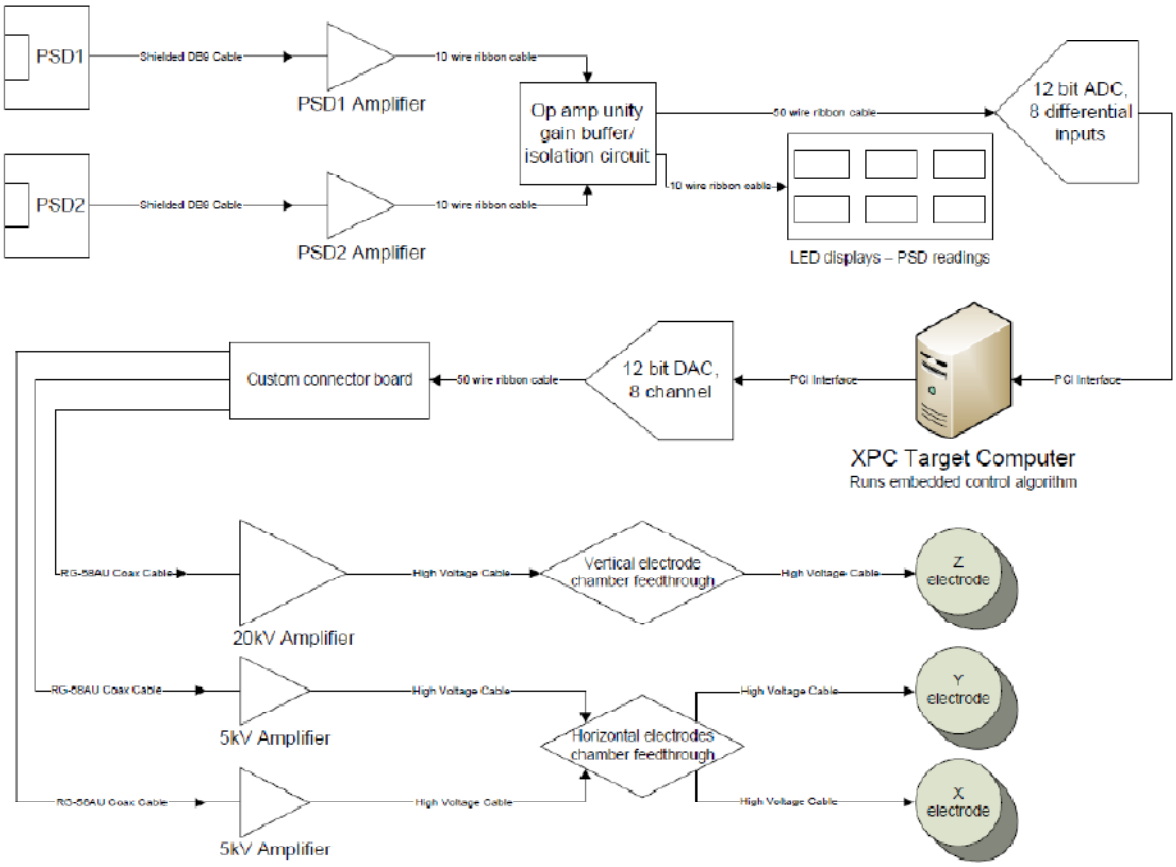


**Figure 4.23-** Schematic block diagram of the positioning system hardware, showing the interconnections between the main components. (Figure reproduced from [34].)

### *4.5.5. Stability Trials*

The positional stability of samples in WU-BESL was determined from density video data, tracking the sample during a typical processing cycle of an isothermal hold at a temperature above the liquidus temperature, followed by a free cool through recalescence. The stability is ~ ± 30μm in the vertical direction and ~ ± 20μm in the lateral directions (Figure 4.24).

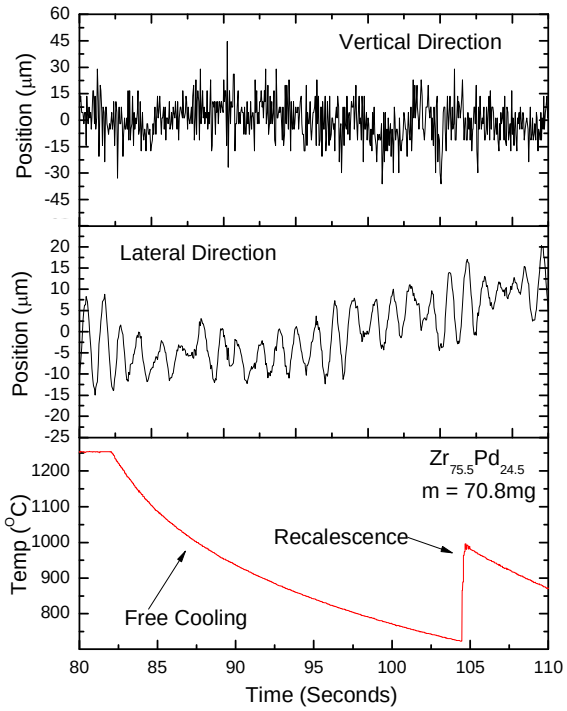


**Figure 4.24-** Position in the vertical (*Z*) and a lateral direction during a typical thermal processing cycle in the WU-BESL. The stability is ~ ± 30 μm in the vertical direction and ~ ± 20 μm in the lateral directions.

## 4.6. Ultraviolet Lamp (UV) Assembly

### *4.6.1. Current Implementation*

Utilizing the photoelectric effect, a Hamamatsu model L1835 200W deuterium lamp is used in the WU-BESL to constantly maintain the sample surface charge by ionizing the surface layers of the sample and ejecting electrons, thereby creating a net positive surface charge. The photoelectric effect depends on the effective work function for the surface, which is the energy barrier for electron ejection. Deuterium ionization produces strong radiation at 121nm and 160nm [31] so a high vacuum (~$10^{-7}$ Torr) is not only necessary for processing, but is also required to prevent the UV lamp from ionizing the atmosphere

in the chamber, which will reduce the radiation intensity on the sample. These wavelengths produce photons of energy 10eV and 7.75eV, respectively, which based on measured and estimated work functions of pure elements (Table 4.2) should be energetic enough to ionize the surface; sample recharge rate should then simply be a matter of maintaining a high UV intensity on the sample. .

**Table 4.2-** Estimated Work Functions for Selected Metals.*

| Element | eV | Element | eV | Element | eV | Element | eV | Element | eV |
|---|---|---|---|---|---|---|---|---|---|
| **Ag:** | 4.52-4.74 | **Al:** | 4.06-4.26 | **As:** | 3.75 | **Au:** | 5.1-5.47 | **B:** | 4.45 |
| **Ba:** | 2.52-2.7 | **Be:** | 4.98 | **Bi:** | 4.34 | **C:** | 5 | **Ca:** | 2.87 |
| **Cd:** | 4.08 | **Ce:** | 2.9 | **Co:** | 5 | **Cr:** | 4.5 | **Cs:** | 2.14 |
| **Cu:** | 4.53-5.10 | **Eu:** | 2.5 | **Fe:** | 4.67-4.81 | **Ga:** | 4.32 | **Gd:** | 2.9 |
| **Hf:** | 3.9 | **Hg:** | 4.475 | **In:** | 4.09 | **Ir:** | 5.00-5.67 | **K:** | 2.29 |
| **La:** | 4 | **Li:** | 2.93 | **Lu:** | 3.3 | **Mg:** | 3.66 | **Mn:** | 4.1 |
| **Mo:** | 4.36-4.95 | **Na:** | 2.36 | **Nb:** | 3.95-4.87 | **Nd:** | 3.2 | **Ni:** | 5.04-5.35 |
| **Os:** | 5.93 | **Pb:** | 4.25 | **Pd:** | 5.22-5.6 | **Pt:** | 5.12-5.93 | **Rb:** | 2.261 |
| **Re:** | 4.72 | **Rh:** | 4.98 | **Ru:** | 4.71 | **Sb:** | 4.55-4.7 | **Sc:** | 3.5 |
| **Se:** | 5.9 | **Si:** | 4.60-4.85 | **Sm:** | 2.7 | **Sn:** | 4.42 | **Sr:** | 2.59 |
| **Ta:** | 4.00-4.80 | **Tb:** | 3 | **Te:** | 4.95 | **Th:** | 3.4 | **Ti:** | 4.33 |
| **Tl:** | 3.84 | **U:** | 3.63-3.90 | **V:** | 4.3 | **W:** | 4.32-5.22 | **Y:** | 3.1 |
| **Yb:** | 2.6 | **Zn:** | 3.63-4.9 | **Zr:** | 4.05 | | | | |

***** Where there is a range quoted, a crystal orientational dependence on the work function is observed [35].

There are complications, though, in predicting the effectiveness of an ionization source against the loss of surface charge in ESL. In has been shown that metal-oxide formation can shift the work function of a surface either up or down depending on the binding site [36, 37], but that shift is rather small, on the order of a few *e*V, which would still put the work function in the range of the deuterium lamp for the materials listed above. Additionally, there doesn't appear to be evidence for a large change in the work function upon the formation of intermetallics [38]. Pure Zr, Ti, Hf, V and Y show a

range in their abilities to be successfully processed, with Zr showing a high success rate, Y showing a very low success rate. The other metals have lie in between these extremes. However, all of these elements have very similar work functions, oxygen solubility and oxide formation tendencies [35, 39, 40].

Previous versions of the ESL [22, 28, 29, 41] have used a deuterium lamp as the ionization source, but the details of the focusing optics are not always clearly stated. The wavelengths emitted are referred to as the *Vacuum Ultra Violet* (VUV) wavelengths and very few materials are effective focusing materials. $CaF_2$ and $MgF_2$ are two materials that have little attenuation compared to other materials, however, for the wavelengths of interest, the transmission is still only 40%—80% over the range indicated [42]. The DLR utilized a mirror optics assembly with aluminum-coated silicon as the reflecting surface; this provides a near maximum photon flux on the sample and aberration effects are minimized. However, because VUV radiation readily ionizes oxygen and water vapor to create ozone, which degrades the aluminum coatings, a high vacuum is required for the UV optics mounting assembly. This design was realized by constructing a separate vacuum chamber with a $MgF_2$ window between the UV optics and the ESL main chamber [43]. Given the relatively poor transmission of the window material and the high cost and complexity for the production of this design, a simpler focusing optics was employed in the WU-BESL (shown in Figure 4.25).

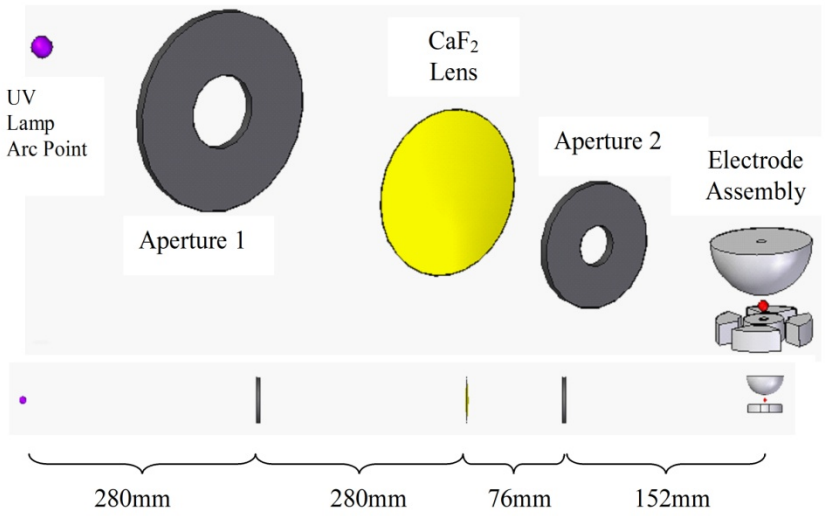


**Figure 4.25-** Schematic diagram of the UV focusing optics. Two apertures are used to contain the light cone (to prevent secondary reflection and interference with other instruments) and a single CaF2 lens is located in high vacuum and focuses the arc point onto the sample. A shutter (not shown) is located in front of the lens to prevent deposition on the lens from sample evaporation after preliminary processing.

A series of apertures and $CaF_2$ lens are used to focus the arc point onto the sample (Figure 4.25). While the index of refraction of $CaF_2$ changes by nearly 3% over the wavelength range indicated [44], the aberration is largely contained within the sample. This design has the added advantage of being simple, easily adjustable, inexpensive, and can be attached directly to the chamber itself and thus doesn't need an additional $MgF_2$ window. The lamp's spectrum extends into the visible violet and the initial alignment is carried out by raising a sample on the post, placing a fluorescent screen behind the sample, and aligning the spot on the sample. The vacuum assembly that contains the optics is pumped by the turbo-pump used in the main chamber; the good vacuum (~$10^{-7}$ Torr) reduces atmospheric ionization and maximizes the UV flux on the sample. The spot size is somewhat adjustable; however, a size of ~2mm diameter is sufficient to

process many liquids. Developmental versions of the UV vacuum chamber had a much poorer vacuum ($10^{-3}$ – $10^{-5}$ Torr). Consequently, the number of accessible systems was greatly reduced and the processing time was increased.

Utilizing the optics described, the initial processing is time limited by the stability and the surface charge. A typical processing cycle is shown in Figure 4.26. There is a competition between the current leaving the sample and the ability of the UV lamp to recharge the surface. If the sample is heated to the melting temperature too quickly, the surface charge decreases too rapidly. During the initial development of the ESL [20] a choice was made of whether or not to make the surface charge positive or negative. In part, the choice was made because at some temperature, the sample enters a regime of *Thermionic Emission* (TE).

Several mechanisms cause charge to leave the sample. When in the liquid state, the surface charge decreases [22] due to evaporation of atoms from the surface of the sample. The evaporation current density is governed by

$$I^{+} = \frac{P_i}{\sqrt{2\pi m_i k_B T}} \tag{26}$$

where $P_i$ is the partial pressure of element $i$, with mass $m_i$, at temperature T. Evaporation of adsorbed gases on the surface can also carry charge away from the sample. Finally, as sufficiently high temperature, the thermal energy of the surface electron will eventually allow them to overcome the barrier for ejection from the surface, a process called thermionic emission (TE). Richardson [45] describes an empirical, classical, relationship between the TE current density, $\Gamma$, the temperature $T$, and the effective work function of the surface, $\phi$':

$$I^{-} = \frac{AT^2}{e}\exp\left(-\frac{\phi'}{k_B T}\right). \tag{27}$$

Here, $A$ is a constant, 120 amp $cm^{-2}K^{-2}$. The effective work function, $\phi$', appears in this expression because there are other factors influencing the potential barrier and ultimately electron ejection. Meister and Herlach [46] provided an expression approximating the effect of the strong levitation electric field, $E$, on the material work function:

$$V = \sqrt{\frac{e^3 E}{4\pi\varepsilon_0}}. \tag{28}$$

Using a nominal potential of 10kV, over the gap spacing of ~10mm, contribution from the field is of order $10^{-2}$ eV, or two orders of magnitude smaller than that of the inherent work function; this is therefore ignored in this treatment.

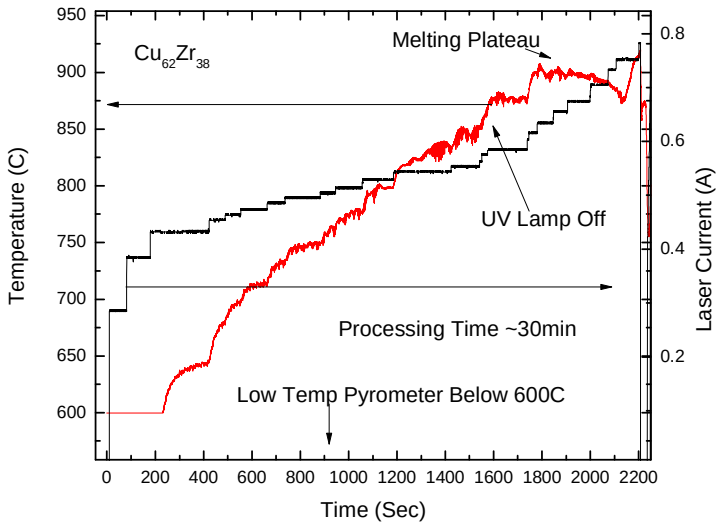


**Figure 4.26-** Initial processing cycle for a Cu-Zr alloy.

It is difficult to estimate the photon flux energy density incident on the sample because no measurements have been made in this group with our specific UV optics. However, collaborators at Ames Laboratory [47] have measured the flux using a UV photon source [31] that emits at roughly the same wavelength, and results in a very similar initial processing profile to that we observe. Using their measurements as an estimate of the photon flux in WU-BESL, approximately $10^{15}$ photons/sec hit the surface of the sample. It is hard to estimate how many of these photons are reflected vs. absorbed and thus the number available for photoelectric ejection, but assuming 10%—100% efficiency, the UV Lamp creates an electron flux of $10^{14} - 10^{15}$ $e^-$/sec. When we compare the estimated thermionic emission as a function of work function and temperature (Figure 4.27) with the effect of the UV lamp and the temperature range where the TE is the dominant process, we find poor agreement with this simple theory. Since the thermionic emission depends strongly on the work function, we find that only a narrow range in work function, $\phi < 3.0eV$, is consistent with the idea that the dominant contribution to the effective work function can be estimated from the values in Table 4.2. There appears to be a different mechanism dominating the effectiveness of the UV lamp, making the metallic work function variability less important. Take Pd- and Pt- based alloys. This research group has been successful in processing Pt-Hf alloys (up to 60 atomic percent Pt), but has had little success in processing Pd-based systems, even though they have similar work functions. Sample reflectivity may play a role: It has been observed that pure Cu, Au and Pt, which have a higher reflectivity than other metallic elements we've examined, are very difficult to process. However, pure Pt and Au have been processed using the NASA ESL [48] while Cu has not.

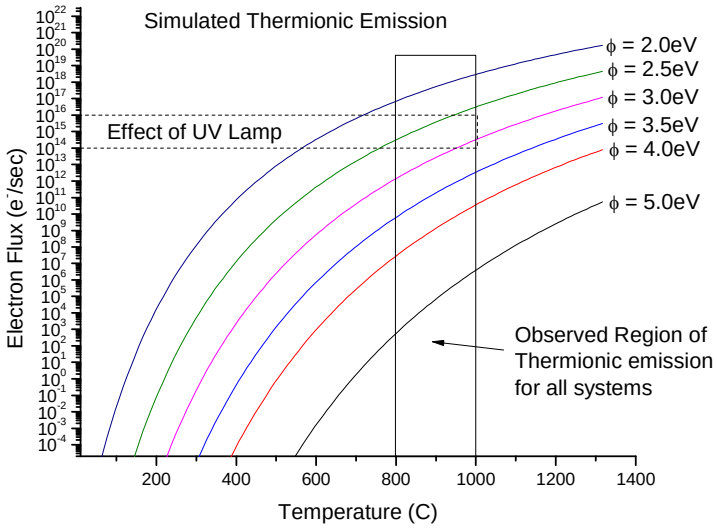


**Figure 4.27-** Simulated thermionic emission curves for various work functions. The flux effect of the UV lamp is shown as well as the observed temperature range where the UV lamp is no longer necessary and thermionic emission is the dominant electron ejection mechanism. The surface area was taken to be $4\pi(1.25mm)^2 = .2cm^2$.

### *4.6.2. Future Directions*

The utility of the ESL is limited by the number and types of alloys that can be processed. As discussed previously, the WU-BESL UV optical assembly has allowed access to some interesting systems, but others remain out of reach. For example, Pd-Si, a low temperature binary bulk former could not be successfully processed; most Al-based alloys are difficult to process; many of the pure 3-d transition metals remain difficult to process; Ge and Si and their alloys are difficult to process. Ultimately we have not seen a high success rate, although similar problems have been found in other ESL systems. Since an increase in the UV photon flux (by improving the vacuum) has a dramatic influence on the ability to process the samples, it is reasonable to explore improvements

of the flux further. As part of planned Neutron ESL development, an alternative UV sources (an Omicron UV source) being tested at Ames Laboratory has shown some promise for improving processing capability.

Another approach to improve processing has been a "hot launch." Because thermionic emission seems to be the dominant contribution to electron ejection for all systems above 1000°C, if a sample were first heated on the bottom electrode to this temperature and then launched into a heating laser aligned with the nominal sample location, processing might be improved. There are two advantages to this method. First is an increased efficiency. Initial processing constitutes a large fraction of the overall experimental time. Often sample loss occurs at elevated temperatures (but below 1000°C) if the UV-induced electron ejection is insufficient to overcome the surface charge loss. All of the time spent in sample processing is therefore lost. It is more time efficient to fail at the outset than to waste 15 to 30 minutes, and then fail. Second, the UV lamp assembly constitutes a significant fraction of the cost and complexity of the ESL experiment. Removing this aspect of the experiment would significantly reduce the WU-BESL beamline integration time and remove a critical weak link in the experiment. This approach has been used by others, although details of the success rate and the applicable systems for which it is successful are absent [49].

## 4.7. Thermophysical Property Measurements and Sample Processing

### *4.7.1. Thermophysical Property Measurements – Temperature*

A typical ESL experiment involves thermally processing a sample into the liquid state, allowing the sample to free cool into the undercooled state and usually recalescing to a polycrystalline sample. Changes in the specific heat are manifestations of structural and chemical ordering or other phase transformations in the liquid during this processing. The specific heat can be obtained from the time derivative of the sample temperature. During free cooling, assuming that there are no radiation sources on the sample, the power lost due to radiation will be equal to the heat release per unit time from the sample

$$mc_p \frac{dT}{dt} = -\varepsilon A_s \sigma_B \left( T^4 - T_0^4 \right). \tag{18}$$

Here, $m$ is the sample mass, $c_p$ is the specific heat, ε is the total hemispherical emissivity, $A_s$ is the sample surface area, $\sigma_B$ is the Stefan Boltzmann constant and $T_0$ is the surrounding temperature. This particular relationship only applies if there is no phase change.

The specific heat is a measure of the available degrees of freedom that couple to the heat bath; it is often expressed as an intensive parameter (as opposed to the total heat capacity, which generally explicitly incorporates the mass of the sample). For any reversible process,

$$c_v = \left( \frac{\partial u}{\partial T} \right)_v \tag{19}$$

and

$$c_p = \left( \frac{\partial h}{\partial T} \right)_p = T \left( \frac{\partial S}{\partial T} \right)_p \tag{20}$$

where *u*, *h* and *s* are the internal energy, enthalpy and entropy, respectively. In practice, there are a number of problems in using free cooling data to extract specific heat from free cooling ESL data. To explore these, we begin with a more rigorous approach to pyrometry in ESL.

In 1900, Max Planck described the distribution of radiated energy from surface, at temperature T, as a function of wavelength λ (per unit solid angle):

$$\varsigma(T,\lambda) = \frac{2hc^2}{\lambda^5}\left(\frac{1}{e^{\frac{hc}{\lambda kT}} - 1}\right). \tag{21}$$

This function peaks at $\lambda = \frac{hc}{4.97}\frac{1}{kT}$ and shifts to shorter wavelength, and the peak sharpens with increasing temperature. There is a long polynomial tail at longer wavelengths for all temperatures, which accompanies a rapid exponential fall at shorter wavelengths. This equation rigorously applies only for materials that emit and absorb with perfect efficiency — no such materials exist. An efficiency factor, called the "emissivity", $\varepsilon = \varepsilon(T,\lambda)$, is used to account for this. It varies between 0 and 1, where an emissivity of 1 corresponds to a so-called "black-body." A temperature measurement could then be made by measuring the intensity of radiated light over a narrow wavelength range

$$I(T,\lambda) = \int_{\lambda_1}^{\lambda_2} \varsigma(T,\lambda)d\lambda = \int_{\lambda_1}^{\lambda_2} \varepsilon(T,\lambda)\frac{2hc^2}{\lambda^5}\left(\frac{1}{e^{\frac{hc}{\lambda kT}} - 1}\right)d\lambda \tag{22}$$

Emissivity as a function of temperature is typically difficult to measure in liquid systems, although experimental setups exist [50, 51]. But, the assumption of constant emissivity over a large temperature range is problematic. Commonly available tables for solid state

emissivities show a wide variety of behaviors [31, 52]; the variation as a function of temperature in a crystalline metal over 250C can range from immeasurably small to a nearly 400% increase if the surface of the metal has an oxide coating, such as in oxidized Al. In liquids, where they exist, the measurements of changes in emissivity are usually limited to easily assessable systems, i.e. non-reactive and low melting temperature liquids. Liquid water, for example shows a modest change of 5% over its entire temperature range, which is only 100 degrees. Measurements of liquid Ga [53] show as much as a 25% increase on the emissivity with an increase in temperature of 200 degrees, although the authors point out that the measurement technique was very sensitive to impurities. However, measurements of liquid Ce-Cu alloys [54] show little change in the emissivity as a function of temperature over large temperature ranges ($\Delta T$ ranges from 200 to 600 degrees depending on composition), but the emissivity varies markedly as a function of composition. Measurements of liquid Si also show little change over a large temperature range [55].

There appears to be little evidence that the emissivity changes rapidly over a temperature window of a few hundred degrees, however, even small changes can have an effect on thermal expansion measurements. The density measurement (discussed in the next section), which is essentially a volume measurement, relies on an accurate temperature measurement in order to compute the thermal expansion. If the emissivity changes by several percent over the temperature range this would be manifest as a deviation of the true slope should the volume versus temperature be linear. These points imply the need for caution when comparing thermal expansions made over an alloy concentration range where the measured temperature ranges are different.

Pyrometer measurements in WU-BESL typically have a noise level less than 1%, with contributions from the device itself, the stability of the sample, and real temperature gradients within that sample. A number of smoothing procedures have been proposed to obtain specific heat data in an typical free cooling cycle [56] with varying degrees of success. Beginning in 2004 [57] ESL work in this group showed some evidence for a peak in the specific heat upon undercooling in some Ti/Zr-based liquids, although the results relied heavily on smoothing and select data rejection. Recently, a similar feature was seen in a Cu-Zr undercooled liquid, but the feature seems to be inconsistent with either a first or second order phase transformation. A high speed pyrometer (Kleiber MI-KMGA-LO, Fiber Coupled with spectral response 1.58μm-2.20μm), which can sample at up to 100kHz over an extended temperature range (500 – 2500C) has been installed to improve specific heat measurements, although none have been conducted to date. Additionally, J. C. Bendert [56] has attempted to employ a modulation calorimetry approach to specific heat measurements in $Ti_{39.5}Zr_{39.5}Ni_{21}$ liquids, although at this time no measurements have been successfully conducted.

In the WU-BESL, temperature measurements are conducted primarily with two pyrometers: A single color unit with spectral response at 1.89μm, a minimum spot size of 1mm (Process Sensors, Model MI18-0160-0800), and a $t_{90}$[9] response time of 1ms can measure the temperature over the range 160°C to 800°C. A two color unit, with responses at 1.40μm and 1.64μm, a minimum spot size of 1.2mm (Process Sensors, Model MQ22-060-2300), and a $t_{90}$ response time of 2ms is used to measure the temperature from 600°C to 2300°C. The high temperature unit is fiber-optic-coupled

[9] The pyrometer takes time to read the temperature input. The $t_{90}$ response time is how long it takes the pyrometer to read 90% of the final temperature, similar to a decay constant in RC circuits.

with a laser aiming system. Due to the short working distance of this unit, a recessed conflat port (not shown) is used to allow the collimation head of the fiber to reach the working distance from the sample ( ~ 4 ”). It should be noted that this pyrometer has a cumbersome alignment procedure. The laser sight requires the user to rely on the reflection of a light spot on the sample to align the pyrometer. Sighting optics would be preferable, however they are not offered with this unit. Future upgrades of the system should include a sighting system with an output to a monitor to allow alignment confirmation.

Wien’s law is often used as an approximation to Planck’s law at long, infrared wavelengths and describes the relationship between the measured temperature $T_E$ (at a given emissivity) and the true temperature:

$$\frac{1}{T} - \frac{1}{T_E} = \frac{\lambda}{14388\,\mu mK} \ln \varepsilon \,. \tag{23}$$

It can be shown that this approximation is accurate to 0.1% as long as the temperature-wavelength product is less than 2897μmK. For our two color pyrometer, which operates at 1.40 and 1.64μm, this translates into maximum temperatures of 1796°C and 1493°C, respectively. While the pyrometers are used outside of this range, the absolute error in the temperature measurement remains less than 1%. The Labview™ program used to interface the pyrometers receives a signal that is equivalent to an actual temperature. An emissivity is chosen and input to the pyrometer, the intensity at the appropriate wavelength is measured, and a temperature is calculated [58]. Because the total hemispherical emissivity is unknown, a correction table is provided that allows the temperature curve to be calibrated to a single reference temperature by changing the

emissivity. The calibration curves for the Process Sensors pyrometers are shown in Figure 4.28. Back correcting the temperature is equivalent to travelling along the curves.

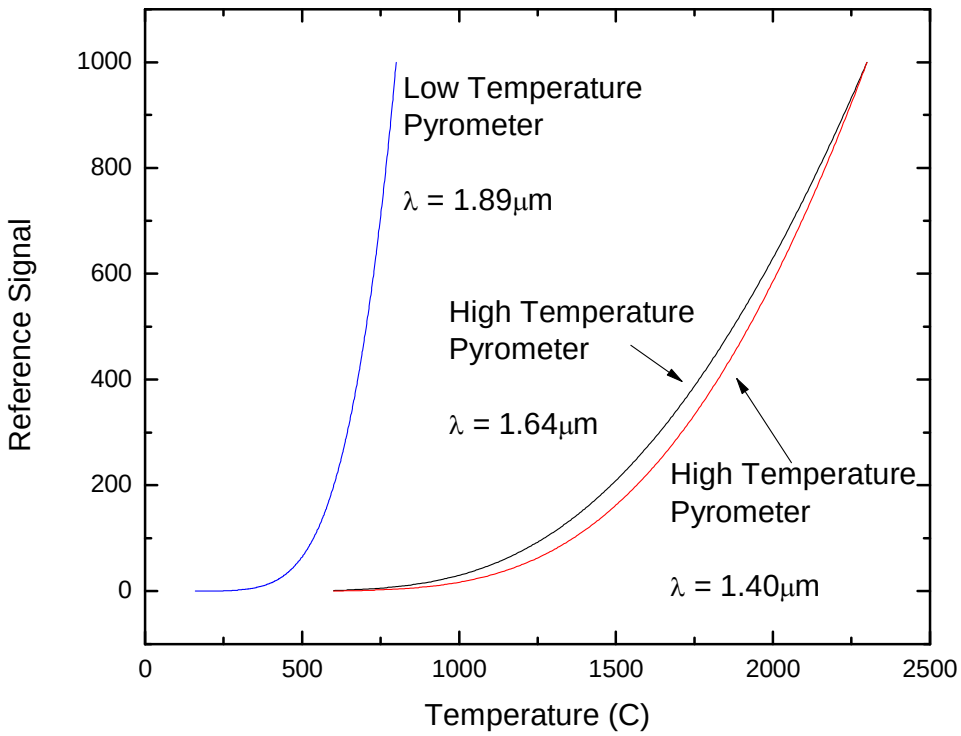


**Figure 4.28-** Calibration curves for Process Sensors pyrometers. The curves are used to back-correct the experimentally determined temperatures to a single reference temperature.

### *4.7.2. Heating Laser Implementation*

The WU-BESL uses a fiber-coupled, solid-state, heating laser to heat the samples. The heating laser (model NL-P2-050-0980-3-R from nLight Corporation) is a 50W, SMA fiber-coupled diode laser at 980nm, whose power output can be controlled by the host computer. The wavelength was chosen to avoid interference with the positioning lasers used for the PSDs, the back-light used for the density measurement and the pyrometers. The cooling unit, an active Thermoelectric Cooling (TEC) unit, transfers the heat from the diode into a water cooled aluminum block. At full power for an extended period of time, a modest (~2gpm) flow of room temperature water is required for operation. The power supply (model mv-21-01, from VueMetrix) was chosen because of its ease of integration into the computer controlled system as it, too, is computer controlled through the Labview$^{TM}$ interface. Additionally, the current output can be modulated with an analog voltage, there are a series of safety interlocks, and the supply is compact.

The TEC is a Peltier device; when current passes through the device, it can actively sink (or supply) heat. There are four important components to the cooling system. These are the TEC devices, a heat sink (water-cooled aluminum block), a power supply (for current supply to the controller and the TEC's), and a controller unit that uses a temperature feedback loop to control the supply of current to the TEC's. A cost effective controller from TE Technology Inc. (TC-48-20) uses two 10kΩ thermistors to monitor the temperature and controls the current through two TEC's in series (TE Technology Inc., model HP-127-1.4-1.15-71). The control thermistor should be on the aluminum block so that the control algorithm isn't susceptible to oscillations due to the smaller thermal mass of the diode. The controller can be used with single or dual power

supplies (one for the controller and one for the TECs); we use a single supply (model W24NT1200, Acopian)).

The heating laser is fiber-coupled and thus requires a high-power collimator with an SMA connector (model OEFOC-401 from O/e Land Inc., 200μm fiber); it has a red diode aiming laser. With an infrared beam, this aiming beam is a necessity. This model from nLight only comes with a red 641nm beam, which is difficult to use during levitation because the reflection of the positioning lasers off the sample is so strong.

### *4.7.3. Thermophysical Property Measurement—Density*

#### *4.7.3.1. General Considerations*

One of the benefits of the ESL is the ability to simultaneously measure several thermodynamic and structural properties at once. Density is related to the first derivative of the Gibbs free energy with respect to the pressure,

$$\rho \equiv m\left(\frac{\partial G}{\partial p}\right)_{T,N}^{-1}, \tag{24}$$

where $m$ is the sample mass. Discontinuities in the density are indicative of a first order phase transformation. In second order phase transformations, the second derivative in a potential (like specific heat, or magnetic susceptibility) is discontinuous, and the first derivatives (like the density) are continuous, but exhibit a localized change in slope. This Ehrenfest classification breaks down for instances where the derivative of the thermodynamic potential diverges, such as the paramagnetic-ferromagnetic transformation, where the specific heat diverges. More modern classification schemes, pioneered by Landau and others, segregate phase transitions into two broad categories.

First order, or discontinuous, transitions are those involving a latent heat of transition. Second order, or continuous, transitions involve divergent susceptibilities, divergent correlation length scales of the transition and generally power law decay of correlations away from the transformation in parameter space. More exotic phase transitions, such as the glass transition (see Chapter 1), have elements of both (or neither) classification, whose governing principles are poorly understood.

The density, then, is a very important quantity to measure. A brief discussion of the measurement theory and the implementation follows; a more detailed description of the various aspects of the measurement will appear in a later dissertation by J. C. Bendert. The density measurement is a non-contact volume measurement, where the mass is assumed to be well known. This assumption is challenged when there is mass loss due to sample evaporation; correction techniques for such losses will be discussed presently. The volume measurement is based on the shadow method [41, 59] where collimated blue light from a LED (Leica DMI Microscopes Collimated LED, $\lambda$= 455nm) passes through the chamber to a diametrically opposed neutral density filter, through a narrow band pass filter, into a lens system (CF-1/B Close Focus Objective, Infinity K2/SC Long Distance Video Microscope) and ultimately to a fast CCD camera (PL-B741 Gig-E Monochrome Camera). The shadow of the levitated sample is passed to the CCD camera face where the objective lens magnifies the sample and the long distance lens (similar to a telecentric lens) corrects for effects of perspective which cause lines parallel to the optic axis to appear to have emerged from a distant point.

#### *4.7.3.2. Difficulties Associated with Density Measurements in the Solid Phase*

The fundamental assumption about the shadow technique is that the true sample volume can be constructed from the projection of the sample shape or that a time averaged measurement of this projection gives the correct value. Two algorithms are employed for calculating the sample volume; the details of these are provided elsewhere [59, 60]. The eigenfunction expansion method, shown in Figure 4.29a, finds the shadow centroid, calculated $r$ vs. $cos(\theta)$ and then fits that to a 6th order polynomial. Expanding the volume in this manner is equivalent to expanding the volume in terms of Legendre functions. We assume that the sample volume is symmetric about the vertical direction, the $z$-axis. The numerical algorithm (Figure 4.29b) (a) finds the width, $2X$, at each pixel height location, $y$, (b) assumes that the volume producing the shadow is made up of disks of radius $x$, and thickness $dy$, and (c) sums over all disks located at heights $y$. The numerical algorithm is faster and has been shown to be only marginally less precise than the eigenfunction expansion method, particularly for liquids.

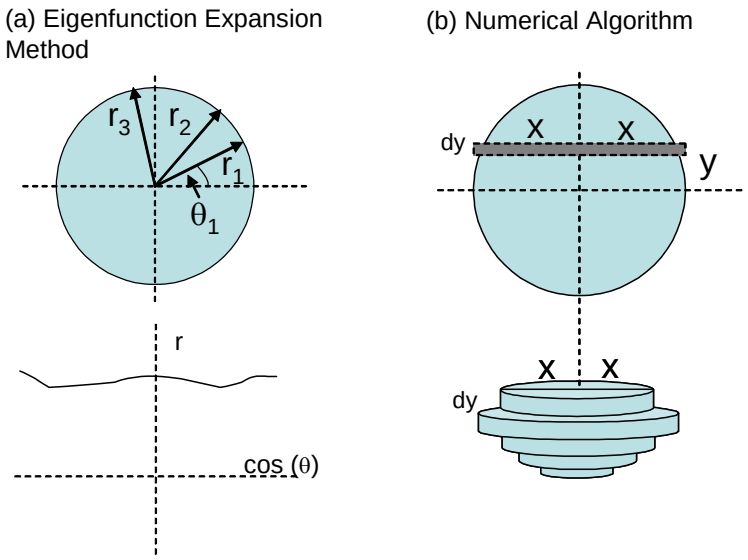


**Figure 4.29-** Geometry for volume determination using the shadow method. (a) The eigenfunction expansion method finds the shadow centroid, constructs *r* vs. *cos*($\theta$) and then fits that to a 6$^{th}$ order polynomial. (b) The numerical algorithm (i) finds the width (2*X*) at each pixel height location (*y*), (ii) assumes that the volume producing the shadow is made up of disks of radius *x*, and thickness *dy*, and (iii) sums overall disks located at heights *y*.

The liquid density calculated by the algorithms described likely is good because the direction of gravity and the electrode geometry are consistent with the assumptions described. Density measurements of the solid phase are less precise, particularly when crystallization causes large shape distortions. Because shape distortions have been observed, this is not a purely academic exercise. The amount and type of shape distortion varies amongst the systems studied and we've seen that the noise in the volume measurement can increase by more than an order of magnitude upon crystallization. This is demonstrated in Figure 4.30, where the noise in the volume is drastically increased

upon recalescence. We can also see an oscillation of the measured temperature, coordinated with the sample rotation at ~3Hz.

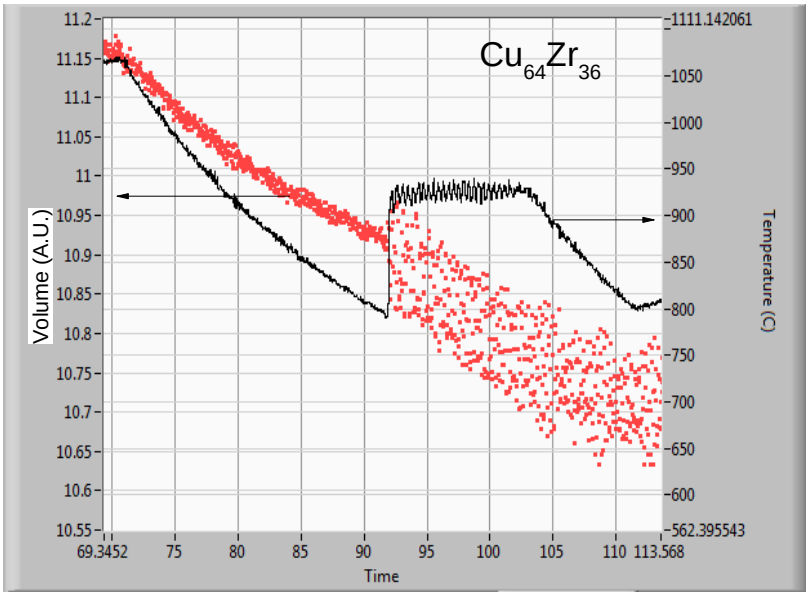


**Figure 4.30-** Temperature and volume (arbitrary units) for a processing cycle of $Cu_{64}Zr_{36}$ bulk metallic glass forming liquid. The noise in the measured volume is drastically increased upon recalescence

While noise in a measurement can often be improved through statistics, the assumption that the uncertainty decreases with the square root of the number of measurements is itself based on the assumption that the average of these measurement is equal to the true value. For the numerical algorithm, we consider a slice at a height *y* and thickness *dy* (see Figure 4.29 for notation). First, imagine a sample with an extreme asymmetry about the *z*-axis, as shown in Figure 4.31, but retaining a convex structure. This shape, a half disk/half diamond (edge length $\sqrt{2}r$ ), has an actual volume of $\left(\frac{\pi r^2}{2} + r^2\right)dy$, but depending on the rotation angle of the sample (Figure 4.31) the shadow method will give between 0.89 and 1.22 times the actual volume. If this were a

BESL measurement, then we would observe a spread (scaled to the lowest value) of 37%. As the number of facets increases and the spherical character improves, the spread in the simulated measurement decreases.

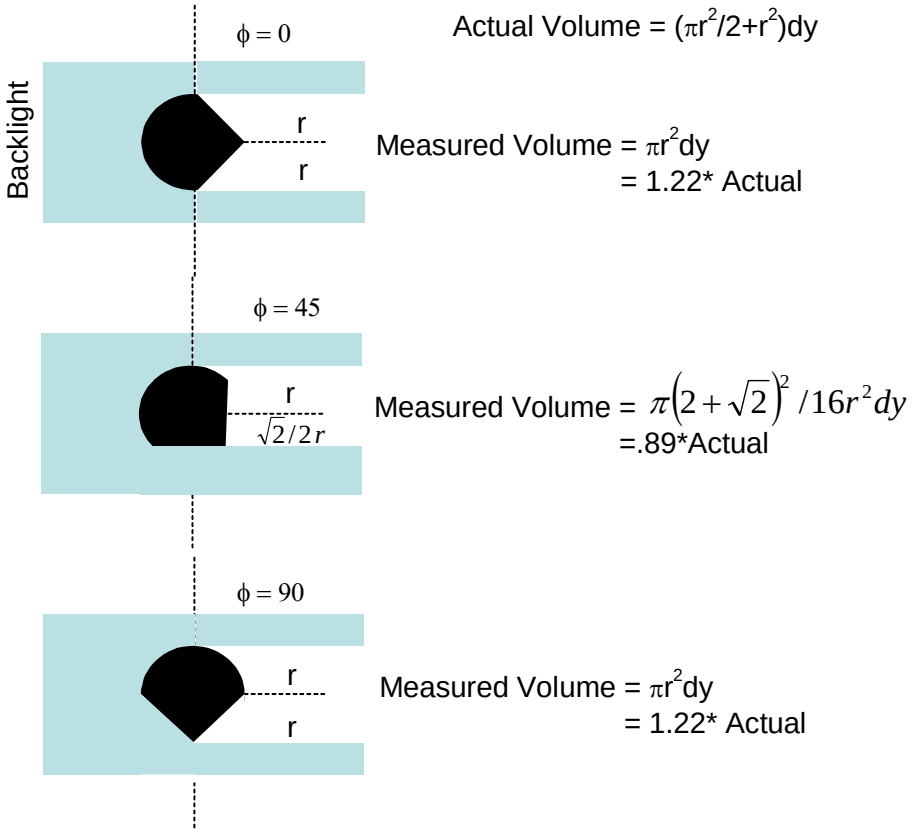


**Figure 4.31-** Simulated measured volume for a highly distorted sample geometry through 90 degrees of rotation.

The spread of the data contains the actual volume, but the spread is asymmetric about that actual value. Assuming a constant rotation rate, $d\phi/dt$, the average volume measurement, using the numerical algorithm used by Bendert [60], can be shown to equal

$$\langle V \rangle_\theta = \frac{\pi}{\pi/4} \int_{\theta=0}^{\theta=\pi/4} \left( \frac{r + r\cos\theta}{2} \right)^2 d\theta \,. \qquad (25)$$

This expression is derived by considering the projection of a pixel length at height *y*, which is considered to be the diameter of the disk of revolution for the volume. For clarity, the geometry for the calculation is shown in Figure 4.32. The rotation of the sample can be broken up into eight equivalent rotations of 45 degrees. By evaluating the integral in Equation (25), we find that the average measured volume is 1.11 times the actual value, and thus, for this extreme example, the average doesn't converge to the actual value. Here, we would measure a smaller density than the actual one. As other facets are added, consistent with a convex hull, the deviation between the average and the actual values decrease as do the extreme maximum and minimum values of the volume. Other geometries also lead to larger measured volume, and lower densities. Of course, such severe distortions in geometry as considered here have never been observed nor do they seem likely. The actual physical measurement shown in Figure 4.30 only shows a maximum spread of 1.5%. The points made here, however, demonstrate that comparisons between the densities of the liquid and solid phases can be problematic.

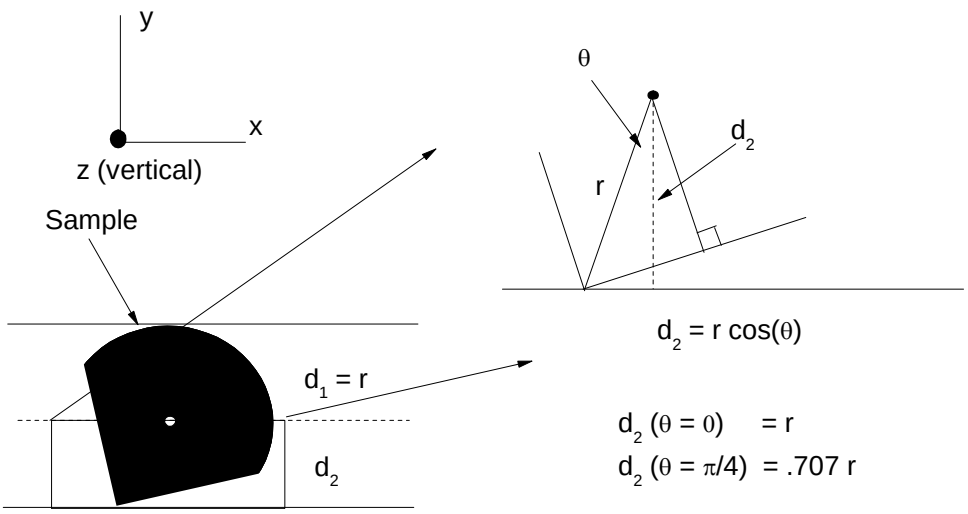


**Figure 4.32-** Geometry for volume determination in the shadow method using the numerical calculation. The radius for the disk is $(d_1 + d_2)/2$.

## 4.8. Beamline Integration

### *4.8.1. General Considerations*

A central focus of this work has been to construct an ESL that is optimized for making scattering studies on containerlessly processed liquids. WU-BESL has been constructed to that end; the design is discussed briefly in this section. At the Advanced Photon Source (APS), where the measurements with WU-BESL have been made, the synchrotron X-rays are generated by 7 GeV electrons that are passed through an undulator insertion device to increase the brilliance. After diffracting these X-rays from a double Si-monochromator the estimated flux is ~ $10^{11}$ - $10^{12}$ photons/sec/mm$^2$ [61]. In studies made at the APS Sector 6ID-D, movable slits downstream of the monochromator

shaped the incident beam to a nominally square cross-section with a variable side length of .5mm to .7mm.

### *4.8.2. X-ray Optics*

WU-BESL was constructed with .015 inch thick beryllium (99.0% purity, PF-60, Brush Wellman Engineered Materials, Inc.) windows that are mounted on 2.75 inch and 8 inch CF flanges to allow synchrotron X-rays to enter and exit the chamber respectively. The inside of the Be windows are lined with Kapton® foil to prevent deposition from sample processing. Despite the generally excellent transmission properties of the Be windows, the intensity of scattering of the direct beam from polycrystalline grains (hexagonal, c/a = 1.5801) in the incident and exit Be windows is comparable to the scattering of the incident X-rays by the sample in some cases. A series of tungsten collimators and a beamstop, shown schematically in Figure 4.33, are used to reduce this background to acceptable levels. The reduction in background in demonstrated in Figure 4.34 by comparing diffraction background images before and after inserting the collimators. Several tungsten collimators were produced, which are interchangeable to accommodate the variety of beam sizes mentioned.

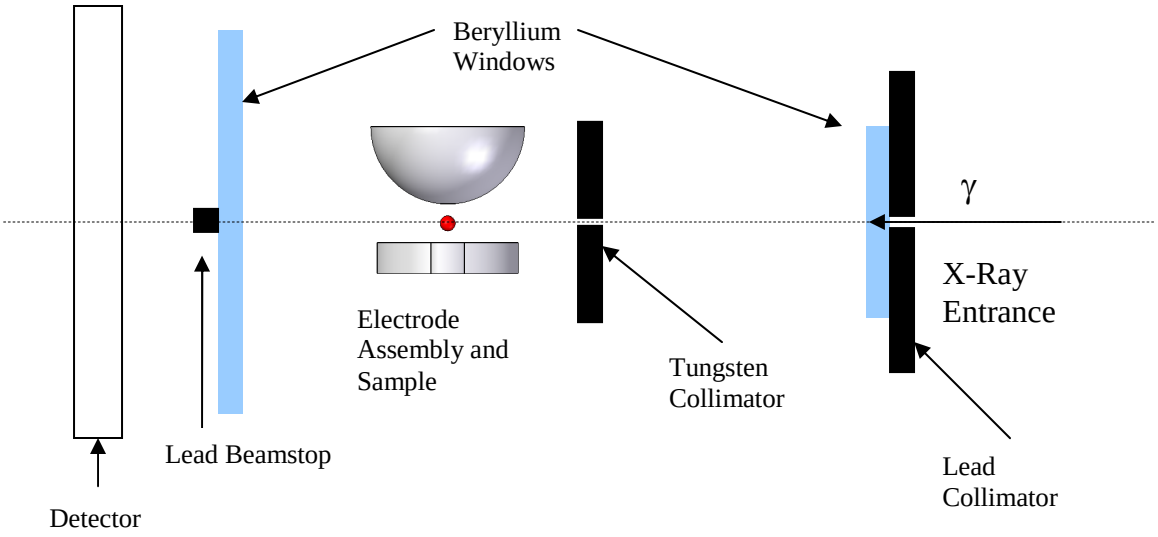


**Figure 4.33-** Schematic diagram of the X-ray Optics for WU-BESL.

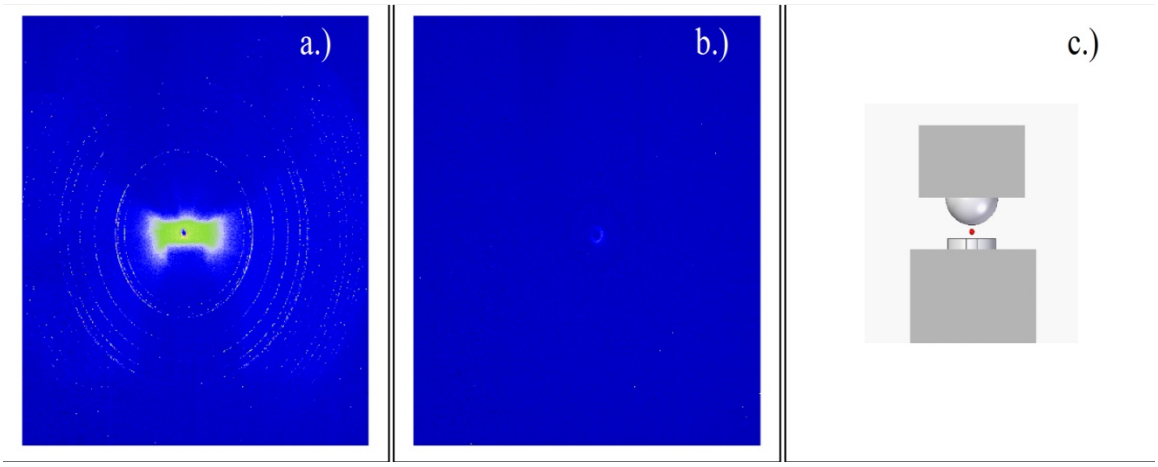


**Figure 4.34-** Background X-ray images before (a) and after (b) inserting the X-ray optical components in **Error! Reference source not found.Error! Reference source not found.**. The intensity scale on both images is the same. For reference, the position of the electrode assembly is shown in (c).

Even with these improvements, a small contribution to the background arises from scattering of the diffracted intensity by the exit polycrystalline Be window. Since for

amorphous systems, the most intense scattering features are at low $q$, scattering from the exit window will redistribute this to higher $q$. To deconvolve this contribution from the primary scattering intensity, it is assumed that each point on the Be window acts as a scattering center. Due to the isotropic nature of the primary scatter, there is a conical symmetry to that scatter, and further, secondary scatter projects the conical scatter from the polycrystalline Be onto the detector face. Under these assumptions, the primary task is to develop the mathematical framework to correct the data. The details of the derivation are presented elsewhere [62], but in Figure 4.35 we show the result of the correction on liquid Ni at 1200°C. Experimental Be diffraction data were taken from the exit window to determine the secondary scatter distribution and the correction applied to BESL liquid data. The correction generally has the effect expected, redistributing intensity to lower $q$, leading to a more intense first peak, for example.

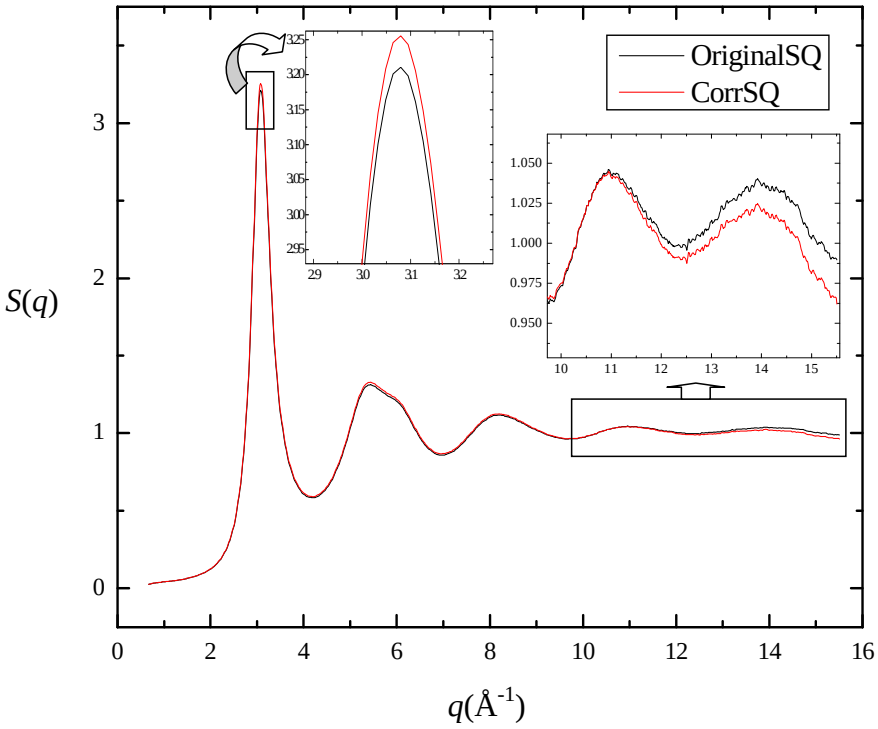


**Figure 4.35-** The effect of the correction for Be secondary scattering in supercooled liquid Ni at 1200°C. 'OriginalSQ' indicates the structure factor, S(Q), without the correction and 'CorrSQ' is the S(Q) after the correction. The primary peak and the high q regions are magnified to show the amount of the correction.

A similar effect arises from secondary scattering from the polycarbonate plate that holds the beamstop and the air between the chamber and the detector. A more comprehensive correction is being implemented to account for all three sources of secondary scatter.

### *4.8.3. Alignment Stage*

Since synchrotron beam time is generally over-subscribed, ease of integration of ancillary equipment into beamline facilities is desirable. The robust levitation algorithm employed

[22] removes the need for large optical tables with active vibration control. This allows the construction of a compact and simple chamber table for equipment support that can be installed easily in a variety of beam lines. Figure 4.36 shows a schematic model of the chamber mounted to a 30" by 30" by 2" custom aluminum equipment table. In Figure 4.36b, a hole pattern is made that allows easy mounting, via a stainless steel cylinder, to a variety of beam line diffractometers. One example is the μ axis of the custom Hubber Psi-geometry diffractometer located in the 6ID-D station on the MUCAT undulator beamline in sector 6 at the Advanced Photon Source at Argonne National Laboratory. However, such a simple design also facilities the fabrication of a universal adaptor for incorporation of the WU-BESL on other diffractometers.

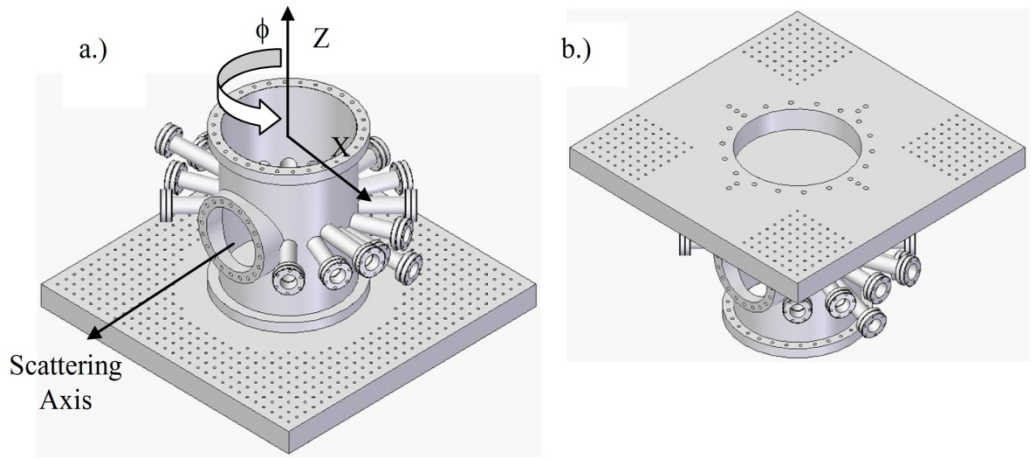


**Figure 4.36-** Schematic diagram of the WU-BESL chamber and the modular alignment table.

Often, however, the attachment of the BESL directly onto a diffractometer is not desirable either because the specific goniometer in the high energy station is incompatible with the BESL geometry, or the beamline only allows incorporation of BESL upstream or downstream of the goniometer. The 2-axis translation stage (schematic shown in Figure

4.37 and Figure 4.38) combined with a rotation stage mounted using the hole pattern in Figure 4.36b allows a positioning of the chamber such that the X-ray beam aligns with the scattering axis of the chamber. A series of 8 stainless steel rails are positioned vertically in an outer cage so that the chamber travels vertically along linear track bearings. A single Z-axis ACME screw drive bears the weight of the chamber, and drives the vertical motion. The chamber is aligned transverse to the X-ray beam on a series of horizontal rails and linear track bearings and driven with a single X-Axis ACME screw with an anti-backlash nut. The alignment stage superstructure is constructed almost entirely out of aluminum T-slot extrusion framing, utilizing its excellent stiffness and modular design.

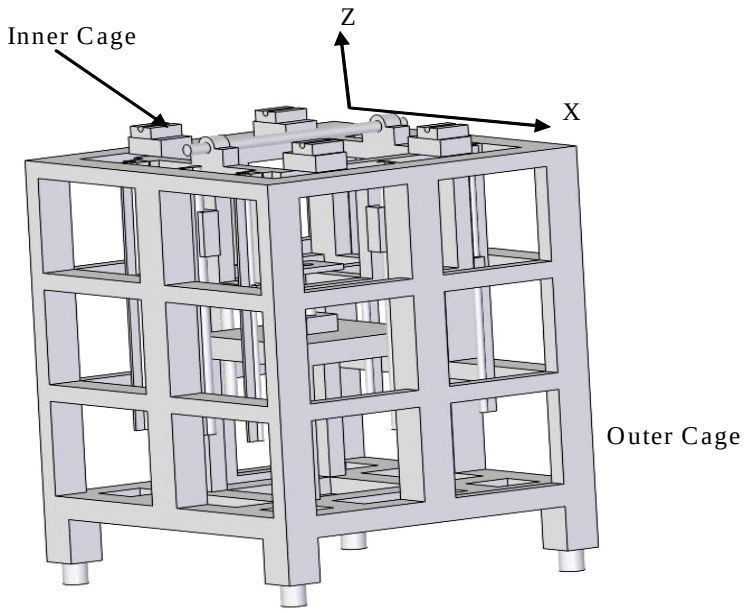


**Figure 4.37-** Alignment stage for WU-BESL. The inner cage travels vertically on eight linear track and bearing sets. The WU-BESL sits on the inner cage on two horizontal linear tracks and bearings**.**

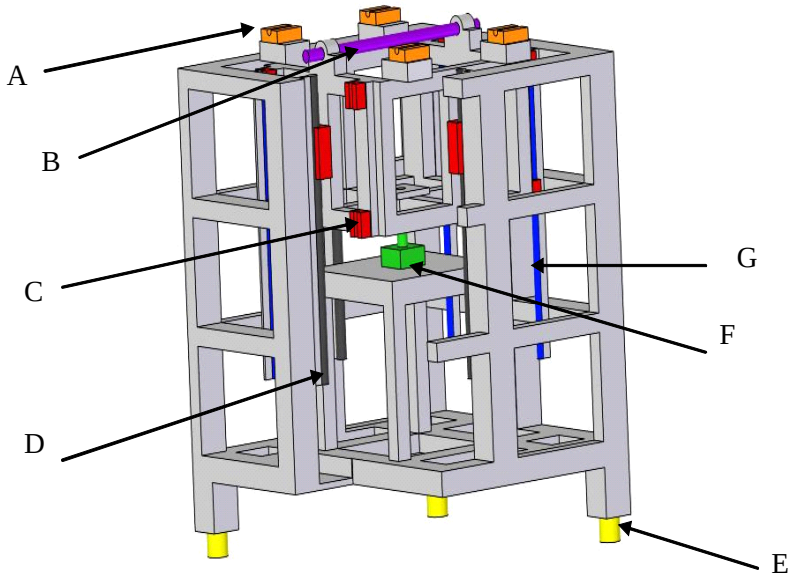


**Figure 4.38-** Outer Cage. (A) Horizontal Linear Track Bearings (Orange); (B) Horizontal, X-Direction Screw Drive (Purple); (C) Vertical Linear Track Bearings (Red); (D) Vertical Linear Rail, 1 inch diameter (Black); (E) Leveling Feet (Yellow); (F) Lifting Screw jack (Green); (G) Vertical Linear Rail, 5/8 inch diameter (Blue).

This alignment stage was designed to interface with SPEC, the program used at station 6ID-D for computerized stepper motor control of the position. For illustration, the positional parameters for integration of the table and chamber into the MUCAT undulator beamline are summarized in Table 4.3. The positioning precision is determined by adjusting the stepping motors' angular step by the appropriate gearing. The *robustness* is an experimentally determined quantity that measures the reproducibility of the alignment. It was measured as the ability to repeatedly return the chamber (and thus the sample) to the equilibrium. The *Z* and *X* robustness was determined by levitating a sample, and using SPEC to scan through the equilibrium alignment. The $\phi$ robustness was determined manually.

**Table 4.3-** Parameters for alignment of WU-BESL*

| Axis | Range of Motion | Positioning Precision | Robustness of alignment |
|---|---|---|---|
| Z | $1323.8\text{mm} \leq Z \leq 1476.2\text{mm}$ | .01mm | .03mm |
| X | $-101.6\text{mm} \leq X \leq 50.3\text{mm}$ | .04mm | .04mm |
| $\phi$ | $-5.0° \leq \phi \leq 5.0°$ | .25° | .25° |

*The *P*ositioning *P*recision is determined by *adjusting* the stepping motors' angular step by the appropriate gearing. The Robustness is an experimentally determined quantity that measures the reproducibility of the alignment.

## 4.9. Conclusion

The design of a portable and inexpensive electrostatic levitation facility that is optimized for high-energy X-ray scattering studies and thermophysical property studies of liquids has been described. The principle utility of this design is its compactness, ease of operation, and low cost. At Washington University it has been used to study the supercooling limit, the density and the specific heat in liquids. A simple and versatile alignment platform allows integration of the facility into a wide range of synchrotron beamlines. The alignment stage is completely contained within the footprint of the chamber table and its portability is desirable for ease of integration into multiple beamlines. It has been tested at the Advanced Photon Source. It is more than sufficiently stable for the diffraction studies of amorphous materials (liquids and glasses) and fine grained crystal phases.

## 4.10. References


[1] J. L. Uriarte, A. R. Yavari, N. Nishiyama, G. Heunen, G. Vaughan, A. Kvick and A. Inoue, *Scripta Mat.* **48,** 809, (2003).

[2] K. S. Bondi, A. K. Gangopadhyay, Z. Marine, T. H. Kim, A. Mukhopadhyay, A. I. Goldman, W. E. Buhro and K. F. Kelton, *J. Non-Cryst. Sol.* **353,** 4723, (2007).

[3] H. W. Sheng, W. K. Luo, F. M. Alamgir, J. M. Bai and E. Ma, *Nature* **439,** 419, (2006).

[4] E. Matsubara, T. Ichitsubo, J. Saida, S. Kohara and H. Ohsumi, *J. Alloys and Comp.* **434-435,** 119, (2007).

[5] A. R. Yavari, N. Nikolov, N. Nishiyama, T. Zhang, A. Inoue, J. L. Uriarte and G. Heunen, *Mat. Sci. Eng. A* **375-377,** 709, (2004).

[6] Y. Suzuki, J. Haimovic and T. Egami, *Phys. Rev. B* **35,** 2162, (1987).

[7] P. Staron, R. Kampmann and R. Wagner, *Physica B* **213-214,** 815, (1995).

[8] G. W. Lee, A. K. Gangopadhyay, T. K. Croat, T. J. Rathz, R. W. Hyers, J. R. Rogers and K. F. Kelton, *Phys. Rev. B* **72,** 174107, 10(2005).

[9] A. K. Gangopadhyay, G. W. Lee, J. R. Rogers, A. I. Goldman, D. S. Robinson, T. J. Rathz and R. W. Hyers, *Rev. Sci. Instrum.* **76,** 073901, (2005).

[10] K. F. Kelton, G. W. Lee, A. K. Gangopadhyay, R. W. Hyers, T. J. Rathz, J. R. Rogers, M. B. Robinson and D. S. Robinson, *Phys. Rev. Lett.* **90,** 195504(2003).

[11] T. H. Kim and K. F. Kelton, *J. Chem. Phys.* **126,** 054513, 054513(2007).

[12] T. H. Kim, G. W. Lee, A. K. Gangopadhyay, R. W. Hyers, J. R. Rogers, A. I. Goldman and K. F. Kelton, *J. Phys. Condens. Matter.* **19,** 455212, (2007).

[13] R. L. McGreevy, *J. Phys. Condens. Matter.* **13,** R877, (2001).

[14] B. J. Alder and T. E. Wainwright, *J. Chem. Phys.* **31,** 459, (1959).

[15] J. D. Honeycutt and H. C. Andersen, *J. Chem. Phys.* **91,** 4950, (1987).

[16] L. Hennet, S. Krishnan, I. Pozdnyakova, V. Cristiglio, G. J. Cuello, H. E. Fischer, A. Bytchkov, F. Albergamo, D. Zanghi, J.-F. Brun, S. Brassamin, M.-L. Saboungi and D. L. Price, *Pure Appl. Chem.* **79,** 1643, (2007).

[17] E. H. Trinh, *Rev. Sci. Instrum.* **56,** 2059, 2059(1985).

[18] D. Holland-Moritz, T. Schenk, P. Convert, T. Hansen and D. H. Herlach, *Meas. Sci. Tech.* **16,** 372, (2005).

[19] T. Schenk, D. Holland-Moritz, V. Simonet, R. Bellissent and D. M. Herlach, *Phys. Rev. Lett.* **89,** 075507, 4(2002).

[20] W.-K. Rhim, M. Collender, M. T. Hyson, W. T. Simms and D. D. Elleman, *Rev. Sci. Instrum.* **56,** 307, (1985).

[21] X-Ray Mass Attentuation Coefficients, National Institute for Standards and Technology (2010).

[22] T. Meister, H. Werner, G. Lohoefer, D. M. Herlach and H. Unbehauen, *Contr. Eng. Pract.* **11,** 117, (2003).

[23] R. E. Honig, Vapor Pressure Curves, RCA Corporation of America, Princeton (1965).

[24] R. M. Besancon, Editor, Vacuum Techniques, Van Nostrand Reinhold, New York (1990).

[25] J. C. Bendert and N. A. Mauro, *Personal Communication* (2010).

[26] J. C. Bendert, Thesis, *Physics*, Washington University, St. Louis (2013 (Expected)).
[27] M. J. Kramer, Discussion of trace impurities in ESL samples, In: N. A. Mauro, Editor (2009).
[28] A. J. Rulison, J. L. Watkins and B. Zambrano, *Rev. Sci. Instrum.* **68,** 2856, (1997).
[29] NASA, Marshall Space Flight Center.
[30] R. Toreki, Materials Safety Data Sheets, (2011).
[31] Omegascope.
[32] B. E. Warren, X-Ray Diffraction, Dover Publications, Inc., New York, NY (1990).
[33] On-Trak Photonics (2010).
[34] A. Logan, A. Lyons and J. Mai, ESL Positioning Control System Hardware, (2010).
[35] CRC Handbook of Chemisty and Physics, (2011).
[36] K. Tse and J. Robertson, *Materials Science in Semiconductor Processing* **9,** 964(2006).
[37] V. Misra, G. P. Heuss and H. Zhong, *Appl. Phys. Lett.* **78,** 4166(2001).
[38] L. Xianming, W. Jianxin and Z. Jingsheng, *Physica B: Condensed Matter* **226,** 399(1996).
[39] Smithells Metals Reference Book, Butterworth Heinemann, Boston (1992).
[40] F. R. D. Boer, R. Boom, W. C. M. Mattens, A. R. Miedema and A. K. Niessen, Cohesion In Metals: Transition Metal Alloys (Cohesion And Structure), Elsevier Science Ltd, (1989).
[41] S. K. Chung, D. B. Thiessen and W.-K. Rhim, *Rev. Sci. Instrum.* **67,** 3175, (1996).
[42] Rocky Mountain Instrument Corperation (2010).
[43] D. Holland-Moritz, S. Klein and N. A. Mauro, *Personal Communication* (2008).
[44] Calcium Fluoride CaF2 Physical and Chemical Properties, Corning Incorperated (2003).
[45] O. W. Richardson, The Emission of Electricity from Hot Bodies, Longmans Green and Company, (1916).
[46] T. Meister, Aufbau und Regelung eines elektrostatischen Levitators, Fakultät für Elektrotechnik und Informationstechnik der Ruhr-Universität Bochum, Bochum (2000).
[47] G. Rustan, Discussion of UV source effectiveness, In: N. A. Mauro, Editor (2010).
[48] V. M. Wessels, K. F. Kelton, J. R. Rogers, A. K. Gangopadhyay and N. A. Mauro, *Personal Communication* (2009).
[49] P.-F. Paradis, T. Ishikawa and S. Yoda, *International Journal of Thermophysics* **26,** 1031, (2005).
[50] C. P. Cagran, L. M. Hanssen, M. Noorma, A. V. Gura and S. N. Mekhontsev, *International Journal of Thermophysics* **28,** 581, (2007).
[51] J. R. Rogers and N. A. Mauro, *Personal Communication* (2009).
[52] Optotherm (2008).

[53] T. J. Tanaka, T. J. Lutz, J. M. McDonald, R. E. Nygren, K. P. Troncosa, R. Bastasz and M. Clift, Sn-25% at. Li Results and Liquid Metal Emissivity Measurements, Sandia National Laboratories, Los Angeles, APEX meeting (2001).
[54] W. Dokko and R. G. Bautista, *Metallurgical and Materials Transactions B* **11,** 309, (1980).
[55] H. Kawamura, H. Fukuyama, M. Watanabe and T. Hibiya, *Meas. Sci. Tech.* **16,** 386, (2005).
[56] A. Gangopadhyay and J. C. Bendert, Discussions of proceedures for Cp determination from ESL Free Cooling and Modulation Techniques, (2009).
[57] G. W. Lee, UNDERCOOLING, LOCAL STRUCTURE AND PHASE TRANSITION IN ICOSAHEDRAL QUASICRYSTAL FORMING Ti-Zr-Ni ALLOY LIQUIDS, *Physics*, Washington University, St. Louis (2004).
[58] Process Sensors (2009).
[59] R. C. Bradshaw, J. R. Rogers, K. F. Kelton, R. W. Hyers and D. P. Schmidt, *Rev. Sci. Instrum.* **76,** 125108, (2005).
[60] J. C. Bendert, Details of implementation of numerical algorithm in ESL density determination, (2010).
[61] J. Almer, D. Haeffner, P. Lee, U. Lienert, S. Rogers, K. Kump, G. Vera, P. Chupas, J. Hanson and Y. Gao, *Internal Report, APS* (2003).
[62] K. K. Sahu and N. Mauro, *Personal Communication* (2010).

# Chapter 5

## Short and Medium Range Order in Zr-based Binary Liquids[€]

[€]Portions of this work appear in the manuscript *"Short and Medium Range Order in $Zr_{80}Pt_{20}$ Liquids."* N. A. Mauro, V. Wessels, J. C. Bendert, S. Klein, A. K. Gangopadhyay, M. J. Kramer, S. G. Hao, G. E. Rustan, A. Kreyssig, A. I. Goldman, K. F. Kelton. *In press, Physical Review B, 2011*.

### 5.1. Introduction

It is well known that Zr-based metallic glasses tend to have a high glass forming ability (GFA) [1, 2]. Some are bulk metallic glasses (BMGs), i.e. glasses with a critical casting thickness of 1 mm or greater. Icosahedral quasicrystal phases (*i*-phases) are frequently found in crystallized Zr-based BMG's [3-7], suggesting that these amorphous structures have a high degree of icosahedral short-range order (ISRO). This is supported by recent high-energy synchrotron X-ray diffraction studies of Zr/Ti-based liquids and glasses, which have linked supercooling and the glass transition to an increase in icosahedral and icosahedral-like local order [8-10]. More quantitative structural studies of BMG's, however, are hindered by their chemical complexity, often containing four or more components. Studies of simpler Zr-based binary alloys have been more successful, providing important insights into the role of local atomic structures in dictating the transformation pathways and supercooling potential for a liquid [11].

It has been reported that $Zr_{80}Pt_{20}$ can be quenched into the amorphous state by melt-spinning [12, 13] and that the X-ray diffraction patterns of the glassy ribbons show a pre-peak near 1.7 $Å^{-1}$ [14]. Studies of $Zr_xPt_{100-x}$ ($73 \leq x \leq 77$) glasses [15] show that the intensity of the pre-peak increases with increasing Pt concentration, suggesting that it arises from Pt-Pt correlations. Pre-peaks, indicating some degree of medium-range order

(MRO), have been observed previously in experimental [15-19] and theoretical [18, 20, 21] studies of metallic glasses and liquids. However, reports of pre-peaks, and therefore MRO, in metal-metal liquids are rare [22, 23], found primarily in metal-metalloid binary [24, 25] and Al-based binary and ternary [17, 26, 27] alloys. In this chapter, we present the results from *in-situ* high-energy synchrotron X-ray diffraction studies of equilibrium and supercooled $Zr_{80}Pt_{20}$ liquids (eutectic composition) using the Beamline Electrostatic Levitation (BESL) [28] technique. These data show that the MRO is very stable, with the pre-peak present from 550°C above the liquidus temperature, $T_l$, to 200°C below $T_l$, the lowest temperature that could be studied before crystallization. Consistent with previous structural studies of melt-spun ribbons of the same composition, the MRO observed in the liquid is dominated by a Pt-Pt correlation. The Honeycutt Andersen (HA) and Voronoi polyhedra (VI) analyses of the atomic structures obtained by Reverse Monte Carlo (RMC) fits to the measured scattering data, in a more limited temperature range, show that the liquid is dominated by icosahedral and icosahedral-like local order. This order increases modestly with supercooling.

Previous RMC fits conducted in this group were unconstrained, or conventional, RMC fits, fitting to only one set of data. The $Zr_{80}Pt_{20}$ liquid allows not only a fundamental study of the local order and structural evolution of a glass forming melt, but also provides the opportunity to study the differences between conventional RMC and RMC fits that are constrained with chemical information provided from molecular dynamics (MD) simulations. While the origin of the MRO remains the Pt-Pt correlation, the details of the distribution of local atomic configurations, as measured by VI, differ markedly between constrained and unconstrained RMC fits.

## 5.2. Experimental

Master ingots (~1.0g) of $Zr_{80}Pt_{20}$ were prepared by arc-melting (as described in Chapter 1) high purity elemental Zr (99.95%, including nominally 3% Hf) and Pt (99.995%) on a water-cooled copper hearth in a high-purity (99.999%) Ar atmosphere. Small spherical samples (~2.5 mm) were prepared for supercooling and *in-situ* liquid structure studies at the Advanced Photon Source (Station 6-ID-D in the MUCAT Sector), using the Washington University Beamline Electrostatic Levitator (WU-BESL). The WU-BESL is described in detail in Chapter 4.

Two optical pyrometers were used to measure the sample temperature over two ranges, 160-800°C and 600-2300°C, with a relative accuracy of better than 2% over the entire temperature range for this series of experiments. To obtain maximum supercooling, the levitated samples were heated approximately 300°C above the liquidus temperature and subsequently free-cooled. Crystallization from the metastable liquid, marked by a sharp rise in temperature (recalescence), limited the lowest temperature that X-ray diffraction studies could be made to 250°C below $T_l$. By controlling the laser power, it was also possible to make isothermal measurements at different temperatures. Given the very low vapor pressure for both elements at this temperature, no deposition was found (< .2 % mass loss). Simultaneous non-contact density measurements were made using the shadow method [29, 30] with a Pixelink PL-B742U CCD camera and a 450 nm backlight. Video was taken at a frame rate of 15 fps averaging of up to 300 frames at each isothermal step. The details of machine vision volume measurement algorithm is described elsewhere [30] and in Chapter 4 of this work. The relative

precision of the density data was ~1.5% over the temperature range studied with an absolute accuracy of 3-5%.

High energy (E = 129 keV, λ = 0.0969Å) diffraction studies of the liquids were made to high-$q$ (15 $Å^{-1}$) in a transmission geometry using a Perkin Elmer XRD 1621 AN/CN Digital X-ray Detector (BESL 2009) and a GE Revolution 41-RT amorphous Si flat panel X-ray detector (BESL 2010) at various sampling rates. The data obtained during the two experimental campaigns were consistent. Structure factors, $S(q)$, were derived from the scattering data according to the procedures laid out in Chapter 2. Liquid diffraction patterns were obtained as a function of temperature by taking 20 second exposures per temperature step, and then converted into static structure factors according to Equation 1,

$$S(q) = \frac{I(q) - \sum_{i}^{n} a_i \left| f_i(q) \right|^2}{\left| \sum_{i}^{n} a_i f_i(q) \right|^2} + 1 \qquad (1)$$

where I($q$) is the experimental intensity, $a_i$ is the atomic fraction of each element, and $f_i(q)$ is the $q$-dependent atomic form factor for each species. The sums range over all species and an isotropic and statistically homogeneous atomic distribution is assumed.

Since Pt has an energy absorption edge near the incident X-ray energy (Figure 5.1), a fluorescence correction was required to the $I(q)$ data before constructing $S(q)$. Without experimental fluorescence data, this correction is difficult to employ, but work done by V. Wessels [31] on Hf containing elements was used as a reference. Wessels plotted the correction for a series of Ti-Zr-Hf-Ni alloys with varying concentrations of Hf and this plot was used as a rough guideline for the correction. When the correction at 20

at. % was applied a very small additional empty chamber correction was required (.05% above 1 to 1 subtraction) to obtain a well behaved $S(q)$.

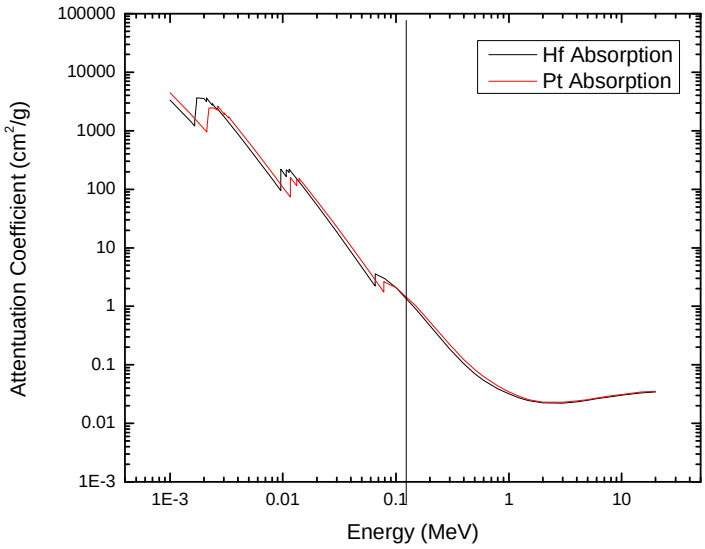


**Figure 5.1-** Attenuation coefficients as a function of energy for Hf and Pt [32].

## 5.3. Results

### *5.3.1. Scattering and Thermophysical Results*

With cooling, the levitated liquid drops show a single recalescence near 978°C (197°C below the liquidus temperature). The diffraction data following that recalescence can be indexed to a phase mixture of $Zr_5Pt_3$ (hexagonal) and β-Zr, consistent with the equilibrium phase diagram for the eutectic liquid [33]. Simultaneous density data were taken with the scattering data. The raw image data were converted into number density, which follows a linear trend that is well approximated by

$$\rho(T) = -1.564 \cdot 10^{-6} \frac{1}{°C \cdot Å^3} T + .047 \frac{1}{Å^3}. \quad (2)$$

The measured liquid X-ray static structure factors determined from 1607°C, 432°C above the liquidus temperature ($T_l$ = 1175°C), down to the maximum supercooling of 197°C (T=978°C) are shown in Figure 5.2. The $S(q)$s oscillate well around unity over the entire range of $q$ (Figure 5.2a.), indicating the high quality of the experimental data and that the appropriate correction were made for absorption, background and Compton scattering. The primary peak (Figure 5.2b.) sharpens, increases in magnitude, and shifts to lower scattering angle with decreasing temperature, reflecting an increasing density and a more ordered liquid with decreasing temperature. The shoulder on the second peak (Figure 5.2c.) becomes more pronounced with supercooling, which is frequently argued to indicate an increase in icosahedral and icosahedral-like order [9]. A pre-peak is observed at ~1.7 $Å^{-1}$ for all temperatures (Figure 5.2d.). The small variation of the pre-peak with cooling indicates that the atomic bonds associated with the MRO are strong compared to thermal energy. This pre-peak is of interest because it doesn't often emerge in X-ray scattering studies of liquids.

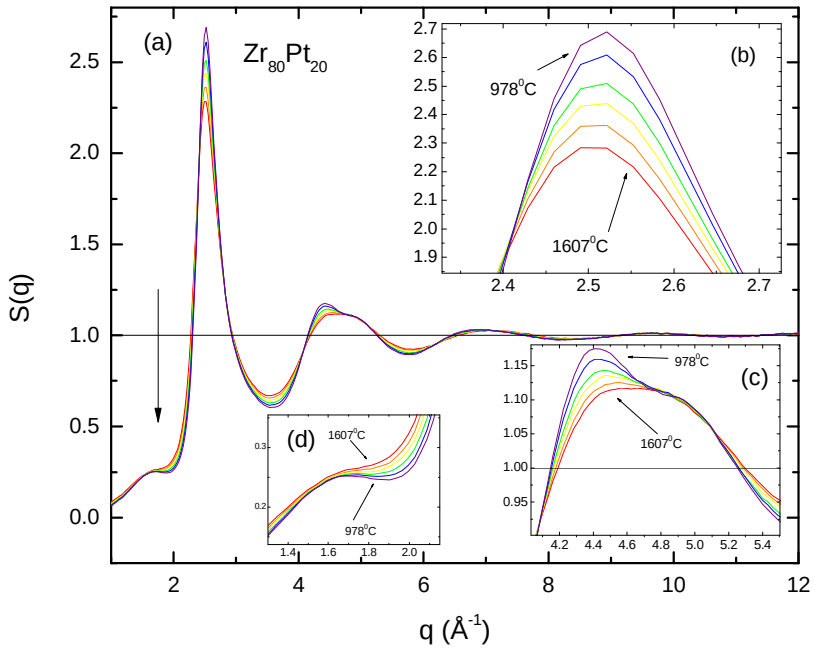


**Figure 5.2-** Static structure factor, $S(q)$ for a.) liquid $Zr_{80}Pt_{20}$ at 1607°C, 1474°C, 1345°C, 1217°C, 1090°C, and 978°C. The inserts show the evolution of $S(q)$ with decreasing temperature for (b) the primary peak, (c) the second peak and (d) the pre-peak (indicated with an arrow in the figure showing the total structure factor).

The total pair correlation function is constructed from a Fourier transform of the structure factor and is presented in Figure 5.3. The nearest-neighbor peak shows a slight trend to larger $r$ with decreasing temperature. This is somewhat counterintuitive: We expect that as the temperature is lowered and the density increases, decreasing thermal motions would decrease the nearest-neighbor distances. However, the peak sharpens at the same time, so the shift to larger length scales is likely an artifact of the simultaneous shifting and sharpening. This is substantiated from the data shown in Figure 5.2; the first peak in the static structure factor shifts to higher-$q$, corresponding to a *shorter* length scale, with

decreasing temperature. The second peak and subsequent peaks in $g(r)$ do show a shift to shorter length scales, as expected. Additionally, it should be noted that the data lower than about $r$ = 2.5Å in the Fourier transform has been removed; these show truncation ripples, but also do not go to zero as expected for $g(r)$. Since $g(r)$ represents the spherically averaged probability of finding an atom at a given distance away from an average central atom, it should go to zero at a distance smaller than the hard sphere cutoff distance. However, the finite $q$ range over which the data were taken results in this artifact in nearly all BESL 2007, 2009 and 2010 data.

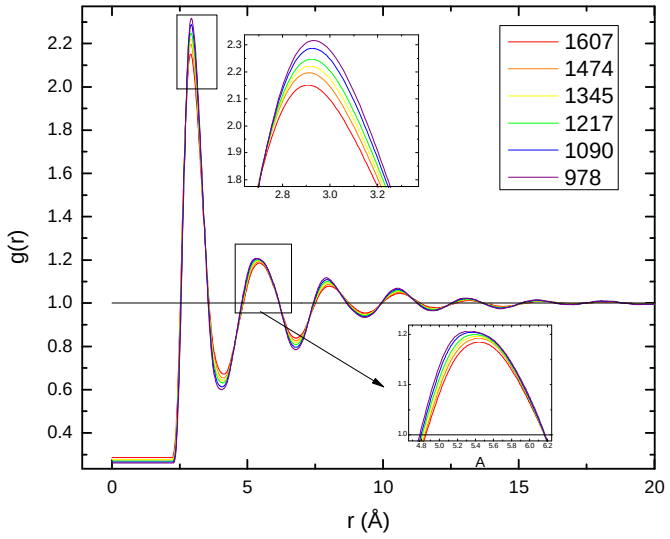


**Figure 5.3-** Total pair correlation functions, $g(r)$, for liquid $Zr_{80}Pt_{20}$ at 1607°C, 1474°C, 1345°C, 1217°C, 1090°C, and 978°C.

Wessels [31] found that in the $Cu_{46}Zr_{54}$ liquid, a notable splitting in the nearest-neighbor peak, which grew in intensity with decreasing temperature, was found when examining the difference between $g(r)$ measured at various temperatures. This feature was

attributed to chemical ordering in the liquid with decreasing temperature. Similar curves were constructed for the $Zr_{80}Pt_{20}$ data, subtracting $g(r)$ at 1607°C from the $g(r)$ at lower temperatures. However, no splitting of the nearest-neighbor peak was observed.

To further investigate atomic structures and chemical ordering in the liquids Reverse Monte Carlo fits were performed on the $S(q)$ data at all temperatures. Two sets of fits were performed. First, conventional RMC fits were made to the data. The description and details of the RMC technique can be found elsewhere [34-36]. For this study, random starting configurations of 10000 atoms with the appropriate stoichiometric composition were confined in a cubic box with dimensions appropriate to the measured density. The RMC cutoff distances were set nominally at 2.26Å for all atomic pairs, consistent with the measured total radial distribution function, $g(r)$. Second, atomic structures were obtained by RMC fits to the measured X-ray static structure factors, $S(q)$, while constraining the fit with partial pair correlation functions (PPCFs) obtained from *ab initio* Molecular Dynamics simulations using the Vienna *ab initio* simulation package (VASP) [37-41]. Partial pair correlation functions were prepared by M. J. Kramer from the MD simulations for this study. The system consisted of 100 atoms (80 atoms of Zr and 20 atoms of Pt) in a cubic box with periodic boundary conditions; this is described more fully in Wang *et al.* [42]. The MD simulations provide partial pair correlation functions out to ~ 12 Å when none are experimentally available. The description and details of the constrained RMC (CRMC) technique can be found elsewhere [34-36]. The CRMC cutoff distances were determined from the MD partial pair correlation functions.

The experimental $g(r)$ data showed that the minimum distance remained approximately constant over the temperature range studied. The SRO of the atomic

structures obtained from the RMC process was evaluated using both the Honeycutt Andersen index (HA) [43] and Voronoi tessellation [44, 45] methods. A nearest-neighbor cutoff distance of nominally 4.08Å was used for these studies, again, determined from the total $g(r)$.

### *5.3.2. Conventional RMC*

Atomic models that are consistent with the experimental scattering data were obtained. All fits gave a reduced chi squared error of between 6.50 and 7.20. An example of the quality of the fit is shown in Figure 5.4 for the $S(q)$ data taken at 1345$^{o}$C. A slightly more detailed look at the fit for the $S(q)$ data taken at 978$^{o}$C is shown in Figure 5.5. In all cases, a good fit was obtained to the primary peaks and higher-$q$ ($q$ > 6.5 Å$^{-1}$) oscillations, with the fit intensity falling slightly below the measured intensity on the shoulder of the second peak. Figure 5.4 shows that that no correlations exist in the starting configuration. The location of the pre-peak was well reproduced, but the intensity of the fit was slightly larger than the experimental data. In this fit, $q$-dependent atomic form factors were used in reconstructing the total $S(q)$. The influence of the $q$-dependence of the form factors on RMC fits is discussed in more detail in Chapter 6, where an analysis of scattering data from Ni-Nb liquids is presented.

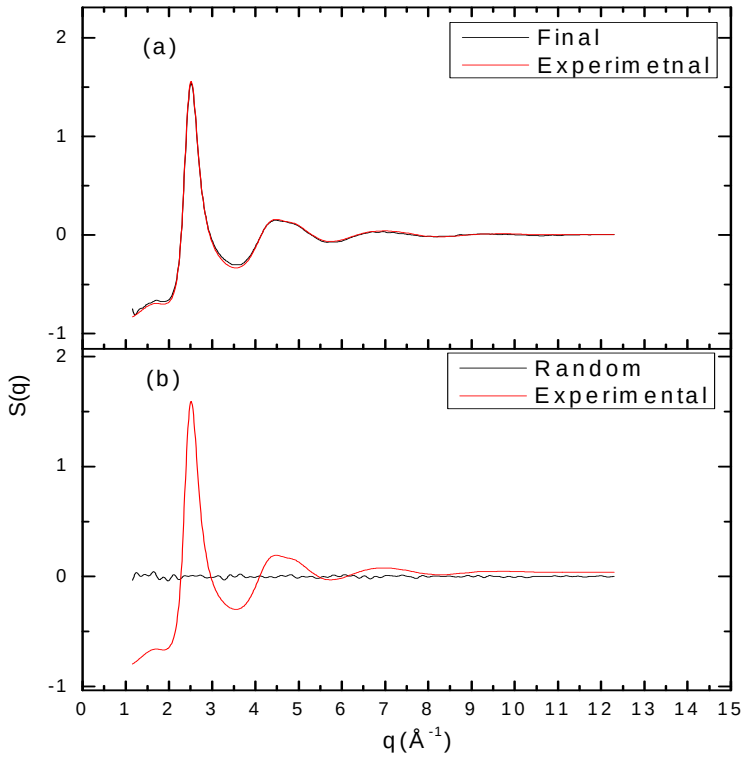


**Figure 5.4-** Experimental $S(q)$ for $Zr_{80}Pt_{20}$ at 1345C. (a) The final conventional RMC fit is shown with the experimental data. (b) The initial random configuration is shown with experimental data to show that no correlations exist in the starting configuration.

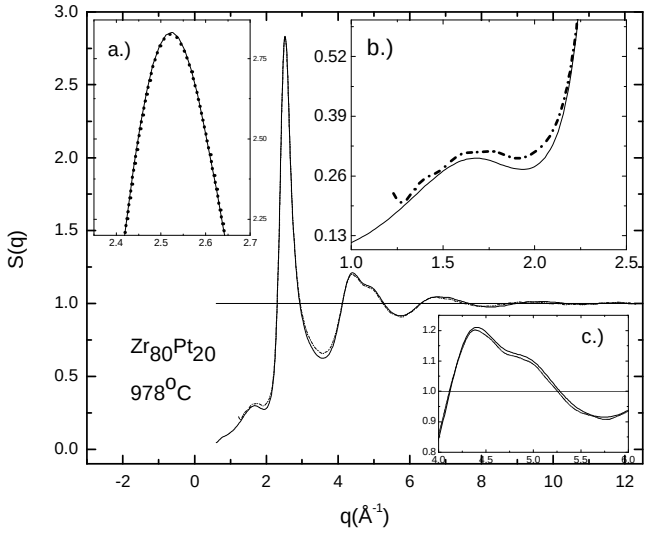


**Figure 5.5-** *S*(*q*) (solid line) and the corresponding RMC fit (dotted line) for liquid $Zr_{80}Pt_{20}$ at 978°C. The inserts show the fits for (a) the primary peak, (b) the pre-peak and (c) the second peak.

The RMC code assumes the Faber-Ziman formalism [46] for isotropic materials to construct the total pair correlation function, $g(r)$, and the structure factor, $S(q)$, from the experimental data. The partial pair correlation functions, $g_{i-j}(r)$, were calculated directly from the final atomic configurations using

$$g_{i-j}(r) = \rho_{ij}^{-2} \left\langle \sum_i \sum_{j \neq k} \delta(\mathbf{r}_i) \delta(\mathbf{r} - \mathbf{r}_j) \right\rangle, \tag{3}$$

where $\rho_{ij}$ is the partial density,

$$\rho_{ij} = \rho_0 \sqrt{a_i a_j}\,, \tag{4}$$

$\rho_0$ is the average atomic density, and $a_i$ and $a_j$ are the atomic concentrations of the two species in the liquid. The partial structure factors (PSFs), $S_{i-j}(q)$, and the partial pair correlation functions, $g_{i-j}(r)$, are related by a Fourier transform:

$$S_{i-j}(q) = 1 + 4\pi\rho_{ij}\int \left(g_{i-j}(r) - 1\right)\frac{\sin qr}{qr} r^2 dr \tag{5}$$

$$g_{i-j}(r) = 1 + \frac{1}{4\pi\rho_{ij}}\frac{2}{\pi}\int \left(S_{i-j}(q) - 1\right)\frac{\sin qr}{qr} q^2 dq\,. \tag{6}$$

The total $S(q)$ is obtained from the three partial structure factors, $S_{i-j}(q)$, the X-ray atomic form factors, $f_i$, and the atomic concentrations,

$$\begin{aligned} S(q) - 1 &= \frac{\sum_i \sum_j a_i a_j f_i f_j \left(S_{i-j}(q) - 1\right)}{\left(a_i f_i + a_j f_j\right)^2} \\ &= \sum_{i,j} \gamma_{ij}(q)\left(S_{i-j}(q) - 1\right) \\ &\equiv S'_{Zr-Zr}(q) + S'_{Zr-Pt}(q) + S'_{Pt-Pt}(q) \end{aligned} \quad . \tag{7}$$

The $\gamma_{ij}$ are the weighting factors for each partial structure factor. In large part, the magnitude and the *q*-dependence of these factors dictate which correlations are manifest in X-ray diffraction studies. The weighting factors for $Zr_{80}Pt_{20}$ are shown in Figure 5.6. The Pt-Pt weighting factor is reduced by a factor of ~4 from the others due to the low concentration of Pt.

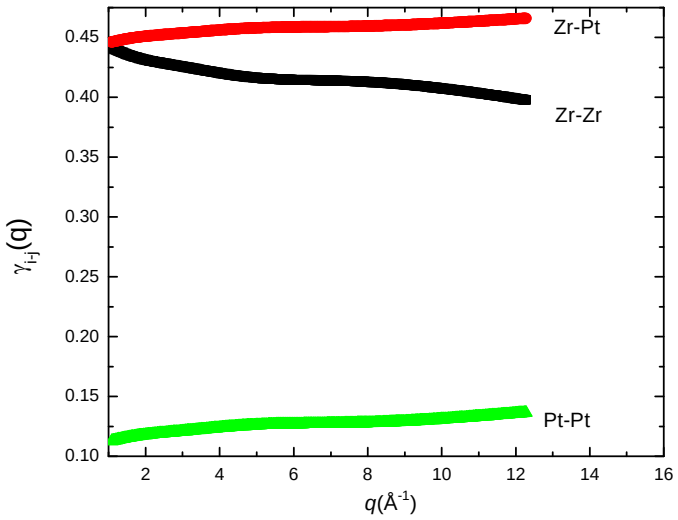


**Figure 5.6-** Faber-Ziman weighting factors for the $Zr_{80}Pt_{20}$ liquid used to construct the total structure factor from the partial structure factors.

Three partials, $S'_{i-j}(q)$, represent the properly weighted contributions from the three species-species correlations to the overall structure factors; they are shown in Figure 5.7. for the 978°C data. Consistent with previous reports for the glass [42, 47], the $S'_{i-j}(q)$ data indicate that the pre-peak originates primarily from a Pt-Pt correlation.

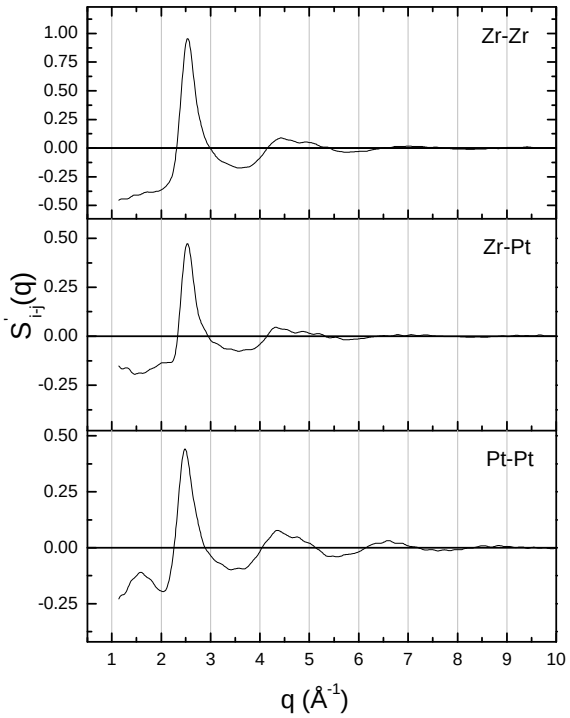


**Figure 5.7-** Properly weighted contributions from the three species-species correlations to the overall structure factors.

Qualitatively, aside from the Pt-Pt pre-peak, the partials are very similar. While the $S'_{Pt-Pt}(q)$ show slightly enhanced high-*q* oscillations compared to the other partials, the primary peak position is similar in all partials, reflecting similar average nearest neighbor correlations due to the large number of similar configurations sampled in the highly mobile liquid. The partial pair correlation functions, calculated by using Equation 6, are shown in Figure 5.8. These partial pair correlation functions have not been scaled according to the Faber Ziman formalism. The length scale corresponding to the pre-peak in $S_{Pt-Pt}(q)$ is not obvious in $g_{Pt-Pt}(r)$. Interestingly, the positions of the first peaks in $g_{i-j}(r)$ are 2.95Å for Zr-Zr, 2.90Å for Zr-Pt and 3.05Å for Pt-Pt (Figure 5.8), deviating

from what is expected from scaling based on atomic size. To confirm this trend, a wide range of closest approaches were used in the RMC fits, with each partial varying between 2.25Å and 2.59Å, in a variety of ratios (Zr-Zr:Zr-Pt:Pt-Pt) including, but not limited to, 2.59:2.42:2.25 (consistent with the atomic radii), 2.49:2.25:2.59 (consistent with peak positions reported by Saida [48]), and 2.40:2.25:2.25 (consistent with the large heat of mixing between Zr and Pt (~100 kJ/mol [49])). In all cases, the first peak in $g_{Pt-Pt}(r)$ is located at slightly larger *r* than the first peak in the other partials; $g_{Zr-Zr}(r)$ and $g_{Zr-Pt}(r)$ have first peaks located at approximately the same position.

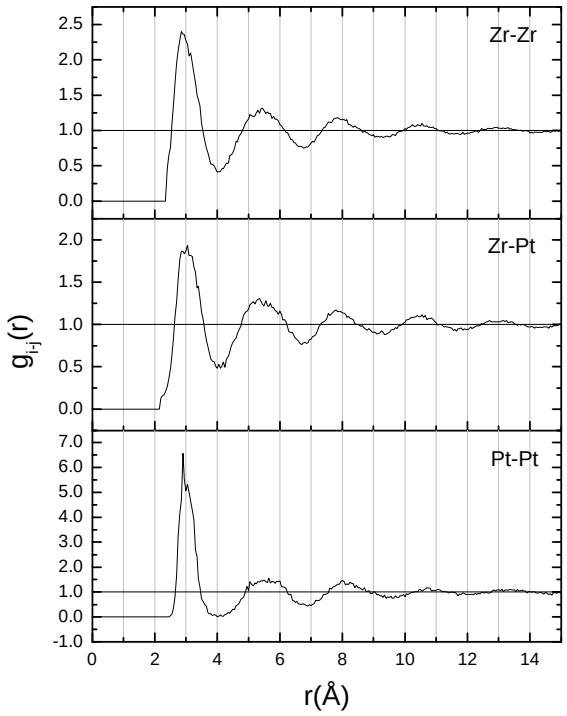


**Figure 5.8-** Partial pair correlation functions from a conventional RMC fit of the $Zr_{80}Pt_{20}$ liquid at 978°C. Note, a Fourier filter was employed to emphasize the peak position, so the artifact in the Zr-Pt partial seen in Figure 5.9 doesn't appear.

The first peak position of the partials in this fit is of concern. The Zr-Zr position is smaller than expected from the atomic radius (3.10-3.20). At elevated temperature, there is no obvious reason why this should occur. Bonding between Zr atoms will not distort this distance appreciably, although the short Zr-Pt distance can be explained by strong bonding. Even the large Pt-Pt distance may be qualitatively understood in terms of clustering between groups of atoms and bond stretching that may occur. In this liquid, Pt is the solute and because pair bonding doesn't exist in isolation of other atoms, clustering likely stretches the Pt-bonding distances in a compromise between atomic size and

bonding enthalpy. This is only speculative, however, but the anomalous Zr-Zr distance is motivation for constrained RMC fits, discussed later in this chapter.

The chemically specific partials are summarized together below in Figure 5.9. As mentioned, all of the partial pair correlation functions have the same qualitative form. Specifically, the first peak is larger than the second and all peaks are smooth. This same behavior in the partials was observed in structures obtained from an RMC fit to Zr-Pd diffraction data [50].

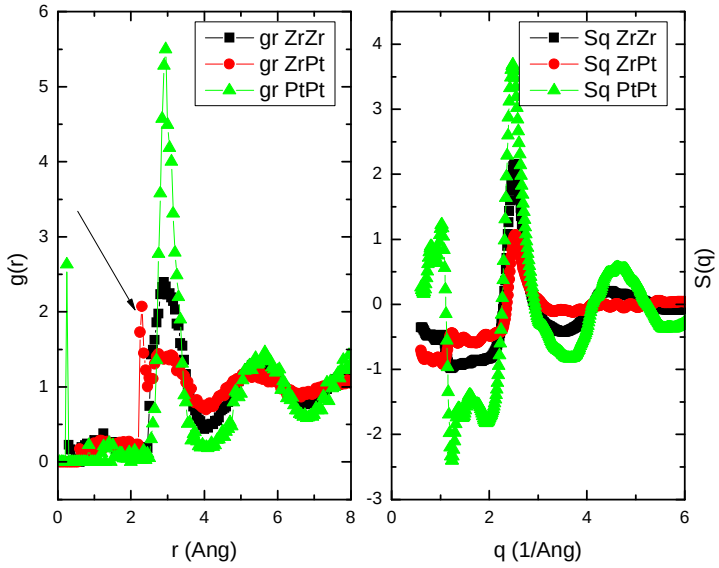


**Figure 5.9-** Partial pair correlation functions and partial structure factors for 1345°C. Note the anomalously small and sharp peak in $g(r)_{Zr\text{-}Pt}$ that is indicated by arrow. This occurs for all physically realistic Zr-Pt cutoff distances.

The results of an HA index analysis of the structures obtained from conventional RMC fits to the data are shown in Figure 5.10. All liquid structures are dominated by icosahedral (1551) and distorted icosahedral (1431+1541) order. Additionally, there is a significant amount of body centered cubic (BCC) (1661) crystal-like order, but no

appreciable face centered cubic (FCC) (1421) or hexagonal close packed (HCP) (1422) order. With cooling, there is a slight increase in the icosahedral and BCC order, as observed in other Zr-based liquids [9, 10, 42]. An examination of the 1551 index shows that the species specific distribution of root-pairs (Zr-Zr, Zr-Pt, Pt-Pt) remains relatively unchanged for all temperatures studied.

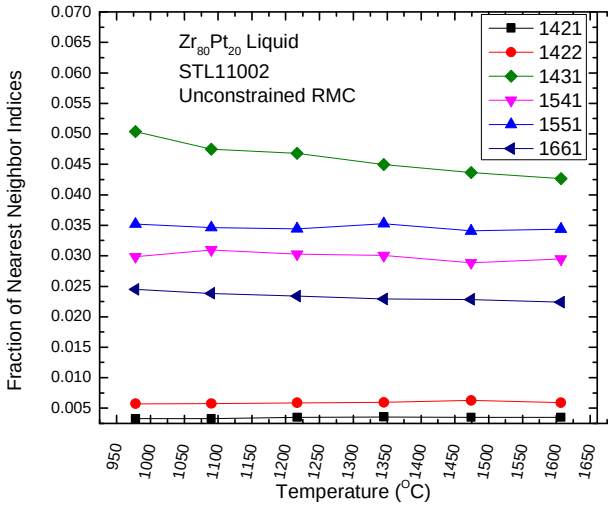


**Figure 5.10-** The prominent HA indices for the RMC liquid structure as a function of temperature.

HA indices provide information about the local short-range order around two given atoms (the root pair). They do not, however, indicate whether complete clusters exist. Voronoi polyhedra analysis provides more complete information about the topological and chemical environment around central atoms. The Voronoi polyhedra are characterized according to the scheme laid out it Chapter 2. Figure 5.11 and Figure 5.12 show the fractions of the most abundant Voronoi polyhedra detected in the RMC atomic structures. Consistent with previous Voronoi analyses of glasses of similar composition to the liquid studied here [42, 48], the most abundant Zr-centered clusters (Figure 5.12) are the 13

coordinated (<0,3,6,4>, <0,1,10,2>), and 12 coordinated (<0,3,6,3>, <0,2,8,2>) polyhedra. The number of <0,3,6,4>, <0,1,10,2>, and <0,2,8,2> structures increase with supercooling, while the average coordination number around the Zr atoms remains unchanged at 13.1±0.1. It should be noted that a Voronoi analysis of the local structure of the primary crystallizing phase, β-Zr (bcc), yields only <0,6,0,8> (truncated octahedrons) around the Zr atoms. This index is not a dominant feature in the RMC liquid structures.

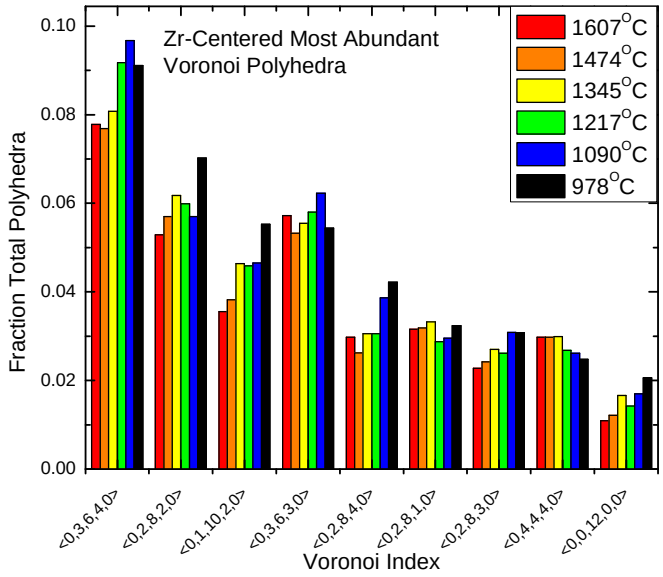


**Figure 5.11**-Dominant Zr-centered Voronoi polyhedra as a function of temperature.

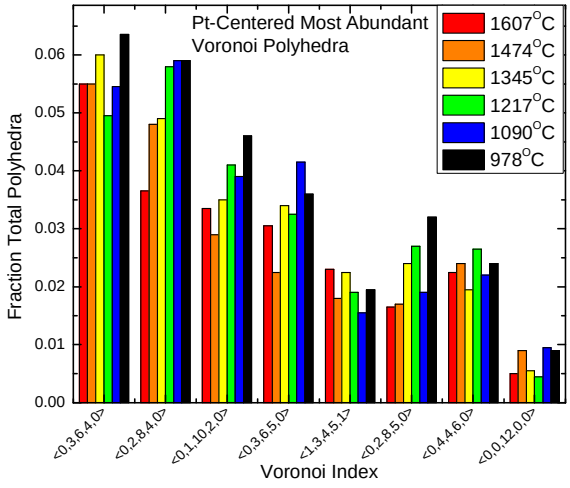


**Figure 5.12-**Dominant Pt-centered Voronoi polyhedra as a function of temperature**.**

The HA analysis indicates that icosahedral and distorted icosahedral order are dominant in the liquid structure, yet the density of <0,0,12,0> Voronoi polyhedra (icosahedral clusters) is low. This may be due partially to the failure of the HA analysis to identify complete clusters. Additionally, Hao *et al* [51] point out that distinct topological classes can be very closely related by simple distortions or coordination number increases. It can be shown (see Appendix II.9) that <0,2,8,2>, <0,1,10,2>, <0,4,4,4> and <0,2,8,4> , which are present in significant concentration, are closely topologically related to <0,0,12,0>.

Based on high-energy X-ray scattering studies [15, 42, 48] and molecular dynamics (MD) simulations [42] of amorphous $Zr_{80}Pt_{20}$ and $Zr_{73}Pt_{27}$, the pre-peak in the structure factor has been attributed to Pt-Pt correlations. Further, Saida *et al*. [48] and Wang *et al.* [42] found that the Pt-centered <0,2,8,1> cluster, which is a structural unit of the hexagonal primary crystallizing phase, $Zr_5Pt_3$, is also dominant in the glass. Interestingly, the distribution of abundant Pt-centered clusters in the undercooled liquid

differs from these reports for the glass, and also differs from the structure of $Zr_5Pt_3$. The discrepancy between the liquid structures determined from conventional RMC fits and the structures for the glasses reported earlier, particularly the small Zr- Zr peak distance, must be explored further through CRMC. To date, there is very little information about the reliability of conventional RMC and even less about the details of how local structures determined through reverse methods change when constrained with experimental of simulated chemical information. The Voronoi analysis demonstrates, very generally, that local structures of the atomic ensemble obtained by conventional RMC have an icosahedral or distorted icosahedral character.

### *5.3.3. Constrained RMC (CRMC)*

Since RMC fits provide the most disordered structures that fit the experimental data, poorly constrained RMC fits can produce partials with nonphysical peak positions. Lacking additional scattering data, MD partial pair-correlation functions are used to force the local atomic order to be consistent with both the experimental $S(q)$ and the results of the MD simulation. Convergence of these constrained RMC fits from different starting configurations was explored, taking both ordered (cubic symmetry) and random initial configurations at each temperature. No statistically relevant differences emerged in the final HA and VI distributions, nor in the partial pair correlation functions obtained from these two initial configuration. The final configurations simulated from the random initial configurations are reported here.

Atomic models that are consistent with both the experimental scattering data and the MD simulations were obtained. The quality of the fit is shown in Figure 5.13 for the

$S(q)$ data taken at 978°C, 1090°C, 1217°C, and 1345°C. In all cases, a good fit was obtained at all scattering *q*. However, the intensities of the CRMC fit for the pre-peak and the primary peak are slightly higher than the experimental data, while the second peak, including the developing shoulder, was fit extremely well. The location of the pre-peak was also reproduced well. The discrepancy between the fit and experimental data for the pre-peak worsens slightly as the temperature is reduced, indicating that a quantitative analysis of the trends in ordering inherent to the second nearest neighbors is less reliable than for the nearest neighbors.

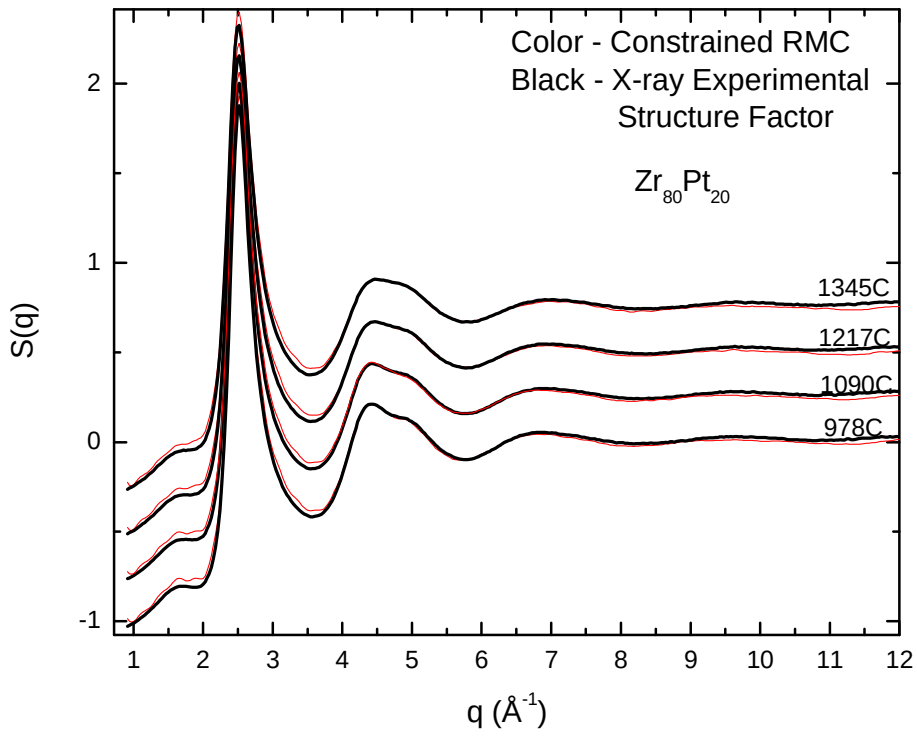


**Figure 5.13-** Experimental *S*(*q*) (solid lines) and the corresponding CRMC fit (dashed lines) for liquid $Zr_{80}Pt_{20}$ at 1345°C, 1217°C, 1090°C, and 978°C**.**

The MD-derived partial pair-correlation functions provide realistic chemical interactions, at least to the first few shells [45]. MD data are often criticized for their small simulation size and fast quench rates. For liquid structure studies, where atomic mobility is high and typically atomic order does not extend beyond next-nearest neighbors, the MD results are expected to be accurate [47]. In Figure 5.14 we show the correspondence between the MD simulation partials and the CRMC partials at one temperature, 1345°C. The CRMC partials agree well with those obtained from the MD simulation.

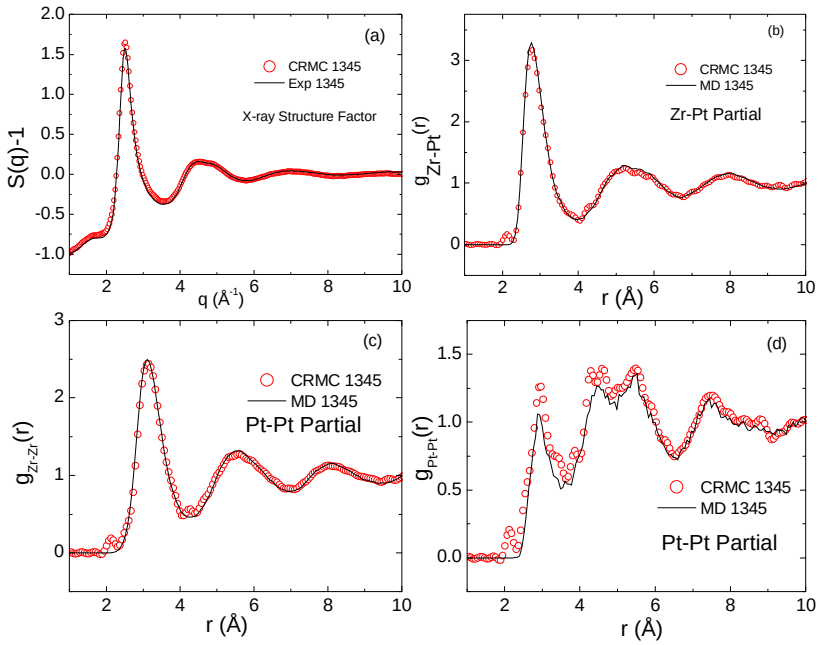


**Figure 5.14**-(a) Structure factor $S(q)$ of $Zr_{80}Pt_{20}$ liquid at 1345°C with the constrained RMC fit. Partial pair-correlation functions $g_{i-j}(r)$ from MD and CRMC fits for (b) Zr-Pt, (c) Zr-Zr, and (d) Pt-Pt.

The small peak that is observed around 2.0Å in all of the partial pair correlation functions is nonphysical and appears to be an artifact of the fit, most likely due to a small difference between the number density for the experimental data and the simulations, and the finite resolution of the experimental data. A similar level of agreement is observed at all temperatures (not shown). With the constraints, the primary peak of the Zr-Pt partial (Figure 5.14b) is near 2.80Å. It grows slightly with decreasing temperature, but doesn't sharpen or shift significantly. The location of the nearest neighbor peak is slightly smaller than would be expected from atomic size considerations alone, but is reasonable given the large negative heat of mixing between Zr and Pt (~100 kJ/mol [49]). The primary peak in the Zr-Zr partial $g(r)$ is approximately 3.12Å, consistent with atomic size considerations. The peak sharpens and moves to lower $r$ with decreasing temperature. The primary peak in the Pt-Pt partial is near 2.95Å. With decreasing temperature, the next-nearest neighbor peak (second peak in $g(r)$) splits to form peaks at 4.50Å and 5.50Å. Interestingly, the intensity of the first peak *decreases* with decreasing temperature while the second peak *increases*; the intensity of the third peak remains relatively unchanged. All peak positions in the Pt-Pt pair correlation function remain unchanged over the temperature range studied and consistent with previous reports for the glass [15, 42, 47]. As in the conventional RMC fits the pre-peak in the $S(q)$ data originates primarily from the Pt-Pt correlation.

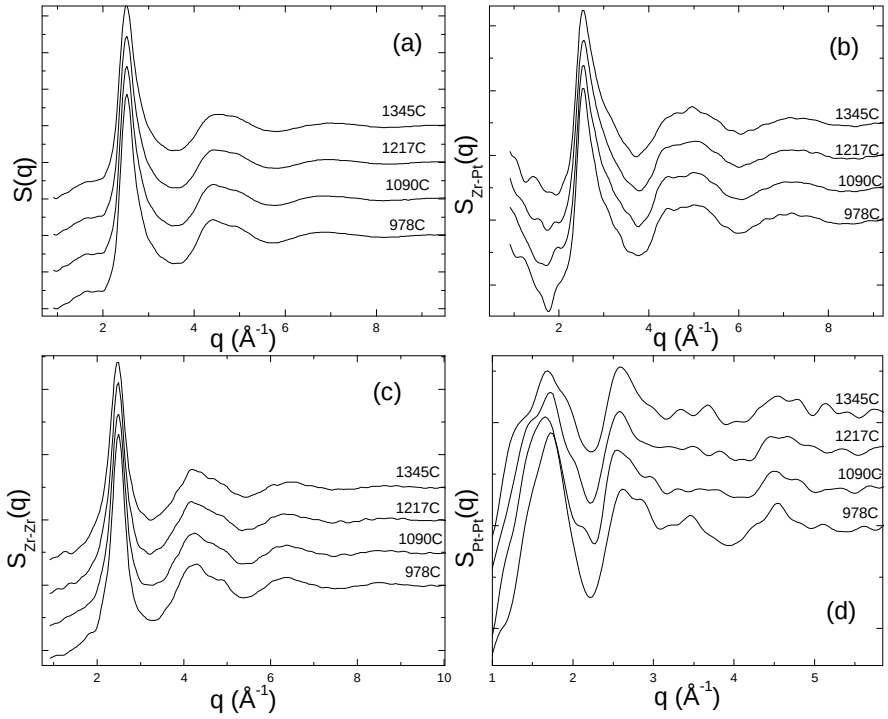


**Figure 5.15-** *S*(*q*) produced from CRMC fits at all temperatures. (a) Total Structure factor; (b) Zr-Pt partial structure factor, showing an asymmetric first peak and no developing shoulder in the second peak; (c) Zr-Zr partial structure factor showing a developing should in the second peak; (d) Pt-Pt partial structure factor displaying a prominent pre-peak at all temperatures**.**

As noted earlier (Figure 5.2), the total structure factor shows a developing shoulder on the high-*q* side of the second peak, which, as shown in Figure 5.15c, is dominated by changes in Zr-Zr correlations. The second peak in the Zr-Pt partial structure factor (Figure 5.15b) is symmetric and does not appear to contribute significantly to the shoulder in the total *S*(*q*). A strong asymmetry is observed in the Zr-Pt partial structure, broadening on the high-*q* side, indicating a relatively large distribution in the nearest neighbor bonding.

The results of an HA index analysis of the structures obtained from the CRMC fits to the data are shown in Figure 5.16 All liquid structures are dominated by icosahedral (1551) and distorted icosahedral (1431+1541) order. While the amount of distorted icosahedral order decreases slightly with decreasing temperature, the amount of icosahedral order increases, causing the overall icosahedral-like order to slightly increase with undercooling. Additionally, there is a significant amount of body centered cubic (1661+1441) crystal-like order, which increases slightly with decreasing temperature, but little face centered cubic (1421) or hexagonal close packed (1422) order. The numbers of 1311, 1321, 1331 bond pairs, representing the rhombus symmetrical features of short-range order, show very modest decreases with decreasing temperature. The small increases in icosahedral and BCC order are consistent with observations in other Zr-based liquids [9, 10, 42], although the amount of change reported there is generally larger than observed here. An examination of the 1551 index shows that the species-specific distribution of root-pairs (Zr-Zr, Zr-Pt, Pt-Pt) remains relatively unchanged for all temperatures studied.

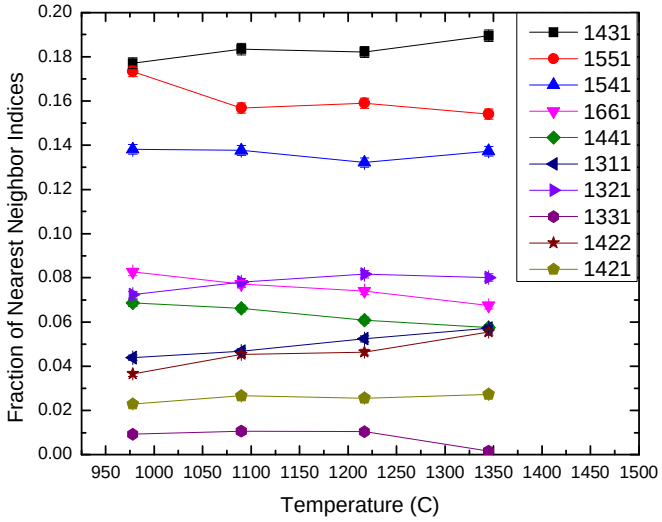


**Figure 5.16-**The prominent HA indices for the RMC liquid structure as a function of temperature**.**

Figure 5.17 and Figure 5.18 show the fraction of the most abundant Voronoi polyhedra detected in the RMC atomic structures. Consistent with previous Voronoi analyses of glasses of similar composition to the liquid studied here [42, 48], as well as the conventional RMC from the previous section, the most abundant Zr-centered clusters are the 14 coordinated (<0,2,8,4>), 13 coordinated (<0,3,6,4>, <0,1,10,2>, <0,2,8,3>), and 12 coordinated (<0,3,6,3>, <0,2,8,2>) polyhedra. The CRMC shows a larger amount of <0,2,8,4> order, but this seems to be the only significant difference. The numbers of all of these polyhedra increase slightly with decreasing temperature and the average coordination number around the Zr atoms changes from 12.75 to 13.05 over the temperature range, becoming largest at the lowest temperature. As with the conventional RMC fit, the <0,6,0,8> (truncated octahedrons) polyhedra is not a dominant feature in the RMC liquid structures

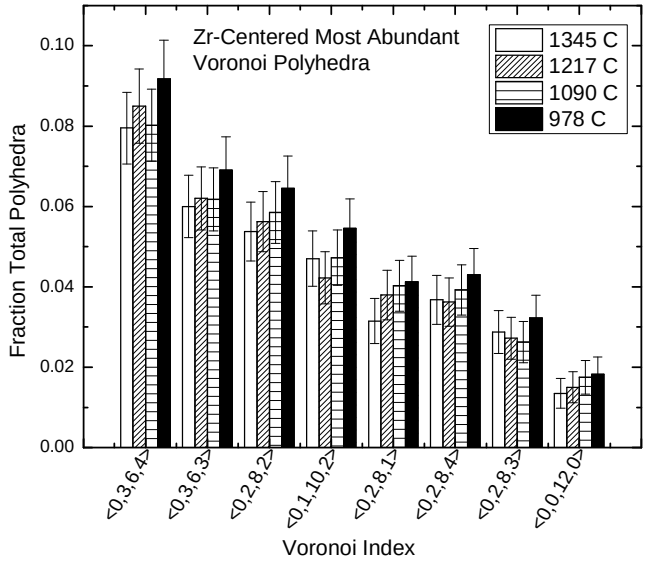


**Figure 5.17-**Dominant Zr-centered Voronoi polyhedra as a function of temperature**.**

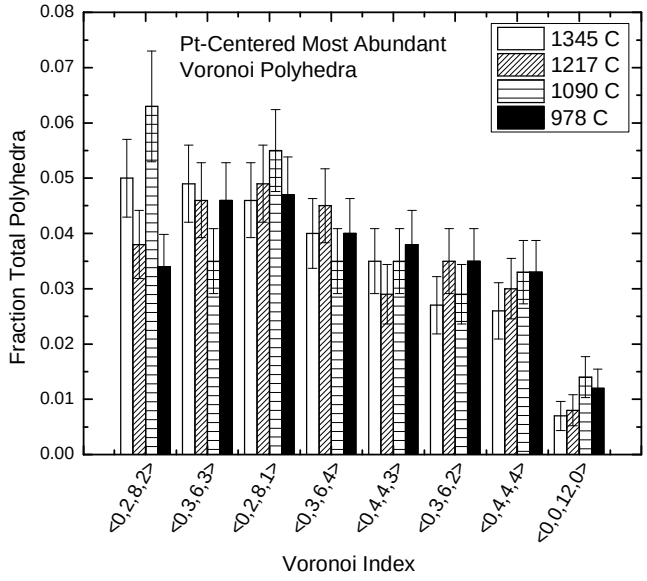


**Figure 5.18-**Dominant Pt-centered Voronoi polyhedra as a function of temperature.

While the HA analysis indicates that icosahedral and distorted icosahedral order are dominant in the liquid structure, the fraction of <0,0,12,0> Voronoi polyhedra (icosahedral clusters) is low, as with the conventional RMC fit. The icosahedral order likely continues to increase during the quench, supported by the observation [12] that the quasicrystalline phase appears first upon devitrification of amorphous ribbons produced by rapid quenching, or in partially crystalline ribbons produced by slower quenching.

Based on the CRMC fit of the $Zr_{80}Pt_{20}$ liquid, the most dominant Pt-centered clusters are the 13 coordinated (<0,3,6,4>), 12 coordinated (<0,2,8,2>, <0,3,6,3>, <0,4,4,4>), and 11 coordinated (<0,2,8,1>, <0,4,4,3>, <0,3,6,2>) polyhedra. The distribution of Pt-centered polyhedra shows no trend that exceeds the statistical noise, and the increase in the <0,2,8,2> index at 1090°C is likely not significant.

The distribution of abundant Pt-centered Voronoi polyhedra that exist in the liquid differs significantly from the unconstrained RMC. Table 5.1, below, shows a direct comparison between the two distributions. The most abundant polyhedra have only a single overlapping index, but more importantly, the unconstrained polyhedra are dominated by 14 and 15 coordinated structures, while the unconstrained have 11, 12 and 13 coordinated structures. The lower coordination makes physical sense, as Pt is small, compared to Zr; direct evidence that in this case, and possibly in other cases, that conventional RMC produces unphysical distributions.

**Table 5.1-** Voronoi index distribution comparison between RMC and CRMC fits in $Zr_{80}Pt_{20}$ liquid

| Coordination | Constrained | Unconstrained |
|---|---|---|
| 15 | | <0,2,8,5> |
| 14 | | <0,2,8,4><br><0,3,6,5><br><1,3,4,5,1><br><0,4,4,6> |
| 13 | <0,3,6,4> | <0,3,6,4><br><0,1,10,2> |
| 12 | <0,2,8,2><br><0,3,6,3><br><0,4,4,4> | |
| 11 | <0,2,8,1><br><0,4,4,3><br><0,3,6,2> | |

The persistence of the Pt-centered <0,2,8,1> polyhedra in the liquid and glassy Zr-Pt, and its existence in the $Zr_5Pt_3$ structure demonstrates the stability of this cluster. The large supercooling that is observed and glass formation indicate a significant nucleation barrier for $Zr_5Pt_3$. That the <0,2,8,1> polyhedra is observed in all phases seems to be inconsistent with this, although it should be emphasized that it is only one of the dominant clusters in the liquid (Figure 5.18). An examination of the Pt-Pt distances in the liquid and in the $Zr_5Pt_3$, show striking similarities between the distances present in the liquid and the crystal. The $Zr_5Pt_3$ has a $Mn_3Si_5$ type structure with a $P6_3/mcm$ (No. 193) space group [52] and room temperature unit cell dimensions $a$ = 8.2Å and $c$ = 5.4Å.

In this structure there are 6 Pt atoms in the unit cell [53] (the 6g site: (x,0,¼)). The Pt-Pt distances were calculated by generating the Cartesian coordinates for the Pt atoms in the crystal structure, based on the 6g site coordinates and simply calculating the distances between them: 3.16Å, 4.33Å, 5.41Å, 7.64Å, etc. As we can see, these match up extremely well with the distances identified in the Pt-Pt liquid partial: first peak 2.89Å; second peak 4.46Å; and third peak 5.49Å. While the first peak is slightly contracted from the smallest Pt-Pt distance in the $Zr_5Pt_3$ structure, the large number of distorted icosahedral structures in the liquid is likely more important for glass formability in this liquid.

The topological and chemical SRO and MRO order in Zr-Pt liquids, then, likely have an impact on glass formation and crystallization. $Zr_{80}Pt_{20}$ is known to form the *i*-phase directly from the melt while $Zr_{70}Pd_{30}$ does not [12], suggesting that the liquid that is richer in Zr contains more icosahedral order. Previous studies of Zr-Pt glasses support this, showing that the devitrification pathway changes with Zr concentration, going from *glass* $\Rightarrow$ $Zr_5Pt_3$ at high Pt concentration, to *glass* $\Rightarrow$ *i-phase* $\Rightarrow$ $Zr_5Pt_3$ with increasing Zr [54] and suggesting that icosahedral clusters are the source of the MRO observed. However, the recent observation of a pre-peak in a Zr-Ni liquid [23] from neutron scattering data, which is reported not to have dominant icosahedral short-range order, suggests that icosahedral order itself isn't the source of MRO. Instead, a pre-peak is a manifestation of chemical and topological ordering originating from the most common polyhedral clusters in each liquid—icosahedral or otherwise. This is further supported by the reports of pre-peaks in marginal Al-TM-RE glass forming alloys and alkali metal alloys with Pb [55]. The pre-peak in a given liquid is enhanced (or reduced) depending on

the atomic scattering factors and alloy composition. X-ray diffraction studies are insufficient to resolve this order in all cases.

This study, along with providing information about MRO in the Zr-Pt liquid, allowed the first case study in this group of the effect of constraining RMC fits. To our knowledge, it is the first study of its kind in a liquid metal. A comparison of the results of the fits leads to the following conclusions and conjectures:

1. The dominance of icosahedral-like order, based on HA indicators, is robust.
2. The details of the average chemical ordering, as measured by the partial structure factors and partial pair correlation functions, vary greatly between the two techniques.
3. The details of the more complete topological order around a given atom, as measured by the Voronoi distribution, are not reliable in conventional RMC.

### 5.4. Scattering Studies of Zr-( Rh, Pd, Ir, Pt, Au) Liquids

The topological and chemical SRO and MRO observed in Zr-Pt liquids reported in the previous sections, likely has an impact on glass formation and crystallization. As indicated, the pre-peak, or more generally order on any particular length scale is enhanced (or reduced) depending on the atomic scattering factors and alloy composition. Since CRMC fits produce different local structures, and structural evolution in a liquid that is believed to be related to glass formability, the importance of the *knowledge* of MRO is important. Here, we quantify the effect of incomplete structural information on the observed local atomic order.

Structural similarities in the Zr-Pd and Zr-Pt liquids were explored. First, Zr-Pd liquids do not display a pre-peak in the X-ray structure factor, as shown in Figure 5.19. This MRO feature is also missing in X-ray diffraction patterns from the Zr-Pd glass [12]. Although not shown here, the structure factors for the other Zr-Pd compositions show no evidence for a pre-peak, just as the other Zr-Pt compositions *do* show a pre-peak. Given that Pd and Pt have very similar sizes ($r$ ~ 1.38 Å) and have very similar heats of mixing with Zr (Pd ~ -90 kJ/mol; Pt ~ -100kJ/mol), in conjunction with the result in the previous report of $Zr_{80}Pt_{20}$ that indicated that the pre-peak resulted from a Pt-Pt correlation, a similar Pd-Pd correlation on the same length scale is expected. It seems likely that the correlation *exists*, but that it cannot be resolved from X-ray studies.

A comparison between Zr-Rh and Zr-Ir is also shown in Figure 5.19. Like Pd and Pt, Rh and Ir have similar sizes ($r$ ~ 1.35 Å) and similar heats of mixing with Zr (Rh ~ -72 kJ/mol; Ir ~ -76 kJ/mol), indicative of strong bonding. However, a pre-peak is observed in Zr-Ir, but not in Zr-Rh liquids.

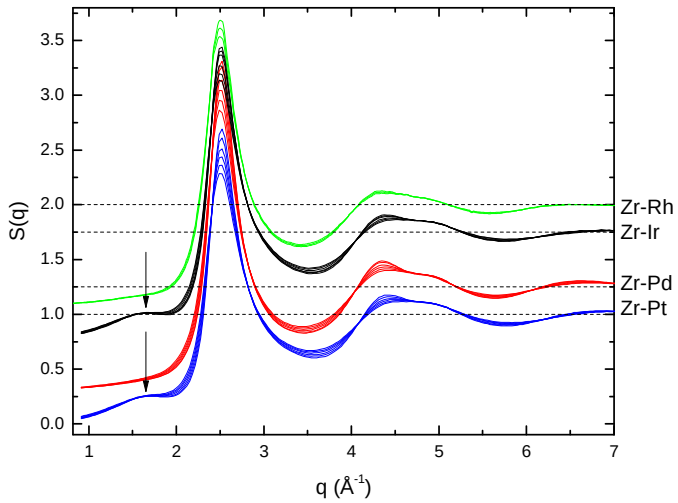


**Figure 5.19-** Static structure factors for eutectic Zr-Pd, Zr-Pt, Zr-Rh, and Zr-Ir liquids. A pre-peak is present in all near eutectic Zr-Pt and Zr-Ir compositions.

There is some evidence from anomalous diffraction experiments [19] that MRO exists in Zr-Pt and Zr-Au glasses, consistent with our findings, but also in Zr-Pd glasses. Like Zr-Pt and Zr-Ir eutectic liquids, a pre-peak is observed in Zr-Au (Figure 5.20). These results indicated that a large contrast in the form factors of the solute and solvent atoms is required to observe the MRO. Both the Zr-Pd and Zr-Rh binary liquids likely have MRO, leading us to speculate that MRO is a very common feature in Zr-based liquids where the solutes have large negative heats of interaction with the Zr solvent.

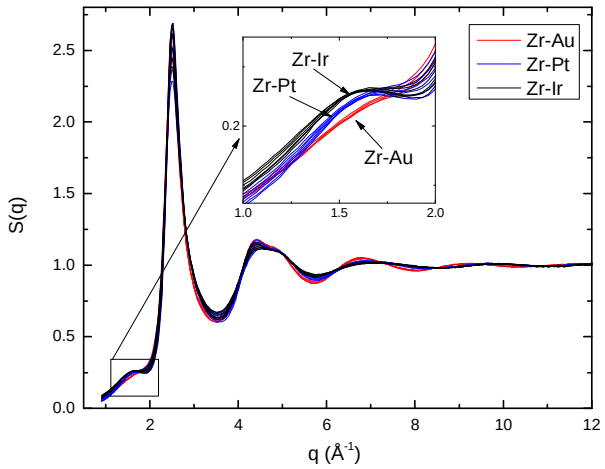


**Figure 5.20-** Static structure factor for eutectic Zr-Ir, Zr-Pt, and Zr-Au liquids.

## 5.5. Effect of limited MRO information in the Zr-Pt liquid

Without chemical information about the correlation in the Zr-Pd liquid, we can explore the effect of the lack of the pre-peak on a RMC fit by removing the pre-peak in the $Zr_{80}Pt_{20}$ liquid $S(q)$ data. This approach has the drawback that in this liquid we *do* have chemical information about the Pt-Pt correlation that we could use to constrain the RMC fit. The use of that, however, would compromise the desired investigation. Conventional RMC is therefore used to explore the effect of the missing MRO information. This study is incomplete, but the conventional RMC fits do reproduce the correct origin of the pre-peak in the partial structure factors. However, the Voronoi distribution of local structures differs. As shown in Figure 5.21, an exponential was fit in the range $0.9\text{Å}^{-1} \leq q \leq 2.25\text{Å}^{-1}$, forcing the intensity of $S(q)$ to smoothly go to zero at $0.9\text{Å}^{-1}$, thus removing the pre-peak. Conventional RMC fits were then made to the original and modified $S(q)$s using the experimental density and cutoff distances of 2.00Å for all atomic pairs. Before the

results are discussed, it should be noted that the technique used here for removing the pre-peak is NOT likely to completely remove the contributions from the MRO in the $S(q)$. Since the pre-peak is not well separated from the main peak, it changes the shape of the main peak, on its low-$q$ side. However, a comparison between the Zr-Pd and Zr-Pt $S(q)$ first peak width near the occurrence of the pre-peak showed very little difference, indicating that the peak widths are roughly the same. Assuming there *is* MRO in Zr-Pd and we can't observe it, it would seem that removing the pre-peak might be a reasonable approximation to not measuring MRO and studying its subsequent effect on the RMC.

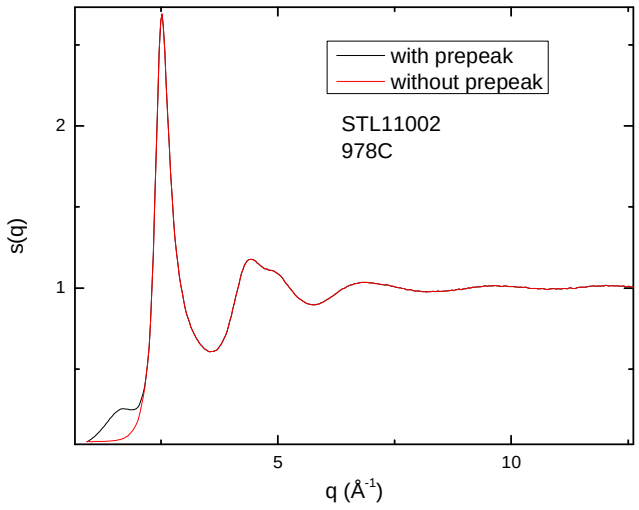


**Figure 5.21-**Experimental $S(q)$ (black) for the $Zr_{80}Pt_{20}$ liquid at 978°C and the manipulated experimental data (red) where the pre-peak has been removed. An exponential was fit in the range $0.9Å^{-1} \leq q \leq 2.25Å^{-1}$, forcing the intensity of $S(q)$ to smoothly go to zero at $0.9Å^{-1}$, thus removing the pre-peak. .

The results of the two RMC fits are shown in Figure 5.22. The fits to the total $S(q)$ with and without pre-peak (Figure 5.22a) show that the fits reproduce the behavior on the low-$q$ side of the main peak well. The Pt-Pt partial structure factors from the two

fits (Figure 5.22b) show that the MRO disappears when we remove the pre-peak in the fashion described above, further validating the experiment. Surprisingly, however, other than this, the partial pair correlation functions show little change when the pre-peak is removed, and no obvious changes to the second coordination shell. The results from both unconstrained RMC fits (Figure 5.23) show the extended Zr-Zr first neighbor distance from the previous section. The only discernable difference between the two occurs in the magnitude of the first peak of the Pt-Pt PPCF. We see again that the MRO is not always manifest strongly in the PPCF, but is in the PSF.

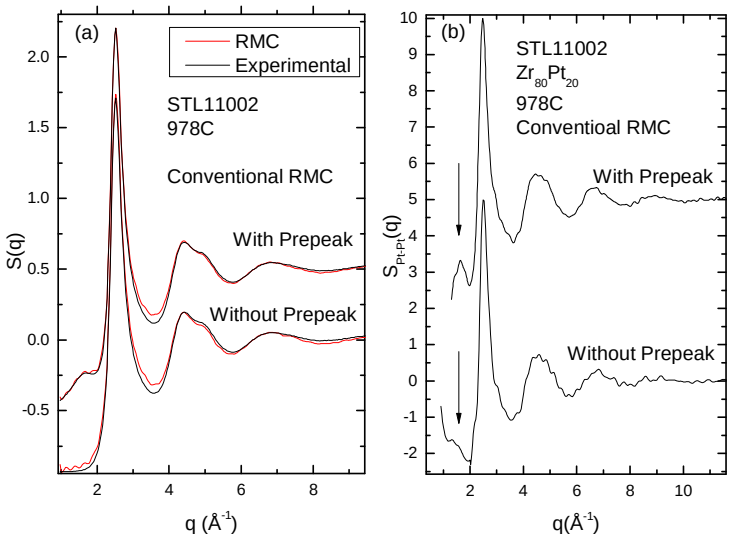


**Figure 5.22-** (a) The results of a conventional RMC fit to an $S(q)$ with the pre-peak and with the pre-peak removed. (b) Pt-Pt partial structure factor contribution to the total $S(q)$.

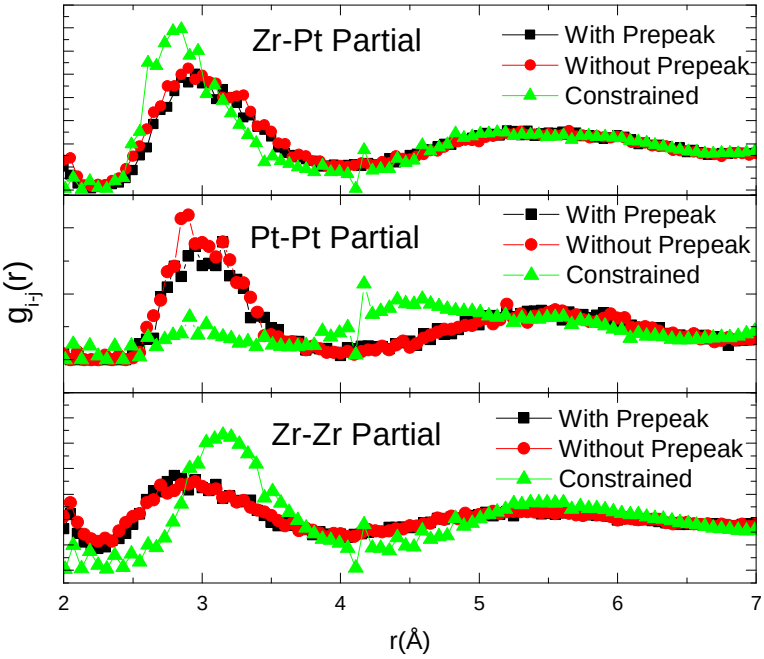


**Figure 5.23-** Partial pair correlation functions for conventional RMC (fit to $S(q)$ with pre-peak (black) and without pre-peak (red)) and constrained (green) RMC using all 3 MD partials. Note the similarities between the two unconstrained RMC fits: when the pre-peak is removed, the changes in the partials are minimal.

To quantify the effect of the pre-peak removal on the local atomic order in the RMC-fit structures, the HA index distributions for conventional RMC with and without the pre-peak were compared to those obtained from the constrained RMC (Figure 5.24). While the conventional and constrained RMC show differences, even with the pre-peak, the trend in the order of most frequent pairs (1431-1551-1541-1661) is robust. We know that the Voronoi distributions change markedly, so a comparison of the complete polytetrahedra distribution is not useful in this study. However, when the pre-peak is removed, the amount of pure icosahedral order drops markedly. Based on the single cluster fits by T. H. Kim [50] and others [56], the intuitive link between icosahedral short

range order and the total structure factor is rooted in the presence of a shoulder on the second peak. In this study, that shoulder, while present in the data, wasn't removed with the pre-peak. Thus, it seems that the SRO is also affected by the presence of the MRO. While this might have been expected, and while it is unclear whether changes to correlations on any length scale can have perturbative effects on the HA index distribution, such a strong influence of MRO on the HA-1551 index (nearly 20%) was unexpected.

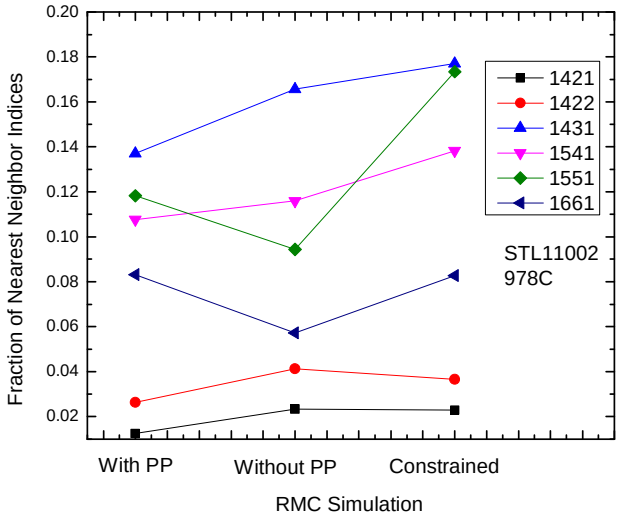


**Figure 5.24**-HA index distributions for conventional RMC with and without pre-peak compared to the distribution from the constrained RMC. While the conventional and unconventional RMC show differences even with the pre-peak, the trend in the order of most frequent pairs (1431-1551-1541-1661) is robust. When the pre-peak (PP) is removed the amount of pure icosahedral order (1551) drops by nearly 20%.

In the previous section, we speculated that the MRO arises from the formation of icosahedral-like clusters. That may be specific to this liquid. As pointed out earlier, MD and experimental diffraction studies of Zr-Pt and Zr-Pd liquids and glasses have

consistently shown a tremendous amount of icosahedral order. Thus, at least in the Zr-Pt liquid, the MRO observed (dominated by the Pt-Pt correlation) is due to icosahedral-like clustering. Other liquids [15-19] also show MRO but aren't necessarily dominated by icosahedral SRO, strongly suggesting that the MRO, whatever their origin, are manifestations of clustering of any type. If we presume that the study discussed here, where the pre-peak was removed and the modified data then fit, is equivalent to an analysis of the experimental scattering data from the Zr-Pd liquid, it follows that:

1. If Pd is substituted for Pt in the $Zr_{80}Pt_{20}$ liquid, given the similarities in size between the two solutes, and the similar enthalpies of mixing of Pd and Pt with Zr, the only substantive difference between the two liquids would be a difference in the scattering contributions from the Pd-Pd correlations.
2. MRO in the Zr-Pd liquid does exist and is dominated by Pd-Pd correlations, which are not observable in an X-ray experiment due to an insufficient atomic form factor contrast between Zr and Pd.
3. The lack of a pre-peak would cause an artificial suppression of the 1551 index.

In fact, previous X-ray diffraction studies and subsequent conventional RMC fits of $Zr_{67}Pd_{33}$ by T. H. Kim [50] support these assertions. With decreasing temperature, the Zr-Pd liquid static structure factor displayed a developing shoulder on the second peak ([50] Figure 6.1, pg 187), but the HA index distribution over the temperature range ([50] Figure 6.5, pg 192) showed a dramatic *decrease* in the amount of 1551 pairs observed. In fact, the frequency of 1551 pairs is less than the observed number of 1421 pairs, which is quite unusual. We propose here that the HA index distribution measured by T. H. Kim [50] does not accurately reflect the physical SRO. The lack of a pre-peak, and the

inability to constrain the RMC fits with MD or additional information about chemically specific correlations changes the observed HA index distributions in a dramatic way. These results suggest that care should be exercised when interpreting atomic configurations that were obtained from unconstrained RMC fits to X-ray diffraction data alone for alloy liquids and glasses. The structures obtained may be unreliable or even misleading, particularly if features are missing in the diffraction data due to, for example, the lack of contrast difference in the atomic form factors, as discussed here.

### 5.6. Constraining with limited chemical information

Information about chemically specific PPCFs is not readily available in most cases. MD simulations are time consuming and lack the authority and reliability of an actual experiment. Neutron data is even more limited in availability—experiments on levitated samples using ESL and more commonly EML are expensive in both cost and time. The third Neutron Electrostatic Levitator (NESL) in the world is currently being designed and built jointly by Washington University, Iowa State University and Oakridge National Lab, but will not be available for use until 2012 at the earliest. However, EXAFS and anomalous diffraction [19, 48] experiments on amorphous systems can provide additional information about chemically specific SRO and MRO. In particular, anomalous diffraction studies of Zr-based binary glasses have provided some evidence for the existence of MRO in Zr-Au and even Zr-Pd binaries [19]. EXAFS experiments in the Zr-Pt eutectic glass [48] provided some information about changes in the local structure during devitrification, however, the reports of nearest neighbor distances were inconsistent with MD simulations and remain suspect. These studies have demonstrated

the possibility of obtaining at least one PPCF. It is possible to constrain RMC fits to $S(q)$ with both the MD PPCFs and with EXAFS data. A key questions is how reliable the fits will be should incomplete chemical SRO and MRO information become available. Fitting to a select number of the available MD partials is a first step in addressing this question.

Three incompletely constrained RMC fits were made to the $S(q)$ data for $Zr_{80}Pt_{20}$ at 978C. The structure obtained was analyzed in terms of the HA indices and a comparison was made to the HA indices obtained from the structure obtained from a fully constrained RMC fit. The same cutoff distances and densities were used in the four RMC fits. The only difference in the four fits was that the first utilized only the Zr-Pt PPCF to constrain the fit, the second used only the Zr-Zr PPCF, the third used only the Pt-Pt PPCF and the last used all three PPCFs to completely constrain the fit, as discussed in section 5.3.3. The correlation functions obtained from these constrained RMC fits, using the different partials from the MD simulations are shown in Figure 5.25. The black curves correspond to the constraints with all PPCFs, the red curves correspond to the use of the Pt-Pt PPCF only, the green curve corresponds to the use of the Zr-Zr PPCF only, and the blue curves correspond to the use of the Zr-Pt PPCF only.

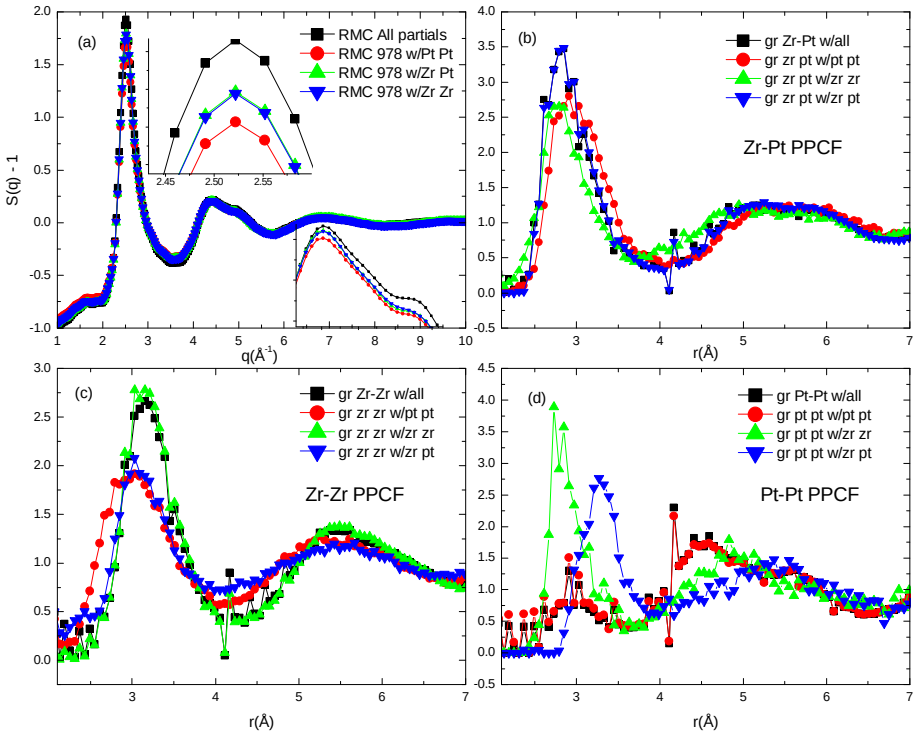


**Figure 5.25-** Correlation functions obtained from constrained RMC, using the different partials from the MD simulations. The black curves correspond to constraining with all PPCFs, the red curves correspond to constraining with just the Pt-Pt PPCF, the green curve corresponds to constraining with just the Zr-Zr PPCF and the blue curves correspond to constraining with just the Zr-Pt PPCF. (a) Total $S(q)$; (b) Zr-Pt PPCF RMC result; (c) Zr-Zr PPCF RMC result; (d) Pt-Pt PPCF RMC result.

The behavior of the PPCFs obtained from the RMC fits to the experimental $S(q)$ data vary with the nature of the PPCF used. As expected, in each case the partial that is used as a constraint has the same value after the fit as it does when all of the MD partials are used to constrain the fits (black curve). However, the other two PPCFs are different from their value when the fit is completely constrained. The total $S(q)$ (Figure 5.25a)

shows some differences in the pre-peak, the first peak and the second peak. These demonstrate that the best fit to $S(q)$ is obtained when all of the PPCFs are used to constrain the RMC and that the use of only the Pt-Pt partial gives the worst fit. This is unfortunate: The Pt-Pt partial (Figure 5.25d) is the one that changes most as the constraint is varied, but it is also the one that can most likely be measured from resonant experiments [57].

Based on the large magnitude of the Faber-Ziman weighting functions (Figure 5.6), we expect that the X-ray diffraction experiments would best capture the Zr-Pt correlations. Constraining the RMC fit with the Zr-Pt PPCF, then, would be least influential. Also, unfortunately, this isn't the case. The RMC Zr-Pt PPCF varies with the specific constraint(Figure 5.25) , as does the HA index distribution (Figure 5.26). If we take the HA index distribution fit to "All" as the correct distribution, the Zr-Pt HA index differs appreciably.

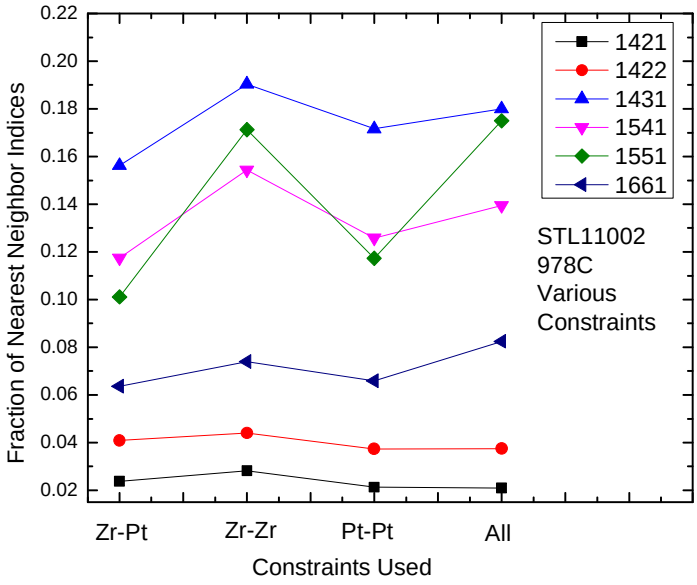


**Figure 5.26**-HA index distribution for constrained RMC fits at 978C using various constraints.

One of the most obvious indications that the unconstrained RMC result was unphysical was the large Zr-Zr peak distance. Thus one test of the importance of a particular constraint is that of nearest-neighbor distance. Again, unfortunately, this distance in the Zr-Zr RMC PPCF (Figure 5.25c) depends strongly on the specific constraint. Constraining to only the Zr-Pt or Pt-Pt PPCF produces an unphysical Zr-Zr distance. Using the Zr-Zr PPCF to constrain the RMC fit produces the HA and overall PPCF behavior that best matches the results from the completely constrained fit. The HA index distribution doesn't match completely, but the ordering of number of indices is preserved, which doesn't happen with the other incompletely constrained fits. The Pt-Pt correlation function suffers the most from using only the Zr-Zr PPCF as a constraint. A comparison of the partial structure factors for constrained RMC fits to the $S(q)$ for $Zr_{80}Pt_{20}$ liquid at 978C using all of the MD PPCFs (dashed lines) and only the Zr-Zr MD PPCF (solid lines) (Figure 5.27) shows good correspondence between the Zr-Zr and Zr-Pt PPCFs. The pre-peak is still reproduced in the Pt-Pt PPCF as are the positions of all the peaks in each PPCF.

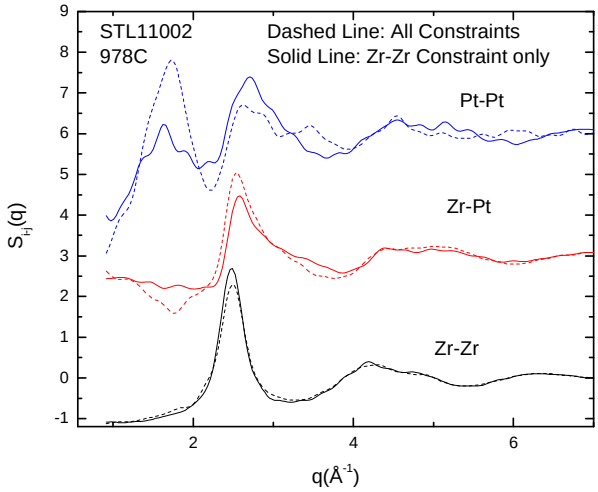


**Figure 5.27-**Partial structure factors for constrained RMC to the $S(q)$ for $Zr_{80}Pt_{20}$ liquid at 978C using all the MD PPCFs (solid lines) and only the Zr-Zr MD PPCF (dashed lines)

## 5.7. Conclusions

X-ray diffraction studies have revealed the existence of a pre-peak at $q \sim 1.7$ Å$^{-1}$ in the static structure factor of $Zr_{80}Pt_{20}$ equilibrium and supercooled liquids, indicating medium-range order in the liquid. An analysis of atomic structures obtained from a RMC fit, constrained by partials obtained from an MD simulation, to the scattering data indicates that the pre-peak is due to a Pt-Pt correlation among Zr-centered clusters having icosahedral/distorted-icosahedral symmetry. The icosahedral order in the liquid likely increases the crystal nucleation barrier, contributing to the ability to supercool and aiding glass formation in these alloys. The importance of chemical information for obtaining realistic structures by RMC fits to the diffraction data has been demonstrated by highlighting the topological and chemical differences that emerge between constrained and unconstrained RMC fits and from incomplete information about MRO in the liquid.

## 5.8. References


[1] T. Zhang, A. Inoue and T. Masumoto, *Mater. Trans., JIM* **32,** 1005, (1991).

[2] A. Peker and W. L. Johnson, *Appl. Phys. Lett.* **63,** 2342, (1993).

[3] J. Saida, C. Li, M. Matsushita and A. Inoue, *J. Mat. Res.* **76,** 55, (2001).

[4] A. Inoue, T. Zhang, J. Saida, M. Matsushita, M. W. Chen and T. Sakurai, *Mater. Trans., JIM* **40,** 1181, (1999).

[5] J. Saida and A. Inoue, *J. Phys. Condens. Matter* **13,** L73, (2001).

[6] L. *Q*. Xing, J. Eckert, W. Loeser and L. Schultz, *Appl. Phys. Lett.* **74,** 664, (1999).

[7] U. Koester, J. Meinhardt, S. Roos and H. Liebertz, *Appl. Phys. Lett.* **69,** 179, (1996).

[8] K. F. Kelton, G. W. Lee, A. K. Gangopadhyay, R. W. Hyers, T. J. Rathz, J. R. Rogers, M. B. Robinson and D. S. Robinson, *Phys. Rev. Lett.* **90,** 195504, (2003).

[9] K. F. Kelton, A. K. Gangopadhyay, T. H. Kim and G. W. Lee, *J. Non-Cryst. Solids* **352,** 5318(2006).

[10] Y. T. Shen, T. H. Kim, A. K. Gangopadhyay and K. F. Kelton, *Phys. Rev. Lett.* **102,** 057801(2009).

[11] M. J. Kramer, M. Xu, Y. Y. Ye, D. J. Sordelet and J. R. Morris, *Metall. Mater. Trans. A* **39,** 1847, (2008).

[12] J. Saida, M. Matsushita and A. Inoue, *J. Appl. Phys.* **90,** 4717, (2001).

[13] B. S. Murty, D. H. Ping, M. Ohnuma and K. Hono, *Acta Mat.* **49,** 3453(2001).

[14] M. Kitada, M. Imafuku, J. Saida and A. Inoue, *J. Non-Cryst. Solids* **312-314,** 594(2002).

[15] D. J. Sordelet, R. T. Ott, M. Z. Li, S. Y. Wang, C. Z. Want, M. F. Besser, A. C. Y. Liu and M. J. Kramer, *Metall. Mater. Trans. A* **39A,** 1908, (2008).

[16] K. S. Bondi, A. K. Gangopadhyay, Z. Marine, T. H. Kim, A. Mukhopadhyay, A. I. Goldman, W. E. Buhro and K. F. Kelton, *J. Non-Cryst. Solids* **353,** 4723(2007).

[17] W. Hoyer and R. Jödicke, *J. Non-Cryst. Solids* **192-193,** 102(1995).

[18] L. Wang, Y. Wang, C. Peng and Y. Zhang, *Phys. Lett. A* **350,** 405(2006).

[19] T. Nakamura, E. Matsubara, M. Sakurai, M. Kasai, A. Inoue and Y. Waseda, *J. Non-Cryst. Solids* **312-314,** 517(2002).

[20] X. Hui, R. Gao, G. L. Chen, S. L. Shang, Y. Wang and Z. K. Liu, *Phys. Lett. A* **372,** 3078(2008).

[21] M. Wakeda and Y. Shibutani, *Acta Mat.* **In Press, Corrected Proof**.

[22] X. Bian, M. Sun, X. Xue and X. Qin, *Materials Letters* **57,** 2001, (2003).

[23] D. Holland-Moritz, St, uuml, S. ber, H. Hartmann, T. Unruh, T. Hansen and A. Meyer, *Phys. Rev. B* **79,** 064204(2009).

[24] I. Kaban, W. Hoyer, A. Il'inskii, A. Shpak and P. Jóvári, *J. Non-Cryst. Solids* **353,** 1808(2007).

[25] L. Wang, H. Cong and X. Bian, *Mater. Sci. Eng.* **341,** 197, (2003).

[26] L. Zhang, Y. Wu, X. Bian, H. Li, W. Wang and S. Wu, *J. Non-Cryst. Solids* **262,** 169(2000).

[27] J. Brillo, A. Bytchkov, I. Egry, L. Hennet, G. Mathiak, I. Pozdnyakova, D. L. Price, D. Thiaudiere and D. Zanghi, *J. Non-Cryst. Solids* **352,** 4008(2006).

[28] A. K. Gangopadhyay, G. W. Lee, K. F. Kelton, J. R. Rogers, A. I. Goldman, D. S. Robinson, T. J. Rathz and R. W. Hyers, *Rev. Sci. Instrum.* **76,** 073901(2005).
[29] S. K. Chung, D. B. Thiessen and W.-K. Rhim, *Rev. Sci. Instrum.* **67,** 3175, (1996).
[30] R. C. Bradshaw, J. R. Rogers, K. F. Kelton, R. W. Hyers and D. P. Schmidt, *Rev. Sci. Instrum.* **76,** 125108, (2005).
[31] V. M. Wessels, PHASE FORMATION, LIQUID STRUCTURE, AND PHYSICAL PROPERTIES OF AMORPHOUS AND QUASICRYSTAL-FORMING ALLOYS, *Physics*, Washington University, St. Louis (2009).
[32] N. I. f. S. a. Technology, X-Ray Mass Attentuation Coefficients, (2010).
[33] H. Okamoto, *J. Phase Equil. and Diff.* **29,** 385, (2008).
[34] T. H. Kim and K. F. Kelton, *J. Chem. Phys.* **126,** 054513(2007).
[35] M. L. McGreevy, *J. Phys. Condens. Matter* **3,** F9, (1991).
[36] D. A. Keen, *Nature (London)* **344,** 423, (1990).
[37] G. Gresse and J. Hafner, *Phys. Rev. B* **47,** 558, (1993).
[38] G. Kresse, Technische Universität Wien (1993).
[39] G. Kresse and J. Furthmüller, *Computational Material Science* **6,** 15, (1996).
[40] G. Kresse and J. Furthmüller, *Phys. Rev. B* **54,** 11169, (1996).
[41] G. Kresse and D. Joubert, *Phys. Rev. B* **59,** 1758, (1999).
[42] S. Y. Wang, C. Z. Wang, M. Z. Li, L. Huang, R. T. Ott, M. J. Kramer, D. J. Sordelet and K. M. Ho, *Phys. Rev. B* **78,** 184204(2008).
[43] J. D. Honeycutt and H. C. Andersen, *J Phys. Chem.* **91,** 4950, (1987).
[44] J. L. Finney, *Nature (London)* **266,** 309, (1977).
[45] J. L. Finney, *Proc. Roy. Soc. London A* **319,** 479, (1970).
[46] T. E. Faber and J. M. Ziman, *Philos. Mag.* **11,** 153, (1965).
[47] J. Saida, T. Sanada, S. Sato, M. Imafuku and A. Inoue, *Appl. Phys. Lett.* **91,** 111901(2007).
[48] J. Saida, K. Itoh, S. Sato, M. Imafuku, T. Sanada and A. Inoue, *J. Phys. Condens. Matter* **21,** 375104, (2009).
[49] F. R. D. Boer, R. Boom, W. C. M. Mattens, A. R. Miedema and A. K. Niessen, Cohesion In Metals: Transition Metal Alloys (Cohesion And Structure), Elsevier Science Ltd, (1989).
[50] T. H. Kim, STRUCTURAL STUDY OF SUPERCOOLED LIQUIDS AND METALLIC GLASSES BY HIGHE ENERGY X-RAY DIFFRACTION AND REVERSE MONTE CARLO SIMULATION, *Physics*, Washington University, St. Louis (2007).
[51] S. G. Hao, C. Z. Wang, M. J. Kramer and K. M. Ho, *J. Appl. Phys.* **107,** 053511(2010).
[52] Pearson's Handbook of Crystallographic Data for Intermetallic Phases, Americal Society for Metals, Metals Park, Ohio (1985).
[53] T. Hahn, Editor, International Tables For Crystallography, D. Reidel Publishing Company, Boston (1987).
[54] M. H. Lee, R. T. Ott, M. F. Besser, M. J. Kramer and D. J. Sordelet, *Scr. Mater* **55,** 737, (2006).
[55] H. T. J. Reijers, M. L. Saboungi, D. L. Price, J. W. Richardson, K. J. Volin and W. van der Lugt, *Phys. Rev. B* **40,** 6018(1989).

[56] D. Holland-Moritz, O. Heinen, R. Bellissent and T. Schenk, *Materials Science and Engineering: A* **449-451,** 42(2007).
[57] N. A. Mauro, A. Kreyssig, A. I. Goldman and K. F. Kelton, Informal discussion of resonances in Zr-Pt, (2010).

# Chapter 6

## Thermophysical and Structural Studies of Bulk Metallic Glass-Forming Liquids

### 6.1. Introduction

The Ni-Nb alloys have received a great deal of attention in part because they form a binary bulk metallic glass at the composition $Ni_{61.5}Nb_{38.5}$ with a critical casting thickness of 1.5mm [1]. These have excellent compressive strength but a small reduced glass transition temperature. The bulk-forming composition range is reported to be extremely narrow [2] based on Cu $K_\alpha$ X-ray diffraction studies. This glass is interesting because the three empirical Inoue rules [3] for BMG formation do not apply. Instead, the region of glass formation, calculated by comparing the enthalpies of formation of the amorphous and crystal phases [4, 5], is in good agreement with experiment. Finally, Ni-Nb is known to form a very fragile glass despite its high number density

Small additions to Ni-Nb improve the critical casting thickness further and can lead to desirable properties [6]. Ni-Nb-Sn and Ni-Nb-Sn-Ta remain somewhat marginal bulk metallic glass-formers, but with high *Tg* (up to 900K). They have a high Young's modulus (200GPa), shear modulus (54-59GPa) and compressive yield strength (2-2.8 GPa). Bulk glass formation improves [7] marginally to reach a maximum when Nb is replaced with Ta, up to 10 atomic percent, and with either Ti, Zr and Hf in a similar fashion [8]. The Zr-containing alloys have an exceptionally good corrosion resistance. Choi-Yim *et al.* [6] report that the strength strongly depends on the Sn and Ta content. Neutron and EXAF [9] studies indicate that phase separation may be responsible for this. Phase separation has been suggested in other glasses, such as the Zr-based BMGs [10,

11] and in Fe-Ni-P [12]. Three dimensional atom probe measurements of Ni-Nb-Y [13] metallic glasses support the conclusion from the neutron and EXAFS measurements. The phase separation is likely due to the large positive heat of mixing between Y and Nb [14]. While there is no large positive heat of mixing between Sn and Nb, in the Ni-Nb-Sn glass, they do have a negligible bonding enthalpy [14]. It has been observed that a high Sn content, up to 7.0 %, lowers the measured strength, possibly indicating different spinodal temperatures.

Ni-Nb alloys have been studied using levitation techniques beginning in 1997 with EML studies of the eutectic composition ($Ni_{59.5}Nb_{40.5}$) [15], which showed a modest amount of undercooling of 135K [16]. A wide range of maximum undercooling values has been claimed for ESL studies of the eutectic. The high vapor pressure of Ni limits processing of Ni-Nb. Mukherjee *et al.* [17] report an undercooling of 126K when the liquid was given 200K of superheating. A large mass loss was found if that superheating limit was exceeded. This study also reported equilibrium phase formation from the liquid and a liquid density that showed a large deviation from a rule of mixtures estimate. This is not surprising given the large negative heat of mixing between Ni and Nb [14]. There is one report of an extremely high undercooling [18], where the liquid persisted to 210K below the solidus with normal size and purity (99.998%) samples. However, this study reports an overheating of 400K, which would place the absolute temperature at 1575°C (1848K) where the vapor pressure is $10^{-2}$ to $10^{-1}$ Torr and evaporation is likely. Mass loss was not reported, so the actual composition was likely not that of the eutectic. The microstructure of the solidified samples indicated surface nucleation on some samples, but no correlation between the undercooling and the number or position of nucleation

sites was reported. This suggests the surface sites are not effective at catalyzing crystal nucleation.

Structural and thermophysical property studies in these Ni-Nb liquids have also garnered attention, due, in part, to the very high number densities found. In a comparison study [19], ESL experiments on Vitreloy (Vit) 1, Vit105, Vit106a and Ni-Nb showed that the viscosity of the best glass former is an order of magnitude larger than that of the poorer glass forming Ni-Nb eutectic alloy. They also showed that the density changes upon recalescence are smallest for the best glass formers. As discussed in section 4.6.3.2, problems associated with volume measurements of solidified ESL samples make this last point questionable. However, the viscosity argument is compelling. Attempts to explain the high density observed in the Ni-Nb binary liquid and in the better glass forming Ni-Nb-Sn one [17] have argued for the presence of collective motion in the liquid, based on the results of neutron scattering studies [20]. The self-correlation functions, measured from quasi-elastic neutron scattering, showed a slowing down of the microscopic dynamics and an increase in the packing fraction. In particular, the self-diffusivity in liquid $Ni_{60}Nb_{34.8}Sn_{5.2}$ decreased by almost two orders of magnitude within a relatively narrow temperature range (~350°). The critical packing fraction obtained is reported to be excellent agreement with predictions from mode-coupling theory. These experimental results have prompted theoretical [21] and experimental [22-24] studies of the role of diffusion in glass formability.

The influence of structure on diffusion [24, 25] and glass formability is also of interest. There have been attempts to determine the partial structure factors (PSFs) in Ni-Nb metallic glasses using neutron isotopic substitution [26-30]. X-ray studies of

$Ni_{60}Nb_{40}$ and $Ni_{50}Nb_{50}$ glasses gave a temperature dependence on $S(q)$ that may indicate a negative temperature coefficient of resistivity [31]. While previous X-ray $S(q)$ measurements show typical behavior found in all transition metal liquids, including a shoulder on the second peak, the neutron studies show a pre-peak in $S(q)$, which is not observed from X-ray scattering studies. Studies [9] on Ni-Nb-Zr glasses show improved GFA with Zr additions of 5 to 10 at % giving glasses with a critical thickness of 1.5mm. Additions of Ti produced similar increases in GFA.

EXAFS studies of the Ni-Nb-Zr glasses reveal the presence of chemical inhomogeneties. EXAFS measurements provide information about the local atomic environment through resonant scattering [32]. With increasing Zr, around the Ni atoms, the main peak shifts to lower *r* and the second peak also shifts but more dramatically. The change observed with the addition of 10 at. % of Zr is much smaller than with 20 at. % Zr, and the peak intensity decreases, indicating a somewhat decreasing correlation at this length scale. The local environment around Nb shows little change up to 10 at % Zr. However, increasing the Zr content from 10 at. % to 20 at. % causes a dramatic shift of the main peak to low *r*. A growing intensity indicates an increase in the correlation. The authors interpret these results to indicate that the addition of Zr above 10 at. % leads to chemical inhomogeneity, or short range ordering (SRO), in the amorphous structure and a decreasing GFA. The chemical inhomogeneity is reportedly connected with positive heat of mixing between Nb and Zr, which manifests itself as an observed miscibility gap in the solid-state section of the Nb–Zr binary phase diagram [33]. No miscibility gap has been reported in the liquid phase, although the high temperature liquid has not been well studied. These results suggest that the addition of Zr can cause a chemical

inhomogeneity to develop as the liquid is cooled, reducing the GFA. This may explain the narrow region of improved GFA ($0 \leq$ Zr at. % $\leq 10$). This study also reports that the SRO and MRO around the Nb increases with larger Zr concentration. Although not discussed in this report, there is likely a continuous partial coordination number change as well, as has been observed in fits in the binary bulk metallic glass-forming Cu-Zr system [34, 35].

A more direct measure of correlation changes in the Ni-Nb binary glass [36] was obtained from elastic neutron scattering studies using isotopic substitution. These studies revealed the presence of a pre-peak in the Ni-Ni partial structure factor and a developing Nb-Nb pre-peak (emergence on the low-$q$ side of the main peak) with increasing Ni content, up to $Ni_{63}Nb_{37}$. Atomic structural models (produced in a similar fashion to RMC), consistent with the experimental data, found that as the Ni content increases, the structure around the Ni atoms develops similarities to the structure around Ni in the $Ni_3Nb$ structure. Since there are no Nb-Nb neighbors in the structure, the same comparison for Nb is not applicable. Taken with MD simulations [26, 37, 38] these studies suggest that persistent chemical and topological features are present in the liquid and glass phases, but more detailed information of the structures is needed.

While one study reported no well-defined structural units or clusters [36], additional MD work and structural analysis [39] identified clustering or cluster networking in the liquid, due in large part to the increased number of solute-solute (Nb-Nb) bonds established, which lowers the enthalpy. Given evidence that the diffusion and dynamics are strongly influenced by length scales and dominant structures, X-ray diffraction studies of Ni-Nb based liquids and subsequent RMC modeling are of

significant interest. These studies are presented in this chapter. The chapter is divided into three general sections. First, the experimental details of the thermophysical, scattering and fit studies are discussed. Second, the thermophysical property and scattering results are presented and discussed. Measurements of the liquid density for compositions near the best metallic glass-forming composition [2] as a function of temperature are presented. In the style of Yi *et al*. [40] these are examined to see if there is a correlation between density and glass forming ability (GFA) in this alloy. $S(q)$ obtained from the X-ray scattering studies are presented for all of the Ni-Nb based alloys studied: $Ni_xNb_{100-x}$ (x = 40, 57, 59.5, 62, 65), $Ni_{60}Nb_{30}Ta_{10}$, and $Ni_{59.5}Nb_{35.5}TM_5$ (TM = Ti, Zr, Hf). Detailed structural comparisons between $Ni_{59.5}Nb_{40.5}$, $Ni_{62}Nb_{38}$ (bulk metallic glass former), and $Ni_{60}Nb_{30}Ta_{10}$ (bulk metallic glass former) are discussed. Finally, RMC fits, constrained using partial pair correlation functions (PPCFs) obtained from *ab-initio* MD studies are presented and discussed for one temperature at the eutectic composition.

## 6.2. Experimental

Master ingots (~ 1.0g) of all compositions were prepared by arc-melting high purity elements on a water-cooled copper hearth in a high-purity Ar (99.999%) atmosphere (as described in Chapter 2). Small spherical samples (~2.5 mm) were prepared for supercooling and *in-situ* liquid structure studies at the Advanced Photon Source (Station 6-ID-D in the MUCAT Sector), using the Washington University Beamline Electrostatic Levitator (WU-BESL). The WU-BESL is described in detail in Chapter 4. Differential Thermal Analysis (DTA) was used to determine the solidus temperature for $Ni_{60}Nb_{30}Ta_{10}$

in order to determine the emissivity by matching the ESL temperature curves following the procedures discussed in Chapter 2 (DTA) and Chapter 4 (emissivity matching).

Two optical pyrometers were used to measure the sample temperature over two temperature ranges, 160-800°C and 600-2300°C, with a relative accuracy of better than 2% over the entire range for this series of experiments. To obtain maximum supercooling, the levitated samples were heated to a maximum of 1400°C, above the liquidus temperatures for all compositions, and subsequently free-cooled. Unless otherwise noted, mass loss was negligible. Initial ESL studies showed that sample processing was greatly improved by conducting two *in-situ* melts on the tungsten pre-processing post, after which, the initial heat-up for all compositions reported here took only 30 minutes. Undercooling is generally poor in this liquid. The eutectic Ni-Nb composition could be superheated by 225°C, but it only achieved a maximum of 100°C of undercooling in BESL studies. The inability to superheat the liquids could be the cause of the poor undercooling. However, anomalous surface features were also observed on liquid samples. Figure 6.1, for example, shows an image taken of a $Ni_{60}Nb_{30}Ta_{10}$ ESL sample. The sample was confirmed to be liquid based on the observed melting plateau, processing above the reported liquidus [7] to the maximum heating of 1400°C, an observed oscillatory character in the droplet, a recalescence after a measurable undercooling, and, most conclusively, X-ray diffraction data with no evidence of crystallites. However, the surface features are clearly visible.

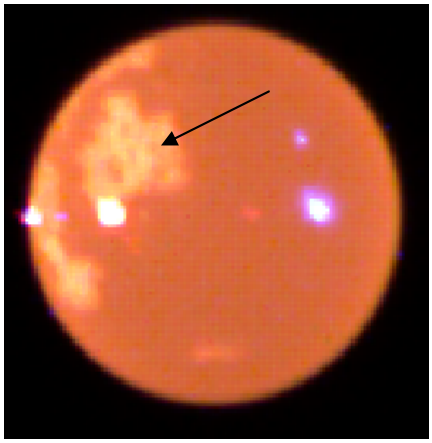

**Figure 6.1**- Surface features observed (indicated by the arrow) on $Ni_{60}Nb_{30}Ta_{10}$.

These features, although presented for $Ni_{60}Nb_{30}Ta_{10}$, occurred for all Ni-Nb based alloys. High purity elements (Ni 99.995%, Nb 99.95%) were used for the preparation of all samples, however, different stock and lot numbers had no effect[10] on the presence of these surface features. The features appear yellow in Figure 6.1, indicating a different temperature or emissivity than the liquid and suggesting that they are a different phase from the liquid. During the BESL2010 campaign, the surface layer was sanded off using Si-C fine grit sand paper and the features seemed to disappear. Approximately 8-10% of the mass was removed and those sanded samples were used in the scattering studies reported here.

Candidates for the anomalous phase are considered. Diffraction data were taken with and without a sanding treatment of the individual ESL samples. Very small peaks were observed on top of the inherent liquid structure in the un-sanded diffraction patterns-no peaks were observed in sanded samples. While the peaks were too small to index, they indicate a high temperature crystal phase such as an intermetallic (Ni-Nb), Ni

[10] Ni: Alfa-S# 42333, L# J12R002; S# 42333, L# D18M33. Nb: Alfa- S#42846, L#I26N13; S# 10265, L# Unknown.

oxide, or Nb oxide.[11] Possible intermetallics are unlikely to persist, since they have relatively low melting temperatures (Table 6.1) and would, therefore, be thermodynamically unstable at the elevated temperatures used to process the liquids.

**Table 6.1-** Possible impurity phases in liquid Ni-Nb systems.

| Phase | Melting Temperature (°C) | Reference |
|---|---|---|
| $NiNb_3$ | 1430 | [12, 15] |
| $Ni_6Nb_7$ | 1290 | [15] |
| NbO | 1945 | [12] |
| $NbO_2$ | 1915 | [12] |
| $Nb_2O_5$ | 1495 | [12] |
| NiO | 1955 | [20] |

An oxide is the more likely possibility. Since oxygen has a large solubility in Nb (up to 4 at %), with limited solubility in Ni (as little as .08 at % by one estimate [41]), it seems likely that the regions are floating NiO that was formed during arc melting. An experiment was conducted where the source ingot of Ni-Nb eutectic was sanded and then ESL samples were prepared: The surface features persisted despite attempts to purify the atmosphere according to the procedures laid out in Chapter 2; some oxygen likely contaminated the atmosphere.

Temperature measurements were coordinated with non-contact density measurement, which were made using the shadow method [42, 43] with a Pixelink PL-B742U CCD camera and a 450 nm backlight. Video data were taken at a frame rate of

[11] While nitrogen (N) constitutes the majority element in air, its stable form, $N_2$, makes it an unlikely reactant.

15 fps averaging of up to 300 frames at each isothermal step. The details of the machine vision volume measurement algorithm are described elsewhere [43] and in Chapter 4 of this work. The relative precision of the density data was ~ 0.3% over the temperature range studied, with an absolute accuracy of 3% for the BESL2010 data. The accuracy of the data is largely determined by the calibration standard used [42, 43]. Grade 200 standards were used to calibrate the BESL2010 density data. The densities of the Ni-Nb liquids at ambient temperature obtained with these standards are shown in Figure 6.2. As can be seen, the accuracy of the data is lower than the relative precision.

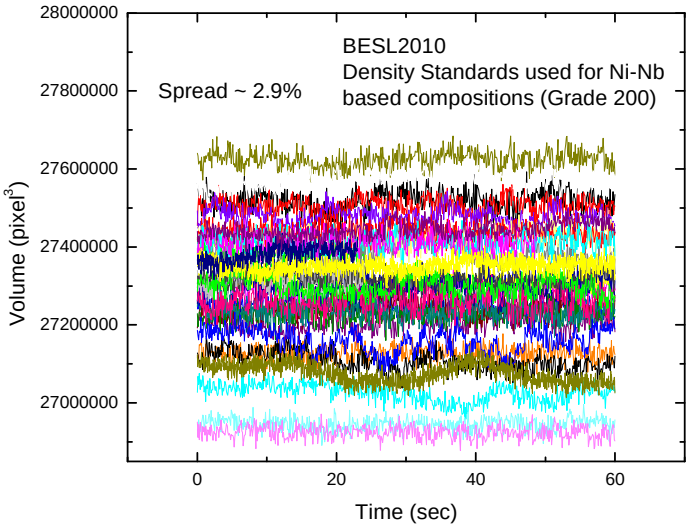


**Figure 6.2-** Density at ambient temperature for grade 200 standards used for studies of Ni-Nb-based compositions in the BESL2010 data.

For the studies of density near the optimum reported bulk metallic glass-forming binary composition, grade 3 standards were used, which reduced the absolute uncertainty to ~ 0.3% while increasing the precision to 0.15% (Figure 6.3).[12]

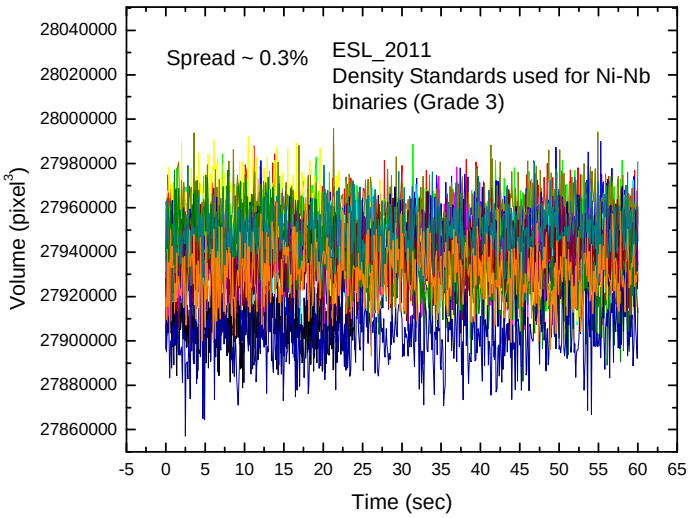


**Figure 6.3**- Density at ambient temperature for grade 3 standards used for studies of Ni-Nb composition near the optimum BMG.

High energy (E = 129 keV, $\lambda$ = 0.0969Å) diffraction studies of the liquids were made in a transmission geometry to high-$q$ (15 Å$^{-1}$) using a GE Revolution 41-RT amorphous Si flat panel X-ray detector for various sampling rates. Structure factors, $S(q)$, were derived from the scattering data according to the procedures laid out in Chapter 2.

To investigate atomic structures and chemical ordering in the liquids, Reverse Monte Carlo fits were performed on the $S(q)$ data at all temperatures and were

[12] The accuracies and precisions quoted are not statistical, but are measured from the plot. The accuracy and precision is improved slightly with statistics, not reflected in the above quotations. However, rigorous uncertainties are propagated in the density studies and statistically relevant error bars are presented.

subsequently analyzed using the HA index and Voronoi polytetrahedral (VI) analysis. Two sets of fits were performed. First, conventional RMC fits were made to the data for select $Ni_{59.5}Nb_{40.5}$, $Ni_{62}Nb_{38}$, and $Ni_{60}Nb_{30}Ta_{10}$ liquids. The description and details of the RMC technique can be found elsewhere [44-46]. For this study, random starting configurations of 5000 atoms with the appropriate stoichiometric composition were used, confined to a cubic box with dimensions appropriate to the measured density. Second, atomic structures were obtained by RMC fits to the measured X-ray static structure factors for $Ni_{59.5}Nb_{40.5}$ at 1400°C, while constraining the fit with partial pair correlation functions (PPCFs) obtained from *ab initio* Molecular Dynamics simulations using the Vienna *ab initio* simulation package (VASP) [47-51]. Partial pair correlation functions were prepared by M. Widom from his MD simulations for this study. The system consisted of 100 atoms, 60 atoms of Ni and 40 atoms of Nb, in a cubic box with periodic boundary conditions, described more fully in Wang *et al.* [52]. The MD simulations provide partial pair correlation functions out to ~ 6 Å when none are experimentally available. The description and details of the constrained RMC (CRMC) technique can be found elsewhere [44-46].

## 6.3. Results and Discussion

### *6.3.1. Survey results: thermophysical property, scattering and discussion*

Y. Li *et al.* [40] reported a novel experiment where the optimum glass forming compositions in the Cu-Zr system were correlated with local maxima in the density of the amorphous phase. The technique used to prepare samples allowed a 0.4 at. % resolution of the composition, and the density maxima around reported BMG compositions were

localized to ~ ± 2 at. %. It is particularly interesting to ask if this correlation exists in the liquid state, or if the maxima occur during the amorphization process. ESL density measurements allow this experiment. Twelve (12) compositions around the reported bulk metallic glass-forming composition, $Ni_{62}Nb_{38}$, were prepared using the techniques described in Chapter 2 with high purity (Ni 99.995%, Nb 99.95%) source materials. The mass loss during ingot preparation was less than 0.2 mg for all compositions, placing an upper bound on the compositional uncertainty around 0.02%, much lower than the Cu-Zr study [40].

Processing of ESL samples was limited to below 1400°C for all compositions to minimize deposition. The density data presented came from the final 2 free cooling cycles to minimize compositional uncertainty, although mass loss was negligible in all cases, within the error (0.1mg) of the analytical balance used. In nearly all cases[13] the measured volume was calibrated with the standard taken afterwards. Samples were not sanded, as BESL samples were, to minimize impurity contamination. Surface features were observed at all compositions.

The density data for liquid $Ni_xNb_{100-x}$ ($55 \leq x \leq 65$) at 1157°C are shown in Figure 6.4. The mass density (shown in the bottom panel) shows no overall trend with changing composition, which is to be expected since Ni and Nb have similar room temperature densities. There are local peaks (indicated by arrows in Figure 6.4) observed at $Ni_{62.8}$ and $Ni_{64.0}$ that were confirmed with a second measurement and which persist when the mass density is converted to number density (top panel). The number density shows an approximately linear increase with increasing Ni concentration, consistent with its

[13] The density measurements at compositions Ni = (60.0, 61.2, 61.6, and 64.4) were calibrated with standards before the experiment because the standards after the measurements dropped out of levitation before calibration could be done.

smaller size compared to Nb. Both peaks are barely above noise, only ~ .25% above the baseline, and are more localized than the density peaks reported by Y. Li *et al.* [40] in Cu-Zr. Further, neither occur at the reported optimal bulk metallic glass-forming composition, although the study by L. Xia *et al.* [2] didn't probe past $Ni_{62.5}$. The critical casting thickness for the compositions discovered in this study will, therefore, be measured in the near future.

At the time of the preparation of this thesis, J. C. Bendert is carrying out the same ESL liquid density experiment, however matching the compositions of Y. Li *et al.* for liquid Cu-Zr to see if density maxima also occur in the liquid.

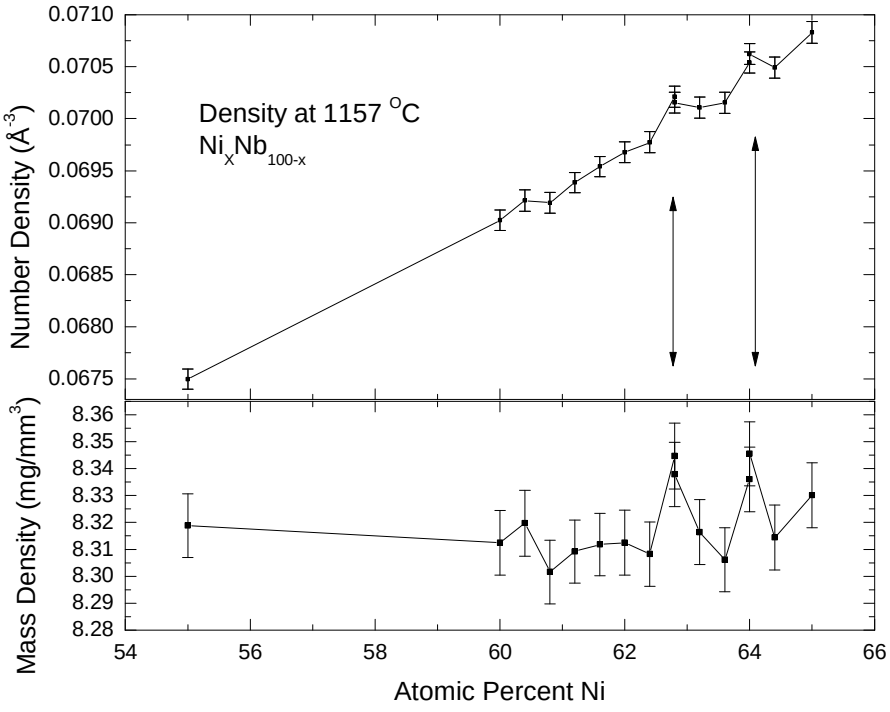


**Figure 6.4-** Density of Liquid $Ni_xNb_{100-x}$ using the ESL technique at 1157°C.

The X-ray static structure factors for $Ni_xNb_{100-x}$ (x = 40, 57, 59.5, 62, 65) and $Ni_{60}Nb_{30}Ta_{10}$ (Figure 6.5) and $Ni_{59.5}Nb_{35.5}TM_5$ (TM = Ti, Zr, Hf) (Figure 6.6) were generated and analyzed to determine if there are any characteristic differences. All compositions show the shoulder on the second peak indicative of icosahedral order, which sharpens with decreasing temperature (not shown). As the Nb content increases, the first peak shifts to lower-*q* reflecting a shift to longer length scales. This is expected considering the larger size of Nb (*r* = 1.46 Å) compared to Ni (*r* = 1.24 Å). This effect is particularly noticeable in $Ni_{40}Nb_{60}$, the highest Nb content alloy studied. The transition metal additions of Ti, Zr and Hf show a shifting of the first peak consistent with this same size effect. As Nb is replaced with Ti (*r* = 1.45 Å) the peak position remains essentially unchanged; as Nb is replaced with Zr (*r* = 1.60 Å) or Hf (*r* = 1.67 Å) the peak shifts to longer length scales. No evidence emerges for anomalous structural or chemical ordering in any composition when compared to the eutectic. Likely, the small positive heat of mixing between Nb and Ti, Zr and Hf (+2 kJ/mol, +4 kJ/mol, and +4kJ/mol, respectively [14]) is overcome by the tendency for bonding to occur between Ni and the same transitions metals. For each composition, difference curves (not shown) between the $S(q)$ at high and lower temperatures, and the $g(r)$ difference curves treated in the same fashion, do not show the chemical ordering found in the Cu-Zr system at specific compositions [53].

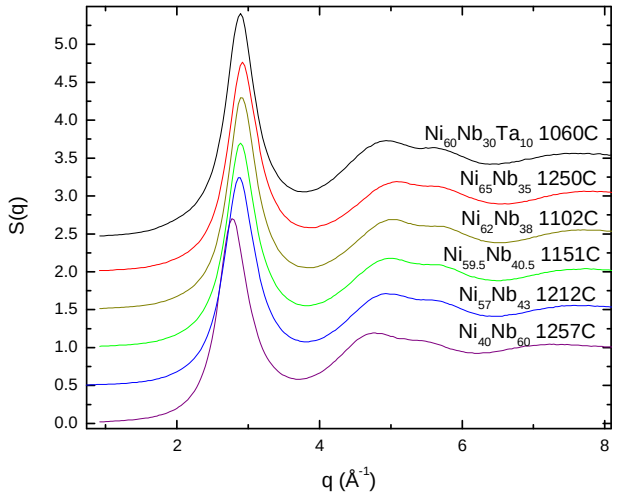


**Figure 6.5**- X-ray static structure factors for Ni-Nb binaries and $Ni_{60}Nb_{30}Ta_{10}$ at their lowest respective undercoolings.

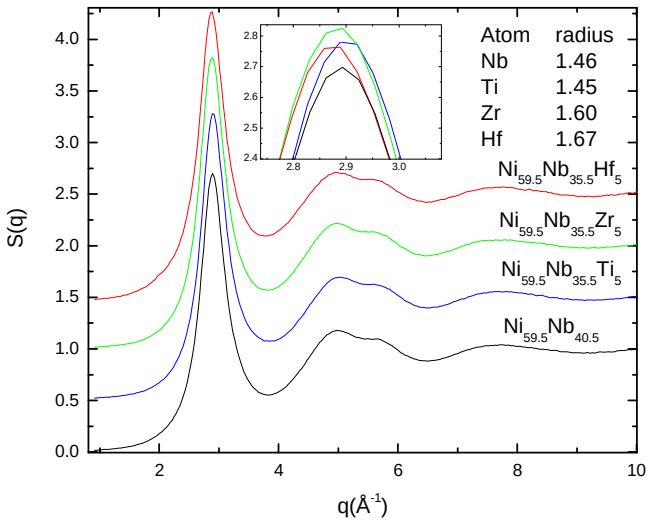


**Figure 6.6**- X-ray static structure factors for $Ni_{59.5}Nb_{40.5}$ and $Ni_{59.5}Nb_{35.5}TM_5$ (TM = Ti, Zr, Hf) at their lowest respective undercoolings.

### *6.3.2. In-depth study of $Ni_{59.5}Nb_{40.5}$ (eutectic), $Ni_{62}Nb_{38}$ (bulk metallic glass-former), and $Ni_{60}Nb_{30}Ta_{10}$ (bulk metallic glass-former)*

#### *6.3.2.1. $Ni_{59.5}Nb_{40.5}$*

The eutectic alloy (BESL designation STL11056) was observed to recalesce in a single, long duration event, after a maximum undercooling of ~100°C. Two well-define peaks are observed for recalescence in a free cool (Figure 6.7). The next cycle shows a single recalescence plateau (Figure 6.9). The diffracted intensity data taken after the first and second recalescence events do not show significant differences (Figure 6.8). The large enthalpy release is unusual given this, but not unheard of [54]. The liquid data presented here were taken from simultaneous X-ray diffraction data (2 Hz, Inc. 4[14]). However, a comparison with free cooling data taken in the next cycle (Inc. 5) showed identical static structure factors. The slow cooling cycle allowed superior temperature resolution compared to the free cooling data.

[14] The "Inc." refers to the specific experimental data file. This will be used, when appropriate, so that group members can easily access specific sets of data.

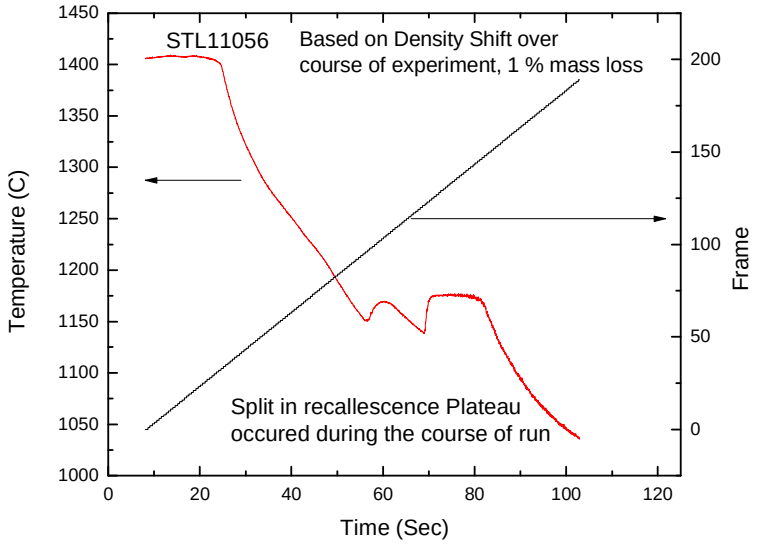


**Figure 6.7**- Slow cooling cycle for $Ni_{59.5}Nb_{40.5}$. The split recalescence shown here was not present in the next free cooling cycle. The frame indicator is also shown in this plot.

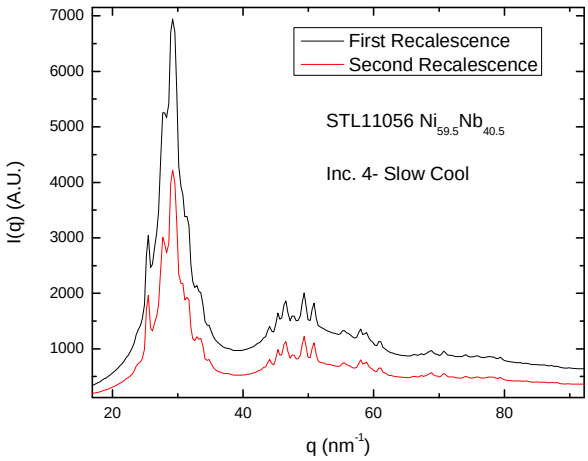


**Figure 6.8**- *I*(*q*) for the first and second recalescence events observed in Figure 6.7.

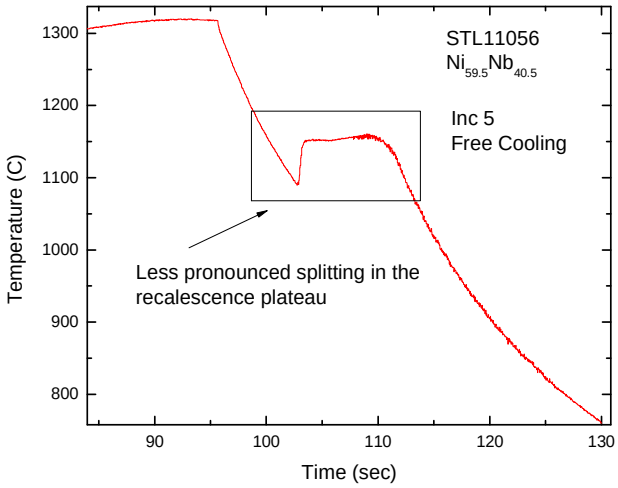


**Figure 6.9-**Free cooling cycle for $Ni_{59.5}Nb_{40.5}$. The split recalescence observed in Inc. 4 (Figure 6.7) is not observed.

The density taken during slow cooling was slightly smaller than the data taken at the beginning of the experiment, indicating a slight mass loss over the course of the experiment. Mass loss measurements confirmed a 2.8% mass decrease at the time that the X-ray data were taken. Since Ni is the primary evaporating species, the mass loss shifted the composition to $Ni_{58.99}Nb_{41.01}$. This was taken into account in the number density calculations (shown below in Table 6.2) and the RMC ensembles.[15]

**Table 6.2-** Frame, temperature and density relationship for the static structure factors analyzed in the eutectic liquid.

| Frame | Temp (C) | Density (incorrect mass) ($Å^{-3}$) | Density (corrected) (up 2.8%) ($Å^{-3}$) |
|---|---|---|---|
| 31-32 | 1400 | 0.06608 | 0.06792 |
| 40-41 | 1340 | 0.0663 | 0.06821 |

[15] This composition will still be referred to as the "eutectic" or $Ni_{59.5}Nb_{40.}$

| | | | |
|---|---|---|---|
| 53-54 | 1281 | 0.06659 | 0.06849 |
| 76-77 | 1216 | 0.06692 | 0.06881 |
| 95-96 | 1151 | 0.06726 | 0.06911 |

The static structure factors were calculated according to the procedures laid out in Chapter 2; they are presented in Figure 6.10. The $S(q)$s oscillate well around unity over the entire range of $q$ indicating the high quality of the experimental data and that the appropriate correction were made for absorption, background and Compton scattering. The primary peak sharpens, increases in magnitude, and shifts to lower scattering angle, reflecting an increasing density and a more ordered liquid with decreasing temperature. The shoulder on the second peak becomes more pronounced with supercooling, which is frequently argued to indicate an increase in icosahedral and icosahedral-like order [55]. The corresponding pair correlation functions, $g(r)$, are shown in Figure 6.11. There is a slight shoulder developing on the high-$r$ side of the second peak with undercooling, which could indicate a slight ordering in the second shell. Unfortunately, without chemical information from neutron experiments or MD simulations, any trends in the partials from conventional RMC would be unreliable. The pair correlation functions do not go to zero at the low-$r$ side of the main peak, corresponding to the hard-sphere nearest approach.

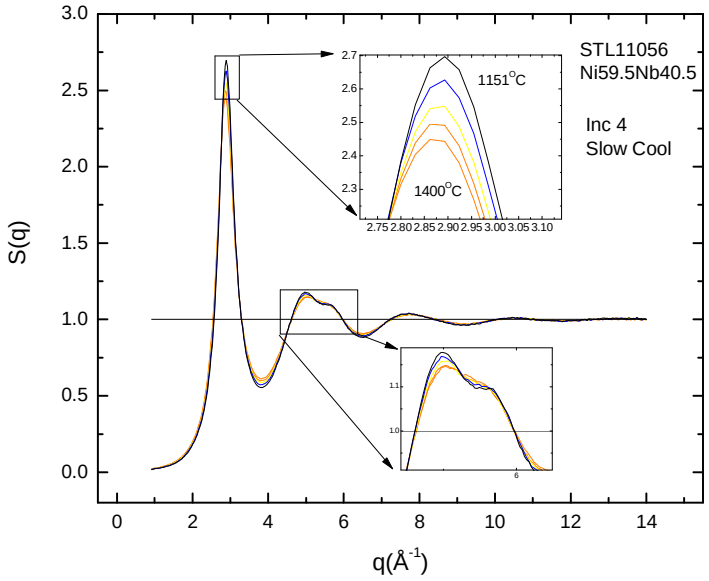


**Figure 6.10-** Static Structure factor for the eutectic liquid at the temperatures indicated in Table 6.2**.** The first peak and shoulder evolution on the second peak are shown in the inserts.

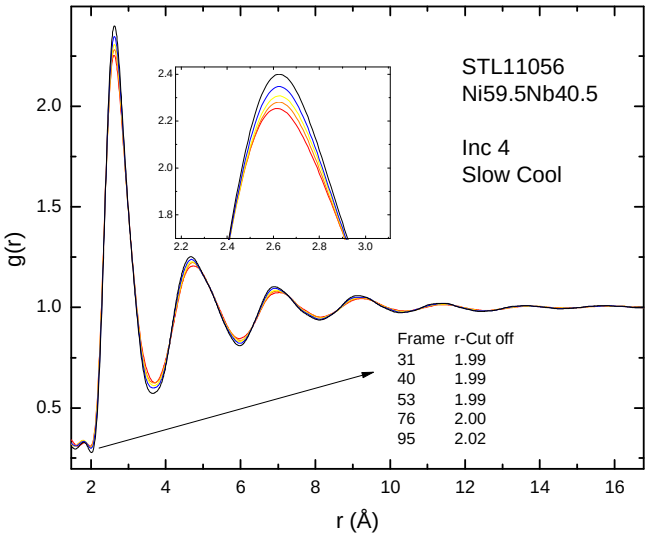


**Figure 6.11-** Pair Correlation Functions corresponding to *S*(*q*)'s presented in Figure 6.10.

This error has been explored by taking the Fourier Transform for $g(r)$ measured at 1400°C and comparing that to the a Fourier Transform where the $g(r)$ is forced to go to zero at the low-$r$ side of the main peak. The $g(r)$ was forced to zero using an exponential function that ranged from $g(r) = 0$ at $r = 1.85$Å to the intensity of the main peak at $r = 2.15$Å. The computer source code for the Fourier Transform is listed in Appendix II.7. The results are shown in Figure 6.12. The $S(q)$ calculated from the forced $g(r)$ differ from those computed from the unforced one mainly in the low-$q$ side of the main peak. Forcing $g(r)$ to zero causes the low-$q$ side of the main peak in $S(q)$ to fall below 0, which is unphysical. This means that the error producing the anomalous $g(r)$ behavior is likely a more complicated systematic error yet to be discovered, and not an efficiency problem in the detector at low-$q$.

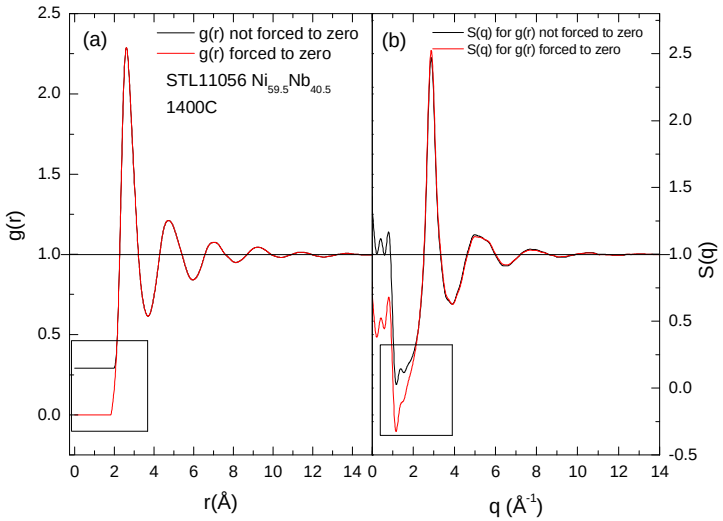


**Figure 6.12-** $S(q)$ generated from direct Fourier Transform of the $g(r)$ for $Ni_{59.5}Nb_{40.5}$ at 1400C with and without forcing the low-$r$ side of the main peak to zero.

### *6.3.2.2. $Ni_{62}Nb_{38}$*

The reported bulk metallic glass-forming composition, $Ni_{62}Nb_{38}$ (BESL designation STL11029) was observed to recalesce in a single, long duration event, after a maximum undercooling of ~160°C, a deeper undercooling than obtained for the eutectic. The value for the liquidus temperature was taken from the published phase diagram [15]. No split recalescence plateau is observed, as seen in Figure 6.13 and no mass loss was observed, as determined by measuring the sample *post-situ*. Also, no mass loss was found during the density measurements taken during processing. The static structure factors have been calculated according to the procedures laid out in Chapter 2 in the free cooling regime in Inc 2; these are presented in Figure 6.14. The frame, temperature and density data for the static structure factors analyzed in the $Ni_{62}Nb_{38}$ liquid are shown in Table 6.3.

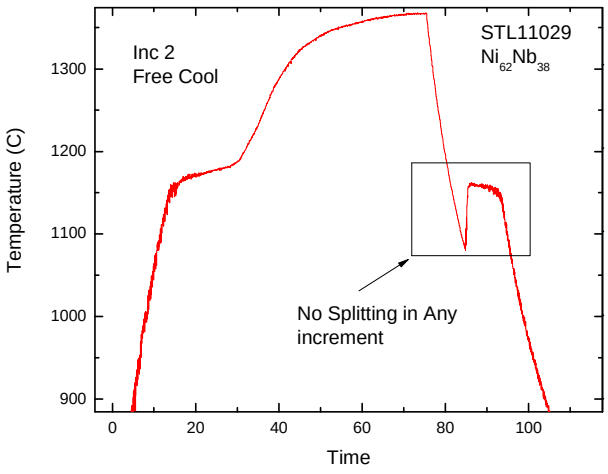


**Figure 6.13**- Free cooling cycle for $Ni_{62}Nb_{38}$. No well-defined splitting in the recalescence plateau is observed.

**Table 6.3**- Frame, temperature and density data for the static structure factors analyzed in the $Ni_{62}Nb_{38}$ liquid.

| Frame | Temp (C) | Density ($Å^{-3}$) |
|---|---|---|
| 65 | 1352 | 0.06979 |
| 67 | 1277 | 0.07018 |
| 69 | 1207 | 0.07051 |
| 71 | 1154 | 0.07076 |
| 74 | 1102 | 0.07102 |

The $S(q)$s oscillate well around unity over the entire range of $q$ indicating the high quality of the experimental data and that the appropriate correction were made for absorption, background and Compton scattering. The primary peak sharpens, increases in magnitude, and shifts to lower scattering angle, reflecting an increasing density and a more ordered liquid with decreasing temperature-similar to the trends observed in the eutectic liquid. The shoulder on the second peak becomes more pronounced with supercooling. Although not shown, difference curves were calculated for the structure factors and pair correlation functions and changes were smooth as with the eutectic.

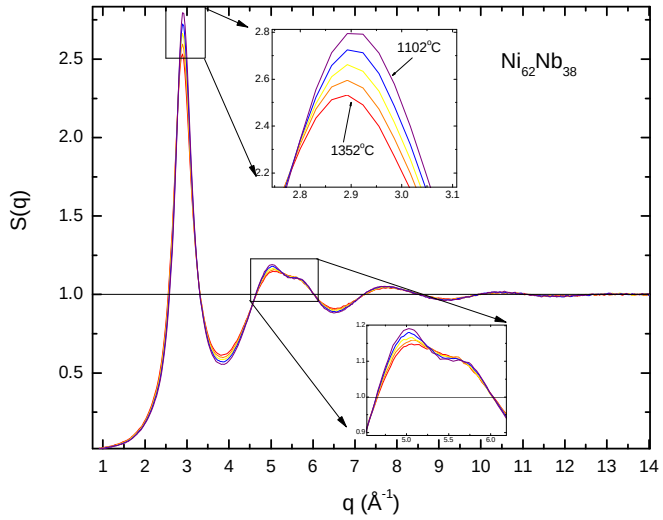


**Figure 6.14** Static Structure factor for the bulk metallic glass-forming liquid at the temperatures indicated in **Table 6.3** The first peak and shoulder evolution on the second peak are shown in the inserts.

Differences between the static structure factors in the eutectic and bulk metallic glass-forming liquids were analyzed in an attempt to understand the differences in glass formability. The first peak position, $q_1$, show a systematic shift to lower $q$ as the Nb content increases, but the first peak height, $S(q_1)$, shows no difference between the bulk metallic glass-forming compositions ($Ni_{62}Nb_{38}$ and $Ni_{60}Nb_{30}Ta_{10}$) and the non-bulk metallic glass- forming ones. The rates of change of $q_1$ and $S(q_1)$ with temperature also show no compositional dependence or anomalous behavior outside of error.

### *6.3.2.3. $Ni_{60}Nb_{30}Ta_{10}$*

The ternary alloy, $Ni_{60}Nb_{30}Ta_{10}$, (BESL designation STL11039) recalesced in a single, long-duration plateau, after a maximum undercooling of ~100°C (Figure 6.15). Density

and X-ray diffraction data (1 Hz, Inc. 4) were collected during this free cooling cycle.. The absolute temperature scale was calibrated from DTA measurements of the ternary alloy, because only liquidus temperature information exists in the literature [7]. Details of the DTA method are presented in Chapter 2, but for this study, Ag, Cu, Mn and Ni were used to calibrate the DTA scans shown in Figure 6.16. Three cycles of DTA curves for $Ni_{60}Nb_{30}Ta_{10}$ with increasing temperature are presented. There is a temperature shift associated with the later cycles, likely a reaction of the sample with the alumina powder that surrounds it. Only the first cycle, then, was used to determine the solidus temperature. Only a few degrees of correction to the measured temperature was indicated from the calibration standards. The onset of melting (taken to be the solidus) is therefore estimated as 1191±5°C.

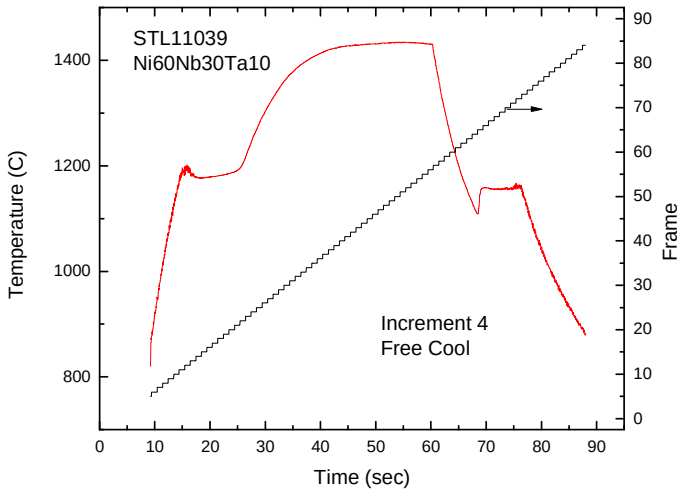


**Figure 6.15-** Free cooling curve for $Ni_{60}Nb_{30}Ta_{10}$, inc. 4. A single, long recalescence plateau is observed.

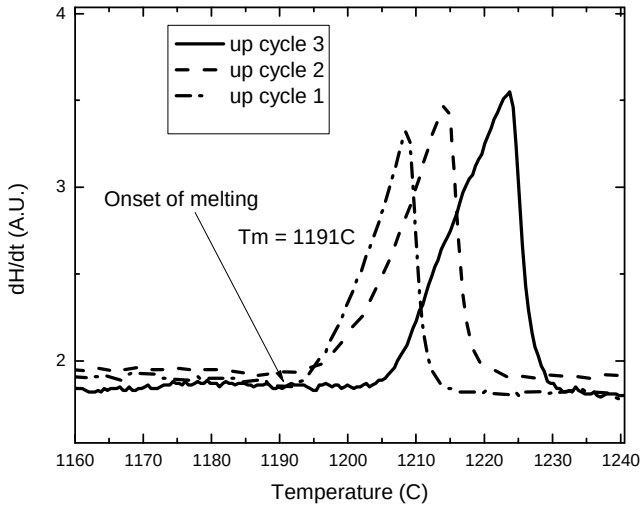


**Figure 6.16-** Three cycles of DTA data for $Ni_{60}Nb_{30}Ta_{10}$ with increasing temperature. There is a shift associated with the later cycles, likely a reaction of the sample with the alumina powder surrounding it. Only the first cycle was used.

A comparison of the density measurements taken over the entire experiment showed no significant shift as a function of time, indicating no mass loss. Direct post-processed mass measurements confirmed this. Table 6.4, below, shows the frame, temperature and density data used for $S(q)$ generation and RMC fitting for $Ni_{60}Nb_{30}Ta_{10}$. This system, like other Ni-Nb based systems, has a high number density relative to Zr- based liquids.

**Table 6.4-** Frame, temperature and density relationship for the static structure factors analyzed in the $Ni_{60}Nb_{30}Ta_{10}$.

| Frame | Temp (C) | Density ($Å^{-3}$) |
|---|---|---|
| 53 | 1430 | 0.0696 |
| 59 | 1390 | 0.06981 |

| | | |
|---|---|---|
| 62 | 1242 | 0.07052 |
| 64 | 1172 | 0.07086 |
| 65 | 1145 | 0.07101 |

An analysis of the $I(q)$ of the diffraction patterns taken as a function of time during recalescence indicated the slow growth of a crystal phase mixture. There was no evidence for two sharp crystallization events, nor did any peak location shift appreciably or any peak disappear throughout recalescence. Additionally, the $I(q)$ pattern from the final diffraction pattern at the end of recalescence is remarkably similar to the $I(q)$ pattern obtained at the end of recalescence for $Ni_{59.5}Nb_{40.5}$. A comparison of these two diffraction patterns is presented in Figure 6.17. Slight differences in the peak heights and positions between the same crystal phases in the two alloys are likely caused by the substitution of Ta for Nb.

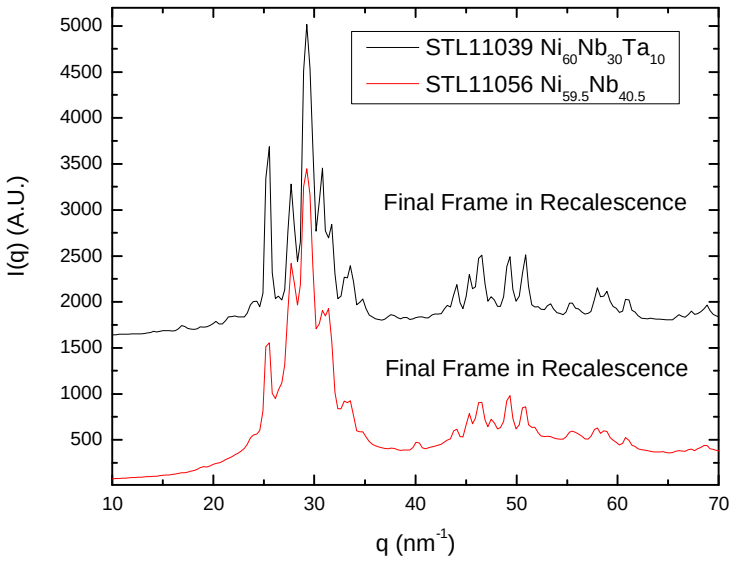


**Figure 6.17-** Comparison of I(*q*) diffraction data taken at the ends of the recalescence plateaus in $Ni_{60}Nb_{30}Ta_{10}$ and $Ni_{59.5}Nb_{40.5}$.

The static structure factors have been calculated according to the procedures laid out in Chapter 2 and are presented in Figure 6.18. The *S*(*q*)s oscillate well around unity and the primary peak sharpens, increases in magnitude, and shifts to lower scattering angle, and the shoulder on the second peak becomes more pronounced with supercooling, just as in the eutectic liquid. Qualitatively, the eutectic and the ternary liquids behave very similarly with undercooling, as can be seen in Figure 6.19, which displays the static structure factors for $Ni_{59.5}Nb_{40.5}$ and $Ni_{60}Nb_{30}Ta_{10}$ at their lowest respective undercoolings, which occur at nearly the same temperature.

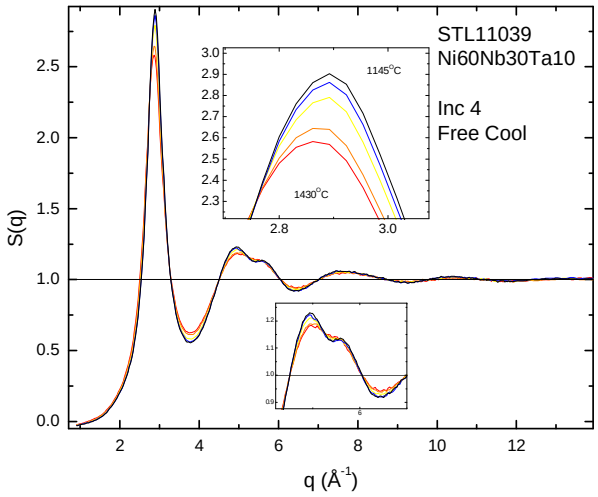


**Figure 6.18**-Static Structure factors for $Ni_{60}Nb_{30}Ta_{10}$ corresponding to the temperatures listed in Table 6.4. The first peak and the shoulder evolution on the second peak are shown in the inserts.

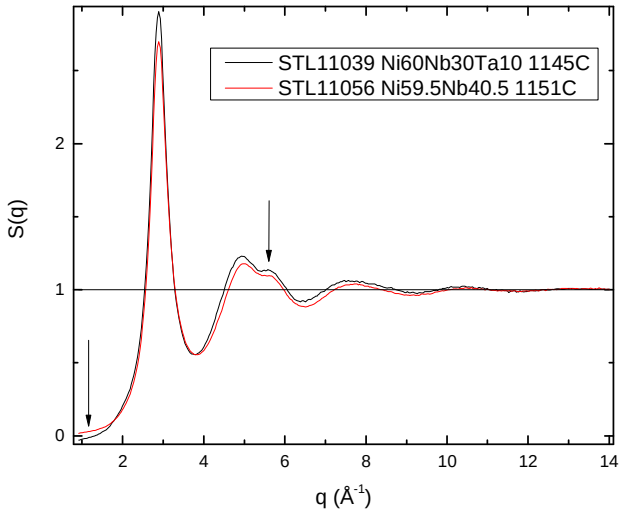


**Figure 6.19-** Comparison of the static structure factors between $Ni_{59.5}Nb_{40.5}$ and $Ni_{60}Nb_{30}Ta_{10}$ at their lowest respective undercoolings.

There are no drastic differences between the two systems, which qualitatively have similar $S(q)$s. The main peak in the ternary liquid is more intense than in the eutectic one, but the peak positions are the same.. The main difference in peak height is likely related to the larger atomic form factor of Ta. The similar positions of the first peaks in $S(q)$ for these two liquids is likely explained by the similar atomic sizes of Ta and Nb and their enthalpies of mixing with Ni [14].

### 6.4. RMC Fits-Results and Discussion

The quantitative aspects of the atomic structures obtained from the RMC fits to the experimentally determined $S(q)$s for $Ni_{59.5}Nb_{40.5}$, $Ni_{62}Nb_{38}$ and $Ni_{60}Nb_{30}Ta_{10}$ were evaluated using the Honeycutt and Andersen (HA) index method [56]. Previous studies of differences in structures obtained by constrained and unconstrained RMC fits, such as presented in Chapter 5, suggest that the HA indices remains a robust metric to quantify and compare local atomic structures and their evolution with temperature. As previously described in Chapter 2, HA indices provide only a partial measure the local atomic environment, focusing on the number and distribution of neighboring atoms around root pairs of atoms. To explore the differences in local order between the eutectic, binary BMG and ternary liquids, we've chosen to focus on the icosahedral (1551), distorted icosahedral (1541+1431), body-centered cubic (BCC) (1661), and close packed (FCC+HCP) (1422+1421) type structures. The nearest-neighbor cut-off distance is calculated from the experimental $g(r)$ for each temperature.

### *6.4.1. $Ni_{59.5}Nb_{40.5}$*

A series of unconstrained RMC fits were conducted with the $S(q)$ data. Previous RMC studies in this group assumed that the atomic form factors, $f(q)$, varied slowly enough that they were assumed constant and equal to the $q \rightarrow 0$ limit, which is the number of total electrons. This is equivalent to analyzing neutron scattering data with RMC where the cross section is localized to a point. As described in Chapter 2, the RMC algorithm generates the partial pair correlation functions (PPCFs) from the atomic distribution, calculates the partial structure factors (PSFs) from a direct Fourier transform of the PPCFs, constructs the total $S(q)$ using the Faber-Ziman formalism, and then compares the result with the input data. Even if the input data is $g(r)$, the comparison is made to the total structure factor, $S(q)$. It has never been fully explored how the assumed dependence of the form factors affects the RMC result. In Figure 6.20 we present the measured structure factor and RMC fit for $Ni_{59.5}Nb_{40.5}$ at 1400°C assuming (a) $q$-dependent form factors (calculated from [57]) and (b) constant atomic form factors. Here, we observe a fit to $S(q)$ that matches the first and second peaks to the data very well. The low-$q$ side of the main peak is well-reproduced as are the higher-$q$ oscillations. In contrast, the fit with constant form factors (Figure 6.20b) is not particularly good. It is slightly less intense than the data for the first and second peaks, and it doesn't decay as fast as the data on the low-$q$ side of the first peak. The third peak and higher-$q$ oscillations in the fit also don't match the data well, but they usually don't.

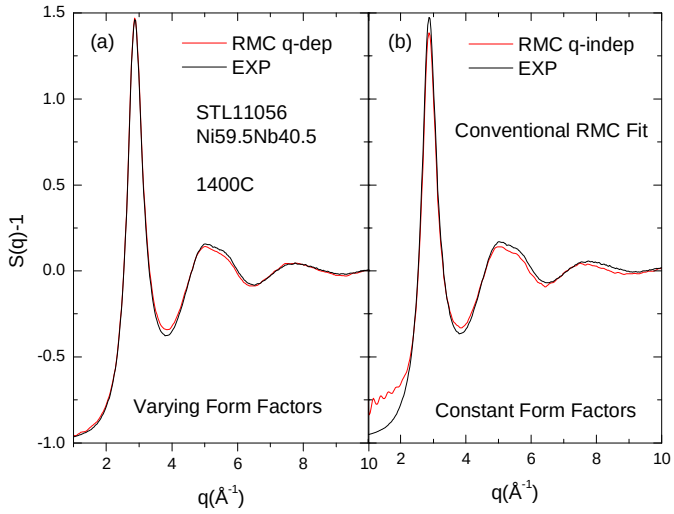


**Figure 6.20-** Structure factors and RMC fits for $Ni_{59.5}Nb_{40.5}$ at 1400°C assuming (a) *q*-dependent and (b) constant atomic form factors.

A comparison of the partial structure factors, $S_{i\text{-}j}(q)$, obtained in the two fits shown in Figure 6.20 are displayed in Figure 6.21. The only significant difference between the *q*-dependent and *q*-independent fitting schemes is a different intensity in the first peak in the Ni-Ni partial. It should also be noted that there is no pre-peak development in any partial, as was observed in neutron diffraction studies [36]. This is not surprising as the X-ray scattering factors lack the sufficient contrast to pick out Nb-Nb or Ni-Ni medium-range order.

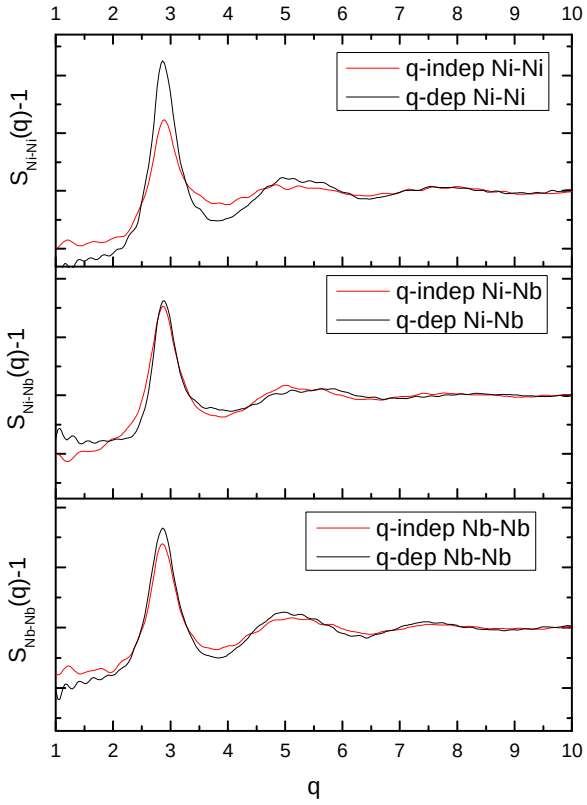


**Figure 6.21-** Partial structure factors $S_{i\text{-}j}(q)$ comparison for RMC fit of $Ni_{59.5}Nb_{40.5}$ at 1400°C.

Based on the results of these studies, conventional RMC fits were made to the experimentally determined $S(q)$ data using $q$-dependent atomic form factors. Fits were made assuming both random and ordered (simple cubic) initial configurations of 5000 atoms in a box of size consistent with the experimentally determined densities shown in Table 6.2. The assumed cutoff distances for Ni-Ni, Ni-Nb, and Nb-Nb were 1.750Å, 1.906Å, and 2.050Å respectively. These values differ from what one would calculate based on standard atomic radii tables. The $g(r)$ calculated from X-ray diffraction experiments of high temperature metallic liquids often show a minimum on the low-$r$ side of the first peak that imply atoms closer together than the standard tables would give. In this case, the cutoffs were determined from the experimental $g(r)$, by first

extrapolating the low *r* side of the main peak to zero as described in section 6.3.2.1. That *r* value corresponding to $g(r) = 0$ is then set as the Ni-Ni cutoff and the cutoffs for the Ni-Nb pairs and Nb-Nb pairs were found by scaling that Ni-Ni cutoff by the ratio of the corresponding atomic sizes. Larger values, more consistent with the experimental $g(r)$ produced poor fits. The extrapolated cutoff distances were used in all of the RMC fits for the $Ni_{59.5}Nb_{40.5}$, $Ni_{62}Nb_{38}$, and $Ni_{60}Nb_{30}Ta_{10}$ liquids, so comparisons between the Honeycutt Anderson (HA) distributions are relevant. A series of RMC fits using cutoff distances determined from the MD simulations discussed in section 6.5. were made and the atomic structures obtained were analyzed in terms of their HA indices: The results were consistent with those presented below, indicating that in this case the local structures obtained are not strongly dependent on the cutoff distances used.

No significant difference was found in the final HA index distribution at any temperature between the results obtained using the random and ordered starting configuration, although the random initial configuration tended to give the lowest chi squared error (as defined in Chapter 2, section 7.4.) for the final fit. Those results will be reported here. The resultant fits to the $S(q)$s at all temperatures are shown in Figure 6.22. The fits are excellent at all *q* values, falling slightly lower than the data on the second peak, but fitting the first peak extraordinarily well. The normalized chi squared error is between 8.0 and 9.7 for all experiments.

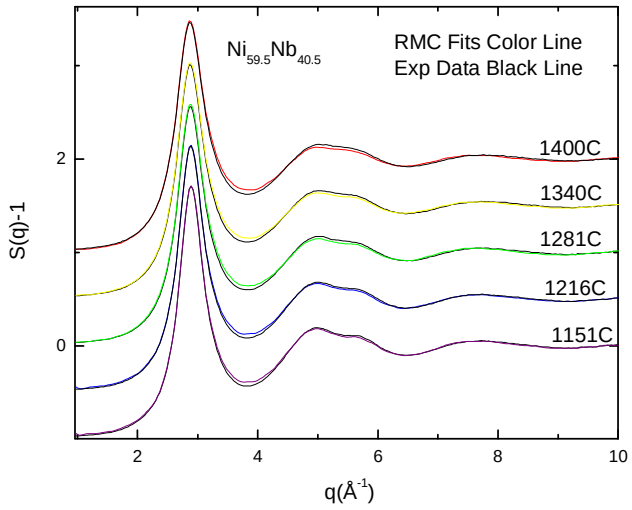


**Figure 6.22**- RMC fits to the $S(q)$ data for a $Ni_{59.5}Nb_{40.5}$ liquid at the temperatures indicated. The form factors were assumed to vary with $q$.

RMC fits to $g(r)$ at all temperatures were also made using the same cutoff distances as for the $q$-dependent RMC fits to $S(q)$. The fits, shown in Figure 6.23, are qualitatively good, although the normalized chi squared errors were close to 20, while fits to $S(q)$ were closer to 7.

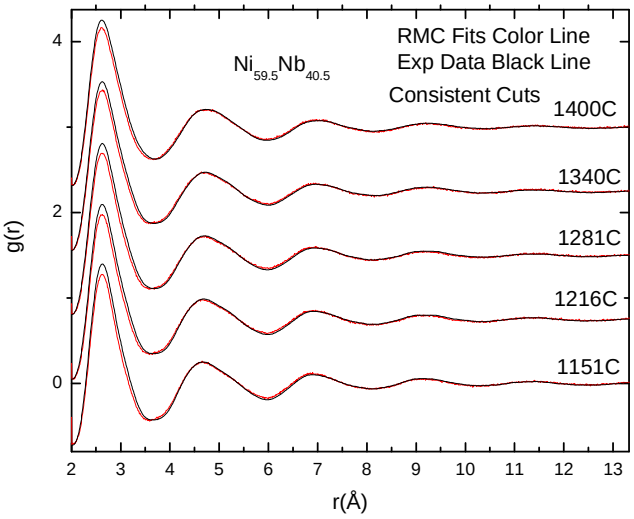


**Figure 6.23-** RMC fits to the $g(r)$ data for a $Ni_{59.5}Nb_{40.5}$ liquid at the temperatures indicated. The form factors are not $q$-dependent in RMC fits to $g(r)$.

RMC fits to $g(r)$ and $S(q)$ were made to try to further understand the importance of fitting $q$-dependent data. In Figure 6.24, the comparison between the HA index distributions for the two fits are presented, which show important differences. The fits to the $S(q)$, which we might consider more reliable since they include the $q$-dependence of the atomic form factors, give structures that are dominated by icosahedral and icosahedral-like order. They show a modest amount of BCC order, and marginal amounts of FCC and HCP order. The fits to the $g(r)$s give structures that contains equal amounts of BCC and icosahedral-type order, but the fractions are all ~0.09. When all the fractions of the BCC and icosahedral-type HA indices are summed, these indices account for 55% of all nearest neighbor structures in the fits to $S(q)$ but on 40% of nearest neighbor structures in the fits to $g(r)$. The structures contain a broader distribution in the fit to $g(r)$. The results obtained for this case suggest that even though the inclusion of the $q$-dependence of the

form factors causes little change in the partial $S(q)$s, it *does* have a strong influence on the local structures obtained from RMC fits to the data.

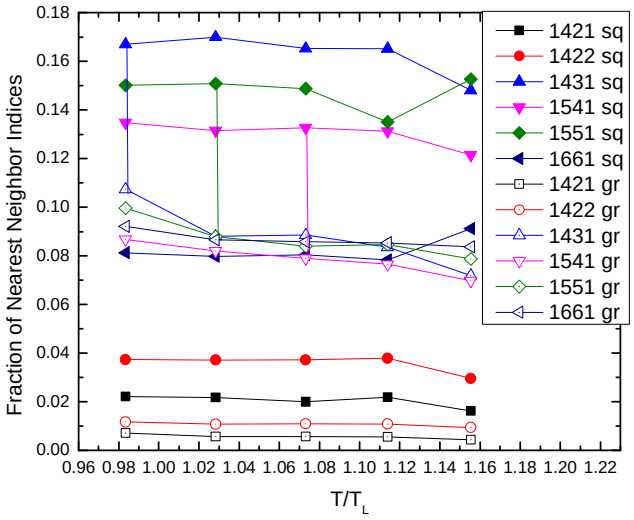


**Figure 6.24-**HA indices for the structures obtained by RMC fits to the $S(q)$ and $g(r)$ data for the eutectic Ni-Nb liquid.

From figure 24, there is little change observed in the fraction of HA indices in the eutectic Ni-Nb liquid over the measured temperature range. The distorted icosahedral order increases slightly with decreasing temperature, while the icosahedral order is nearly constant. The anomaly in the fraction of 1551 (icosahedral order) near $T/T_L = 1.11$ was explored by varying slightly the cutoff distances, and running the fit several times. The feature persists, contrary to the smooth trends that have been observed in other RMC studies of metallic liquids [53, 58]; it is being studied further. It should be noted that caution should be used in interpreting these data since there may be a different temperature dependence in structures obtained from constrained RMC fits.

### *6.4.2. $Ni_{62}Nb_{38}$*

Conventional RMC fits were made to experimentally determined $S(q)$ data using $q$-dependent form factors. Random initial configurations of 5000 atoms in a box of size consistent with the experimentally determined density were assumed. The resultant fits to the $S(q)s$ at all temperatures are shown in Figure 6.25. Excellent fits were obtained at all $q$ values, falling slightly lower than the data in the second peak, but fitting the first peak extraordinarily well. The normalized chi squared is between 7.5 and 9.0 for all experiments. The partial structure factors, and partial pair correlation functions (not shown) are qualitatively identical to those observed in the eutectic liquid.

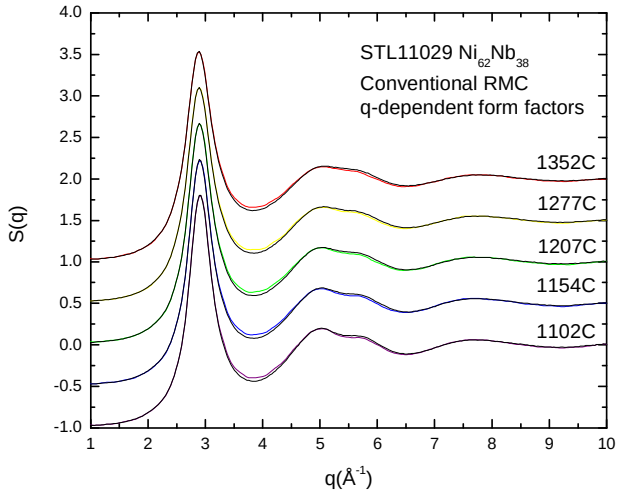


**Figure 6.25** RMC fits to the $S(q)$ data for the $Ni_{62}Nb_{38}$ liquid at the temperatures indicated. The form factors were assumed to vary with $q$.

The HA indices for all temperatures for the $Ni_{62}Nb_{38}$ liquid and, for comparison, the Ni-Nb eutectic liquid are shown in Figure 6.26. Like the eutectic liquid, the bulk metallic glass-forming liquid ($Ni_{62}Nb_{38}$) shows little FCC and HCP order, a moderate amount of

BCC order, and a dominant amount of icosahedral and icosahedral-like order. However, the bulk metallic glass-forming liquid shows a larger amount of *pure* icosahedral order (1551) than does the eutectic, which may constitute the most important difference between the two liquids.

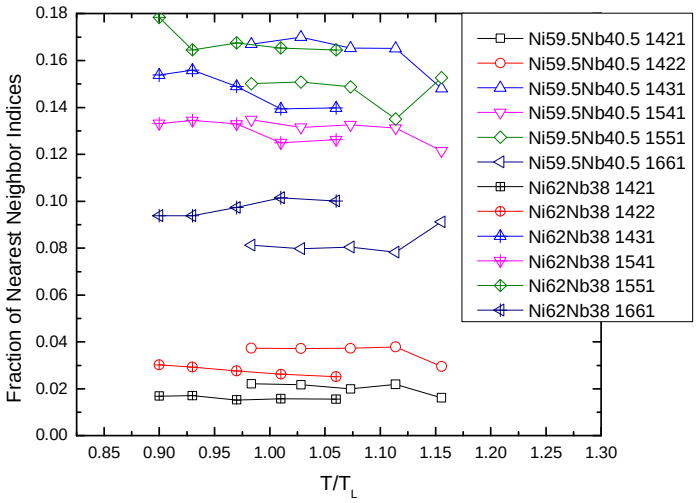


**Figure 6.26**-HA indices at all temperatures for the eutectic ($Ni_{59.5}Nb_{40.5}$) and bulk metallic glass-forming ($Ni_{62}Nb_{38}$) liquids. All RMC fits were assumed to have a *q*-dependence.

### *6.4.3. $Ni_{60}Nb_{30}Ta_{10}$*

As with the eutectic and bulk metallic glass-forming binary liquids, a series of RMC fits were made to $S(q)$ data obtained for $Ni_{60}Nb_{30}Ta_{10}$. First, conventional RMC fits were made assuming *q*-independent form factors. As with the eutectic alloy, the fit is poor compared with fits obtained with *q*-dependent form factors (Figure 6.27).

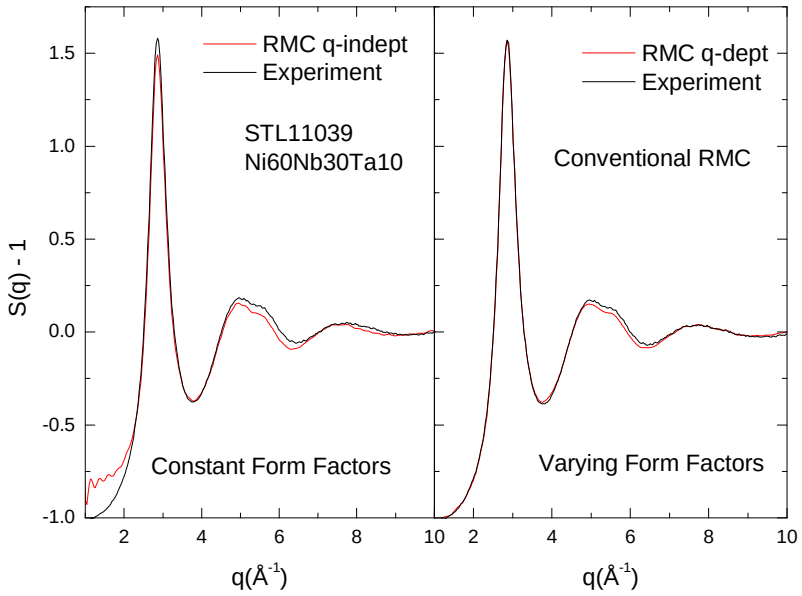


**Figure 6.27-** Measured structure factor and RMC fits for $Ni_{60}Nb_{30}Ta_{10}$ at 1430°C assuming constant and *q*-dependent atomic form factors.

A series of RMC fits to *g*(*r*) were made using cutoff distances that were identical to those used for fits to the eutectic alloy. As before, when using the *g*(*r*) as the input data, *q*-independent form factors were assumed. Random, cubic and the final configuration from the eutectic at 1400°C were all used for initial configurations in the fits. In all cases, however, the RMC fit converged to a configuration that produced a fit like that shown in Figure 6.28. Since there is a large difference in the atomic scattering factor between Ta and Nb, and, we suspect, a substitution of Ta for Nb in the liquid, the fit results are not realistic because the partials are not weighted by the appropriate *q*-dependent form factors.

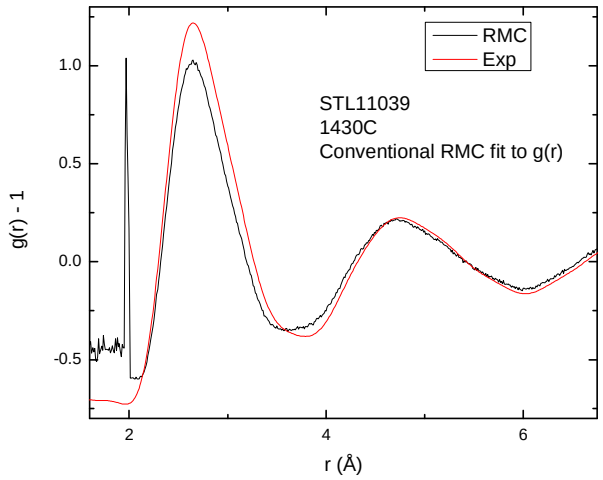


**Figure 6.28**- RMC fit to $g(r)$ for $Ni_{60}Nb_{30}Ta_{10}$ at 1430°C using a random starting configuration.

Based on these results, RMC fits as a function of temperature were made using the $S(q)$ data and $q$-dependent from factors. As for the analysis of the eutectic Ni-Nb liquids, the initial configurations were random and ordered (simple cubic) configurations of 5000 atoms in a box of size consistent with the experimentally determined density. As for the eutectic liquid, both initial configurations produced atomic structures that had the same HA index distributions at all temperatures. The results reported here, then, will be limited to those obtained assuming a random starting configuration. The resultant fits to the $S(q)$ data at all temperatures are shown in Figure 6.29. Excellent agreement is obtained at all $q$ values, falling slightly lower than the data on the second peak, but fitting the first peak extraordinarily well. The normalized chi squared error is between 6.0 and 7.5 for all experiment, which is slightly better than the fits to the eutectic liquid.

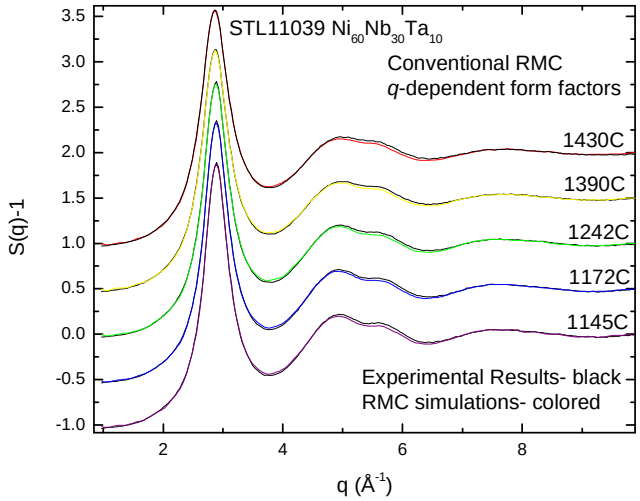


**Figure 6.29-** RMC fits to the $S(q)$ produced in the $Ni_{60}Nb_{30}Ta_{10}$ system at the temperatures indicated. The form factors were assumed to vary with $q$.

### *6.4.4. HA Analysis: $Ni_{59.5}Nb_{40.5}$, $Ni_{62}Nb_{38}$, and $Ni_{60}Nb_{30}Ta_{10}$*

The HA indices for the structures obtained from the RMC fits, using $q$-dependent form factors, for both $Ni_{59.5}Nb_{40.5}$ (labeled NiNb) and $Ni_{60}Nb_{30}Ta_{10}$ (labeled Ta10) are shown in Figure 6.30. The temperatures are scaled to the respective liquidus temperatures and the number of HA indices are normalized at all temperatures to the total number of identified 1xxx pairs. Both liquids show only minimal amounts of FCC and HCP type structures. Both liquids are dominated by icosahedral and icosahedral-like order. However, as for the comparison between the eutectic and the binary bulk metallic glass-former (section 6.4.3.), the Ta10 shows more *pure* icosahedral order than the eutectic does.

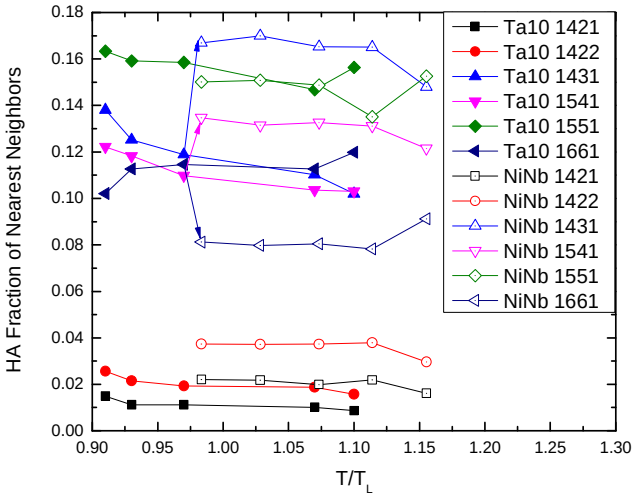


**Figure 6.30-** HA distribution for $Ni_{59.5}Nb_{40.5}$ (labeled NiNb) and $Ni_{60}Nb_{30}Ta_{10}$ (labeled Ta10) over the temperature range measured. The temperatures have been scaled to the liquidus temperature ($T_L$)

The HA indices for the RMC-fit structures for both bulk metallic glass-forming liquids ($Ni_{62}Nb_{38}$ and $Ni_{60}Nb_{30}Ta_{10}$) are shown in Figure 6.31. The structures of both liquids are dominated by *pure* icosahedral order (1551), and have roughly the same amount of BCC order, different from the structure of the binary eutectic liquid, which contains more distorted icosahedral order (1541 + 1431). Therefore, the only robust commonality that the two bulk metallic glass-forming liquids ($Ni_{62}Nb_{38}$ and $Ni_{60}Nb_{30}Ta_{10}$) share, as compared with the eutectic liquid, seems to be a slightly higher amount of pure icosahedral order, as measured by the HA metric.

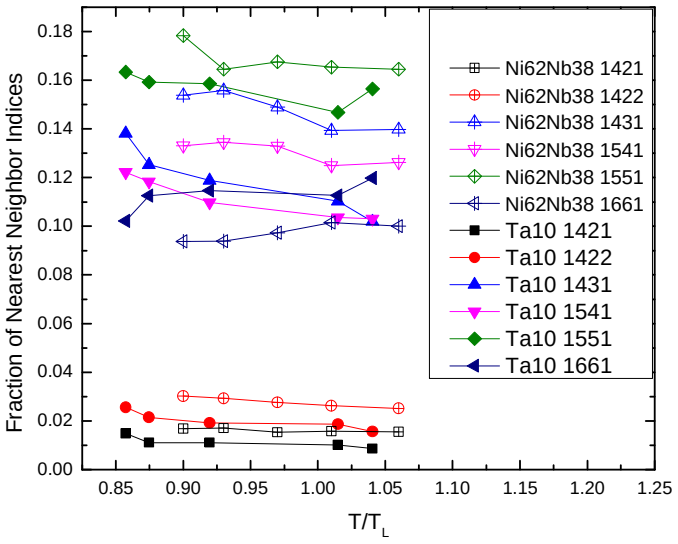


**Figure 6.31-** HA indices for the RMC-fit structures for the bulk metallic glass-forming liquids ($Ni_{62}Nb_{38}$ and $Ni_{60}Nb_{30}Ta_{10}$) for all temperatures measured. All RMC fits were assumed to have a $q$-dependence. The temperatures have been scaled to the liquidus temperature ($T_L$)

## 6.5. Constrained RMC Results and Discussion

The first in a series of constrained RMC fits to the $S(q)$ data for Ni-Nb liquids were made using PPCFs from MD simulations of the eutectic liquid at 1400°C [59]. Previous work in the Zr-Pt liquid (Chapter 5) showed that the details of the HA and VI distributions can change markedly when the PPCFs are constrained in this manner. In the previous section, we found that the HA indices for the RMC-fit structures for $Ni_{59.5}Nb_{40.5}$, $Ni_{62}Nb_{38}$, and $Ni_{60}Nb_{30}Ta_{10}$ liquids were all dominated by icosahedral and distorted icosahedral short-range order. Although the bulk metallic glass-forming liquids tend to display a larger fraction of the 1551 index, whether or not this is a characteristic difference between low GFA and high GFA Ni-Nb liquids must be tested using

constrained RMC fits. A comparison between the PPCFs from the MD simulation and the PPCFs obtained by a constrained RMC fit to the eutectic liquid at 1400°C is shown in Figure 6.32. The results from two different RMC fits are shown. One of these uses the cutoff distances obtained from the experimental $g(r)$ data and one uses those obtained from the MD simulations. Clear differences in the PPCFs emerge between these two conventional RMC fits and the MD results, manifesting most prominently in the Ni-Ni (Figure 6.32b) and Nb-Nb (Figure 6.32c) PPCFs. Note, however, that there is essentially no difference in the PPCFs obtained from the two RMC fits using the two sets of cutoff distances. The positions of the first peaks in the PPCFs from the MD simulations agree with expectations from atomic size considerations; this is not true for the PPCFs obtained from the RMC fits.

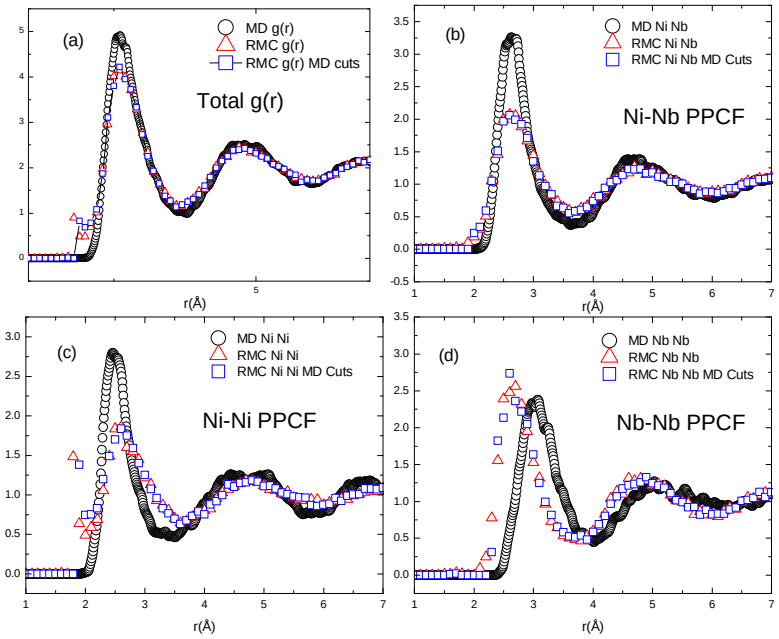


**Figure 6.32-** Comparison between the partial pair correlation functions obtained from an ab-initio MD simulation and from unconstrained RMC fits to the scattering data for the eutectic liquid at 1400°C. Two different RMC results are shown, one using the cutoff distances obtained from the experimental $g(r)$ data and one using those obtained from the MD simulations (a) Total g(r), (b) Ni-Ni partial pair correlation function, (c) Ni-Nb partial pair correlation function, (d) Nb-Nb partial pair correlation function.

To identify the dominant length scales in the structures, the PPCFs in Figure 6.32 were Fourier transformed to produce the partial structure factors in Figure 6.33. Studies of Zr-Pt (Chapter 5) show that medium-range order, for example, does not always clearly manifest in the PPCFs. In this case, pre-peaks do emerge in the Ni-Ni and Nb-Nb PSFs, suggesting the presence of medium-range order. The extreme shape asymmetry in the first peak of the Nb-Nb PDF suggests that a pre-peak is located near 1.5 $Å^{-1}$, although it

can't be clearly resolved form the first peak, made more difficult by a truncation error ripple near that location. The qualitative shape for each PSF is similar to that obtained from neutron diffraction studies of Ni-Nb glasses [26, 36]. Such excellent agreement suggests that the MD simulations are physically relevant.

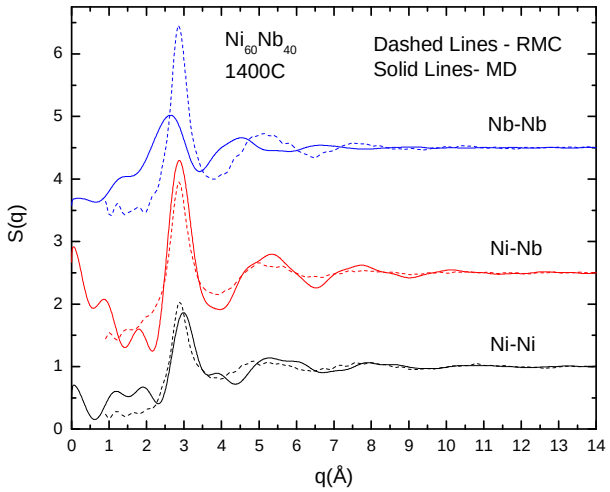


**Figure 6.33-** Comparison between the partial structure factors obtained from an ab-initio MD simulation and from an unconstrained RMC fit to the scattering data for the eutectic liquid at 1400°C. These were calculated by a Fourier transform of the partial pair correlation functions.

Atomic structures from constrained RMC fits were analyzed using HA and VI analysis and compared to the results from conventional RMC fits presented earlier. Despite the fact that only one set of MD partials is currently available (1400°C), some insight into the reliability of the analysis presented in 6.4. can be achieved. In the CRMC fit, the cutoffs were set by the MD PPCFs, and the fits converged from a random initial configuration with a density used in the conventional RMC fit, and consistent with the experimental data. A comparison between the HA index distributions obtained from the

structures produced by CRMC and by conventional RMC (using *q*-dependent atomic form factors) is given in Figure 6.34. The indices have been scaled to the number of nearest neighbor (1xxx) indices. Although the value of each index changes, the relative ordering remains the same in each liquid, as was observed in the Zr-Pt study. While we cannot state that this good agreement between the HA index distributions for structures obtained from conventional and constrained RMC fits will hold for all temperatures, it seems likely that icosahedral and icosahedral-like order will remain dominant.

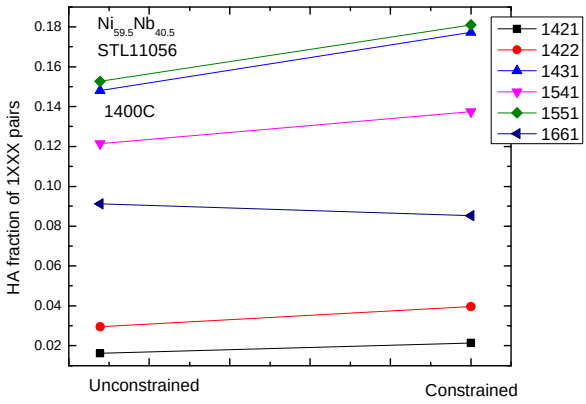


**Figure 6.34-** Comparison of the HA indices for structures obtained from unconstrained (conventional) and constrained RMC fits to the diffraction data for the eutectic liquid at 1400°C. The indices have been scaled to the number of nearest neighbor (1xxx) indices.

Figure 6.35 shows the fraction of the most abundant Ni-centered Voronoi polyhedra detected in the constrained and conventional RMC atomic structures. In both cases the most abundant clusters are the 14 coordinated (<0,2,8,4>), 13 coordinated (<0,3,6,4>, <1,2,6,3,1>), and 12 coordinated (<0,3,6,3>, <0,2,8,2>, <0,4,4,4>) polyhedra. The only discrepancies between the Ni-centered clusters in the structures from the two

fits are in one 13 coordinated index (RMC - <1,3,4,4,1> versus CRMC - <0,1,10,2>) index and one 11 coordinated index (RMC - <0,4,4,3> versus. CRMC - <0,2,8,1>). However, there is a tightening of the distribution of dominant clusters in the CRMC structure, containing fewer distinct polyhedra. The average coordination number around Ni, as measured by the VI, also decreases from 13.28 for the RMC structure to 12.95 when the fit is constrained.

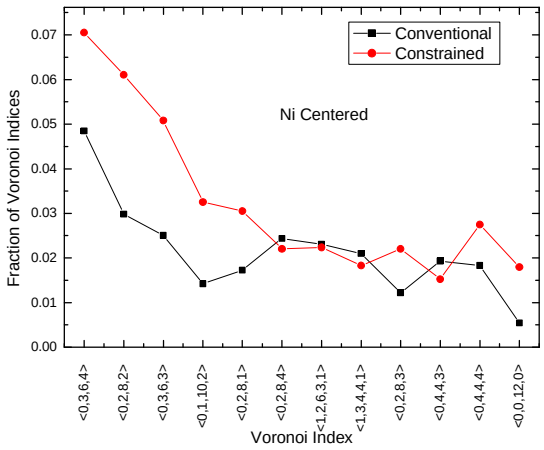


**Figure 6.35-** Dominant Ni-centered Voronoi Indices for the structures obtained by conventional and constrained RMC fits to the diffraction data for the eutectic liquid at 1400°C.

The comparison between the two distributions is summarized in Table 6.5.

**Table 6.5-** Dominant Ni-Centered polyhedra for the structures obtained by conventional and constrained RMC fits to the diffraction data for the eutectic liquid at 1400°C

| Ni-Centered | | | Nb-Centered | | |
|---|---|---|---|---|---|
| Coordination | Constrained | Unconstrained | Coordination | Constrained | Unconstrained |
| 11 | <0,2,8,1> | <0,4,4,3> | 11 | <0,2,8,1> | <0,2,8,1> |
| 12 | <0,2,8,2> | <0,2,8,2> | | | <0,4,4,3> |
| | <0,3,6,3> | <0,3,6,3> | | | <0,3,6,2> |
| | <0,4,4,4> | <0,4,4,4> | 12 | <0,2,8,2> | <0,2,8,2> |
| 13 | <0,3,6,4> | <0,3,6,4> | | <0,3,6,3> | <0,3,6,3> |
| | <0,1,10,2> | <1,3,4,4,1> | 13 | <0,3,6,4> | <0,3,6,4> |
| | <1,2,6,3,1> | <1,2,6,3,1> | | <0,1,10,2> | <0,1,10,2> |
| 14 | <0,2,8,4> | <0,2,8,4> | | <0,2,8,3> | <0,2,8,3> |
| | | | 14 | <0,2,8,4> | <0,2,8,4> |
| | | | | <0,3,6,5> | |
| | | | | <0,1,10,3> | |

The VI for the dominant Nb-centered clusters in the structures obtained by the constrained and unconstrained RMC fits are also similar (Figure 6.36). Here, the distribution doesn't tighten in the same fashion as the Ni-centered clusters did with constraining, and the coordination number increases from 12.29 to 13.04 instead of decreasing.

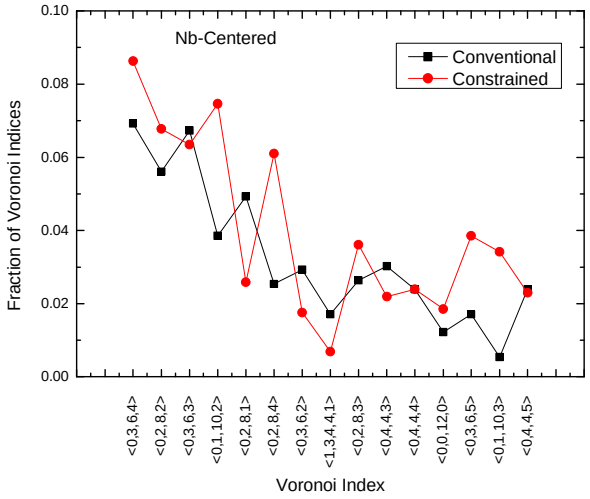


**Figure 6.36-** Dominant Nb-centered Voronoi Indices for structures obtained by conventional and constrained RMC fits to the diffraction data for the eutectic liquid at 1400°C.

In both cases the most abundant clusters are the 14 coordinated (<0,2,8,4>), 13 coordinated (<0,3,6,4>, <0,1,10,2>, <0,2,8,3>), 12 coordinated (<0,3,6,3>, <0,2,8,2>) and 11 coordinated (<0,2,8,1>) polyhedra. The only differences in the dominant Nb-centered clusters are the appearance of two additional 14 coordinated indices appearing in the structure obtained by the constrained RMC fit, replacing two 11 coordinated indices in the structure from the conventional RMC fit. The VI for the Nb-centered dominant clusters are summarized with the Ni-centered ones in Table 6.5.

In the comparison between the constrained and unconstrained RMC results, the differences in the VI distributions of the structures obtained (either for Ni-centered or Nb-centered) are not nearly as large as those observed for the Pt-centered clusters in $Zr_{80}Pt_{20}$. This is despite the indicated MRO in the MD PPCFs for both the Ni-Ni and Nb-Nb correlations. There is also a striking similarity between the polyhedra observed in the

Zr-Pt and Ni-Nb liquids, indicating that the two systems share many common structures despite a different chemical composition and enthalpy of mixing between constituents. The ratio of atomic radii are approximately the same in both systems, however, ($r_{Zr}/r_{Pt}$ = 1.15; $r_{Nb}/r_{Ni}$ = 1.17) indicating that packing may play a prominent role in determining the local structures in these systems.

## 6.6. Conclusions

A systematic survey of the liquid densities of $Ni_xNb_{100-x}$ near the reported bulk metallic glass-forming composition ($Ni_{62}Nb_{38}$) showed no maximum there, but instead showed local maxima at $Ni_{62.8}Nb_{37.2}$ and $Ni_{64}Nb_{36}$, suggesting new candidates for bulk metallic glass formation. A survey of several liquids in the Ni-Nb-TM family found very similar X-ray static structure factors. However, a detailed comparisons between $Ni_{59.5}Nb_{40.5}$, $Ni_{62}Nb_{38}$ (bulk metallic glass former), and $Ni_{60}Nb_{30}Ta_{10}$ (bulk metallic glass former) was conducted by performing conventional RMC fits to the $S(q)$s and analyzing the resulting atomic structures in terms of HA indices. The high GFA compositions exhibited a higher degree of pure icosahedral order than the low GFA composition. While constrained RMC fits to the data are required at other temperatures, the similarities between the constrained and unconstrained fits to $S(q)$s at 1400°C lend validity to the HA results obtained from the unconstrained fits.

## 6.7. References


[1] Z. Zhu, H. Zhang, D. Pan, W. Sun and Z. Hu, *Advanced Engineering Materials* **8,** 953, (2006).

[2] L. Xia, W. H. Li, S. S. Fang, B. C. Wei and Y. D. Dong, *Journal of Applied Physics* **99,** 026103(2006).

[3] A. Inoue, *Acta Materialia* **48,** 4986, (2000).

[4] A. Takeuchi and A. Inoue, *Materials Transactions* **42,** 1435, (2001).

[5] T. Shindo, Y. Waseda and A. Inoue, *Materials Transactions* **43,** 2502, (2002).
[6] H. Choi-Yim, D. Xu and W. L. Johnson, *Materials Science and Engineering A* **449-451,** 134, (2007).
[7] Z.-Z. Yuan, S.-L. Bao, Y. Lu, D.-P. Zhang and L. Yao, *Journal of Alloys and Compounds* **459,** 251, (2008).
[8] Z. W. Zhu, H. F. Zhang, B. Z. Ding and Z. Q. Hu, *Materials Science and Engineering A* **492,** 221, (2008).
[9] H. J. Chang, E. S. Park, Y. S. Jung, M. K. Kim and D. H. Kim, *Journal of Alloys and Compounds* **434-435,** 156, (2007).
[10] J. F. Loffler and W. L. Johnson, *Applied Physics Letters* **76,** 3394, (2000).
[11] S. C. Glade, R. Busch, D. S. Lee, W. L. Johnson, R. K. Wunderlich and H. J. Fecht, *Applied Physics Letters* **87,** 7242, (2000).
[12] R. Gerling, F. P. Schimansky and R. Wagner, *Nuclear Science and Engineering* **110,** 374, (1992).
[13] N. Mattern, G. Goerigk, U. Vainio, M. K. Miller, T. Gemming and J. Eckert, *Internal Report* (2009).
[14] F. R. D. Boer, R. Boom, W. C. M. Mattens, A. R. Miedema and A. K. Niessen, Cohesion In Metals: Transition Metal Alloys (Cohesion And Structure), Elsevier Science Ltd, (1989).
[15] B. Predel, *SpringerMaterials - The Landolt-Börnstein Database*.
[16] M. Leonhardt, W. Loser and H.-G. Lindenkreuz, *Acta Materialia* **47,** 2961, (1999).
[17] S. Mukherjee, Z. Zhou, W. L. Johnson and W.-K. Whim, *Journal of Non-Crystalline Solids* **337,** 21, (2004).
[18] M. B. Robinson, D. Li, J. R. Rogers, R. W. Hyers and L. Savage, *Applied Physics Letters* **77,** 3266, (2000).
[19] S. Mukherjee, J. Schroers, Z. Zhou, W. L. Johnson and W.-K. Rhim, *Acta Materialia* **52,** 3689, (2004).
[20] S. M. Chathoth, B. Damaschke, M. M. Koza and K. Samwer, *Physical Review Letters* **101,** 037801(2008).
[21] T. Fujita, P. F. Guan, H. W. Sheng, A. Inoue, T. Sakurai and M. W. Chen, *Physical Review B* **81,** 140204.
[22] S. M. Chathoth and K. Samwer, *Applied Physics Letters* **97,** 221910.
[23] S. M. Chathoth, B. Damaschke, J. P. Embs and K. Samwer, *Applied Physics Letters* **94,** 201906(2009).
[24] S. M. Chathoth, B. Damaschke, J. P. Embs and K. Samwer, *Applied Physics Letters* **95,** 191907(2009).
[25] S. M. Chathoth, B. Damaschke, T. Unruh and K. Samwer, *Applied Physics Letters* **94,** 221906(2009).
[26] P. Lamparter, M. Shaal and S. Steep, *Proceedings of the International Conference on Neutron and X-Ray Scattering: Complementary Techniques* **101,** 51, (1990).
[27] S. Steeb and P. Lamparter, *Proceedings of the 8th International Conference on Liquid and Amorphous Metals* **156-158,** 42, (1993).
[28] E. Svab, F. Forgacs, I. Hajdu, N. Kroo and J. Takacs, *Journal of Non-Crystalline Solids* **46,** 125, (1981).

[29] E. Svab, L. Koszegi, G. Meszaros and J. Jakacs, *Zeitschrift für Physikalische Chemie* **157,** 5, (1988).
[30] E. Svab and S. N. Ishmaev, *Experimental Techniques in Physics* **36,** 89, (1988).
[31] S. Basak, R. Clarke and S. R. Nagel, *Physical Review B* **20,** 4278, (1979).
[32] T. Egami and S. J. L. Billinge, Underneath the Bragg Peaks, Pergamon, Oxford (2003).
[33] B. Predel, *SpringerMaterials - The Landolt-Börnstein Database*.
[34] S. G. Hao, C. Z. Wang, M. J. Kramer and K. M. Ho, *Journal of Applied Physics* **107,** 053511(2010).
[35] Y. Q. Sheng and E. Ma, *Progress in Materials Science* **56,** 379, (2011).
[36] P. Lamparter, *Physica Scripta* **T57,** 45, (1995).
[37] Q. Zhang, W. S. Lai and B. X. Liu, *Journal of Non-Crystalline Solids* **261,** 137, (2000).
[38] G. Kreuch and J. Hafner, *Journal of Non-Crystalline Solids* **189,** 227, (1995).
[39] H. W. Sheng, W. K. Luo, F. M. Alamgir, J. M. Bai and E. Ma, *Nature* **439,** 419(2006).
[40] Y. Li, Q. Guo, J. A. Kalb and C. V. Thompson, *Science* **322,** 1816(2008).
[41] J.-W. Park and C. Altstetter, *Metallurgical and Materials Transactions A* **18,** 43(1987).
[42] S. K. Chung, D. B. Thiessen and W.-K. Rhim, *Review of Scientific Instruments* **67,** 3175, (1996).
[43] R. C. Bradshaw, J. R. Rogers, K. F. Kelton, R. W. Hyers and D. P. Schmidt, *Review of Scientific Instruments* **76,** 125108, (2005).
[44] T. H. Kim and K. F. Kelton, *J. Chem. Phys.* **126,** 054513(2007).
[45] M. L. McGreevy, *J. Phys. Condens. Matter* **3,** F9, (1991).
[46] D. A. Keen, *Nature (London)* **344,** 423, (1990).
[47] G. Gresse and J. Hafner, *Phys. Rev. B* **47,** 558, (1993).
[48] G. Kresse, Technische Universität Wien (1993).
[49] G. Kresse and J. Furthmüller, *Computational Material Science* **6,** 15, (1996).
[50] G. Kresse and J. Furthmüller, *Phys. Rev. B* **54,** 11169, (1996).
[51] G. Kresse and D. Joubert, *Phys. Rev. B* **59,** 1758, (1999).
[52] S. Y. Wang, C. Z. Wang, M. Z. Li, L. Huang, R. T. Ott, M. J. Kramer, D. J. Sordelet and K. M. Ho, *Phys. Rev. B* **78,** 184204(2008).
[53] V. M. Wessels, PHASE FORMATION, LIQUID STRUCTURE, AND PHYSICAL PROPERTIES OF AMORPHOUS AND QUASICRYSTAL-FORMING ALLOYS, *Physics*, Washington University, St. Louis (2009).
[54] N. A. Mauro and A. J. Vogt, Cu-Hf BESL2010 analysis, (2010).
[55] K. F. Kelton, A. K. Gangopadhyay, T. H. Kim and G. W. Lee, *Journal of Non-Crystalline Solids* **352,** 5318(2006).
[56] J. D. Honeycutt and H. C. Andersen, *J Phys. Chem.* **91,** 4950, (1987).
[57] I. Szaloki, *X-ray Spectrometry* **25,** 21, (1996).
[58] T. H. Kim, STRUCTURAL STUDY OF SUPERCOOLED LIQUIDS AND METALLIC GLASSES BY HIGHE ENERGY X-RAY DIFFRACTION AND REVERSE MONTE CARLO SIMULATION, *Physics*, Washington University, St. Louis (2007).

[59] M. Widom, Partial Pair Correlation Functions for Ni60Nb40 liquid at 1400C, (2011).

# Chapter 7

## High Energy X-ray Scattering Studies of the Local Order in Liquid Al[€]

[€]Much of this work appears in the manuscript *"High Energy X-ray Scattering Studies of the Local Order in Liquid Al."* N. A. Mauro, J. C. Bendert, A. J. Vogt, J. M. Gewin, and K. F. Kelton. *Accepted for publication in the Journal of Chemical Phsyics, April 2011.*

### 7.1. Introduction

The solidification of liquid metals is an open area of study. Ever since the discovery of the first metallic glass in a Au-Si alloy the study of glass formation and the transition from the undercooled liquid to the solid has generated an entire field of study. The development of X-ray and neutron scattering techniques and their subsequent application to disordered systems has shown that local atomic structural evolution is important in understanding solidification and glass formation. While solidification from the undercooled liquid involves a complicated interplay between local topological and chemical ordering, thermodynamics, and kinetics, the study of the crystallization processes in Al-based alloys has drawn considerable interest in the materials science community due to the alloys' generally favorable strength to weight ratio, low cost, availability and ease of processability.

Recent advances in levitation techniques have led to the development of facilities that enable X-ray and neutron scattering studies on containerlessly processed liquids. Studies have demonstrated that equilibrium metallic liquids often contain significant amounts of short-range (SRO) and even medium-range (MRO) order. In transition metal liquids, this is frequently dominated by icosahedral and icosahedral-like order. In most cases, the order becomes more extensive and better defined in the supercooled liquid. This order can have a significant impact on phase transitions in the liquid, including

crystal nucleation [1], chemical ordering [2], and glass formation [3], The technological importance of aluminum (Al) and the absence of d-band bonding, make structural studies of this liquid of fundamental as well as practical interest. Additionally, growing computing capabilities make possible increasingly realistic *ab initio* molecular dynamics studies of liquid structures and crystal nucleation and growth. It is important to check the accuracy of these simulations in such a simple metallic liquid by a comparison with experimental data.

Although Al and Al-based alloys and liquids generally have low reactivities when compared to other metallic liquids [4], interactions with container walls and dynamical gas environments, which are sources of contamination and heterogeneous nucleation, make containerless environment studies desirable. Additionally, X-ray diffraction studies of low-*Z* amorphous phases, liquid Al being a prime example, are complicated by container scattering, which can make it difficult to deconvolve the scattering signal from the sample. Despite these problems, some experimental measurements of the structures of Al liquids in containers have been made.

The earliest study by Stallard and Davis [5] provide measurements of the structure factors, $S(q)$, at 43K and 369K above the melting temperature ($T_m$ = 933K = 660°C). Their data show that the intensity of the first peak in $S(q)$ is 2.17 and occurs at a momentum transfer, $q$, of 2.67 $Å^{-1}$ for temperatures near the melting temperature. Subsequent neutron diffraction studies of Al in a container [6, 7] give a static structure factor at the same $q$ position, but with an intensity that is ~12% larger. Other X-ray diffraction studies of liquid Al in a container at and above the melting temperature [7-9] found $S(q)$s that are consistent with the neutron scattering results.

Here, we report the results of high-energy synchrotron X-ray diffraction studies of liquid Al in the temperature range of 850°C to 1000°C (1123K to 1273K) using BESL. High quality density data are presented and correlated with the scattering data, which was collected to 13 $Å^{-1}$. Both $S(q)$ and the pair distribution function, $g(r)$, are calculated from the data and atomic structures for the liquid are obtained at all temperatures by making Reverse Monte Carlo (RMC) fits to these data. The topology of these configurations are examined in terms of their Honeycutt-Andersen (HA) indices [10]. Consistent with previous MD simulations, the results of these studies show that the liquid is dominated by icosahedral-like short range order. However, the MD simulations over estimate the amount of face-centered cubic (FCC) and hexagonal close-packed (HCP) type order, based on the RMC results.

### 7.2. Experimental and RMC Fitting Methods

Approximately 3 mm diameter spheres of Al were prepared by arc-melting high purity Al (99.999%) on a water-cooled copper hearth in a high-purity Ar (99.999%) atmosphere according to the procedures laid out in Chapter 2. These were used for *in-situ* liquid structure studies using the Beamline Electrostatic Levitation facility (BESL) [11, 12], described in Chapter 4. Before processing, the samples were partially melted on a tungsten post in the BESL vacuum chamber (pressure ~$5x10^{-7}$ Torr) using a high-power diode laser. This was found to aid levitation processing, presumably by removing trapped gas during arc-melting.

For the structural studies, diffraction images were taken at 1 Hz, following the procedures described in Chapter 2, until adequate statistics were obtained. The distance from the sample to detector, the detector center and the detector tilt were calibrated by

fitting the diffraction pattern of a levitated polycrystalline Si sample positioned at the nominal position of the Al sample. The images were corrected for oblique incidence, absorption, multiple scattering, fluorescence, polarization, sample geometry and Compton scattering contributions by using Fit2d [13] and PDFGetX2 [14] analysis packages, described in Chapters 2, 5, and 6, and the measured intensities, $I(q)$, were extracted. The static structure factors, $S(q)$, were computed using

$$S(q) = \frac{I(q)}{|f_{Al}(q)|^2}, \tag{1}$$

where $f_{Al}(q)$ is the $q$-dependent atomic form factor for Al. The pair distribution function, $g(r)$, is related to the Fourier transform of $S(q)$

$$g(r) = \frac{\rho(r)}{\rho_0} = 1 + \frac{1}{2\pi^2 \rho_0} \int (S(q) - 1) \frac{\sin(qr)}{qr} q^2 dq \tag{2}$$

where $\rho_0$ is the experimentally measured average atomic density and $\rho(r)$ is the density at a distance $r$ from an average atom located at the origin.

A two color optical pyrometer (Process Sensors model MQ22 with spectral response 1.45μ to 1.80μ) was used to measure the sample temperature with a precision of greater than 2% over the temperature range studied. A fiber coupled diode laser (980nm, 50W maximum operating in continuous mode) was used to melt the samples and to maintain a constant liquid temperature for the isothermal scattering measurements. Simultaneous non-contact density measurements were made with the shadow method [15, 16] using a Pixelink PL-B742U CCD camera and a 450 nm backlight. Video data were taken at a frame rate of 25 frames per second (fps), allowing averages to be taken of up to 500 frames at each isothermal step. The relative precision of the density data was ~1.5% over the temperature range studied, with an absolute accuracy of 3% (grade 200

standards were used for image calibration), and were in good agreement with previously published density measurements for liquid Al [17]. The uncertainty in these measurements has contributions from small patches of thin alumina on the sample surface, which were observed visually. These patches rotate in and out of the pyrometer field of view, increasing the temperature noise.

Atomic structures were obtained by Reverse Monte Carlo (RMC) [18-20] fits to the measured $S(q)$ and $g(r)$ data at all temperatures. In contrast to the differences that emerge in the Ni-Nb system (Chapter 6) between the HA distributions from fits to $S(q)$ and $g(r)$, no statistically significant differences emerged in the Al system. This is likely due to the simplicity of the scattering contributions in the pure Al liquid. The results reported here are exclusively from fits to $g(r)$. In RMC it is assumed that only statistical errors exist in the data, which have a normal distribution, and that no systematic errors exist in the input data. The details of the RMC fitting process is described in detail in Chapter 2.

For this study, both random and ordered cubic starting configurations were assumed, confined to a cubic box with dimensions appropriate to the measured density. The RMC minimum distances were set nominally at 2.15Å, varying with the temperature, but consistent with the measured pair distribution function. The short-range order (SRO) of the atomic structures obtained was evaluated in terms of their HA indices. A nearest-neighbor distance of nominally 3.90Å was used for these studies, again determined from the temperature dependent $g(r)$ data.

### 7.3. Results and Discussion

Data were collected from 1123K to 1273K. Charge loss from the Al samples made levitation difficult and the persistence of a thin surface layer of $Al_2O_3$ limited the supercooling that could be achieved. Fortunately, this temperature range corresponded to ranges obtained in other studies, allowing comparisons to be made to those reports. The measured X-ray static structure factors, $S(q)$, are shown in Figure 7.1. All oscillate around unity, indicating the high quality of the experimental data and that the appropriate corrections were made for absorption, background and Compton scattering. Four oscillations are clearly visible out to 11 $Å^{-1}$, with a fifth oscillation truncated by the finite $q$-range of the measurement. No smoothing was applied to these data. With decreasing temperature, the first (lowest $q$) peak sharpens, increases in magnitude, and shifts very slightly to higher scattering angle, reflecting an increasing density. The heights of the first ($q_1$) and second ($q_2$) peaks, and the ratio of those peak heights, $S(q_2)/S(q_1)$, are shown in Figure 7.2. Over this limited temperature range the primary peak position remains nearly unchanged at 2.685±0.005 $Å^{-1}$, but the amplitude increases from 1.89 at 1273K to 2.11 at 1123K. Qualitatively, the structure factors show the behavior expected for a single component liquid. $S(q_1)$ for all temperatures is consistent, to within experimental error, with other X-ray studies of Al liquids made with containers [7, 9]. Recently, J. C. Bendert has calculated a correction to $S(q)$ attempting to account for the secondary scatter of the diffracted intensity from the beryllium exit window (see Chapter 4 for more details of the beryllium window geometry). When this correction is applied, the $S(q_1)$ increases, systematically, by ~ 4%. This calculation is preliminary and constitutes an estimate for the upper bound on an error bar, and will not be included in detail

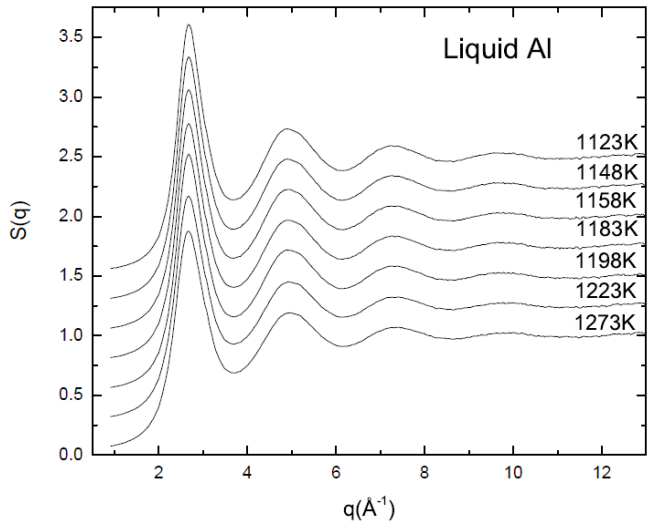


**Figure 7.1-** The X-ray static structure factors, $S(q)$, calculated from the measured scattering data for liquid Al at all temperatures.

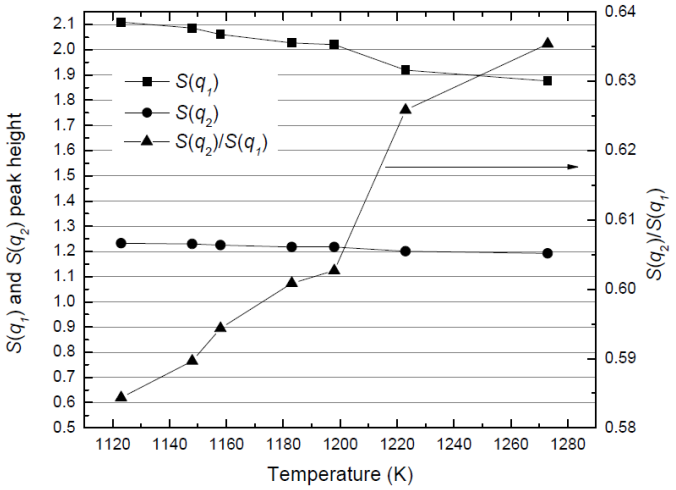


**Figure 7.2-** Heights of the first peak, $S(q_1)$, and second peak, $S(q_2)$, in the structure factor, and the ratio of the first to second peak heights , $S(q_2)/S(q_1)$ as a function of temperature for liquid Al.

The pair distribution functions, $g(r)$, calculated using Equation 2 are shown as a function of temperature in Figure 7.3. Since the values of the $S(q)$ were nonzero at the highest $q$

measured, a decaying exponential is used for damping to reduce truncation errors. The number density and the peak intensities for $S(q)$ and $g(r)$ for all temperatures are summarized in Table 1. Like $S(q)$, the first (nearest-neighbor) peak position, $r_1$, shows little change with temperature, remaining approximately constant at 2.763±.007 Å. The heights of the first ($r_1$) and second ($r_2$) peaks, and the ratio of those peak heights, $g(r_2)/g(r_1)$, are shown in Figure 7.4. An integration of the area under the first peak up to the first minimum for all temperatures gives a coordination number of ~13, which is likely an over estimate, since the first and second shells are not well separated. A fit to the first peak and subsequent integration under the curve gives a coordination number that is approximately 8% less, depending on the curve used in the fit.

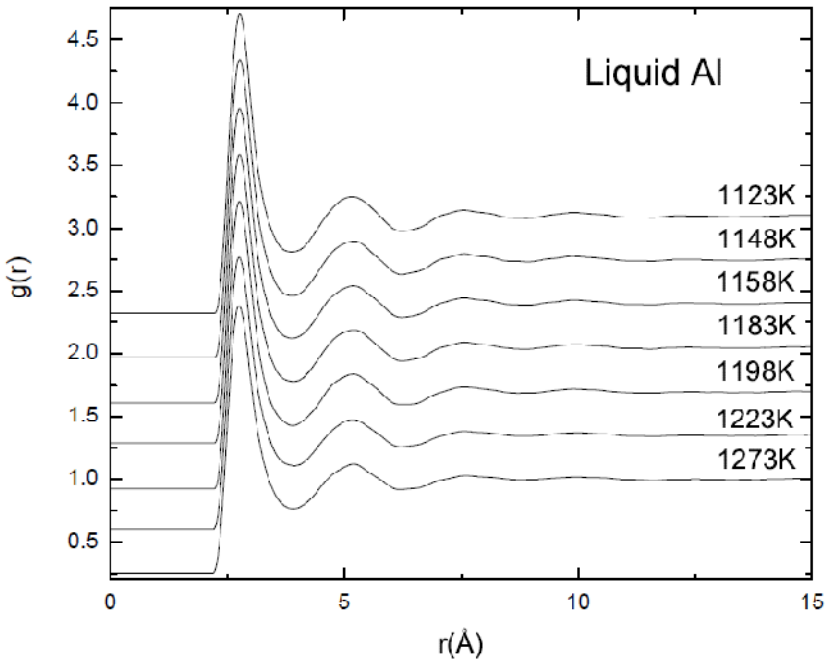


**Figure 7.3-** The pair distribution function, $g(r)$, calculated from the scattering data for liquid Al at all temperatures.

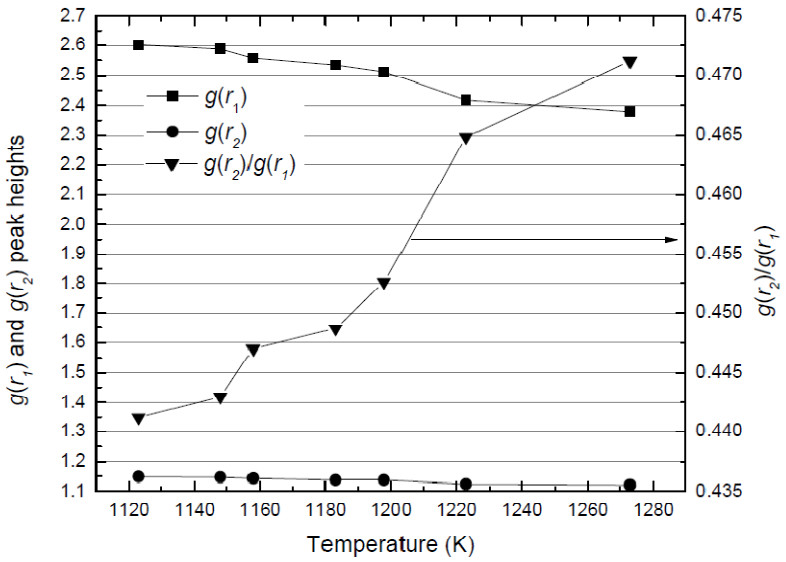


**Figure 7.4-** Heights of the first peak, $g(r_1)$, and second peak, $g(r_2)$, in the pair distribution function, and the ratio of the first to second peak heights, $g(r_2)/g(r_1)$ as a function of temperature for liquid Al.

**Table 7.1-** Thermophysical and structural parameters for liquid Al at each step in this study.

| Temperature (K) | Density (1/ Å$^3$) | $S(q_1)$ | $S(q_2)$ | $g(r_1)$ | $g(r_2)$ |
|---|---|---|---|---|---|
| 1123 | .0531 | 2.110 | 1.233 | 2.602 | 1.148 |
| 1148 | .0528 | 2.086 | 1.230 | 2.587 | 1.146 |
| 1158 | .0527 | 2.061 | 1.225 | 2.557 | 1.143 |
| 1183 | .0525 | 2.027 | 1.218 | 2.534 | 1.137 |
| 1198 | .0524 | 2.021 | 1.218 | 2.512 | 1.137 |
| 1223 | .0522 | 1.919 | 1.201 | 2.418 | 1.124 |
| 1273 | .0516 | 1.876 | 1.192 | 2.379 | 1.121 |

The atomic structures of the liquid as a function of temperature were obtained from Reverse Monte Carlo (RMC) fits to $g(r)$. Reverse Monte Carlo produces an average structure that is consistent with the experimental data. Since the RMC method is an inverse method that uses 1-dimensional scattering information to deduce a 3-dimensional structure, some caution should be exercised when interpreting the results. Given that the liquid is exploring many different configurations over the time of the measurement, RMC fits produce average structures for such ergodic liquids. Extensive discussions of the method and the interpretation of the results exist in the literature [19, 21-23].

While there is no unique configuration in a RMC ensemble, the exploration of convergence in configuration space from different initial configurations to a final one is of interest. Liquid Al offers a simple system for investigating this. The robustness of the converged atomic structures was examined as a function of the structure of the initial starting configuration: random, simple cubic (SC), face-centered cubic (FCC) and body-centered cubic (BCC). To track convergence, intermediate configurations were collected at approximately 10% of the total run time. The HA indices of these configuration were determined and compared with those from the final configurations (referred to here as the *extended runs*). The total run time was set to be the time when $\chi_o^2$ had small amplitude oscillations about an asymptotic value. Only the SC initial configuration produced an intermediate HA distribution that differed appreciably from that of the extended run. In all cases the converged $\chi_o^2$ were larger for the ordered starting configurations than for the random one, with the BCC and FCC initial configurations being least consistent with the experimental data (Figure 7.5).

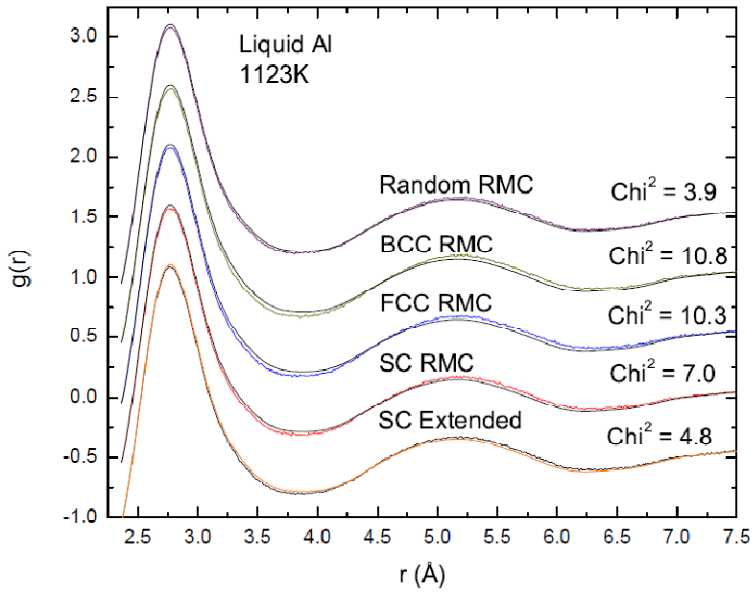


**Figure 7.5-** A comparison between the $g(r)$ experimental data for 1123K and the results of RMC fits with various starting configurations. "Random RMC," "BCC RMC," "FCC RMC," and "SC RMC" refer to the configurations collected at the intermediate time. "SC Extended" refers to the configuration collected at the extended time.

The HA analysis results for the converged RMC structures at 1123K, obtained using ordered and random initial configurations, are shown in Figure 7.6. Common to all final configurations is a dominance of icosahedral (1551) and distorted icosahedral (1431 and 1541) short-range order, although the amount of each is a function of the starting configuration. All final configurations also showed a modest amount of BCC order (1441 and 1661), as well as some 1311 and 1322 local order, which represent rhombus symmetrical features [24]. The HA indices for the converged structures obtained for FCC and BCC starting configurations showed a greater degree of icosahedral (1551) and BCC (1661) order than the structure obtained from a random starting configuration. These indices are often observed to trend in tandem [25]. Indices that are not represented on the

plot showed little prevalence in the final configurations. In particular, the common measures of the close-packed structures, FCC and HCP (1421 and 1422) showed only marginal prevalence.

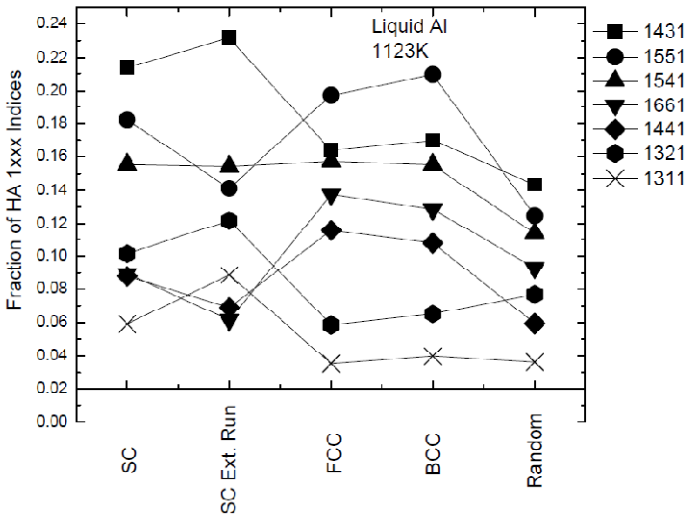


**Figure 7.6-** Fraction of HA indices for the converged RMC structures at 1123K, obtained using ordered and random initial configurations.

As noted earlier, the SC starting configuration was the only one that gave significantly different HA indices between the intermediate and final configurations. Both have a large amount of icosahedral (1551) and distorted icosahedral (1431) order compared with that from other starting configurations. The amount of 1431 order increases, while that of 1551 order decreases, with longer run times. The converged amount of 1551 is similar to that for the random configuration, but the amount of 1431 is much larger. Since the random starting configuration gave a smaller converged $\chi_o^2$, however, it is unclear that this difference is meaningful.

Convergence was explored by relaxing the constraints on the atomic motions in the random moves in the fit. There are local minima in the $\chi_o^2$ landscape, corresponding to metastable configurations, which the metropolis algorithm attempts to avoid. However, there is no guarantee that the fit has reached the global $\chi_o^2$ minimum. The converged configurations for the SC, FCC and BCC starting configurations were used as starting configurations for a second RMC fit, but this time increasing the maximum distance for an atomic move from 0.3Å to 0.9Å. After running this for an intermediate amount of time, the maximum atomic move was again reduced to 0.3Å and the RMC fit was allowed to converge. The final $\chi_o^2$ and the HA index distributions for the converged structures differ negligibly from those shown in Figure 7.3 suggesting that the configurations obtained were at least deeply metastable.

Assuming a random starting configuration of $10^4$ atoms, consistent with the experimentally determined number density (Table 1), RMC fits were made to the $g(r)$ data for all measurement temperatures. Three independent RMC calculations were made at each temperature, beginning with different random configurations. Good agreement with the data was found, with the values for the converged $\chi_o^2$ in the range of 3.5 to 4.2. The fits (Figure 7.7) show the same qualitative trends for each temperature. Compared with the data, the converged fit is slightly high for the first peak, slightly low for the second peak, and nearly indistinguishable for high-$r$ oscillations.

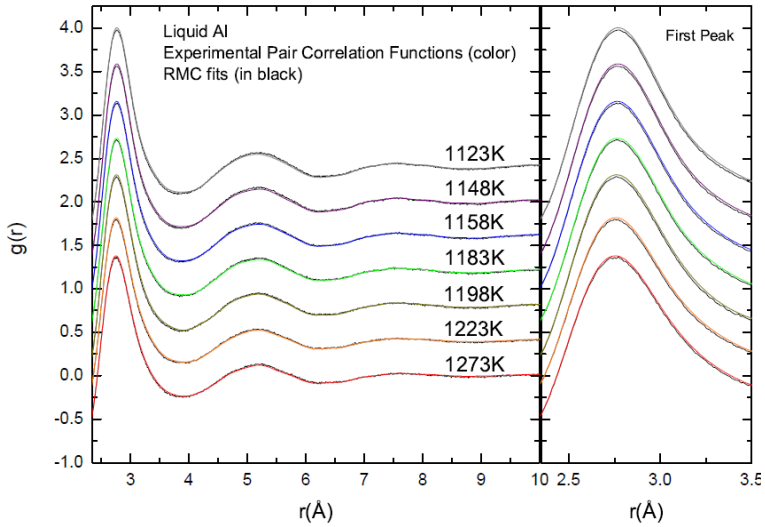


**Figure 7.7**- RMC fits made to the $g(r)$ data for all measurement temperatures. The initial configuration is random in all cases.

The HA analysis results for the converged distributions are shown as a function of temperature in Figure 7.8, including the 1123K data already discussed. Only the most prevalent indices are presented, and the scale is normalized to the total number of nearest neighbor (1xxx) HA pairs identified. The error bars reflect the standard deviation in the number of indices obtained in the converged configurations for the three random starting configurations. All temperatures show a prevalence of icosahedral (1551), and distorted icosahedral (1541 and 1431) order, with a modest amount of icosahedral-like order (1321) and BCC order (1661+1441). These are all consistent with MD simulations by Hui and Pederiva [24] at ambient conditions. However, the MD simulations generate a slightly larger amount of closed-packed structures, 1421 and 1422, than the RMC fits to the experimental data reported here, which show only negligible quantities of these structures. The 1123K and 1148K HA distributions contain a slightly enhanced amount of 1551 pairs relative to those at other temperatures, which appears to be robust for the

three fits made at each temperature. Because of the limited temperature range available, this trend cannot be extended to lower temperatures, but an increasing amount of 1551 order was also observed by Hui and Pederiva.

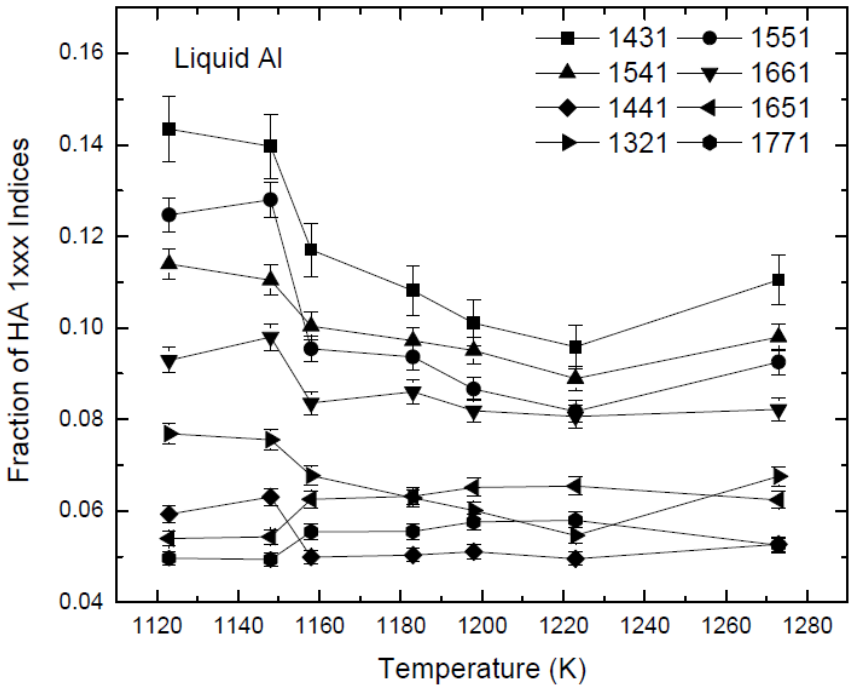


**Figure 7.8-** HA analysis results for the converged distributions shown as a function of temperature. All initial configurations for the RMC fits were random.

## 7.4. Conclusions

High quality X-ray scattering and density data from levitated equilibrium Al liquids in the range from 1123K to 1273K are presented. The static structure factor, $S(q)$, and pair distribution function, $g(r)$, were determined from the scattering data and Reverse Monte Carlo fits were made to obtain plausible atomic structures. A study of the convergence behavior for ordered and random starting configurations demonstrates that even for this

simple system, not all starting configurations converge to the same structure, as measured by the distribution of Honeycutt-Andersen indices, although icosahedral and icosahedral-like order is the dominant short-range order in all cases. The $g(r)$s calculated from the converged configuration of an initially random configuration of atoms were most consistent with the experimentally determined $g(r)$s. The HA analysis of those configuration give amounts of icosahedral-like order that are consistent with those obtained in previous MD simulations of liquid Al at ambient pressure. However, the MD predictions for the amount of close-packed face-centered cubic and close-packed hexagonal order is higher than obtained from the RMC fits.

## 7.5. References


[1] K. F. Kelton, G. W. Lee, A. K. Gangopadhyay, R. W. Hyers, T. J. Rathz, J. R. Rogers, M. B. Robinson and D. S. Robinson, *Phys. Rev. Lett.* **90,** 195504, (2003).

[2] V. Wessels, A. K. Gangopadhyay, K. K. Sahu, R. W. Hyers, S. M. Canepari, J. R. Rogers, M. J. Kramer, A. I. Goldman, J. W. Lee, J. R. Morris and K. F. Kelton, *Physical Review B (in press)* (2011).

[3] Y. T. Shen, T. H. Kim, A. K. Gangopadhyay and K. F. Kelton, *Phys. Rev. Lett.* **102,** 057801(2009).

[4] N. N. Greenwood and A. Earnshaw, Chemistry of the Elements, Reed Educational and Professional Publishings, Ltd., Boston (1997).

[5] J. M. Stallard and J. C. M. Davis, *Physical Review A* **8,** 368, (1973).

[6] N. Iqbal, N. H. v. Dijk, V. W. J. Verhoeven, W. Montfrooij, T. Hansen, L. Katerman and G. J. Kearley, *Acta Mat.* **51,** 4497, (2003).

[7] S. Takeda, S. Harada, S. Tamaki and Y. Waseda, *Journal of the Physical Society of Japan* **60,** 2241, (1991).

[8] S. Mudry and T. Lutsyshyn, *Journal of Alloys and Compounds* **367,** 289, (2004).

[9] C. A. Becker and M. J. Kramer, *Modelling and Simulation in Materials Science and Engineering* **18,** 074001, (2010).

[10] J. D. Honeycutt and H. C. Andersen, *J Phys. Chem.* **91,** 4950, (1987).

[11] A. K. Gangopadhyay, G. W. Lee, K. F. Kelton, J. R. Rogers, A. I. Goldman, D. S. Robinson, T. J. Rathz and R. W. Hyers, *Rev. Sci. Instrum.* **76,** 073901(2005).

[12] P.-F. Paradis, T. Ishikawa and S. Yoda, *J. Non-Cryst. Solids* **312-314,** 309(2002).

[13] A. P. Hammersley, FIT2D: An Introduction and Overview, *ESRF Internal Report, ESRF97HA02T* (1997).

[14] I. K. Jeong, J. Thompson, T. Proffen, A. M. P. Turner and S. J. Billinge, *J. Appl. Crys.* **34,** 536, (2001).
[15] S. K. Chung, D. B. Thiessen and W.-K. Rhim, *Rev. Sci. Instrum.* **67,** 3175, (1996).
[16] R. C. Bradshaw, J. R. Rogers, K. F. Kelton, R. W. Hyers and D. P. Schmidt, *Rev. Sci. Instrum.* **76,** 125108, (2005).
[17] M. J. Assael, K. Kakosimos, R. M. Banish, J. Brillo, I. Egry, R. Brooks, P. N. Quested, K. C. Mills, A. Nagashima, Y. Sato and W. A. Wakeham, *Journal of Chemical Reference Data* **35,** 285, (2006).
[18] T. H. Kim and K. F. Kelton, *J. Chem. Phys.* **126,** 054513(2007).
[19] M. L. McGreevy, *J. Phys. Condens. Matter* **3,** F9, (1991).
[20] D. A. Keen, *Nature (London)* **344,** 423, (1990).
[21] R. L. McGreevy and P. Zetterström, *Current Opinion in Solid State and Materials Science* **7,** 41(2003).
[22] R. L. McGreevy, *J. Non-Cryst. Solids* **156-158,** 949(1993).
[23] R. L. McGreevy, *J. Phys. Condens. Matter* **13,** R877, (2001).
[24] L. Hui and F. Pederiva, *Journal of Chemical Physics* **118,** 10707, (2003).
[25] S. Y. Wang, C. Z. Wang, M. Z. Li, L. Huang, R. T. Ott, M. J. Kramer, D. J. Sordelet and K. M. Ho, *Phys. Rev. B* **78,** 184204(2008).

# Chapter 8

## Summary and Conclusions

In this dissertation, the results of structural studies of metallic liquids and glasses using high energy X-ray diffraction have been presented. The overarching goal of this work is to understand how atomic structural evolution relates to undercooling and glass formation in metallic liquids. To address this problem, the Beamline Electrostatic Levitator (BESL) was built to allow structural X-ray studies to be combined with coordinated thermophysical property measurements in supercooled liquids. While X-ray diffraction is a powerful tool for probing structure in an amorphous material it only provides angular averaged information of the two-body correlations, the pair correlation. Phase information and many-body correlations, which are critical for determining the absolute positions of atoms, are lost. As a result, Reverse Monte Carlo (RMC) fits to the experimental data are used to reconstruct reasonable three dimensional models of structures based on the one dimensional diffraction information. The atomic configurations determined from those fits are then quantitatively analyzed in terms of their Honeycutt-Anderson (HA) indices and Voronoi polytetrahedra (VI).

In Chapter 3, the first evidence for nanoscale phase separation into Al-rich and Al-poor regions in in rapidly quenched $Al_{88}Y_7Fe_5$ alloys was presented. The pure Al zones in the Al-rich regions likely are the sites for the rapid nucleation of $\alpha$-Al, due to the smaller nucleation barrier. Further, we show that the transformation initially proceeds by rapid nucleation and not by coarsening as was proposed earlier. The tendency for many Al-based metallic glasses to crystallize to an amorphous/nanocrystal composite and the

recently reported evidence for phase separation in a related glasses ($Al_{89}Ni_6La_5$) raises the question of whether nanoscale phase separation is common in Al-based glasses.

In Chapter 4, the design of WU-BESL, a portable and inexpensive electrostatic levitation facility that is optimized for high-energy X-ray scattering studies is described. The principle utility of this design is its compactness, ease of operation, and low cost. A simple and versatile alignment platform allows integration of the facility into a wide range of synchrotron beamlines. The alignment stage is completely contained within the footprint of the chamber table and its portability is desirable for ease of integration into multiple beamlines. It is more than sufficiently stable for the diffraction studies of amorphous materials (liquids and glasses) and fine grained crystal phases.

In Chapter 5, X-ray diffraction studies revealed the existence of a pre-peak at $q \sim 1.7$ $Å^{-1}$ in the static structure factor of $Zr_{80}Pt_{20}$ equilibrium and supercooled liquids, indicating medium-range order in the liquid. An analysis of the atomic structures obtained from a RMC fit that was constrained by partials obtained from an MD simulation to the scattering data indicates that the pre-peak is due to a Pt-Pt correlation among Zr-centered clusters having icosahedral-like symmetry. The icosahedral order in the liquid likely increases the crystal nucleation barrier, contributing to the ability to supercool and aiding glass formation in these alloys.

In Chapter 6, a survey of several liquids in the Ni-Nb-TM family revealed very similar X-ray static structure factors. However, a detailed comparison between $Ni_{59.5}Nb_{40.5}$, $Ni_{62}Nb_{38}$ (bulk metallic glass former), and $Ni_{60}Nb_{30}Ta_{10}$ (bulk metallic glass former) was conducted by performing conventional RMC fits to the $S(q)$s and analyzing the resulting atomic structures in terms of HA indices. The high GFA compositions

exhibited a larger amount of pure icosahedral order than did the low GFA compositions. While constrained RMC fits to the data are required at other temperatures, the similarities between the constrained and unconstrained fits to $S(q)$s at 1400°C lend validity to the HA results obtained from the unconstrained fits.

In Chapter 7, high quality X-ray scattering and density data from levitated equilibrium Al liquids in the range from 1123K to 1273K were presented. The static structure factor, $S(q)$, and pair distribution function, $g(r)$, were determined from the scattering data and Reverse Monte Carlo fits were made to obtain plausible atomic structures. The HA analysis of those configuration give amounts of icosahedral-like order that are consistent with those obtained in previous MD simulations of liquid Al. However, the MD prediction for the amount of closed-packed face-centered cubic and close-packed hexagonal order is higher than obtained from the RMC fits. Increasing computational abilities make MD simulations of complex liquids possible and allow their accuracy to be checked, as was done in this system.

The highly modular WUBESL has proven to be an effective way to acquire high quality X-ray diffraction data on liquids while simultaneously correlating that data with thermophysical property measurements. The importance of chemical information for obtaining realistic structures by RMC fits to the diffraction data is also demonstrated by highlighting the topological and chemical differences that emerge between constrained and unconstrained RMC fits and from incomplete information about MRO in the liquid. The first structural studies of liquids in the Ni-Nb family using the WUBESL identified a large amount of icosahedral-like order present at all compositions and may have

identified an important distinction between high GFA and low GFA composition: The prevalence of pure icosahedral order in better glass-formers.

# Appendix II.1.
## X-ray Generation

### *Low Energy X-ray Generation*

There are two commonly-used methods to create X-rays. In the first fast electrons interact with stationary, extremely massive, metal targets. When the electrons are accelerated or deflected by another charged particle a broad spectrum of radiation, which is called the Bremsstrahlung spectrum, is observed. Bremsstrahlung radiation [1], or "breaking radiation", is characterized by a continuous (but highly asymmetric) distribution of radiation, with a long tail in the longer wavelengths, which becomes more intense and shifts toward higher energies as the energy of the bombarding electrons is increased. The distribution is peaked near .45Å and .50Å when the electrons are accelerated through 50kV and 35kV, respectively, both in the X-ray range. The spectrum that emerges is qualitatively similar for all metal targets; the quantitative parameters vary with target materials. The energy spectrum of X-rays due to the deceleration in the field of atomic nuclei depends on the energy levels of the atomic electron, the screening effect they have on the moving particle and on the particle velocity.

There is a narrow distribution of incoming velocities, but varying degrees of deceleration upon energy transfer to the material lead to the broad X-ray spectrum, extending up to quanta of the energy of the moving particle. Details can be found elsewhere [1-3], but the Bremsstrahlung is a side effect of the generation of usable intense but narrow (in wavelength distribution) X-ray lines due to electron transitions in the material. For high enough incident electron energies, electrons in lower levels of the target atoms can be excited to metastable higher states or can actually knock electrons in

the lowest states out. This will cause electrons from upper shells to drop down and fill the created gap. In the process, a photon with a characteristic wavelength corresponding to the energy difference in the two levels is emitted. Transitions down to the n = 1 level are referred to as K transitions [4] (giving rise to X-ray K-lines) and those down to the n = 2 level are referred to as L transitions. The X-rays produced by transitions from the n = 2 to the n = 1 levels are called $K_\alpha$ x-rays, those or n = 3 → 1 are called $K_\beta$ x-rays, with $K_\beta$ being more energetic than $K_\alpha$. The transition probability for $K_\beta$ is generally lower, leading to a less intense usable X-ray source. The lines are generally split because there are degeneracies in the energy levels. The $K_\alpha$ line, the most useful line, is split into two different wavelengths, $K_{\alpha1}$ and $K_{\alpha2}$ While the two of the most common elements used to create X-rays in this fashion are copper and molybdenum, some other relatively common target materials are shown in Table 1. Often, a rotating anode (target) is used since typically only ~.1% of the incident electron energy is converted into X-rays while the rest is lost to thermal dissipation [1, 5, 6].

**Table 0.1-** $K_{\alpha1}$ and $K_{\alpha2}$ wavelengths for some common X-ray tube target materials.

| Element | $K_{\alpha1}$ Line (Å) | $K_{\alpha2}$ Line (Å) |
|---|---|---|
| Cr | 2.294 | 2.290 |
| Co | 1.793 | 1.789 |
| Cu | 1.544 | 1.541 |
| Mo | 0.714 | 0.709 |
| Rh | 0.618 | 0.613 |

***Synchrotron X-ray Generation***

The alternative to low energy X-ray generation is to use synchrotrons which are usually linear electron accelerators combined with storage rings. Modern synchrotron sources are immensely complicated and sophisticated user facilities. Electrons are produced, accelerated up to nearly the speed of light in a linear accelerator, and then stored in a circular ring. Once the high-energy electron beam has been created, it is directed into auxiliary instruments such as bending magnets, wigglers and undulators, where the useful X-rays are produced. The brilliance of the X-rays generated by synchrotron techniques far surpasses that of those created by characteristic radiation, which are generally limited to laboratory uses. Synchrotron facilities are extremely versatile utilizing multiple beamlines with specialized applications and technologies. It is beyond the scope of this work to discuss them all, but a description of the generation and characteristics of the beams used in BESL experiments is important and therefore included in this section.

While it is qualitatively understood that accelerating charges radiate, the specifics of the charge distribution, the acceleration, and the appropriate velocity regime dictate the details of the radiation field, which is used for scattering studies. Deflection of ultra-relativistic particles is of interest here and we begin with the retarded electric field produced by a single charged particle of mass *m*, charge *e*, and traveling with velocity $\beta = \mathbf{v}/c$

$$\mathbf{E}(\mathbf{x},t) = e\left(\frac{\mathbf{n}-\beta}{\gamma^2(1-\beta\cdot\mathbf{n})^3R^2}\right)_{\mathrm{Re}\,t} + \frac{e}{c}\left(\frac{\mathbf{n}\times((\mathbf{n}-\beta)\times\dot{\beta})}{(1-\beta\cdot\mathbf{n})^3R}\right)_{\mathrm{Re}\,t} \qquad (1)$$

where $\gamma = \frac{1}{\sqrt{1-\beta^2}}$ and **n**R is the observation displacement from the sample in the field.

This is not a transparent equation, nor a particularly intuitive place to start, although this follows a standard derivation in any classical electrodynamics text [1, 4, 7]. The above

form is derived by considering the appropriate 4-vector potential in the presence of no external fields and deriving the field strength tensor. The details can be found elsewhere [1], but the above form is written explicitly to distinguish the inherently acceleration independent (first term) and acceleration dependent (second term) parts. This is useful as the first term falls off rapidly as $1/R^2$ and the second term more slowly as 1/R.

Non-relativistic motions reduce to the "Larmor Formula" for power dissipation of an accelerated particle, which is not for synchrotron sources, in part because this regime produces little power dissipation compared to ultra-relativistic motions where factors of $\gamma$ enter the power dissipation enhancing usable radiation flux. However, Larmor's formula for power dissipation,

$$P = \int \frac{dP}{d\Omega} d\Omega = \frac{2}{3}\frac{e^2}{c^3}\left|\dot{\mathbf{v}}\right|^2 \tag{2}$$

can be generalized by arguments about transformation under Lorentz Transformations since the power (dE/dt) is a Lorentz invariant [8]. It can be shown that the appropriate generalization begins with writing Larmor's formula as

$$P = \frac{2}{3}\frac{e^2}{m^2c^3}\left(\frac{d\mathbf{P}}{dt}\cdot\frac{d\mathbf{P}}{dt}\right) = -\frac{2}{3}\frac{e^2}{m^2c^3}\left(\frac{dP^\mu}{d\tau}\cdot\frac{dP_\mu}{d\tau}\right) \tag{3}$$

where $d\tau$ is the proper time and $P^\mu$ is the particle momentum 4-vector. Substituting the relativistic energy, $E = \gamma mc^2$, and momentum, $\mathbf{p} = \gamma m\mathbf{v}$, expressions into the expanded 4-vector scalar product,

$$-\frac{dP^\mu}{d\tau}\cdot\frac{dP_\mu}{d\tau} = \left(\frac{d\mathbf{p}}{d\tau}\right)^2 - \beta^2\left(\frac{d|\mathbf{p}|}{d\tau}\right)^2 \tag{4}$$

we come to a relativistic expression for the power radiated by an accelerated charged particle:

$$P = \frac{2}{3}\frac{e^2}{c}\gamma^6\left(\dot{\beta}\cdot\dot{\beta} - \left(\beta\times\dot{\beta}\right)^2\right). \tag{5}$$

This expression is often referred to as the Lienard result. Here, we can see that power is generated by acceleration both tangential and perpendicular to the path. If we break the acceleration of the particle into components in these coordinate directions,

$$\dot{\beta} = \dot{\beta}_{Perp} + \dot{\beta}_{Tan} \tag{6}$$

and substitute this in for the total power, we can see that the total power can be written as having two contributions $P_{Perp}$ and $P_{Tan}$.

$$\begin{aligned}
P &= \frac{2}{3}\frac{e^2}{c}\gamma^6\left(\dot{\beta}\cdot\dot{\beta} - \left(\beta\times\dot{\beta}\right)^2\right)\\
&= \frac{2}{3}\frac{e^2}{c}\gamma^6\left(\dot{\beta}_{Perp}^2 + \dot{\beta}_{Tan}^2 - \left(\beta\times\left(\dot{\beta}_{Perp} + \dot{\beta}_{Tan}\right)\right)^2\right)\\
&= \frac{2}{3}\frac{e^2}{c}\gamma^6\left(\dot{\beta}_{Perp}^2 + \dot{\beta}_{Tan}^2 - \left(\beta\times\dot{\beta}_{Perp} + \beta\times\dot{\beta}_{Tan}\right)^2\right)\\
&= \frac{2}{3}\frac{e^2}{c}\gamma^6\left(\dot{\beta}_{Perp}^2 + \dot{\beta}_{Tan}^2 - \left(\beta\times\dot{\beta}_{Perp} + 0\right)^2\right)\\
&= \frac{2}{3}\frac{e^2}{c}\gamma^6\left(\dot{\beta}_{Perp}^2\left(1-\beta^2\right) + \dot{\beta}_{Tan}^2\right) = \frac{2}{3}\frac{e^2}{c}\gamma^6\left(\dot{\beta}_{Perp}^2\frac{1}{\gamma^2} + \dot{\beta}_{Tan}^2\right)
\end{aligned} \tag{7}$$

So we can see that we get synchrotron radiation (power) from both parallel and transverse acceleration of the electron:

$$P_{\parallel} = \frac{2}{3}\frac{e^2}{c}\gamma^6\dot{\beta}_{\parallel}^2 \tag{8}$$

$$P_{\perp} = \frac{2}{3}\frac{e^2}{c}\gamma^4\dot{\beta}_{\perp}^2 \tag{9}$$

where $P_{||}$ is the parallel contribution and $P_{\perp}$ is the perpendicular contribution. Further, for highly relativistic velocities, the same acceleration leads to much less radiation if the acceleration is parallel to the motion compared to perpendicular acceleration. Parallel acceleration is related to the accelerating momentum change by

$$m\dot{\mathbf{v}}_{\|} = \frac{1}{\gamma^3}\frac{d\mathbf{p}_{\|}}{dt}. \tag{10}$$

However, when the accelerating force is perpendicular to the motion (for synchrotrons, this is a Lorentz force) [8]

$$m\dot{\mathbf{v}}_{\perp} = \frac{1}{\gamma}\frac{d\mathbf{p}_{\perp}}{dt}. \tag{11}$$

The additional factors of $\gamma$ in Equation 10 make the same acceleration far more effective when directed perpendictular to the motion. We replace $P_{Tan}$ with $P$ in Equation 7, and

$$P = \frac{2}{3}\frac{e^2}{c}\gamma^4\dot{\beta}^2. \tag{12}$$

For circular motion, with electrons traveling around a ring at and angular frequency, $\omega$, we can substitute

$$\left|\frac{d\mathbf{P}}{d\tau}\right| = \gamma\omega|\mathbf{P}| \tag{13}$$

into the power equation (Equation 8) and come up with the familiar equation relating the orbit radius, *r*, velocity and the power:

$$P = \frac{2}{3}\frac{e^2 c}{r^2}\gamma^4\beta^4. \tag{14}$$

Here we can see the importance of the relativistic regime of the electron velocities, as the power radiated is proportional to $\gamma^4$. As an example, a 7GeV synchrotron (like the APS) radiates more than 2000 times that of a 1GeV synchrotron. As the speed of the electrons

approaches the speed of light, the radiation profile approaches the so-called “headlight” distribution, where the radiation is directed tangentially in the circular orbit. The evolution of the profile is shown in Figure 0.1.

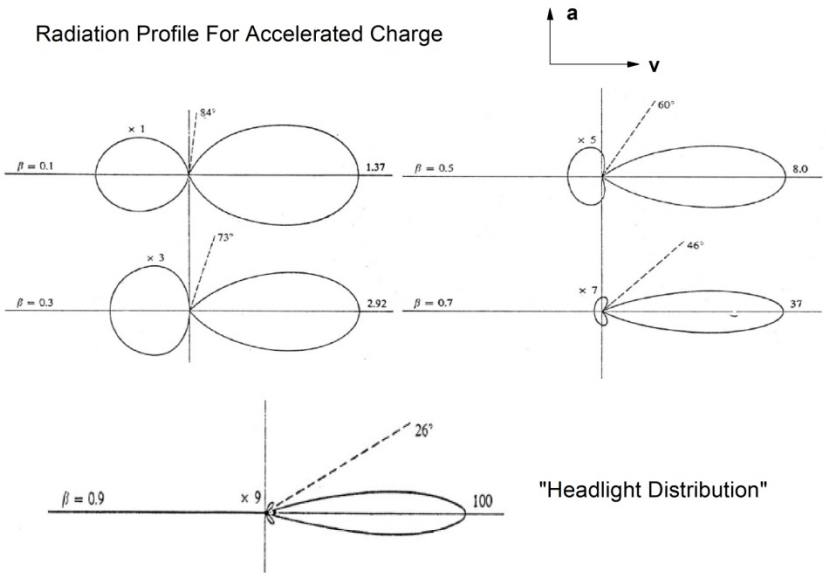


**Figure 0.1**- Radiation profile for an accelerated charge. As the speed approaches the speed of light, the radiation profile approaches the so-called “headlight” distribution (Figure from [10]).

A comprehensive discussion of synchrotron radiation and generation physics is vast and well beyond the scope this thesis. Excellent and comprehensive discussions can be found in Jackson [1], Wiedemann [9], and Duke [11].

Before developing a formalism for structural analysis of amorphous materials, we will discuss a few of the essential components of modern synchrotrons and focus on the Advanced Photon Source (APS) at Argonne National Laboratory (ANL) where BESL experiments, to date, have taken place. The process of X-ray generation begins with the production of electrons from a heated cathode (~1100°C) porous tungsten matrix

impregnated with barium calcium aluminate and coated with osmium. The electrons are accelerated by high-voltage alternating electric fields in a linear accelerator (LINAC). The use of selective phasing of the electric field accelerates the electrons to 450 MeV. At 450 MeV, the electrons are relativistic: they are traveling at > 0.99999c, making $\gamma = 881$. These electrons are injected tangentially into the booster synchrotron, a racetrack-shaped ring of electromagnets, and accelerated to 7 GeV. This happens in roughly 500mSec imparting roughly 13.1MeV of energy, per electron, every millisecond, increasing $\gamma$ from 881 to 14000 ($\gamma = E/m_e c^2 = 7$ GeV/.511MeV). The electrons are now traveling at > 0.99999999c. The accelerating force is supplied by electrical fields in four radio frequency (rf) cavities. The electrons orbital path is maintained by using a mixture of multipole bending and focusing magnets. The electrons are tangentially injected into the storage ring. The 1104m circumference storage ring (r = 176m), contains more than 1000 bending and focusing magnets keeping the electrons in circular orbit inside vacuum paths (including 80 dipole, 260 skew and conventional quadrapole and 280 sextupule magnets [10]).

The storage ring contains 40 straight sections, of which 35 can be used as experimental beamlines. The APS is a third generation synchrotron, employing two categories of radiation sources: Bending Magnets and "insertion devices." A detailed discussion of the radiation sources is provided in Appendix II.2. and includes a comprehensive picture of the photon spectra produced. An undulator is installed in Sector 6, and BESL experiments take place with X-rays generated using this technique. As a result a highly coherent, extremely non-divergent, and intense beam of X-rays can be produced over the spectrum. As discussed in Appendix II.2., since the peak magnetic

field is a tunable parameter, the spectrum can also be tuned (to a somewhat limited extent) to place a resonant peak in the photon energy for a specific application. The beam is highly linearly polarized in the plane of the ring and the beam divergence is generally considered quite small, making this ideal for high energy (~100keV, $\lambda \sim 0.1$Å$^{-1}$) X-ray studies of amorphous materials.


[1] J. D. Jackson, Classical Electrodynamics, John Wiley & Sons Inc., (1999).
[2] B. B. He, Two-dimensional x-ray diffraction, Wiley, Hoboken (2009).
[3] R. J. Gould, Electromagnetic Processes, Princeton University Press, Princeton (2006).
[4] D. J. Griffiths, Introduction to Electrodynamics, Upper Sadle River (1999).
[5] J. H. Fang, X-ray diffraction tables : determination of d, sin [theta], or Q for 0.01 intervals of 2 [theta] for the wavelenghts Kalpha, Kalpha1, Kalpha2, and Kbeta of copper, iron, molybdenum and chronium radiation, Southern Illinois University Press, Carbondale (1966).
[6] D. J. Dyson, X-ray and electron diffraction studies in materials science, Maney, London (2005).
[7] H. C. Ohanian, Classical Electrodynamics, Infinity Science Press, Hingham (2007).
[8] F. Rohrlich, Classical charged particles; foundations of thier theory, Addison-Wesley Pub. Co., Reading, Mass (1965).
[9] H. Wiedemann, Synchrotron Radiation, Springer, New York (2003).
[10] D. M. Mills, Synchrotron Radiation: Properties and Production, *National School for Neutron and X-ray scattering*, Oakridge, TN (2010).
[11] P. J. Duke, Synchrotron Radiation, Oxford University Press, Inc., New York (2000).


# Appendix II.2.

### Photon Spectra for radiation sources in synchrotrons

Bending magnets produce radiation that is highly aperture controlled and produces a smoothly varying brightness vs. energy (Figure 0.1). The polarization is elliptical with components in and out of the plane of the electron orbit. For comparison with the insertion devices, the flux is quoted at $10^{13}$ photons/sec/mRad/.1% bandwidth.

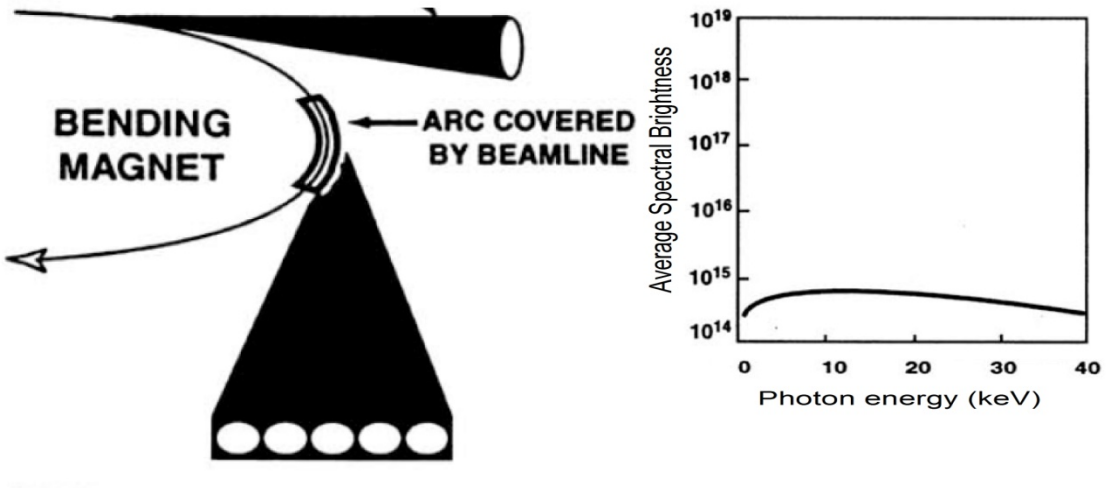


**Figure 0.1-** Radiation Profile for a bending magnet. The average spectral brightness (units photons/sec/mm$^2$/mRad$^2$) is a smooth function of energy[1].

Insertion devices are used to further increase the usable flux and tune the energy and beam profiles available for experimentation. Wigglers and undulators are periodic arrays of magnets that force the electrons to deflect and oscillate as the pass, shown schematically in Figure 0.2. Insertion devices are characterized by a deflection parameter, $\kappa$, given by

$$\kappa = \frac{ecB_{Peak}\lambda_{ID}}{2\pi m_e c^2} \cong .093\lambda_{ID}(cm) * B_{Peak}(kGauss)$$

Where $\lambda_{ID}$ is the period of the magnetic array in the insertion device and $B_{Peak}$ is the peak magnetic field in the array. By simple geometry, the maximum deflection angle of the electron beam is then

$$\theta_{\max} = \pm\kappa/\gamma$$

and the amplitude of the oscillations of the electrons is

$$x_{\max} = \pm \frac{\kappa}{\gamma} \frac{\lambda_{ID}}{2\pi}.$$

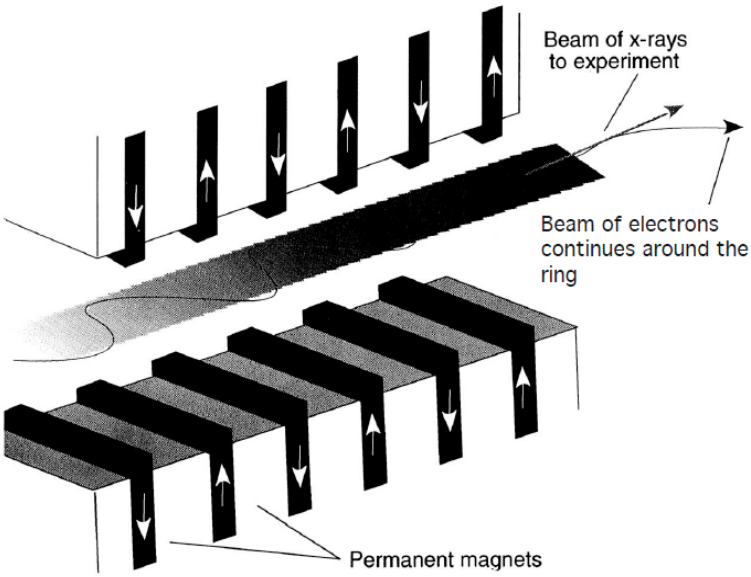


**Figure 0.2-** Insertion Device. An array of alternating magnets case oscillations in the electrons as they pass through [2].

Wigglers and undulators work in different regimes in the deflection parameter. In both cases, alternating N and S poles act to bend the electron path back toward the nominal flight direction (in the ideal case with the front and back poles cancelling to return the electrons to the ring). Wigglers act primarily to harden the X-ray spectrum produced, and produce an angular deflection that is much greater than the "natural opening angle", i.e. $1/\gamma$, and thus $\kappa >> 1$. If there N sets of dipoles, the output looks like 2N dipole sources. The number of sets of poles is somewhat limited practically, but somewhere between 6 and 10 sets is often referred to as standard [3, 4]. The spectral brightness is shown in Figure 0.3 and the flux is quoted at $10^{14}$ to $10^{15}$ photons/sec/mRad/.1% bandwidth. As

mentioned, the physical process of undulator radiation is the same as for wigglers. However, undulators work in the regime where the deflection parameter is $\kappa \sim 1$, where the maximum deflection angle is approximately equal to the opening angle. In this case the radiation from each pole overlaps, causing interference effects in the photon spectral distribution and deviates from the 2N dipole sources observed in wiggler radiation.

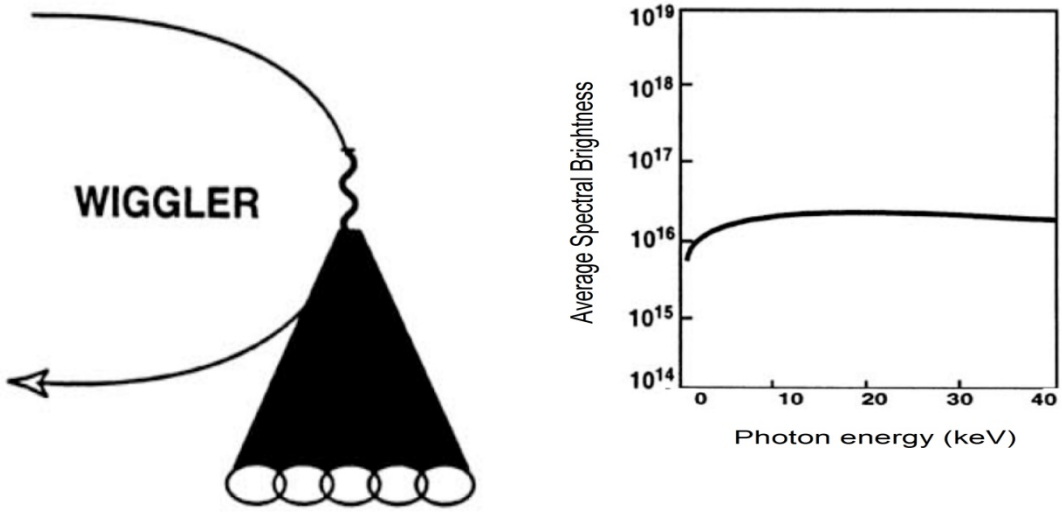


**Figure 0.3-** Radiation Profile for a wiggler insertion device. The average spectral brightness (units photons/sec/mm$^2$/mRad$^2$) is a smooth function of energy [1].

Undulator radiation is coherent superposition of radiation from each pole of the undulator, and this causes the spectral distribution to morph from a smooth distribution for a Wiggler (Figure 0.3) into a set of discrete spectral lines (Figure 0.4). The derivation of the spectral and spatial distribution is described in Wiedmann[4]. When electrons travel through an undulator, they travel in a sinusoidal path, however the transverse motion is non-relativistic, and the behavior is very similar to that of a single electron undergoing simple harmonic motion. In a frame where the electron has no longitudinal motion, the electron essentially sees a series of equally spaced oscillators exciting the

electron into standing waves, for an approximately infinite undulator, but with a period that is Lorentz contracted. Additionally, since the electron is traveling toward the experiment, the radiation is blue shifted to shorter wavelengths. The various harmonics contribute to produce the spectrum shown in Figure 0.4. As a result a highly coherent, extremely non-divergent, and intense beam of X-rays can be produced over the spectrum. An undulator is installed in Sector 6, and Beamline experiments take place with X-rays generated using this technique. Since the peak magnetic field is a tunable parameter, the spectrum can also be tuned (to a somewhat limited extent) to place a resonant peak in the photon energy for a specific application. The beam is highly linearly polarized in the plane of the ring and the beam divergence is generally considered quite small, making this ideal for high energy (~100keV, $\lambda \sim .1$ Å$^{-1}$) X-ray studies of amorphous materials.

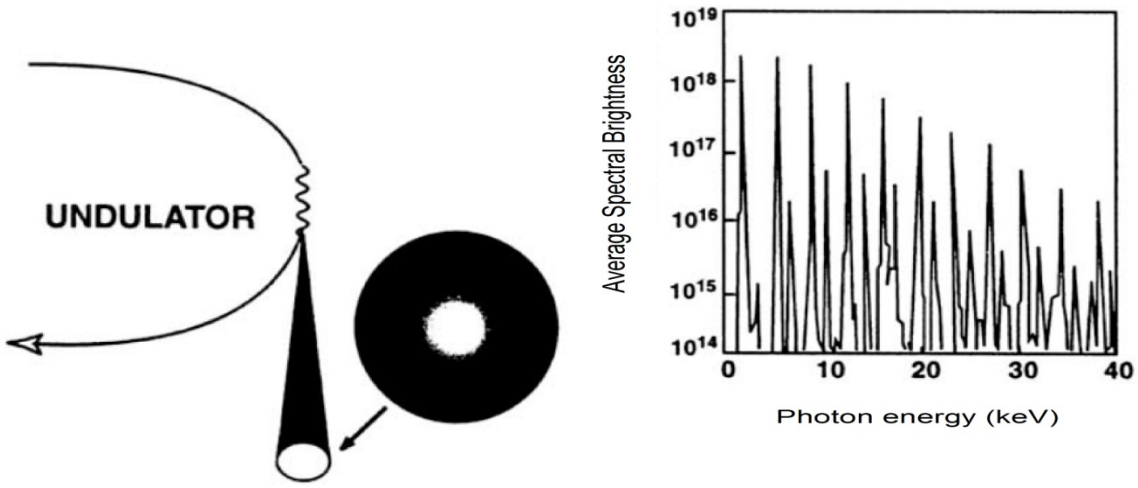


**Figure 0.4-** Radiation Profile for an undulator insertion device. The average spectral brightness (units photons/sec/mm$^2$/mRad$^2$) is a smooth function of energy [1].

[1] D. M. Mills, Synchrotron Radiation: Properties and Production, *National School for Neutron and X-ray scattering*, Oakridge, TN (2010).

[2] A. P. Source.
[3] P. J. Duke, Synchrotron Radiation, Oxford University Press, Inc., New York (2000).
[4] H. Wiedemann, Synchrotron Radiation, Springer, New York (2003).

# Appendix II.3.

**Quantum mechanical treatment of the solution to the dynamical scattering problem**

The formalism of derives from a plane wave on the sample of interest (Figure 0.1), spherical waves re-radiated at the same energy (appropriate for elastic scattering only) and we consider the detector to be in the far field.

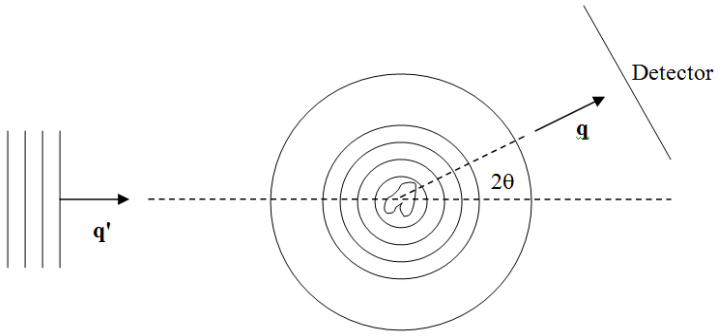


**Figure 0.1--** Scattering of incident plane wave from electron distribution in sample. In the far field limit, the outgoing scattered wave is approximated by a plane wave, thus validating the ballistic picture of scattering.

If scattering process can be described as a perturbation of the original Hamiltonian, get asymptotic plane wave solutions. The steady state solutions are the well-defined[1-4] momentum space Eigenstates, totally delocalized in position space, and in the asymptotic

limit ($r \to \infty$) is the superposition of the incoming plane wave and the radiating spherical wave, given by Equation 1,

$$\left\langle \mathbf{r} \middle| \psi_{\mathbf{q}} \right\rangle = \psi_{\mathbf{q}}(\mathbf{r}) \propto \left( e^{i\mathbf{q}'\cdot\mathbf{r}} + f_{\mathbf{q}}(\theta,\varphi)\frac{e^{iqr}}{r} \right). \tag{1}$$

The scattered waves are assumed to have an angular dependence to them, manifesting in $f_{\mathbf{q}}(\theta,\varphi)$, also known as the scattering amplitude, which it turns out (details omitted) to be related to the differential scattering cross section-a fundamental property associated with the scattering process,

$$\frac{d\sigma}{d\Omega} = \left| f_{\mathbf{q}}(\theta,\varphi) \right|^2. \tag{2}$$

Issues of normalization have been conveniently ignored in this brief treatment, but extensive literature exists on the topic. Abers[4], provides a discussion about wave packet solutions to the time-dependent Schrödinger Equation that gives physical intuition into the solution to this issue.

A Green's function approach to the solution to the scattering problem is most enlightening. If a solution, $G(\mathbf{r},\mathbf{r}')$ can be found that satisfies

$$\left(\nabla^2 + \mathbf{q}^2\right) G(\mathbf{r},\mathbf{r}') = -4\pi\delta(\mathbf{r}) \tag{3}$$

then the function

$$-\frac{1}{4\pi}\int G(\vec{r},\vec{r}')U(\vec{r}')\psi(\vec{r}')d\vec{r}' \tag{4}$$

provides a formal solution to the original Schrödinger Equation. A variety of linearly independent solutions can be found by Fourier Transforming Equation 3 [3] giving, the incoming wave, outgoing wave and standing wave solutions. The outgoing wave condition requires that as $r \to \infty$, the probability goes to zero, thus two distinct Eiginsolutions emerge (Equation 5).

$$G(\vec{r},\vec{r}') = \frac{\exp\left(\pm iq|\vec{r}-\vec{r}'|\right)}{|\vec{r}-\vec{r}'|} \tag{5}$$

Ignoring the negative term (which corresponds to an incoming wave), the solutions satisfy the integral equation,

$$\psi_{\mathbf{q}}(\mathbf{r}) = Ne^{i\mathbf{q}\cdot\mathbf{r}} - \frac{1}{4\pi}\int \frac{e^{\left(iq|\mathbf{r}-\mathbf{r}'|\right)}}{|\mathbf{r}-\mathbf{r}'|}U(\mathbf{r}')\psi_{\mathbf{q}}(\mathbf{r}')d\mathbf{r}' \tag{6}$$

The cross section can be interpreted as the behavior of the wave function solution for r large enough so that it is well outside the range of the potential, so that only $r' \le r$ contributes in the integral. Expanding for small $r'/r$, and keeping second order terms, Equation 6 becomes

$$\psi_{\mathbf{q}}(\vec{r}) \to Ne^{i\mathbf{q}\cdot\vec{r}} - \frac{1}{4\pi}\int \frac{e^{iqr}}{r}e^{-iq\mathbf{r}\bullet\mathbf{r}'}U(\vec{r}')\psi_{\mathbf{q}}(\vec{r}')d\vec{r}' \tag{7}$$

in the limit of large r. The scattering amplitude can be read of as

$$f_{\mathbf{q}}(\theta,\phi) = -\frac{1}{4\pi N}\int e^{-i\mathbf{q}\cdot\mathbf{r}'}U(\mathbf{r}')\psi_{\mathbf{q}}(\mathbf{r}')d\mathbf{r}' \tag{8}$$

where this expression is most commonly reduced to the first term in Born Approximation, replacing wave function in the integrand with $e^{i\mathbf{q}\cdot\mathbf{r}}$. In the Born approximation, a single term represents the transition from one momentum state to another. Higher order terms, probabilities of intermediate scattering events before final state, considered small. These "virtual multiple scattering" events are extremely unlikely, particularly in real experiments where the energy of the incident radiation is large, and interaction cross-sections are small. Transitions from in the incoming momentum state to the outgoing state are given by the matrix element $\langle \mathbf{Q}' | u(\mathbf{r}) | \mathbf{Q} \rangle$ which is the Fourier transform of the real space scattering potential, given by

$$\langle \mathbf{Q}' | u(\mathbf{r}) | \mathbf{Q} \rangle = \frac{1}{V}\int d\mathbf{V}\Psi^{*}_{\mathbf{Q}'}(\mathbf{r})u(\mathbf{r})\Psi_{\mathbf{Q}}(\mathbf{r}). \tag{9}$$

In the far field limit, ignoring multiple scattering into the final state, the scattering amplitude is related to the Fourier Transform of the electron density, which describes the spatial extent of the interaction potential $u(\mathbf{r})$. In this case, the transition element $\langle \mathbf{Q}' | u(\mathbf{r}) | \mathbf{Q} \rangle$ is the scattering of the incident plane wave $|\mathbf{Q}'\rangle$, $\langle \mathbf{r} | \mathbf{Q}' \rangle = \Psi_{\mathbf{Q}'}(\mathbf{r})$, to an outgoing plane wave $|\mathbf{Q}\rangle$, $\langle \mathbf{r} | \mathbf{Q} \rangle = \Psi_{\mathbf{Q}}(\mathbf{r})$.

In a scattering experiment, unfortunately, we can't measure amplitude directly, which includes phase information about the difference between the incoming wave to the scattered state. If it could, the scattering potential could be reconstructed. For multiple atomic scattering sites, the potential is written as a superposition of local potentials centered on points, $\mathbf{R}_i$, but the validity of the formalism just laid out allows us to cast this problem in a simpler, classical, formalism.


[1] N. W. Ashcroft and N. D. Mermin, Solid State Physics, Rinehard and Winston, New York (1976).
[2] J. D. Jackson, Classical Electrodynamics, John Wiley & Sons Inc., (1999).
[3] E. Merzbacher, Quantum Mechanics, Wiley, New York (1998).
[4] E. S. Abers, Quantum Mechanics, Pearson/Prentice-Hall, Upper Saddle River (2004).


# Appendix II.4.

## Mathematics of the orientational average in scattering problems

For isotropic form factors, orientational average:

$$I(q) = Nf(q)^2 + f(q)^2 \left\langle \sum_i \sum_{j \neq i} \exp\left(-i\mathbf{q} \cdot (\mathbf{r}_j - \mathbf{r}_i)\right) \right\rangle \tag{1}$$

Let

$$\mathbf{r}_{ij} \equiv \mathbf{r}_i - \mathbf{r}_j \tag{2}$$

then

$$\left\langle e^{i\mathbf{q}\bullet\mathbf{r}_{ij}} \right\rangle = \frac{\int e^{iqr_{ij}\cos\theta} \sin\theta d\theta d\phi}{\int \sin\theta d\theta d\phi} = \frac{\int e^{iqr_{ij}\cos\theta} \sin\theta d\theta d\phi}{4\pi} \tag{3}$$

by the definition of the average. Explicitly carrying out the $\phi$ integration gives

$$\int e^{iqr_{ij}\cos\theta} \sin\theta d\theta d\phi = 2\pi \int_0^\pi e^{iqr_{ij}\cos\theta} \sin\theta d\theta . \tag{4}$$

A change of variables gives

$$2\pi\int_0^{\pi} e^{iqr_{ij}\cos\theta}\sin\theta d\theta = 2\pi\frac{1}{iqr_{ij}}\int_{-iqr_{ij}}^{iqr_{ij}} e^{x}dx = 4\pi\frac{\sin qr_{ij}}{qr_{ij}}. \quad (5)$$

Giving

$$\left\langle e^{i\mathbf{q}\bullet\mathbf{r}_{ij}}\right\rangle = \frac{\sin qr_{ij}}{qr_{ij}} \quad (6)$$

and finally

$$I(q) = Nf^2(q) + \sum_i\sum_{j\neq i} f^2(q)\frac{\sin(qr_{ij})}{qr_{ij}}. \quad (7)$$

# Appendix II.5.

## Batch Processing Script for BESL2010

This script takes the raw GE detector image file, averages the indicated files together, subtracts the indicated empty chamber, and outputs processed image files.
*Original Author M. Blodgett

```
#!/usr/bin/perl
use strict;
use warnings;
use File::Spec::Functions;
use Cwd;

#input options
my $dataPath ='C:\Users\user\Desktop\BESL2010\STL11062_temp_NAM';
my $xrayFile ='STL11062_Increment_4_Step_750_up_to_800_08192010_0404';
my $xrayStartFrame = 238; #0-indexed
my $xrayEndFrame = 259; #warning: summing too many frames can cause bad stuff to
happen,

#as unsigned short only holds up to ~57k counts for a single pixel
my $EmptyChamberFile =
$dataPath.'\\STL11057_EmptyChamber_1Hz_08182010_1702';
my $EmptyChamberStartFrame = 10;
my $EmptyChamberEndFrame = 29;
my $EmptyChamberScalar= .998;#default 1, usually need a little less
my $GainMapFile = 'C:\Users\user\Desktop\BESL2010\EF44064-
```

```
6N_GainCal_Record_High_GainMap.img';

my $rows = 1024;
my $Header = 8192;

my $executable = 'C:\Users\user\Desktop\FramePreprocessor\FramePreprocessor';

#output options
my $out_path = $dataPath.'\\Analysis_NAM_08192010';
#the output path doesn't have to exist, perl will create it if necessary.
my $outputFilename = $xrayFile.'_'.$xrayStartFrame.'_'.$xrayEndFrame;

#output flags (1 ON/0 OFF)
my $copy = 0; #output all frames in a single file, sans header, without empty chamber
subtraction
my $split = 0; #output frames in individual files, with empty chamber subtraction
my $sum = 1; #sum frames into a single frame file, with empty chamber subtraction

# Below here DO NOT change.  Here there be dragons.
$outputFilename=~s/Increment/Inc/;
$outputFilename=~s/StepCool/Step/;
$outputFilename=~s/_down_/_/;
$outputFilename=~s/_up_/_/;
mkdir($out_path,0777);
chdir($out_path);



my @options = (
        "-d $EmptyChamberStartFrame",
        "-e $EmptyChamberEndFrame",
        "-x $xrayStartFrame",
        "-z $xrayEndFrame",
        "-r $rows",
        "-i $dataPath\\$xrayFile",
        "-o $out_path\\$outputFilename",
        "-h $Header",
        "-p $EmptyChamberFile",
        "-k $EmptyChamberScalar",
        "-a $split",
        "-g $GainMapFile",
        "-v $sum",
        "-u $copy"
        );
```

```
foreach (@options) {
        $executable .= " ".$_;
}
system($executable);
```

# Appendix II.6.

## FIT2d Macro used in BESL2010 *.chi* file generation

```
%!*\ BEGINNING OF GUI MACRO FILE
%!*\
%!*\ This is a comment line
%!*\
EXIT
POWDER DIFFRACTION (2-D)
%!*\INPUT
%!*\#IN
X-PIXELS
1024
Y-PIXELS
1024
DATA TYPE
INTEGER (2-BYTE)
SIGNED
NO
BYTE SWAP
NO
STARTING BYTE
1
O.K.
DARK CURRENT
NO
DC FILE
\\
FLAT-FIELD
NO
FF SCALE
NO
SPATIAL DIS.
NO
O.K.
INTEGRATE
X-PIXEL SIZE
400
Y-PIXEL SIZE
400
```

```
DISTANCE
912.144
WAVELENGTH
.095604
X-BEAM CENTRE
497.223
Y-BEAM CENTRE
516.686
TILT ROTATION
107.026
ANGLE OF TILT
-0.283
O.K.
SCAN TYPE
Q-SPACE
CONSERVE INT.
NO
POLARISATION
YES
FACTOR
0.990000
GEOMETRY COR.
YES
MAX. ANGLE
19.98
MAX. D-SPACING
16
O.K.
EXIT
MACROS / LOG FILE
%!*\ END OF IO MACRO FILE
```

# Appendix II.7.

**Fortran program for manual Fourier Transform of PDFGetX2 S(q) data into g(r)**

```
program ft
        implicit none

c       THIS IS COPIED FROM S2g.f ... SO READ S AS g AND q AS r AND VICE
VERSA
        integer i, j, n, nmax
        real dr, gg, pi, q0, qmax, r, rho, rmax
         parameter (dr=0.1, nmax=1000000, rmax=20)
        !parameter (nmax=1000000, rmax=20)
        real q(nmax), S(nmax)
```

```
      character*32 sq_input_file, file_prefix
      character*32 indexfile

      print*, "Fourier Transform Sq to gr"
      print*, "Enter number density, 1/A^3"
      read(*,*) rho

      pi=4*atan(1.0000000000)

      print*, "g(r) input file"
      read*, sq_input_file

      print*, "file_prefix, for the output"
      read*, file_prefix
      indexfile = Trim(file_prefix) // '_gr.dat'
      open(unit=2,file=sq_input_file)

    open(unit=3,file=indexfile,status='unknown',
   :    access='sequential',form='formatted')

      write(3,*) rho

    qmax=0
      j=1
      do i=1,nmax
            read(2,*,end=1000) q(i), S(i)
            if (q(i).gt.qmax) qmax=q(i)
            j=j+1
            print*, q(i),S(i)
    enddo
      !dr=2*pi/5/qmax
1000  n=j
      q0=.8*qmax
      close(2)
      print*, dr
      pause
      do i=1,int(rmax/dr)
            r=(i-0.5)*dr
            gg=1
            do j=1,n-1
              if (q(j).gt.q0) S(j)=(S(j)-1)*exp(-(q(j)-q0)/(qmax/100))+1
              gg=gg+(S(j)-1)*q(j)*sin(q(j)*r)*(q(j+1)-q(j))/(2*pi*pi*rho*r)
            enddo
            write(3,*) r,gg
      enddo
      close(3)
```

```
stop
end
```

# Appendix II.8.

## RMCA Initial Configuration File Header

```
(Version 3 format configuration file)
 Random configuration

        0        0        0 moves generated, tried, accepted
        0                  configurations saved

      10000 molecules (of all types)
         3 types of molecule
         1 is the largest number of atoms in a molecule
         0 Euler angles are provided

         F (Box is not truncated octahedral)
          Defining vectors are:
           26.187880    .000000    .000000
            .000000  26.187880    .000000
            .000000    .000000  26.187880

       6000 molecules of type  1
         1 atomic sites
             .000000    .000000    .000000

       3000 molecules of type  2
         1 atomic sites
             .000000    .000000    .000000

       1000 molecules of type  3
         1 atomic sites
             .000000    .000000    .000000

    .5101606   .2685245  -.9082399
   -.7878443   .7005966   .9266755
    .6350555  -.6219625   .6758774
   -.5281851   .7938683   .5443215
    .4112552  -.0346968   .8501749
    .8899056   .6428528   .4266149
    .1171384   .7444671   .2586594
   -.7109683   .7550524   .1651497
   -.3291413   .1230655   .3613908
.
.
.
```

*RMC++ Initial Configuration File.*

(Version 3 format configuration file) !file created by SimpleCfg::save !
BESL 2009 STL1015 Pt20Zr80 1588 K

```
      0       0       0 moves generated, tried, accepted
      0           configurations saved

    5000 molecules of all types
      2 types of molecules
      1 is the largest number of atoms in a molecule
      0 Euler angles are provided

      F (box is cubic)
       Defining vectors are:
        24.127186   0.000000   0.000000
         0.000000  24.127186   0.000000
         0.000000   0.000000  24.127186

    4000 molecules of type  1
      1 atomic sites
         0.000000   0.000000   0.000000

    1000 molecules of type  2
      1 atomic sites
         0.000000   0.000000   0.000000

  0.0582578   0.8412347   0.6365174
 -0.7791531  -0.2157116   0.9421052
.
.
.
```

# Appendix II.9.

**Sampling of distortions of the icosahedral Voronoi polytetrahedron**

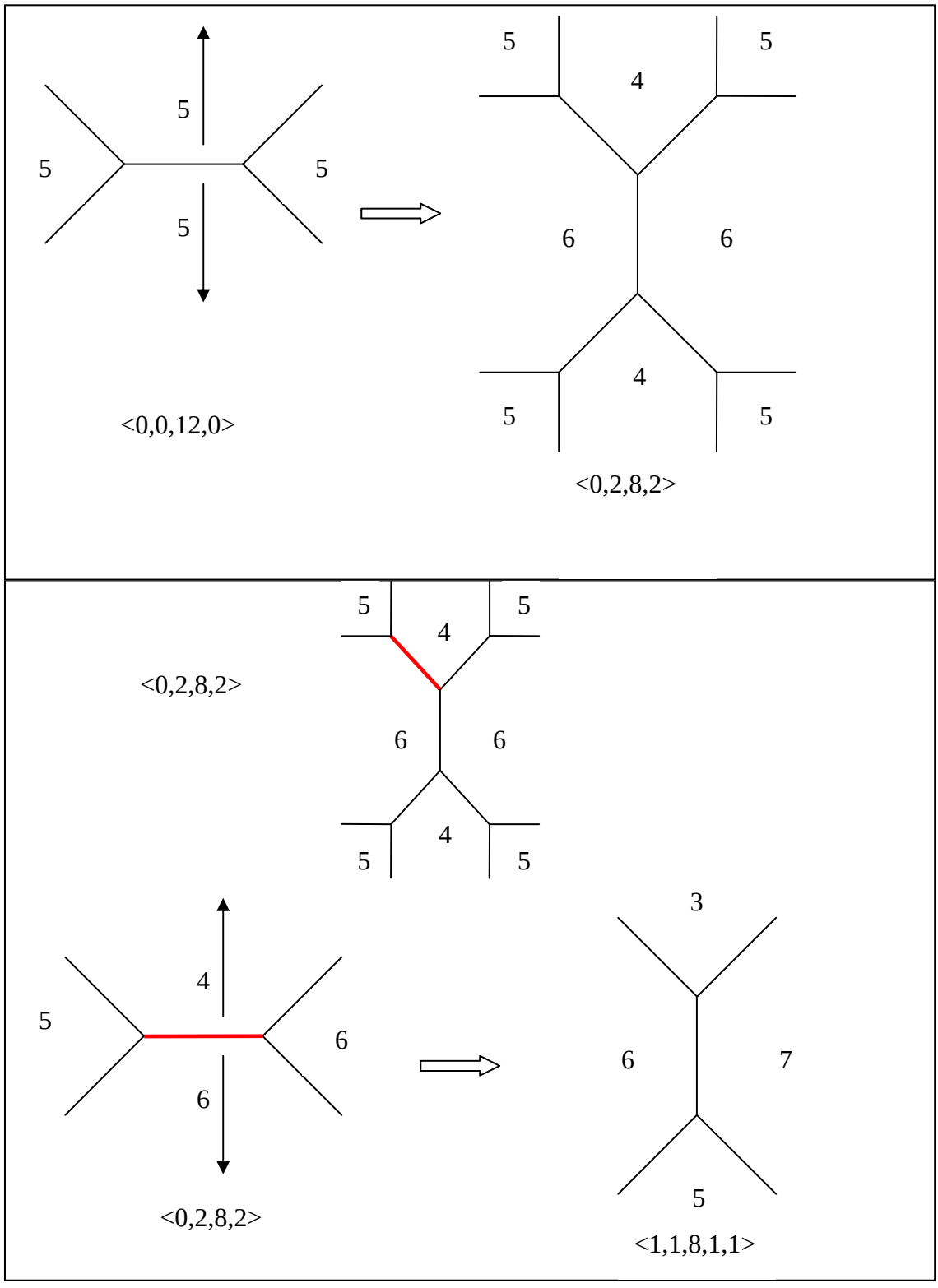

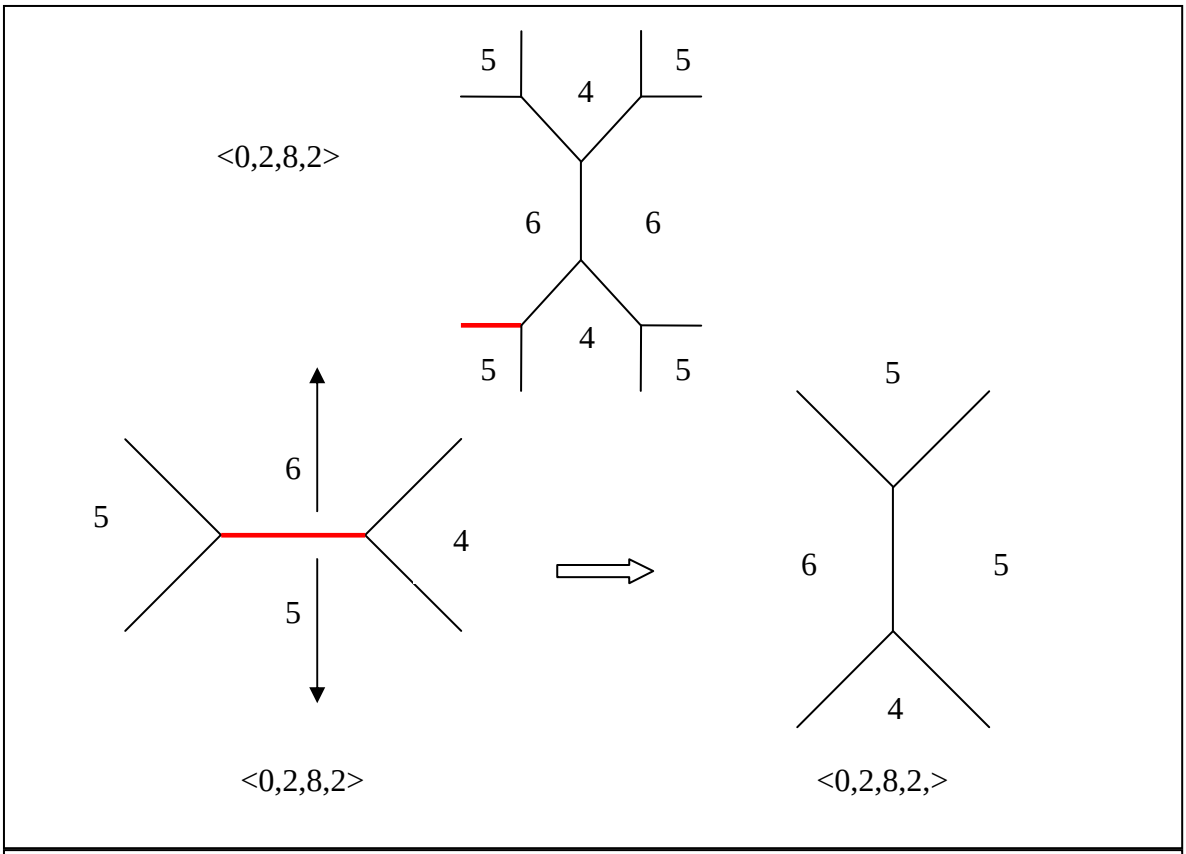
5
5
4
<0,2,8,2>
6
6
4
5
5
6
5
4
5
6
5
<0,2,8,2>
6
5
4
<0,2,8,2,>

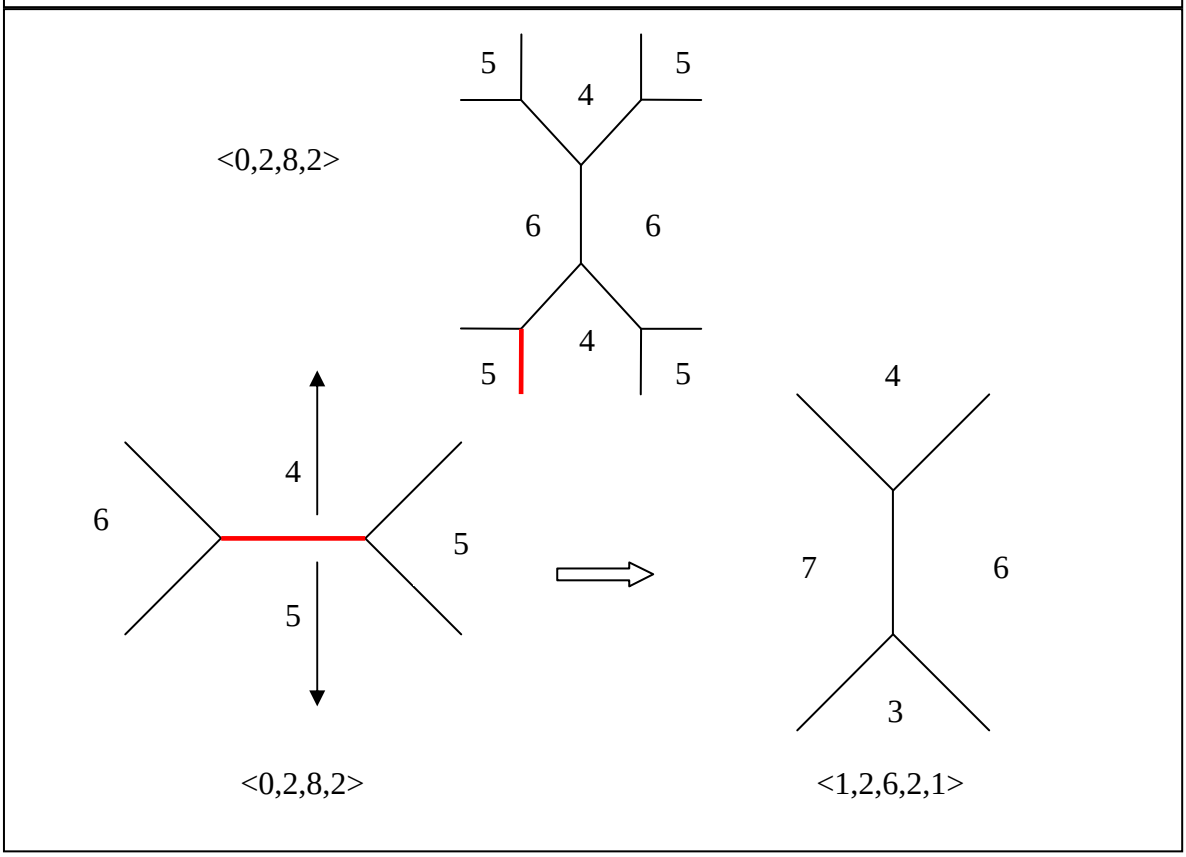
5
5
4
<0,2,8,2>
6
6
4
5
5
4
6
5
5
4
7
6
3
<0,2,8,2>
<1,2,6,2,1>

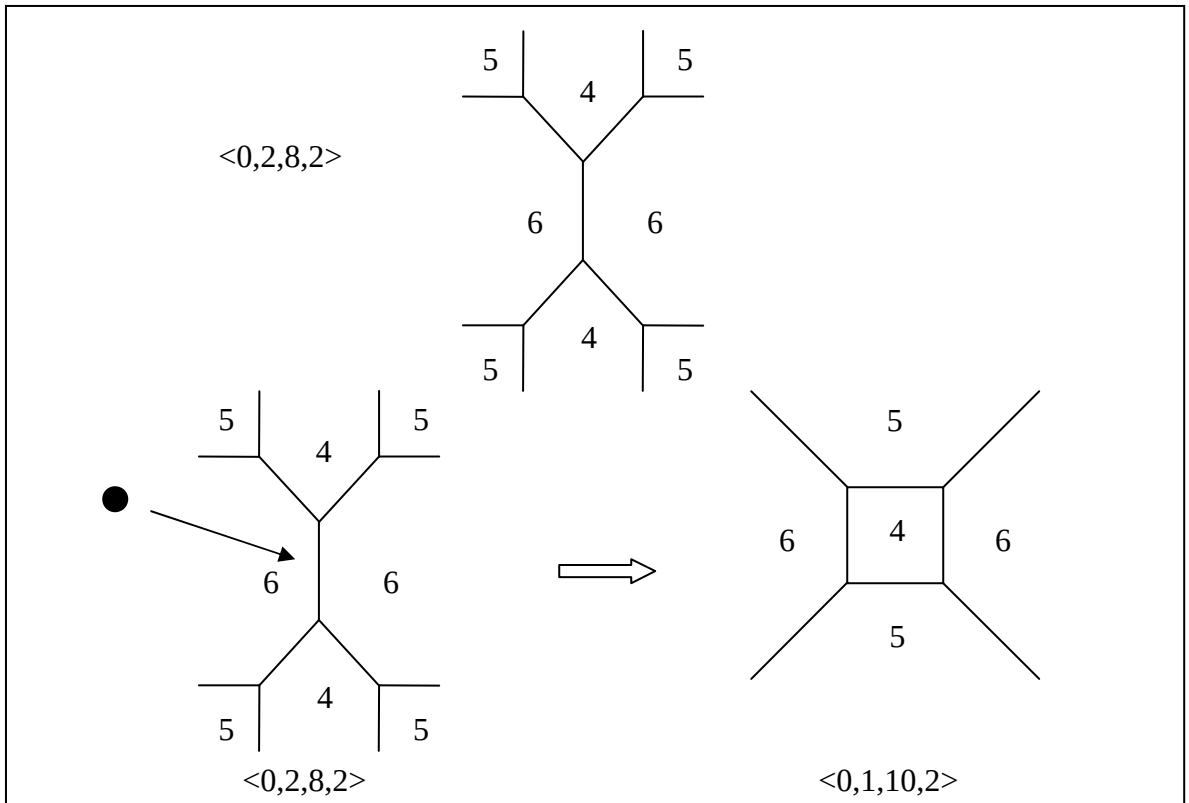
<0,2,8,2>
5
5
4
6
6
4
5
5
5
5
4
6
6
4
5
5
<0,2,8,2>
5
6
4
6
5
<0,1,10,2>

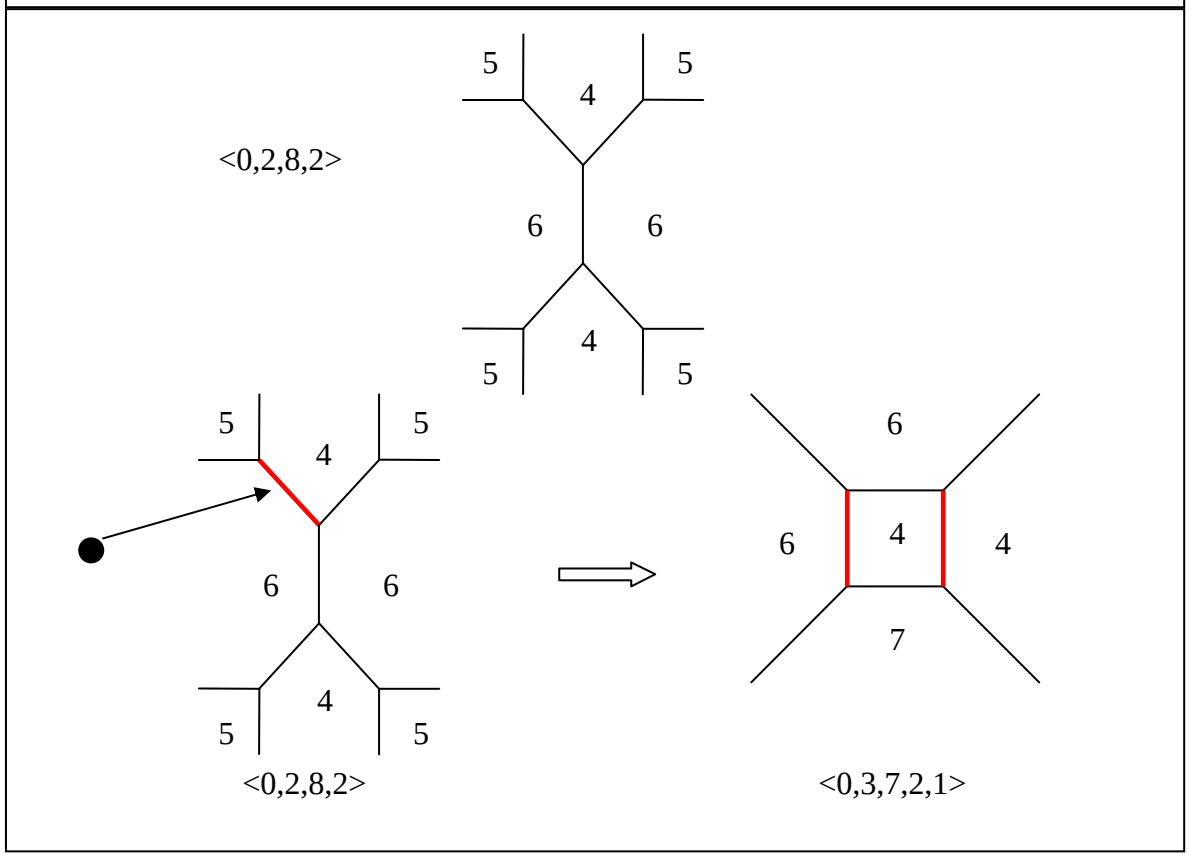
<0,2,8,2>
5
5
4
6
6
4
5
5
5
5
4
6
6
4
5
5
<0,2,8,2>
6
6
4
4
7
<0,3,7,2,1>

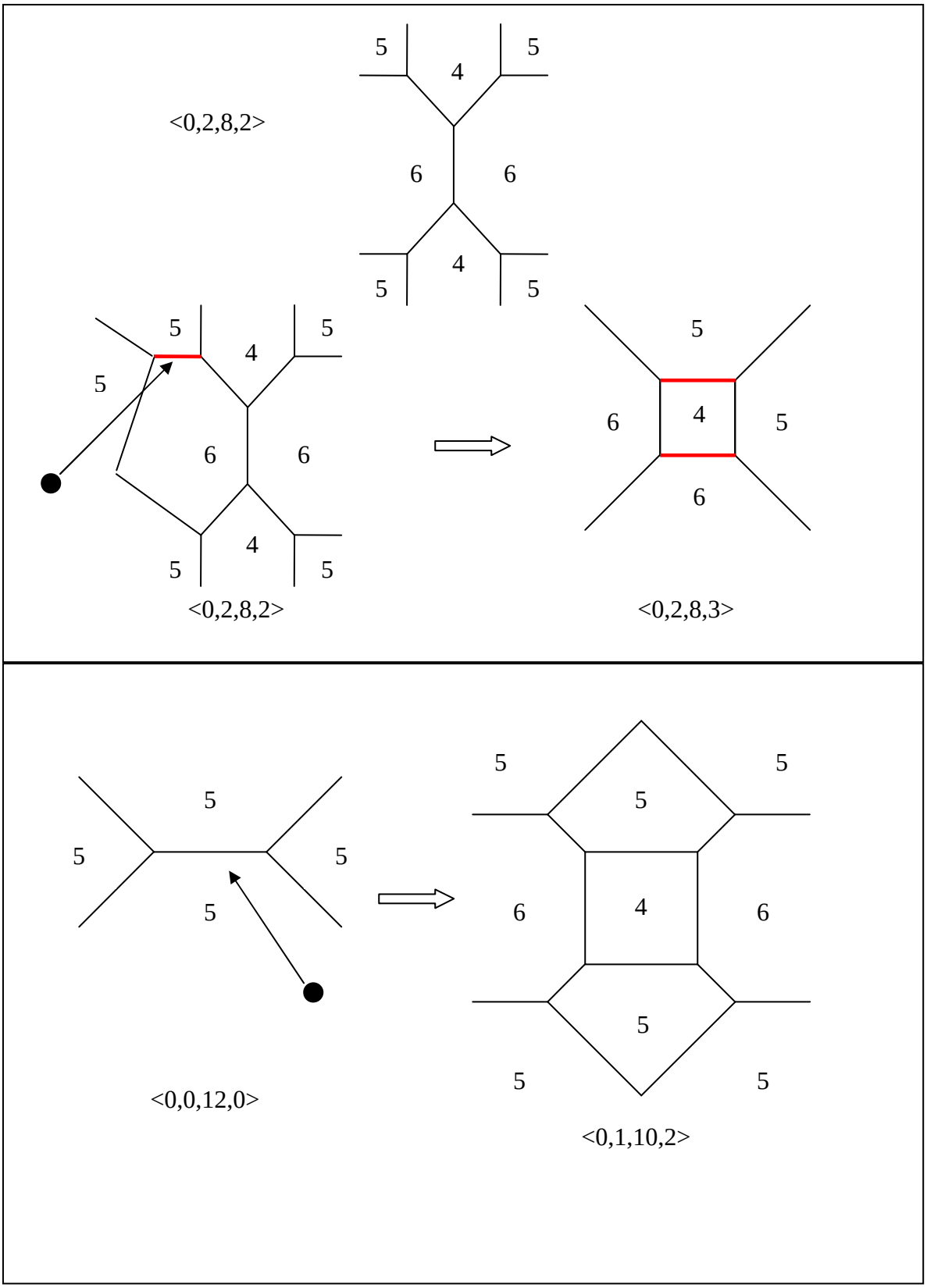
<0,2,8,2>
<0,2,8,2>
<0,2,8,3>
<0,0,12,0>
<0,1,10,2>

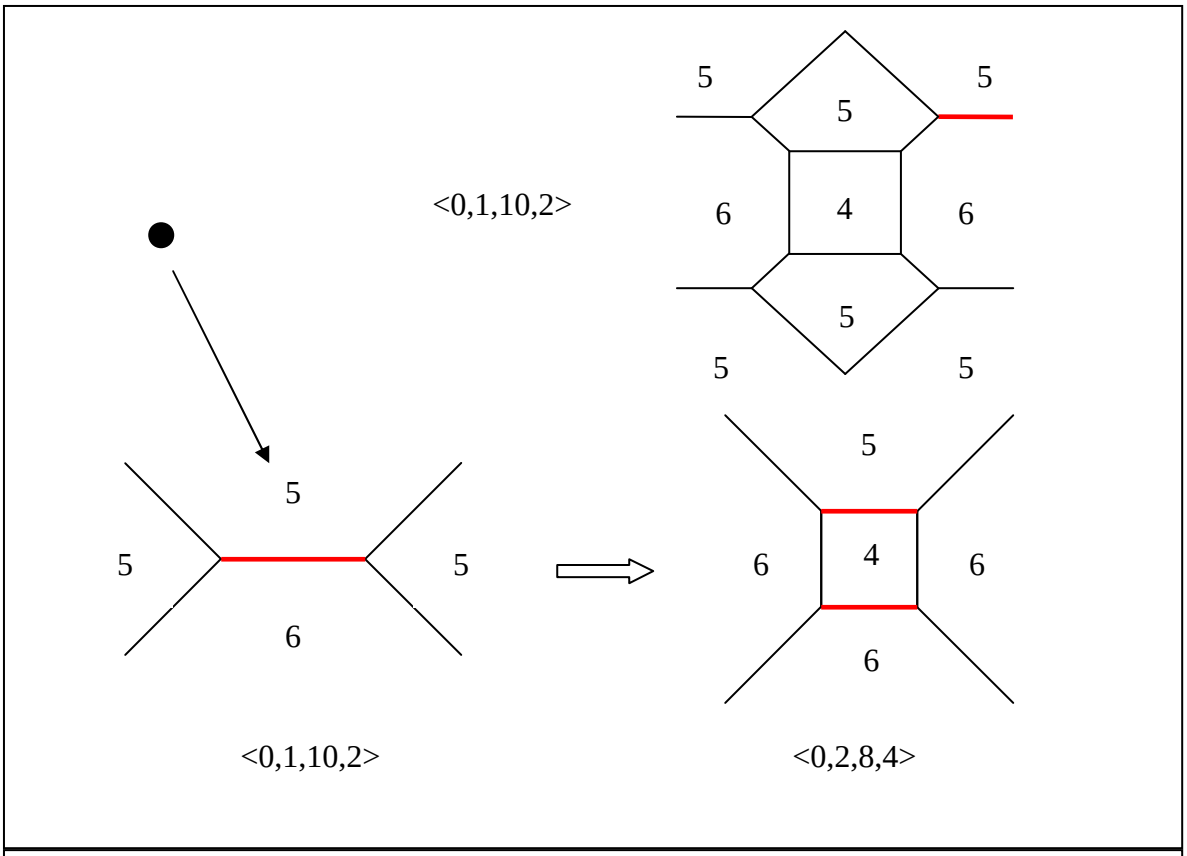
5
5
5
6
5
5
<0,1,10,2>
5
5
6
4
6
5
5
5
<0,1,10,2>
5
5
6
4
6
6
<0,2,8,4>

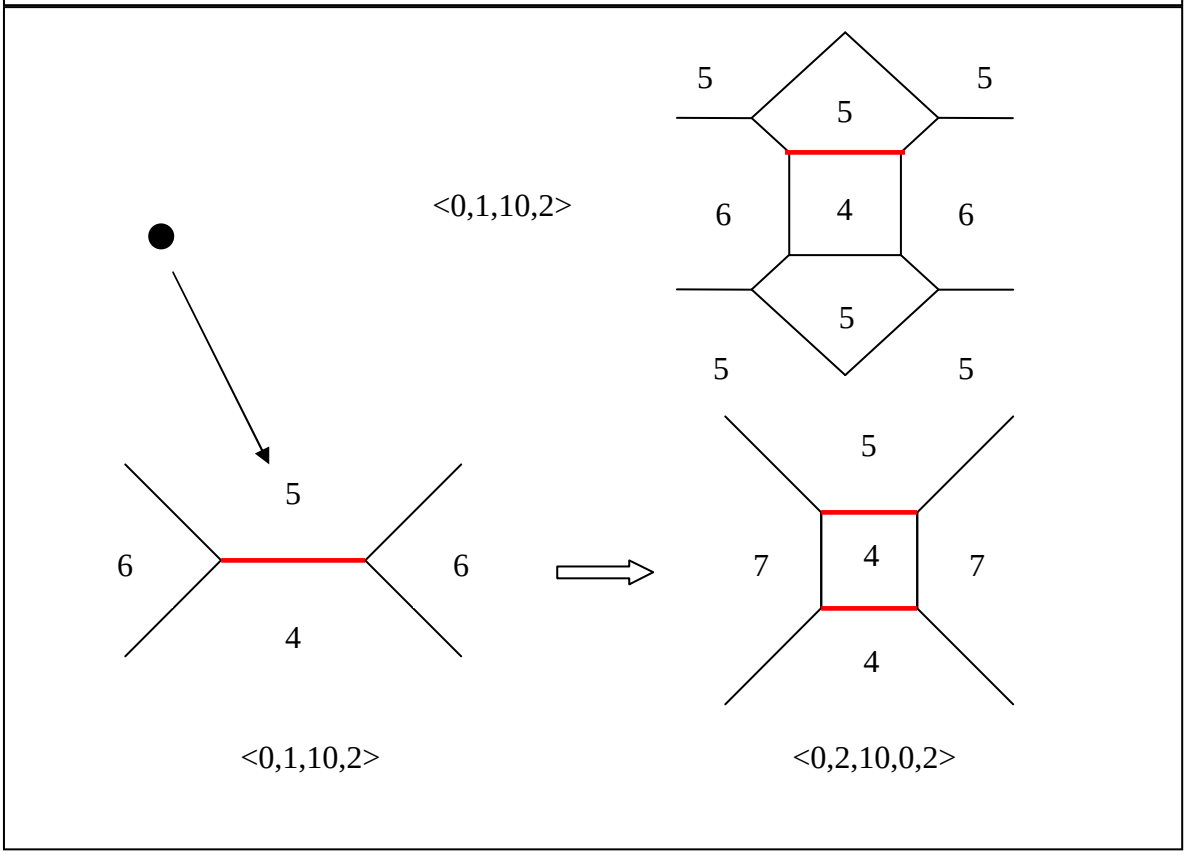
5
6
4
6
<0,1,10,2>
5
5
5
6
4
6
5
5
<0,1,10,2>
5
5
7
4
7
4
<0,2,10,0,2>

# Appendix IV.1.

## Specifications for the BESL Chamber

| ITEM NO. | PART NUMBER | DESCRIPTION | QTY. |
|---|---|---|---|
| 1 | 36-00018 | ROLL-UP, 11.75"OD x 7GA (.188) | 1 |
| 2 | 800-600NT | FLANGE, CF,8" X 6",NON-ROT, TAPPED | 1 |
| 3 | 275-150N | FLANGE,CF 2.75" X 1.5" NON ROT | 28 |
| 4 | 1400-000N(MOD) | FLANGE,CF 14" NON ROT BLANK | 2 |
| 5 | 133-075N | FLANGE,CF 1.33" X 0.75 NON ROT | 2 |
| 6 | R-SST-150 | 1.5"OD X .065"w | AR |
| 7 | R-SST-075 | 3/4"OD X .035"W | AR |
| 8 | R-SST-600 | 6"OD X .083"W | AR |

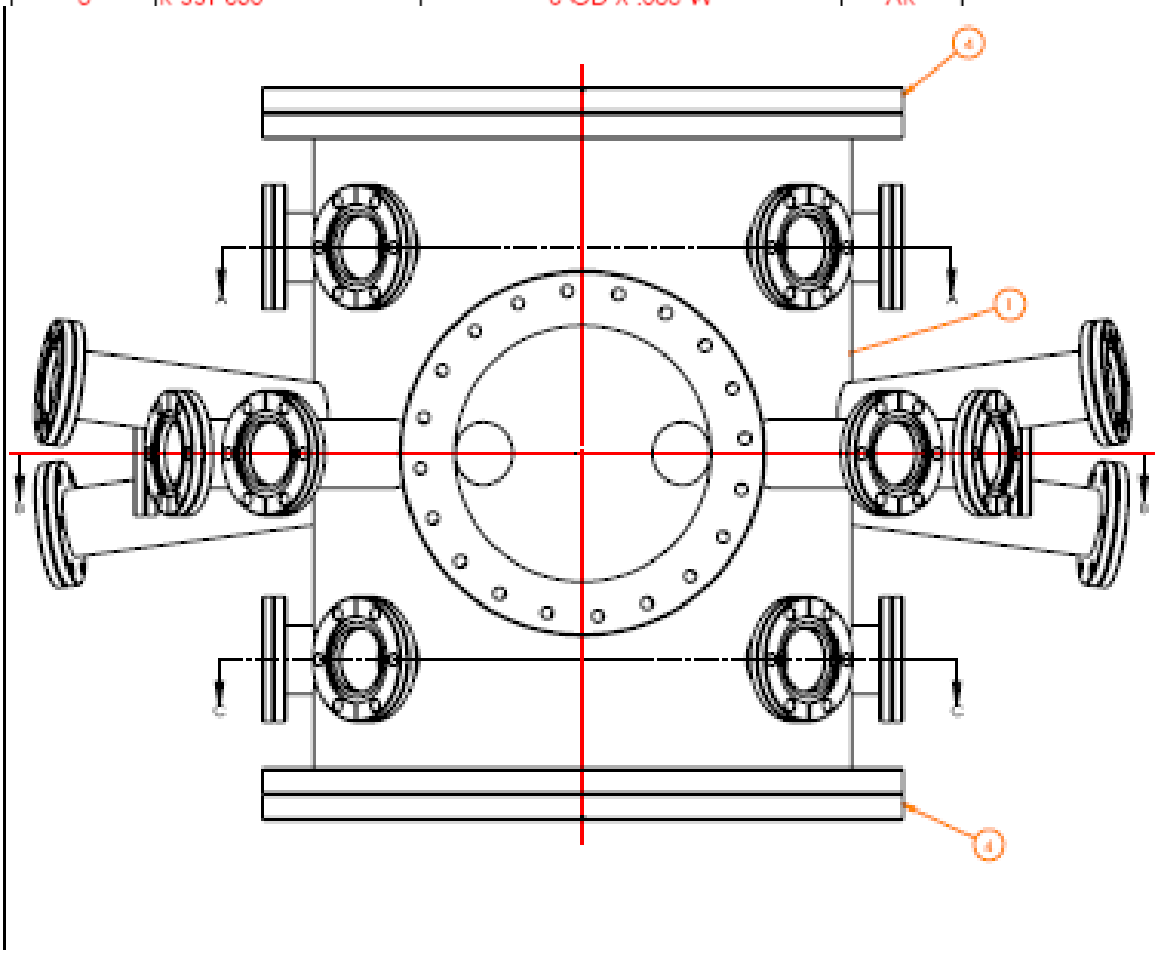

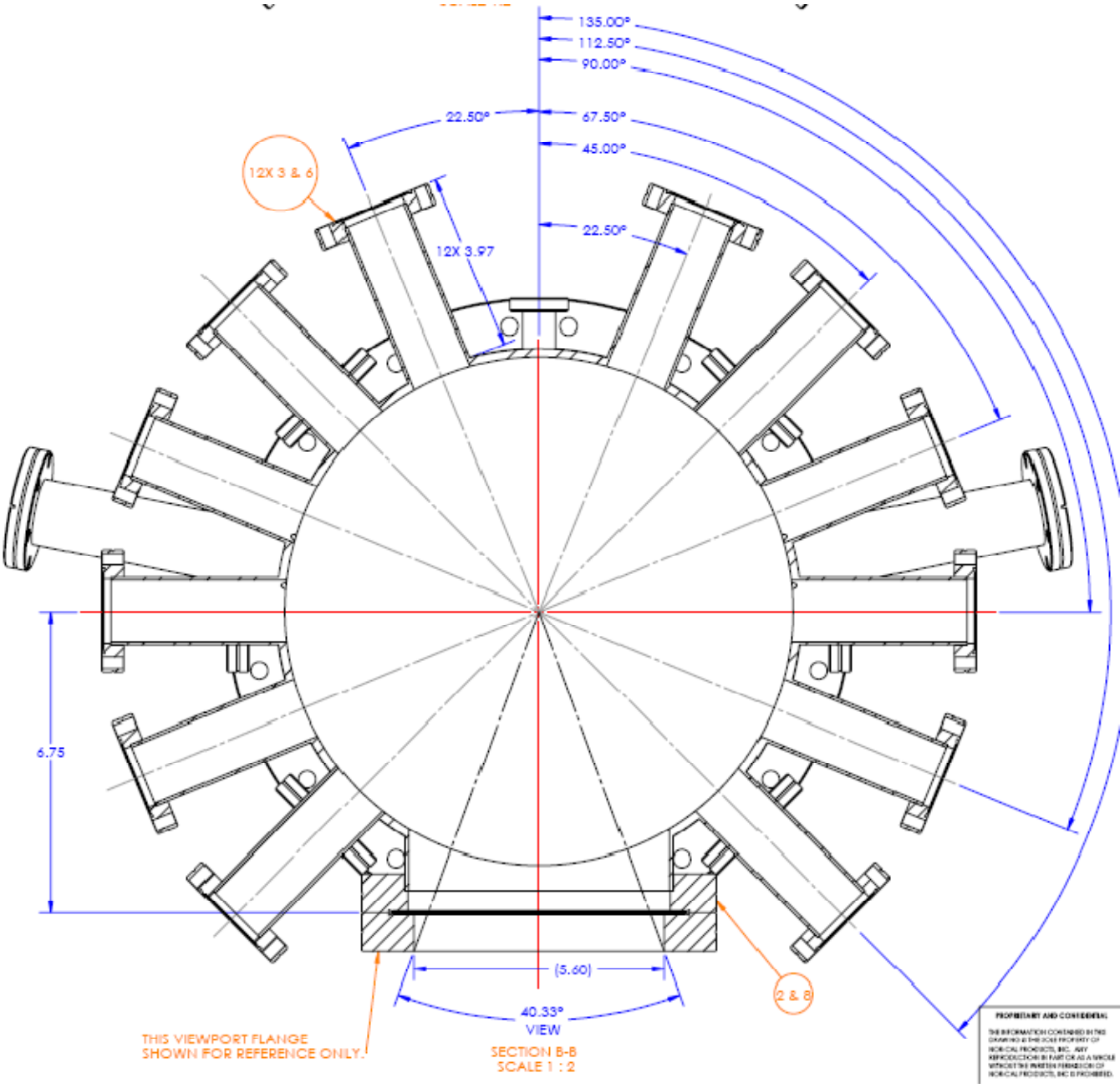
135.00°
112.50°
90.00°
22.50°
67.50°
45.00°
22.50°
12X 3 & 6
12X 3.97
6.75
(5.60)
40.33°
VIEW
2 & 8
THIS VIEWPORT FLANGE
SHOWN FOR REFERENCE ONLY.
SECTION B-B
SCALE 1 : 2

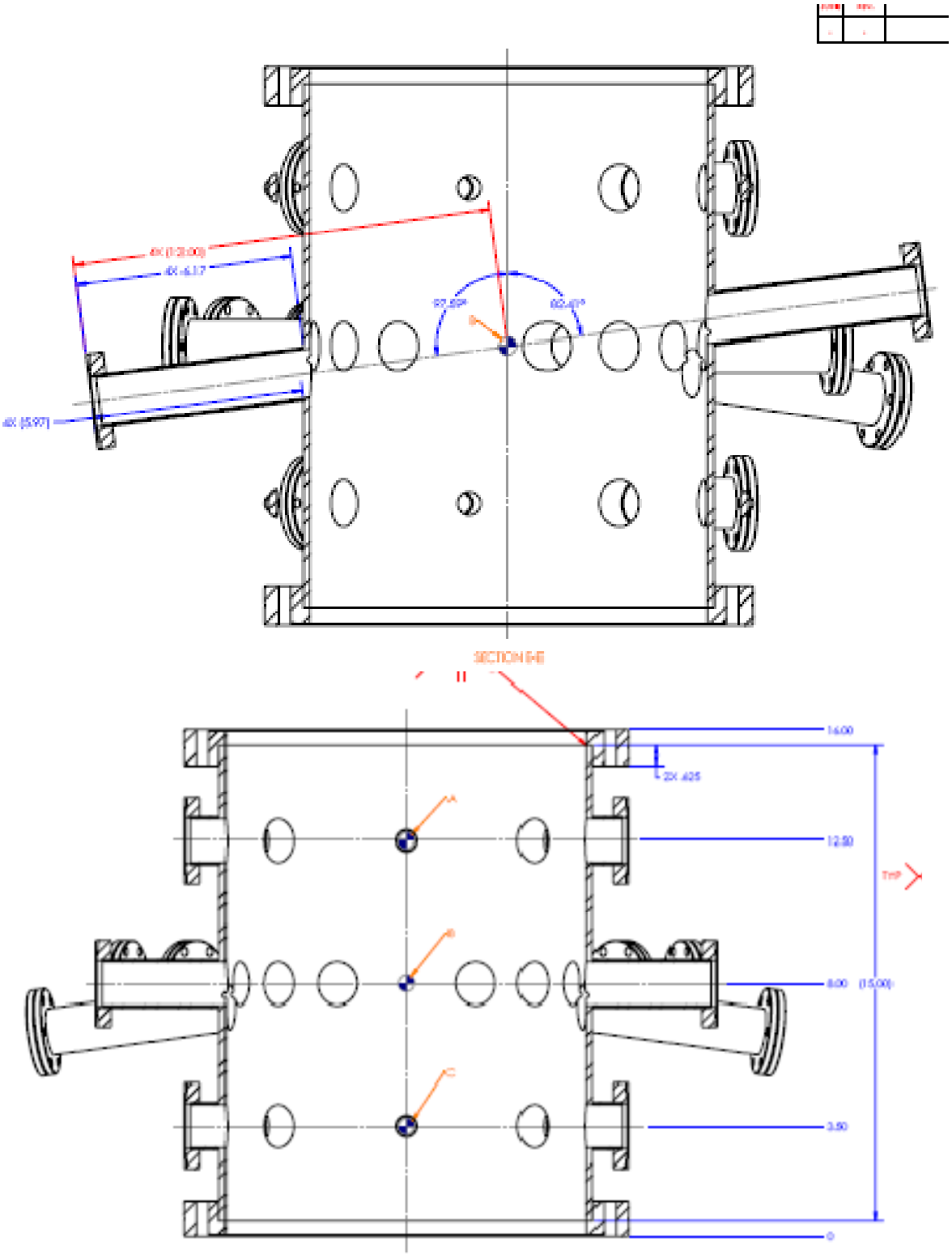
SECTION H-H
14.00
12.00
8.00
(15.00)
3.50
0
TYP

# Appendix IV.2.

## Vapor Pressure Tables

Reproduced from Radio Corporation of America, Princeton, N.J.

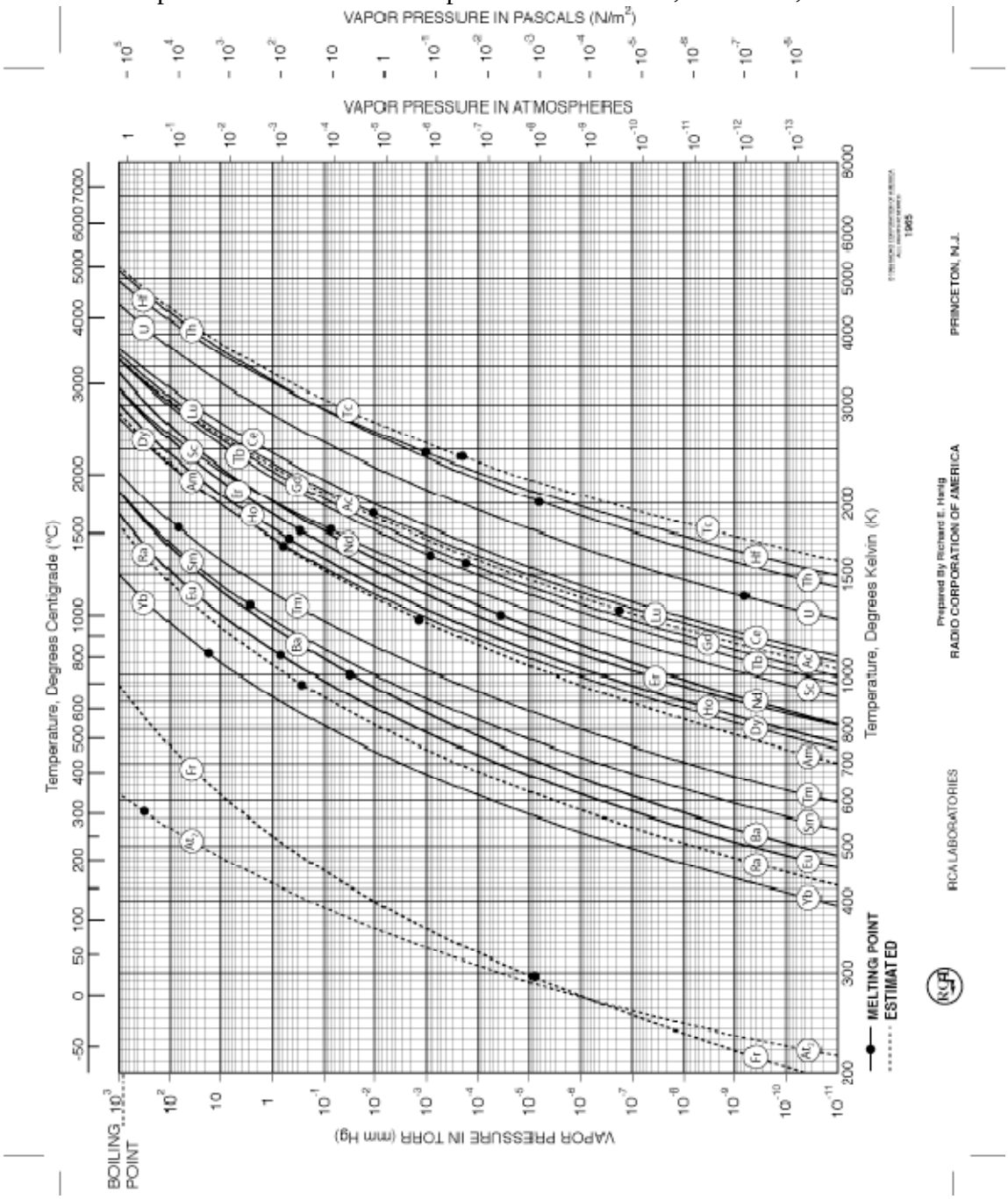

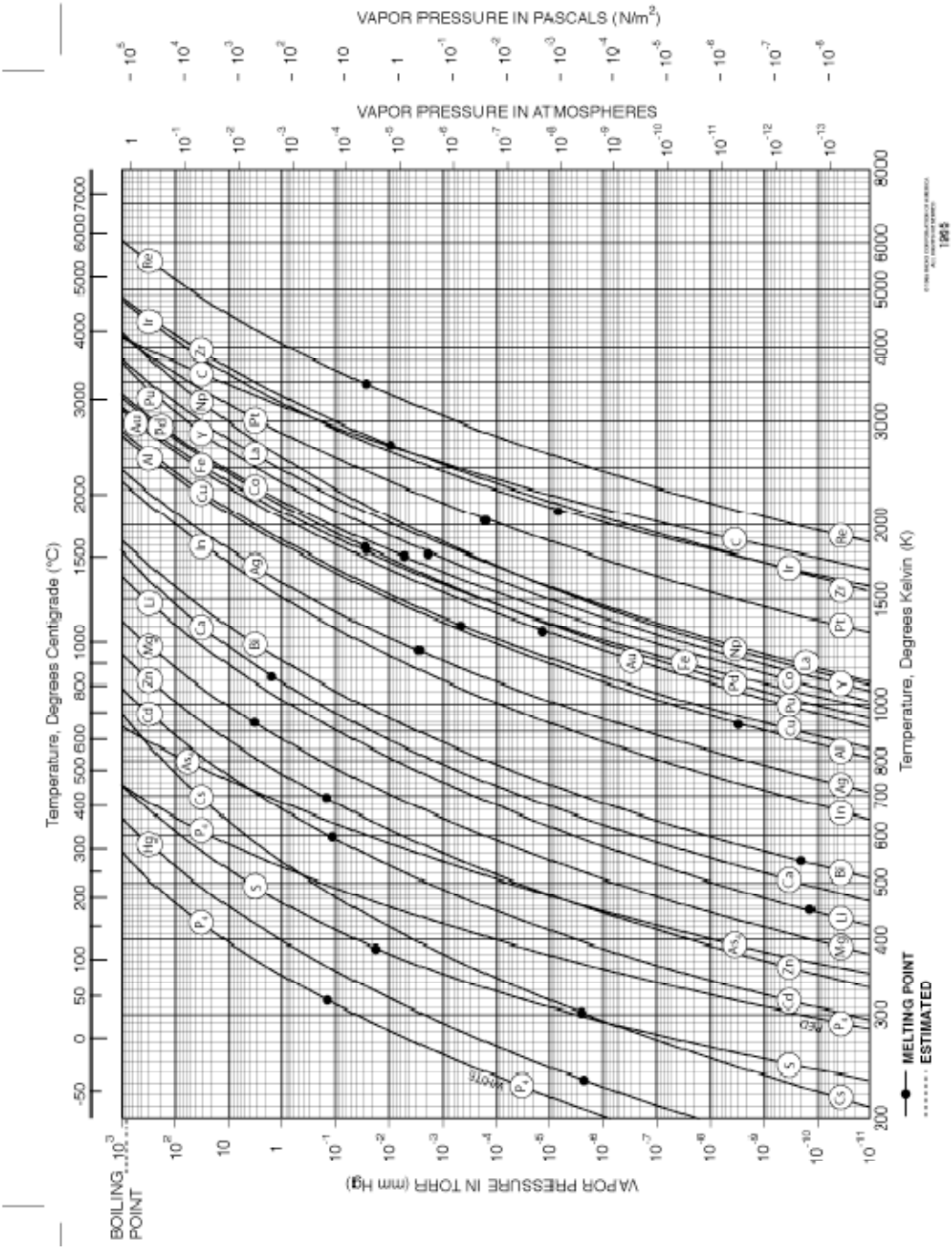
VAPOR PRESSURE IN PASCALS (N/m²)
VAPOR PRESSURE IN ATMOSPHERES
Temperature, Degrees Centigrade (°C)
Temperature, Degrees Kelvin (K)
VAPOR PRESSURE IN TORR (mm Hg)
BOILING POINT
MELTING POINT
ESTIMATED
RCA LABORATORIES
Prepared By Richard E. Honig
RADIO CORPORATION OF AMERICA
PRINCETON, N.J.

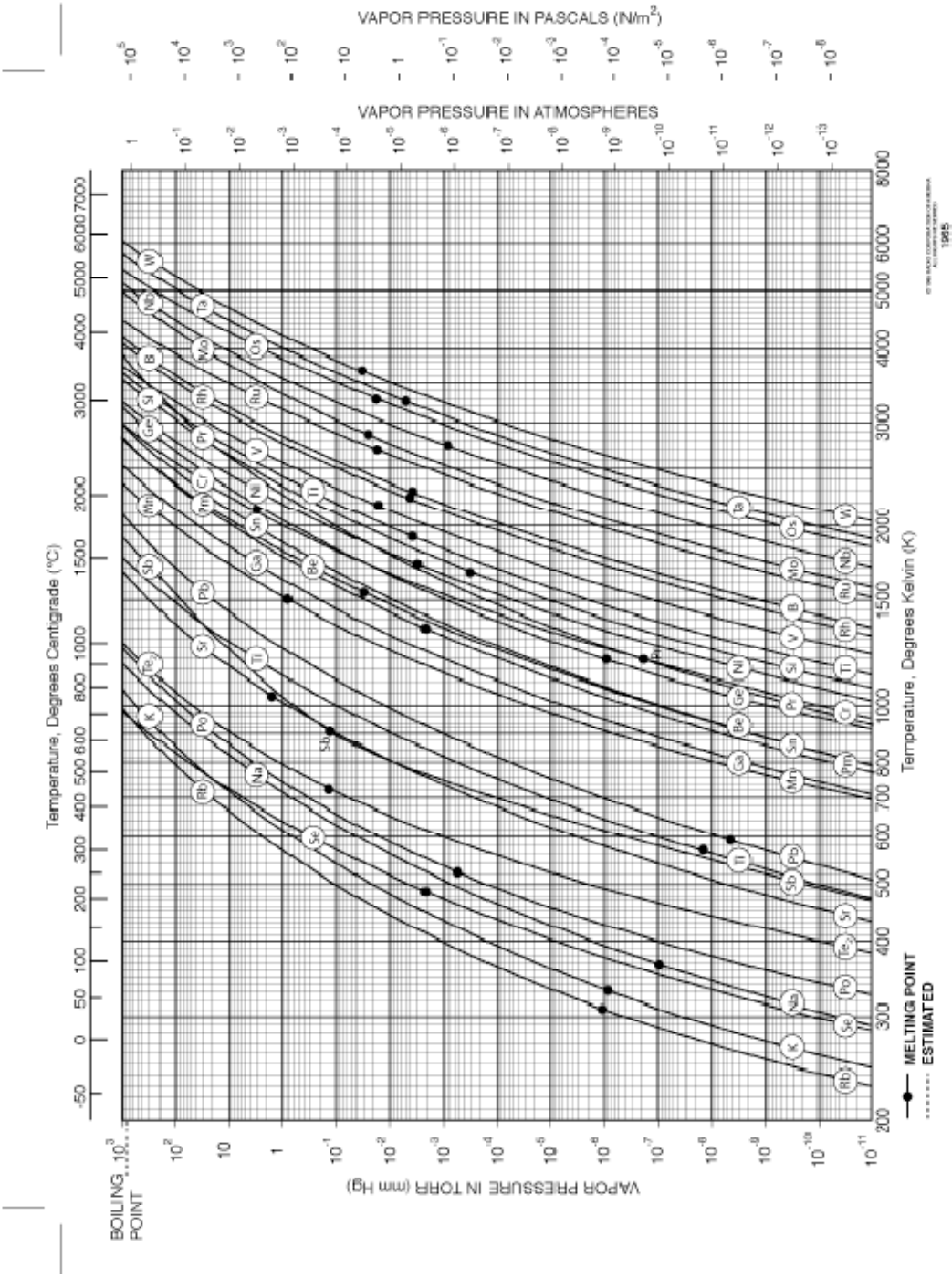
VAPOR PRESSURE IN PASCALS (N/m²)
VAPOR PRESSURE IN ATMOSPHERES
Temperature, Degrees Centigrade (°C)
Temperature, Degrees Kelvin (K)
VAPOR PRESSURE IN TORR (mm Hg)
BOILING POINT
MELTING POINT
ESTIMATED
RCA LABORATORIES
Prepared By Richard E. Honig
RADIO CORPORATION OF AMERICA
PRINCETON, N.J.
1965

# Appendix IV.3.

**PSD Laser/PSD Optomechanics, Version 1.0.**

Entry Optics

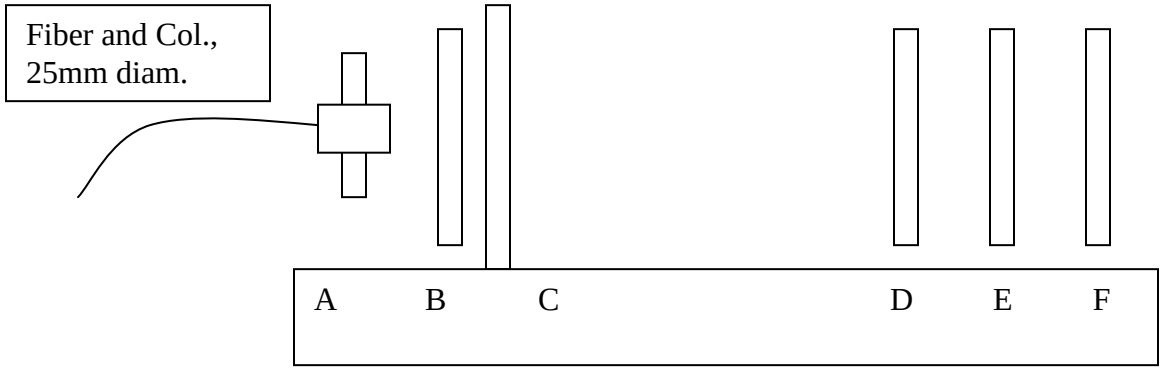


A: Collimator with holder (to 1 inch, non threaded), need Linos G061010000, (gets to microbench).

B: Then Linos Achromat, 3mm aperature, 4mm focal length G052001000, 3mm aperature, 5mm focal length G052002000, 6mm aperture, 8mm focal length G052021000. To adapt to holder, Linos G050309000, screws, G051520000, holder Linos G061010000. Rods, microbench Linos 30mm G061213000 (10), Linos 75mm G061214000.

C: Get to 2" frame. Thor LCP02. Rods, Thor SR1 (x5), SR2 (x5), ER8 (x5), ER3 (x5), ER2 (x5)

D: Second Achromat, Thor AC508-080-A1-ML (80mm, 2inch aperture), AC508-100-A1-ML (100mm, 2 inch aperture) mounted on 2 inch threaded. Adjustable mount upon rotation Thor SM2V10, mounted in Thor LCP01,

E: Iris Thor SM2D25, mounted in LCP01 (threaded 2 inch)

F: 60mm/30mm Thor LCP02, rods Thor ER1 (x4), rotation stage Thor CRM1P, reducer Thor SM1A6, Retaining rings SM1RR (x5), SM2RR (x5), SM05RR (x5), Polarizer LPVIS050 (1/2 inch linear polarizer)

PSD Optics

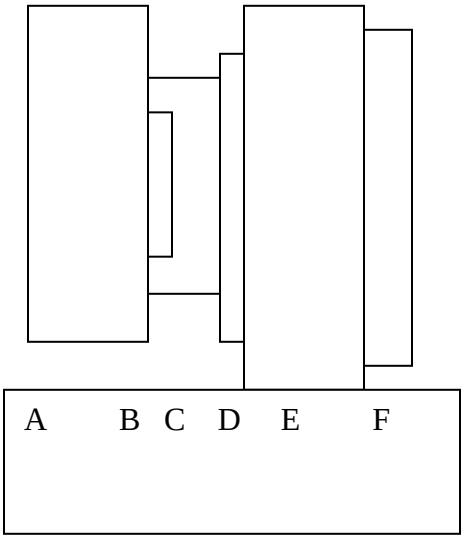


A:  PSD (SM1 thread)

B:  Band Pass Filter inside.

C:  SM1 .5inch tube

D:  Male Male SM1, Thor SM1T2, Extra locking nut, SM1NT (x2).

E:  30mm cage, SM1 thread Thor CP02T

F  Insulator to block light Thor CPG3, Rods, Thor ER1 (x4), rotation stage Thor CRM1P, reducer Thor SM1A6, Retaining rings SM1RR (x5), SM2RR (x5), SM05RR (x5), Polarizer LPVIS050 (1/2 inch linear polarizer)

# Appendix IV.4.

## Preprocessing Post/Carousel Mechanism

The post is removed for clarity, but the universal joints and the fixed-rotationally post mount are clearly visible.

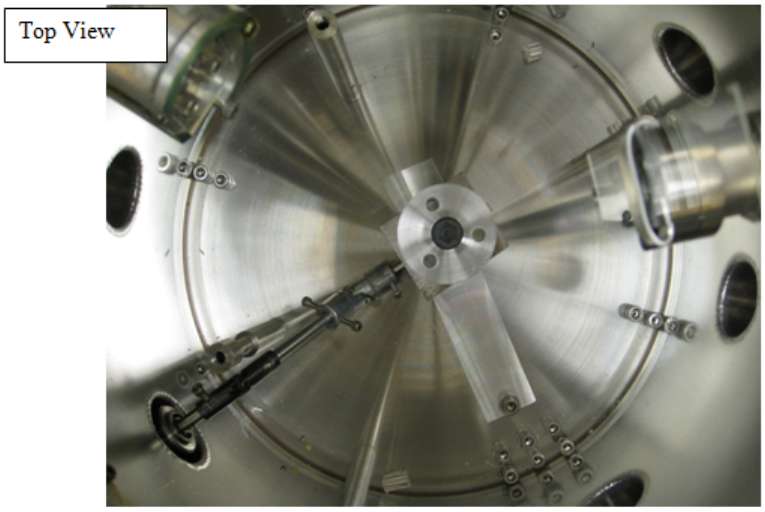


**Figure 0.1**- Preprocessing Post, Top View.

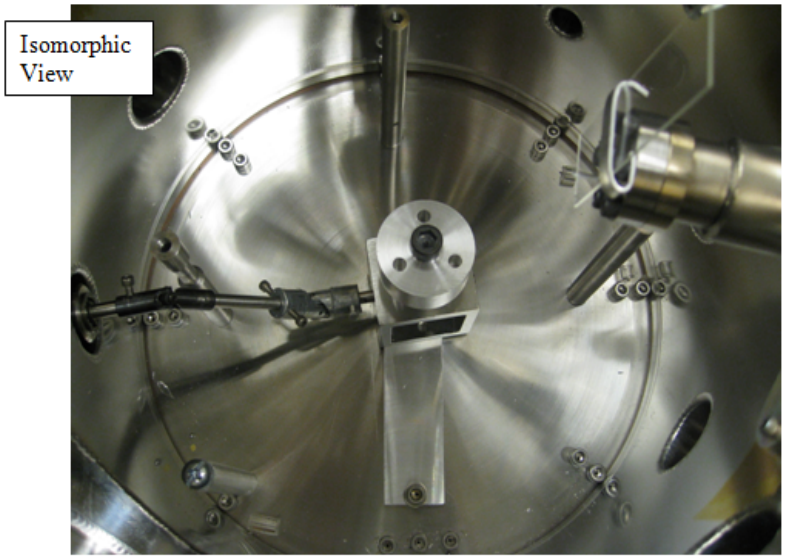


**Figure 0.2-** Preprocessing Post, Isomorphic View.

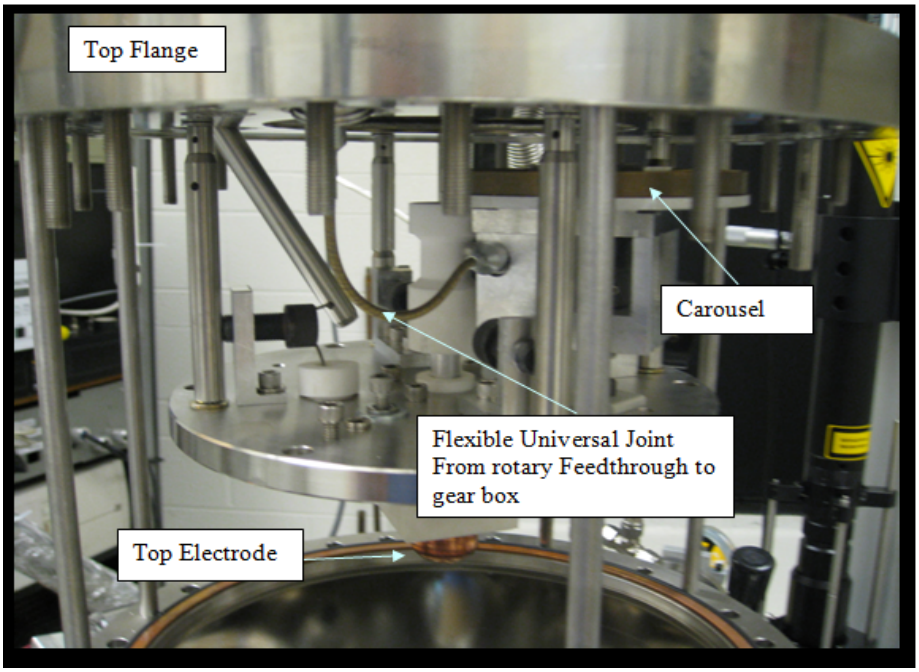


**Figure 0.3-** Carousel installed in top flange of WUBESL chamber.

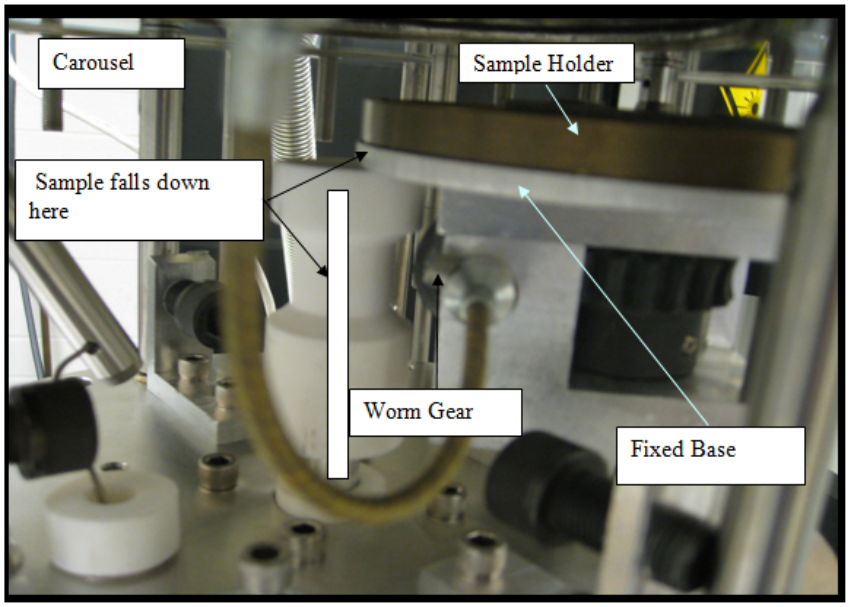


**Figure 0.4-** Carousel installed in top flange of WUBESL chamber, tight perspective.

At the time of the writing of this document, several flaws in the design had been identified, and improvements were under consideration [1]. First, in the course of an experiment, when the WUBESL is running smoothly, about 90% of samples are processed on the first attempt. However, some systems require more than one experiment conducted, either because of compositional change during a single experiment, samples of different sizes are required, or incomplete data is taken due to sample instability. This means that the carousel should be loaded with several samples of the same composition for redundancy. However, when a sample is successfully processed completely on the first attempt, the carousel design precludes the option of skipping samples. Additionally, the more samples are loaded, the more difficult it is to identify and conduct post-mortem analyses (SEM, TEM, EDS, mass loss, etc.) A solenoid shutter mechanism has been proposed to allow samples to be skipped, thus remaining in the carousel.

A complication exists, however: in the current setup, users can keep track of the samples which are loaded by counting the number of samples that fall. Unfortunately the flexible universal joint that connects the feedthrough to the worm gear has a great deal of torsional give and a proportionality between the stepper rotations and the indexing of the carousel doesn't exist with enough accuracy to predict carousel index position without an independent measure. This is being improved [1]. The flexible joint should be replaced, but an independent indexing method is also recommended. The carousel should be altered to have an additional set of holes (Figure 0.5) to allow for a brush contact that is open when the sample is aligned with the hole and closed between samples.

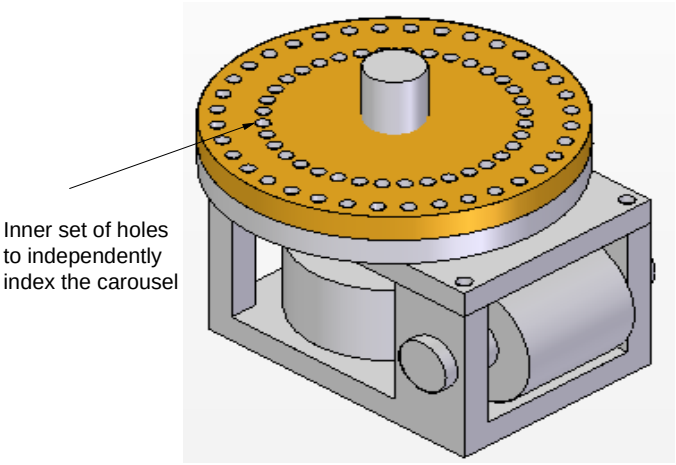


**Figure 0.5-** Proposed change in carousel to allow for independent indexing.

[1] M. Blodgett and A. Vogt, (2010).

# Appendix IV.5.

## BESL Control Algrorithm: Overview, Calling Structure, and Implementation in Matlab™.

As noted in chapter 4, the implementation of the control algorithm is done in Matlab and Simulink. The gain scheduled feedback program developed by DLR and supplied in 2008 to the Kelton research group, needed to be modified for the WUBESL. In the original development, the algorithm was written in Matlab's Simulink, converted to an executable and implemented on a dedicated PC running Reallink-32, a program that dedicates all computer functions to running the control program. The company that produced this

program was purchased by Mathworks and a similar implementation is realized through the *Realtime Workshop* and *Xpc Target*, both available through Mathworks. By and large, the programs used in the control algorithm needed little modification from their DLR form, but the changes are detailed here. A few notes on these programs: First, Simulink allows the construction of the programs of interest in a flow-diagram manor. The programs "gain3dvarq.mdl" and "echtgain3d.mdl", in particular, are written this way. Second, Real Time Workshop and xPC Target allow the creation of executable files to be run, exclusively, on a remote, or "target", PC.

A boot disk is created for the target PC on the PC running Matlab (called the "Host") and then the target is booted from the disk.[16] When xPC Target is purchased, an Ethernet PCI card is provided, and the drivers for the card can be easily downloaded. By connecting a switched Ethernet cord between the host and target, xPC Target is able to create the boot disk specific to the target, and any compiled program on the host can be downloaded to the target. Additionally, scopes of various kinds can be added to programs. Host scopes (displaying real-time data on the host) and target scopes (displaying real-time data on the target monitor) are the most useful. Third, programs can be written to output data to a target drive. An addition to Real Time Workshop can be purchased that would allow data to be downloaded to the host, but since the programs written in Matlab are used exclusively for the control, it isn't needed in the current version of the control algorithm.

[16] As of the creation of this document, and to the best of the author's knowledge, the bootdisk must be a floppy.

The flow diagram of signal routing and coordinate conventions is shown in Figure 0.1. It should be noted that the Z-direction (vertical) is a redundant measurement in this setup. However, for convenience that coordinate is read off PSD1 (Y) because this PSD is accessible during a BESL experiment, and located nearest the Beryllium exit window. These conventions should be followed whenever rewiring the BESL apparatus, however, as a test for the connectivity, if the algorithm is started without a sample floating, the directionality can be determined as follows:

-For either lateral direction, zero the PSD on the laser. When the algorithm is started the high voltage reading should be near zero, but will likely drift given even the smallest offset.

-Place an obstacle at either periphery of the PSD (extreme X or –X, for example) and watch the response of the amplifier. The shadow of the obstacle acts as the sample.

-The algorithm will act to try and bring the sample to the center. Since the field points toward decreasing potential it is a simple matter to check if the field produced conforms to the convention in Figure 0.1.

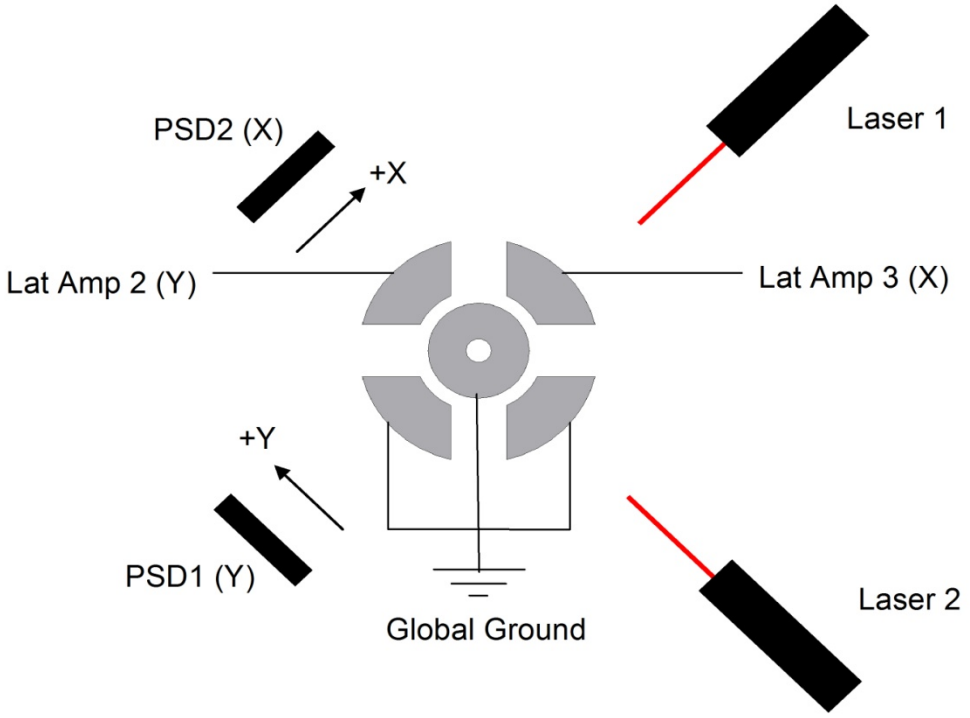


**Figure 0.1-** Top-down diagram showing the horizontal levitation positioning plane, the connections to the horizontal electrodes, and the nomenclature for the positioning system components in WUBESL.

A more detailed discussion of the positioning electronics, wiring, expected voltage behavior and performance characteristics can be found in the manual "ESL Positioning Control System Hardware" by Aaron Logan, Austin Lyons, Justin Mai available from A. I. Goldman, at Ames Laboratory, Iowa State University. This manual is an excellent reference for the details of the Op Amp wiring and signal routing.

In the WUBESL, there are three levels of gain-scheduled control implementation. First, the mass and radius of the sample are input and the control parameters are determined. Second, the launch and the response to rapid charge modulation are modeled

and the *x*, *y* and *z* positions are analyzed. Finally, the model is build, downloaded to the target and run. A few notes: The details of and principles behind the control algorithm can be found in T. Meister *et al., Gain-scheduled control of an electrostatic levitator* [2]. Tilo Meister's thesis also describes the DLR development of the ESL and the algorithm, however, the document is written in German. A functional translation of *Handbuch_ESLII Christians Erweiterung* is available which outlines the components and basic principles of operation of the DLR ESLII.

Below is the list of programs required for the implementation of WU-GSF. All of the programs have to be in the Matlab directory or in the working directory.

echtgain_fix_08102010_4_xx_mxxx_rxxx.mdl

gain3dvarq.mdl

hinfpar.m

ControlGUI.m

ControlGUI.fig

ControlGUI.asv

inter_new_controller_gain.m

gainmexkoeff.c

kalm3_3d_decplz.c

sislevit2d.mdl

Slevit2d.m

Slevit3d1.m

DMSFSYN.m

gainslevit3d1.m

gainslevit3d2.m

The Following Table outlines the calling structure and brief description of the various routines and subroutines. A more practical document with details about sample specific parameters, "Standard Operating Procedure - Washington University Beamline Electrostatic Levitator, version 2.1."

| **Program** | | **Purpose** | |
|---|---|---|---|
| ControlGui.m | | This program takes as input mass and radius and passes those parameters through the subroutines by rewriting the files. | |
| gainmexkoeff.c | | This program takes p1 and p2 and calculates control parameters | |
| kalm3_3d_decplz.c | | This program takes the mass, m, as input and discretizes the extended kalman filter. | |
| inter_new_controller_gain.m | | This program takes the mass, m, and the radius, r, as input and then the goes through the process of selecting the parameters for the LMI region for gain scheduled control. The user enters the coordinates of the elliptical region for horizontal and vertical control, and the program attempts to find feasible eigenvalues in that region. | |
| | gainslevit3d1.m | | |
| | DMSFSYN.m | | |
| | hinfpar.m | | |

| | | | |
|---|---|---|---|
| | gainslevit3d2.m | | |
| | sislevit2d.mdl | | |
| | | Slevit2d.m | |
| gain3dvarq.mdl | | This programs simulates launching and charge change based on the eigenvalue solutions in the LMI pole region. | |
| | kalm3_3d_decplz.c | | |
| | gainmexkoeff.c | | |
| | Slevit3d1.m | | This program discretizes and evolves the state space model. |
| echtgain3d.mdl | | This program is compiled last, and then downloaded to the target and actively controls the levitation algorithm. | |
| | kalm3_3d_decplz.c | | |
| | gainmexkoeff.c | | |

To execute the programs, in Matlab, change the working directory to wherever the files are located (copy the entire folder on the hard disk).

-Run ControlGui.m and enter the relevant parameters. For instance, a r = 1.25 and m = 53.3 for Zr.

-run inter_new_controller_gain.m

Type *e* ↵ (enter)

0.69 ↵

0.3 ↵

0.1 ↵

*q* ↵

*e* ↵

0.67 ↵

0.3 ↵

0.01 ↵

*q* ↵

-when gain3dvarq.mdl opens, press play and double click on the z, x, and y plots. This simulates the launch and then activation of the UV source (change in charge).

- echtgain_fix_08102010_4_xx_mxxx_rxxx.mdl opens, and rename the file, replacing the xx's with the appropriate parameters (i.e. echtgain_fix_08102010_4_Zr_m533_r125.mdl)

-Go to *tools-realtime workshop-build model.* This model can now be downloaded to the target and run.